DISCLAIMER

Identification of Faults Susceptible to Induced Seismicity

Final Report

1. DOE Award and Report Information:

Federal Agency and Organization: DOE Office of Fossil Energy

Award Number: DE-FE0031685

Project Title: Identification of Faults Susceptible to Induced Seismicity

Principal Investigator: Scott Frailey, PhD, PE
Senior Reservoir Engineer
sfrailey@illinois.edu
217-244-7412

Date of Report Submission: July 6, 2023

UEI: Y8CWNJRCNN91

Recipient Name: University of Illinois at Urbana-Champaign

Recipient Address: 1901 South First Street, Suite A, Champaign, IL 61820

Original Project Period: October 1, 2018 through September 30, 2021

Revised Project Period: October 1, 2018 through December 30, 2022

Signature 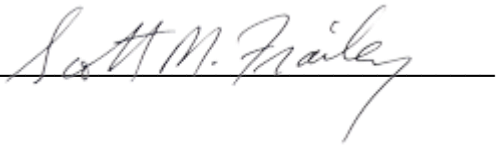 **Date: July 6, 2023**

ACKNOWLEDGEMENT OF FEDERAL SUPPORT

This material is based upon work supported by the Department of Energy under Award Number DE-FE0031685.

ADDITIONAL ACKNOWLEDGMENTS

Scott Frailey, Principal Engineer at the Illinois State Geological Survey (ISGS) at the University of Illinois at Urbana-Champaign (UIUC), coordinated the multi-institute research effort including data transfers and protocols, defining the scope of the project, and facilitating project meetings. Additionally, he led the ISGS pressure modeling calibration process, interpreted modeling results, and proposed new geologic features that would improve the calibration. He directed the teams use of the proposed workflow.

Mansour Khosravi, Associate Reservoir Geologist at the ISGS-UIUC, led Task 2 and developed the geologic conceptual and geocellular models for the SoS project. His expertise in regional geologic studies, formation microimager (FMI) analysis and interpretation, and geocellular modeling contributed to the final report, in which he authored the sections related to these subtasks.

James Damico, Assistant Geologist with ISGS-UIUC, contributed to the SoS project by constructing the Precambrian fracture model. His work provided insights into the subsurface structure and geological history of the region. Using the Petrel software, Damico developed a representation of the fracture model, which was an important component in the project.

Hongkyu Yoon, Principal Member of Technical Staff at Sandia National Laboratories (SNL), led Task 3 of the SoS project and contributed to the final report with a focus on the development of multiple machine learning models for event detection of continuous raw microseismic data, clustering and focal mechanism analysis of located events, source location identification of newly detected events, and fault plane identification in the Precambrian formation.

Ruben Juanes, Professor of Civil and Environmental Engineering at the Massachusetts Institute of Technology (MIT), was the lead of Task 4 and responsible for the work on computational modeling of coupled flow and geomechanics. This work allowed making predictions of the state of stress in faults associated with seismicity at the IBDP site and elucidated the role of basement faults as fluid conduits for pressure propagation, which ultimately allowed explaining the observed seismicity. He interacted closely with the other project Task Leaders and was the research supervisor of Josimar Silva, whose contribution is listed below.

Ahmed Elbanna, Associate Professor of Civil and Environmental Engineering at the UIUC, was the lead of Task 5 and oversaw the task's overall progress. He led the discussions on the design of numerical simulations and the analysis of the results, as well as edited and reviewed Task 5's text in the final report. He advised two graduate students, Mohamed Abdelmeguid and Md Shumon Mia, whose contributions are listed below.

Oladipupo Babarinde, Assistant Geologist at ISGS-UIUC, contributed to the pressure modeling effort for the SoS project. His expertise in geologic modeling, carbon storage, structural and geomechanical characterization, and seismic interpretation contributed to the final report, in which he authored the pressure modeling section of Task 4.

Josimar Silva, a postdoc at MIT, conducted the coupled flow-geomechanics modeling in Task 4. This involved generating an unstructured mesh adapting to faults and horizons, populating this mesh with hydraulic and mechanical properties from a geocellular model provided by ISGS, and running the flow

model and the geomechanics model with variable parameters to match history and extract state of stress at the faults.

Junzhe Jiang, a former visiting research scholar to ISGS from Texas Tech University, conducted several reservoir simulations and data analyses for the pressure modeling subtask of the SoS Project.

Michael Fehler, a Senior Research Scientist at MIT, contributed to the construction of fault planes using located events in the catalog for Tasks 2 and 4 modeling.

Norimitsu Nakata, a former postdoc at MIT, contributed to travel time analysis of waveform data in the catalog for source location estimation.

Daniel Lizama, a PhD intern student at SNL, conducted development of multiple machine learning models for event detection of continuous raw microseismic data and source location identification of newly detected events, and contributed initial draft content for the final report.

Rachel Willis, a former PhD intern student at SNL, conducted development of unsupervised fingerprint-based machine learning model for clustering of microseismic events and focal mechanism analysis and contributed initial draft content for the final report.

Mohamed Abdelmeguid, a graduate student at UIUC, conducted numerical simulations, carried out data analysis of the results, prepared figures, and contributed initial text to the final report.

Md Shumon Mia, a graduate student at UIUC, conducted numerical simulations, carried out data analysis of the results, prepared figures, and contributed initial text to the final report.

Michelle Johnson, certified research administrator for ISGS-UIUC, was the lead administrator on the project and handled all non-technical aspects including reporting, budget, meetings, and communication between team members.

Jill Monroe, technical editor for ISGS-UIUC, handled the editing for the SoS project's quarterly reports and final report, and helped with communication between team members.

Hannes Leetaru and Sherilyn Williams-Stroud, senior geologists from ISGS-UIUC, provided guidance and expertise in geocellular modeling, fracture modeling, and structural geology of the Illinois Basin. Their input proved invaluable in ensuring the accuracy and reliability of the models and interpretations made throughout the project.

We acknowledge Schlumberger for the use of their Petrel and Techlog software, MathWorks for the use of MATLAB and the MATLAB Reservoir Simulation Toolbox (MRST), Computational Infrastructure for Geodynamics for the use of PyLith, and finally Landmark Graphics for use of their software via the University Donation Program.

DISCLAIMER

This report was prepared as an account of work sponsored by an agency of the United States Government. Neither the United States Government nor any agency thereof, nor any of their employees, makes any warranty, expressed or implied, or assumes any legal liability or responsibility for the accuracy, completeness, or usefulness of any information, apparatus, product, or process disclosed, or represents that its use would not infringe privately owned rights. Reference herein to any specific commercial product, process, or service by trade name, trademark, manufacturer, or otherwise does not necessarily constitute or imply its endorsement, recommendation, or favoring by the United States Government or any agency thereof. The view and opinions of authors expressed herein do not necessarily state or reflect those of the United States Government or any agency thereof. The findings, opinions, and recommendations expressed are those of the author and not necessarily those of the University or its Project Director.

Sandia National Laboratories is a multimission laboratory managed and operated by National Technology & Engineering Solutions of Sandia, LLC, a wholly owned subsidiary of Honeywell International, Inc., for the U.S. Department of Energy's National Nuclear Security Administration under contract DE-NA0003525.

TABLE OF CONTENTS

ABSTRACT

Central to the work documented in this report is the capability of geocellular models to represent the geologic conceptual model updated with fault identification from machine learning and joint inversion modeling of microseismic data measured and recorded as a consequence of CO_2 injection at a field demonstration site: the Illinois Basin - Decatur Project (IBDP). This work required seven unique geocellular models with 100s of simulated variations to gain a very high degree of confidence in the identification of geologic features present that contributed to induced microseismicity at IBDP. All forward modeling: pressure modeling, stress modeling, and seismic modeling used the same geologic conceptual model and representations of that model at different scales. The pressure modeling and poroelastic modeling created "snapshots" of pore pressure and stress field changes at different times during CO_2 injection, in which microseismic events were clustered (in time). These pressure and stress snapshots, within the framework and architecture of the geologic conceptual model via the geocellular model, informed the single fault and fault network models to ascertain the likelihood of fault movement (seismic or aseismic).

The outcomes of the pressure, stress, and fault/fault network (seismic) modeling confirmed that the faults in the geologic conceptual model in Task 2 were likely the source of microseismic events measured at IBDP and acted as conduits for pressure to be transmitted from the injection interval into the Precambrian crystalline basement rock. This closely coordinated and integrated unique modeling approach was conducted to prove the viability of our proposed workflow 1) to better resolve crystalline basement faults, 2) detect subseismic faults that could be activated by injection, 3) increase the certainty in fault detection and their susceptibility to release seismic energy, and 4) understand transmission of pressure vertically from the well to the underlying fractured crystalline basement.

The proposed methodology was effective in guiding an iterative process of calibrating forward modeling results based on similar geocellular models while honoring the geologic conceptual model (i.e., characterization data and knowledge of regional geology); this led to higher level of certainty in the identification of fault/faults zones to control seismicity and transmission of pressure to the regions of recorded and located injection induced seismicity.

INTRODUCTION

Predicting and controlling the subsurface seismic response to fluid injection continues to be a challenge to all subsurface injection, including CO_2 storage. Research is ongoing to identify geologic features that contribute to injection-induced seismicity and the role of stress and pore pressure variations in triggering these seismic events. Pre-existing, critically stressed faults that underlie injection intervals in a crystalline basement rock tend to be the most likely geologic feature that may release seismic energy.

The physical mechanisms associated with induced seismicity due to anthropogenic activities have been extensively studied in the past decade due to the increase in seismicity in central U.S. associated with wastewater injection in the subsurface (Segall and Lu, 2015; Keranen and Weingarten, 2018; Zhai et al., 2019; Alghannam and Juanes, 2020). Other anthropogenic activities associated with induced seismicity cases are natural gas storage (Dost and Haak, 2007; Cesca et al., 2014), hydraulic fracturing (Eyre et al., 2019; Schultz et al., 2020), enhanced geothermal system stimulation (Deichmann and Giardini, 2009; Ellsworth et al., 2019) and, to a lesser extent, carbon capture and storage (CCS) in geological formations (White and Foxall, 2016). Although CCS programs have yet to store significant amounts of CO_2 in the subsurface, its similarity with wastewater injection raises concerns regarding its potential to induce seismicity that might result in CO_2 leakage to shallower formations (Zoback and Gorelick, 2012). Therefore, it is imperative to understand the hydraulic and geomechanical conditions that enable induced seismicity associated with CO_2 injection activities (Juanes et al., 2012; Vilarrasa and Carrera, 2015).

However, neither large nor pilot-scale carbon storage projects have induced any perceivable earthquake to date (White and Foxall, 2016; Vilarrasa et al., 2019). The Decatur, Illinois, carbon capture and storage (CCS) site—also called the Illinois Basin – Decatur Project (IBDP)—is the first commercial site in the United States. Since November 2011, over 1,000 tonnes of CO_2 per day have been injected into the Mt. Simon saline reservoir. The reservoir targeted for CO_2 injection is the lower part of the Mt. Simon Sandstone, which is laterally extensive with porosity as high as 28% and permeabilities of over 1,000 mD. During CO_2 injection, microseismicity (magnitude 1.17) was detected (Birkholzer and Zhou, 2009; Leetaru and Freiburg, 2014). The formation covers the Argenta and Precambrian crystalline basement with a sharp unconformity (Leetaru and Freiburg, 2014). The keys to understanding the release of seismic energy are the physical, hydraulic, mechanical, and seismic characteristics of the fault and the magnitude and direction of the in situ principal stresses. However, the mechanisms of stress transfer from highly permeable storage units to very low (matrix) permeability but fractured and faulted crystalline basements to the locations in the earth where seismicity has been located is not well understood.

During the three-year period (2011-2014) of CO_2 injection and subsequent shut-in, microseismicity was recorded at the Illinois Basin Decatur Project (IBDP), and over 10,000 events were recorded, and 4,848 events were located (Bauer et al., 2019). Many of the locatable events were in the underlying crystalline basement, while very few were located in the relatively high permeability storage unit. The data from this site was used intensely for this work.

For storage purposes, the deepest, porous, and permeable geologic formation has noted advantages. Generally, there are no mineral resources below or within this formation (e.g., oil or coal); consequently, there are fewer wellbore penetrations of the caprock, which is the most noted source of a caprock breach. Additionally, there are fewer legal issues when mineral ownership is not a part of the storage site development. Deeper storage units have higher pressure; therefore, CO_2 can be stored with greater density, which increases storage efficiency.

Large-volume wastewater disposal into sedimentary rocks immediately overlying crystalline basement rocks has been directly attributed to earthquakes in the central US (Zoback and Gorelick, 2012; Ellsworth, 2013; Keranen et al., 2014; Hincks et al., 2018). CO_2 injection, as part of a storage demonstration project, into similar formations has caused microseismicity (IEAGHG, 2013; White and Foxall, 2016; Makhnenko et al., 2020). With few exceptions, crystalline basement rocks (e.g., granites and rhyolites) are fractured and, depending on the geological history, include faults. Therefore, large-scale CO_2 injection into basal sedimentary rocks is expected to exhibit similar seismic challenges associated with large-volume wastewater disposal.

The term "fracture" includes two subsets: those with no movement or offset (joints) and those with movement or offset (faults). Characteristics of joints are limited to the fracture or discontinuity within the host rock and are expected to change the pressure distribution that causes fluid flow due to different hydraulic properties of the fracture compared to the surrounding host rock. The poroelastic effect of a fracture compared to the intergranular/intercrystalline porosity of a host rock will change the means by which changes to the stress field are distributed within the host rock. Unlike joints, faults may be associated with larger regions (i.e., fault zones) adjacent to the actual fracture. (In this report, use of "fault" includes any zone around the fault that causes alternation of rock properties from the host rock.) The hydraulic and mechanical properties of the fault zone can be grossly different from a host rock and a joint (Scholz, 2002). Fault zones may be more or less permeable (relative to host rock) and act as a partial or complete barrier to fluid flow. Moreover, a fault zone may be relatively softer or harder and transmit stress differently than the host rock. Because faults are a consequence of the movement of large bodies of rocks moving passed each other, there is likely a buildup of stress near the fault that can be released when the stress field is changed (e.g., through injection). This is a CO_2 storage challenge: predicting and controlling injection-induced seismicity from changes to the stress field.

The primary objective of this project (herein referred to as the State of Stress project or SoS project) was to predict the presence of faults susceptible to movement in the presence of fluid injection as a consequence of vertical pressure migration from the storage unit to the crystalline basement. These faults included those difficult to resolve with traditional interpretations of surface seismic: faults with no or minimal offset, faults in the crystalline basement where no seismic reflectors are present, subseismic faults (due to size), and faults undetected (e.g., due to unfavorable orientation with surface seismic survey). To accomplish the primary objective, the following sub-objectives were to: 1) identify the presence of faults at a well characterized field site using traditional interpretations of surface seismic and interpretation of injection induced seismicity, 2) model changes to the in situ stress field before and after fault slippage, and 3) explain transmission of pressure and stress perturbations between the storage unit and the crystalline basement.

CURRENT STATE-OF-THE-ART TECHNOLOGIES

Surface seismic surveys are the most common technology used to identify faults that have vertical offset that is greater than the vertical resolution of the seismic data's resolution. Faults identifiable with surface seismic data must have vertical offset of correlatable seismic reflections); consequently, there is always uncertainty related to the presence of additional faults (i.e., subseismic faults) from seismic interpretation. These challenges are known but have historically been of less importance because objectives were to find larger features that cause trapping of fluids and, to a lesser degree, injection-induced seismic activity. However, large-scale injection projects necessitate understanding of the presence of all faults that may lead to seismic events.

Faults can be identified in drilled wellbores only when they coincidentally intersect the wellbore. Nevertheless, when this happens, the fault is a distinguishable feature in extracted core and on modern well logs (e.g., formation microresisitivity imaging tools) (Gaillot et al., 2007). However, this is usually limited to a single fault characterization and the happenstance that a drilled well crossed a fault zone. Various wellbore phenomena (e.g., wellbore breakouts) can indicate stress directions. After completion, injection tests (e.g., step rate tests) can measure fracture propagation pressure, which is related to the strength of rocks and may lead to understanding the characteristics of existing fractures. Single (e.g., injection fall-off) and multiwell (e.g., pulse) pressure transient tests may detect faults depending on the contrast of flow properties between the fault and the host rock. For a multiwell test, the fault would have to be located between two or more wells.

In addition to the presence of a fault, the state of stress and orientation of the fault with respect to the stress field are of equal importance. Surface seismic surveys are not able to assess stress in the subsurface. Therefore, calculations are required based on geophysical surveys of drilled wellbores or laboratory tests on rock samples. From direct injection, analyses and interpretation of injection pressures are useful to understand near wellbore features but provide less unique results in the farfield primarily because numerous combinations of various geologic heterogeneities can yield the same injection pressure response. Most analyses of microseismic data have been limited to identifying and locating individual events from the recorded data, including estimates of the energy released.

Our research used existing models that were tested in similar environments as separate and unique models but not as an integrated method, validated with field data from a CO_2 injection storage site.

SCIENTIFIC AND ENGINEERING PRINCIPLES

The geologic conceptual model, which was derived from IBDP characterization data and well-established regional geology, was the basis of every forward simulation model. In forward modeling, a geocellular model represented the geologic conceptual model. An essential part of the iterative methodology (Figure 1) was changing hydraulic and mechanical properties of the fault/fault zones and host rocks to improve each model's calibration to IBDP data; however, before accepting the change in any property, a check was necessary to ensure consistency with the geologic conceptual model. If the change was not consistent, a rigorous review of the geologic conceptual model was made so that the change was believable and had geologic context supported by data. If the geologic conceptual model could not support the change, it was rejected, and the forward modeling calibration process continued in search of geocellular model that could be supported geologically.

Machine learning and inversion modeling were used to develop the fault/fault zone aspect of the geologic conceptual model by applying new methods to the recorded IBDP microseismic data. There have been considerable advances in multivariate (joint) inversion methods that used coupled flow–geomechanics to model the propagation of pore pressure, fluid saturations, and fault stresses. This permitted the assimilation of time-varying data, e.g., reservoir pressure (multi-level downhole pressures at wells), and passive seismic (i.e., microseismic data). Machine learning for fault detection and interpretation of microseismic wave fields explored a recent deep-learning success (Perol et al., 2018) in classification problems (e.g., convolutional neural network) to identify seismic phases from microseismic events and their wave patterns (Yoon et al., 2015; Rong et al, 2018). This extracted salient features in the data set, e.g., local discontinuity. All faults identified and characterized had to be consistent with the

geologic conceptual model through an iterative process before inclusion in a geocellular model used in forward modeling.

We tested methodology that included a series of integrated forward and physics-constrained, data-driven (inverse) models of faults to estimate changes to the in situ stress field, and to explain pressure perturbations between the injection interval and the basement (Figure 1).

Three forward modeling types were used: pore pressure modeling, poroelastic modeling, and seismic modeling. The pore pressure modeling used multiphase flow principles using relative permeability. The primary purpose of this modeling was to identify a finely gridded geologic model (of the geologic conceptual model) that would lead to the best calibration of IBDP pressure and saturation data. Compared to other models, the pore pressure model would run faster with smaller grid cells to improve the calibration.

The poroelastic model couples multiphase flow with geomechanics capable of simulating static and dynamic stress evolution with localized deformation and frictional failure along faults. A distinctive feature is the geometric complexity, by adapting to the various sets of faults present, within and below the injection interval. We tested correlations between the spatio-temporal distribution of micro-seismic events at IBDP and propagation of the pore pressure perturbation as well as the elastic stress changes. For faults hydraulically connected to the injection interval, direct diffusion of pore pressure was assessed to destabilize faults. For isolated and sealed faults, direct diffusion ability to destabilize a fault was simulated by varying basement properties and injection operations. Indirect transfer of stresses to perturb faults without direct diffusion of pore pressure was studied.

To understand the evolution and clustering of microseismicity in the context of fault movement, we forward modeled the relationship between injection and fault slip using a novel finite element-spectral boundary integral model of slip instabilities on a single fault (Hajarolasvadi and Elbanna, 2017). Our approach was unique in resolving near-fault heterogeneities by studying the response of a fault subjected to slow, long-duration tectonic loading, intermitted with different fluid injection scenarios.

Using system modeling, we studied the response of interacting faults to fluid injection and the seismicity rate and magnitude based on the changes in Coulomb stress (Dietrich, 1994; Segall and Lu, 2015; Kanamori and Brodsky, 2001; McGarr, 2014; Galis et al., 2017). This was done by using a fully coupled poroelastic model (Jha and Juanes, 2014) and simplified boundary element representation of fault slip coupled with the complex fluid pressure distribution from the injection process (Richards-Dinger and Dieterich, 2012). Physics of slip on each fault was approximated so that longer periods of time could be simulated, thereby producing statistically meaningful seismicity patterns.

The integration of these models' results hinged on the geological/geocellular model. A comparison of the models' output and available field data (e.g., microseismicity) informed the conceptual geologic model. The difference between numerical and conceptual model predictions was resolved iteratively by updating the geocellular models with new geological features identified from the numerical modeling results. In other words, all models were required to have complete basis in the geologic conceptual model.

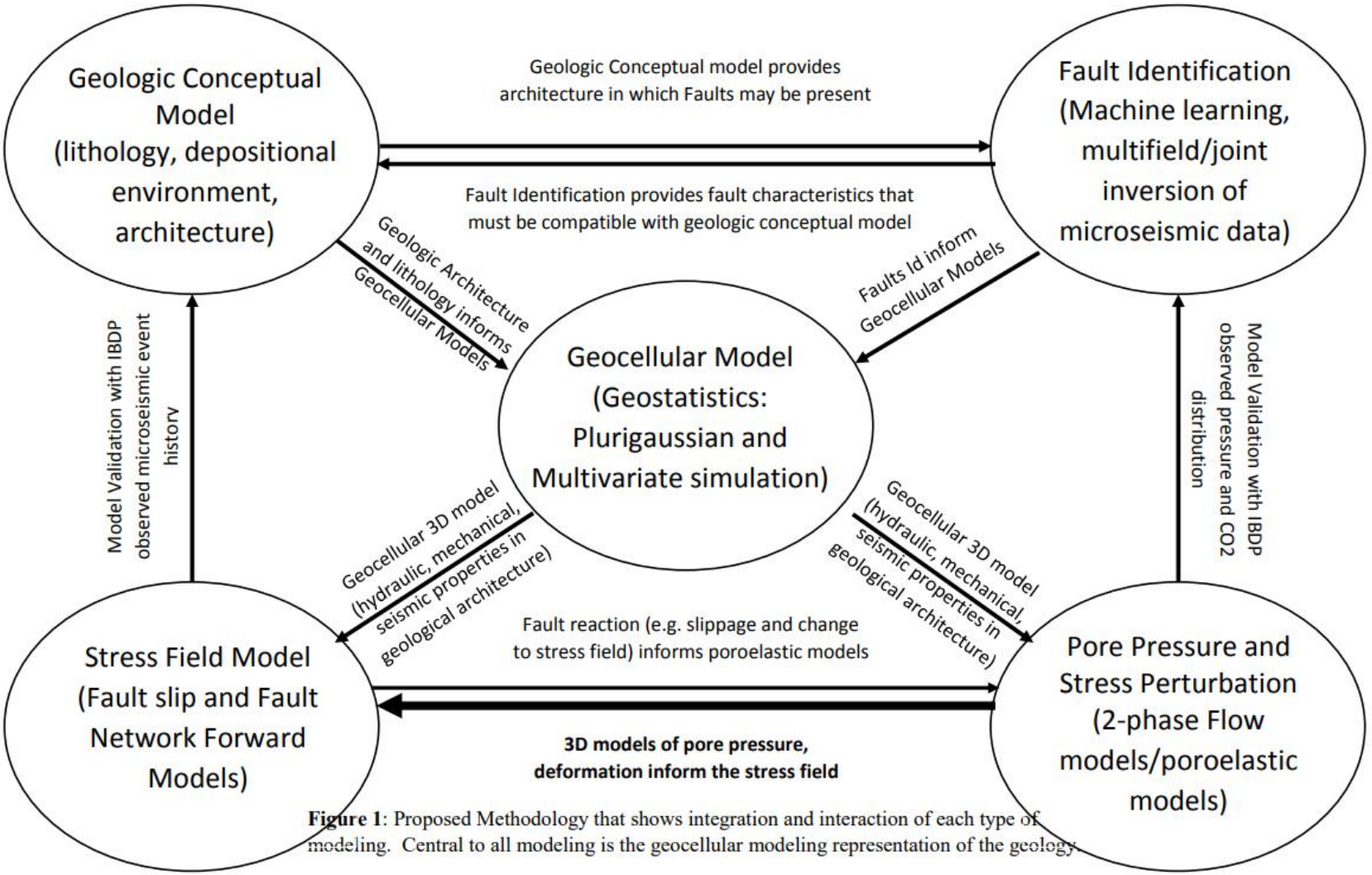

Figure 1: Proposed Methodology that shows integration and interaction of each type of modeling. Central to all modeling is the geocellular modeling representation of the geology.

GEOLOGY

ILLINOIS BASIN SEDIMENTARY AND CRYSTALLINE ROCKS

The Illinois Basin, as shown in Figure 2, contains over 4 miles (7 km) of sedimentary rocks, ranging from Cambrian to early Permian (Collinson et al., 1988). The Cambrian rocks are entirely underlain by the Precambrian crystalline basement with a sharp unconformity contact (Figure 3; McBride et al., 2016). The sharp unconformity between the Argenta and the Precambrian crystalline basement is estimated to represent a gap of 600 to 900 million years (Willman et al., 1975). The crystalline basement is primarily composed of granite, granodiorite, or rhyolite (Bradbury and Atherton, 1965; Atekwana, 1996). The crystalline basement beneath the Paleozoic sediments is constrained by scattered data sources, such as regional seismic profiles (Bertagne and Leising, 1991; Heigold and Oltz, 1991; Pratt et al., 1992; Bear et al., 1997; Potter et al., 1995, 1997; McBride and Kolata, 1999; McBride et al., 2003) and data of deep wells that penetrate the Precambrian rocks. Although the Illinois Basin can be categorized as a sag basin (Buschbach and Kolata, 1991), the geology of the deep subsurface includes a complex history of faulting, folding, and basement uplifts (Nelson, 1995; McBride and Nelson, 1999; Leetaru and McBride, 2009). The crystalline basement in the Illinois Basin is a part of the Eastern Granite-Rhyolite Province (EGRP), which formed between 1.48 and 1.38 billion years ago (Bickford et al., 1986; Lidiak, 1996; Van Schmus et al., 1996). This province is characterized by undeformed, normomorphic rhyolite to granite of extensional tectonic origin (Bickford et al., 1986). Seismic reflection data also reveal that the EGRP is structurally complex in Illinois (Pratt et al., 1989). Furthermore, granites were intruded within the EGRP between 1.58 Ga and 1.35 Ga (Van Schmus et al., 1996). High-resolution 2D seismic profiles and 3D seismic volume around the IBDP site, as studied by McBride et al. (2016), revealed new insight regarding the structures and composition of the crystalline basement. McBride's findings indicated that the concentration of mafic igneous activity within the EGRP suggested an episode of Proterozoic crustal extension and rifting. The data from wells penetrating the crystalline basement and seismic profiles indicated that subsurface paleo-topographic relief in the Illinois Basin can range from 500 ft (150 m) up to 1,400 ft (427 m) in southern and western Illinois, where the Mt. Simon Sandstone is either absent or very thin (Workman and Bell, 1948; Dean and Baranoski, 2002; Reuter and Watts, 2004; Leetaru et al., 2009). The seismic profile around the IBDP site revealed the paleo-topographic relief between the Precambrian crystalline basement and the Argenta. The relief was influenced by the thickness of overlying sedimentary successions where, on the hills, the thickness of overlying formations significantly decreased and, on the trough, the thicknesses increased. The Precambrian crystalline basement at the IBDP site is composed of rhyolite, granite, granodiorite, and gabbro (Freiburg et al., 2020). The uppermost part of the crystalline basement consists of a maroon-colored, brittle rhyolite which is heavily weathered and fractured (Leetaru and Freiburg, 2014).

The crystalline basement is directly covered by the Argenta, which is composed of well-consolidated, well-compacted, sub-lithic arenite to quartz arenite, formed in marine to fluvial environments (Figure 3; Freiburg et al., 2020). It has a maximum thickness of 50 ft (15 m) with an average porosity of 9% and permeability of 2.3 mD. The Mt. Simon Sandstone is a regional blanket-like sandstone that is primarily composed of quartz arenite with a small presence of shale and dolomite. The area where the Mt. Simon Sandstone is most extensively deposited is in the northeastern part of Illinois, where it reaches a thickness of 2,600 ft (790 m).

The Mt. Simon Sandstone has been divided into three major intervals based on depositional environment and reservoir quality (Figure 3; Freiburg et al., 2020). The lower part of the formation mainly

consists of Arkose sandstone. The Arkose zone of the Lower Mt. Simon is considered a promising zone for CO_2 injection, with an average porosity of 22% and average permeability of 200 mD. However, the intervals also contain interlayers of discontinuous siltstone, which have a porosity as low as 2% and permeability as low as 0.008 mD.

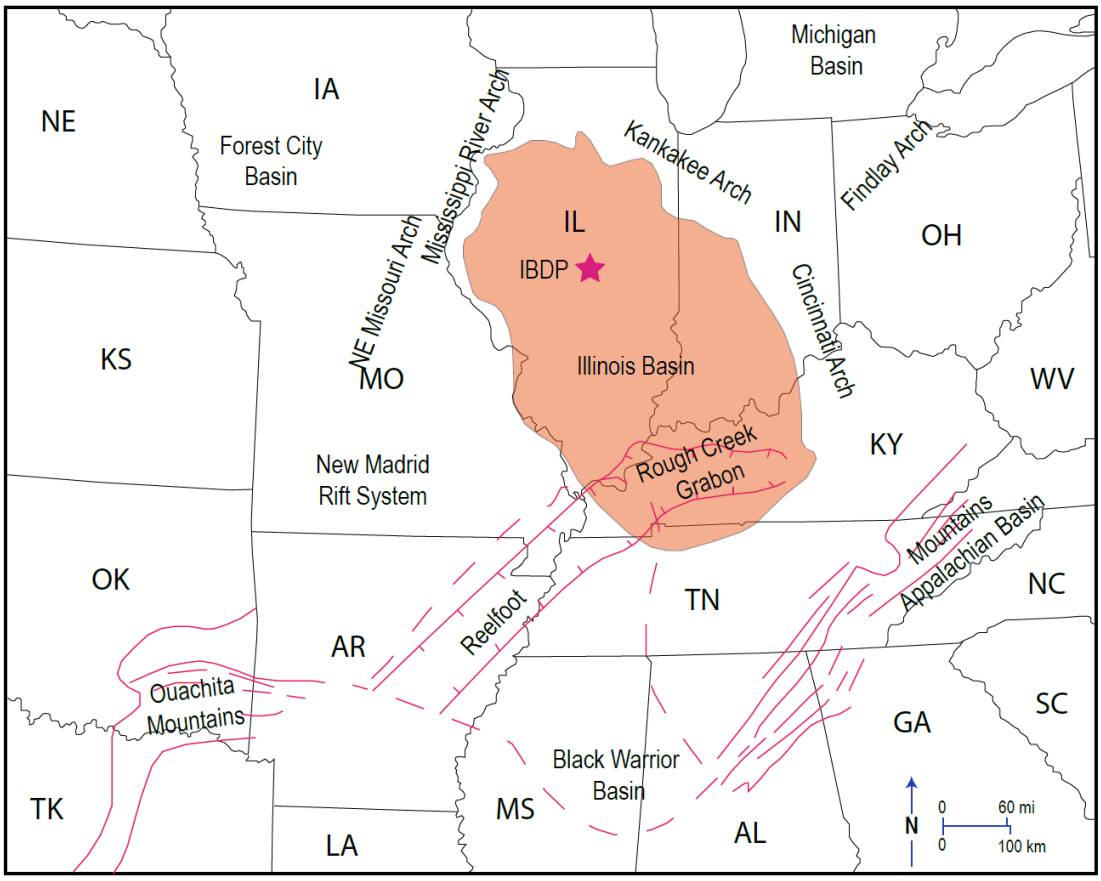

Figure 2. Map showing the location of the Illinois Basin (brown color) and important regional structural features. The location of the IBDP site is labeled with a star (Leetaru and Freiburg, 2014).

The Eau Claire Formation overlies the Mt. Simon and is considered the primary unit that prevents CO_2 migration into shallow formations and surface. The lower part of the Eau Claire is primarily composed of thick siltstone and shale interval, transitioning to dense carbonate interlayers. The upper part consists of dense carbonates. The shale of the Eau Claire Formation shows the maximum transgression of marine system. The presence of interlayers of limestone, siltstone, and dolomite suggests that the Eau Claire Formation deposited in a shallow marine that was a tidally influenced marine environment (Freiburg et al., 2020). Mt. Simon has been divided into five distinct units, labeled A, B, C, D, and E, as determined by changes in the depositional environment and sedimentology (Freiburg et al., 2020). These units are situated within the Lower, Middle, and Upper Mt. Simon Formations, with units A and B located in the Lower Mt. Simon, units D and C in the Middle Mt. Simon, and unit D in the Upper Mt. Simon.

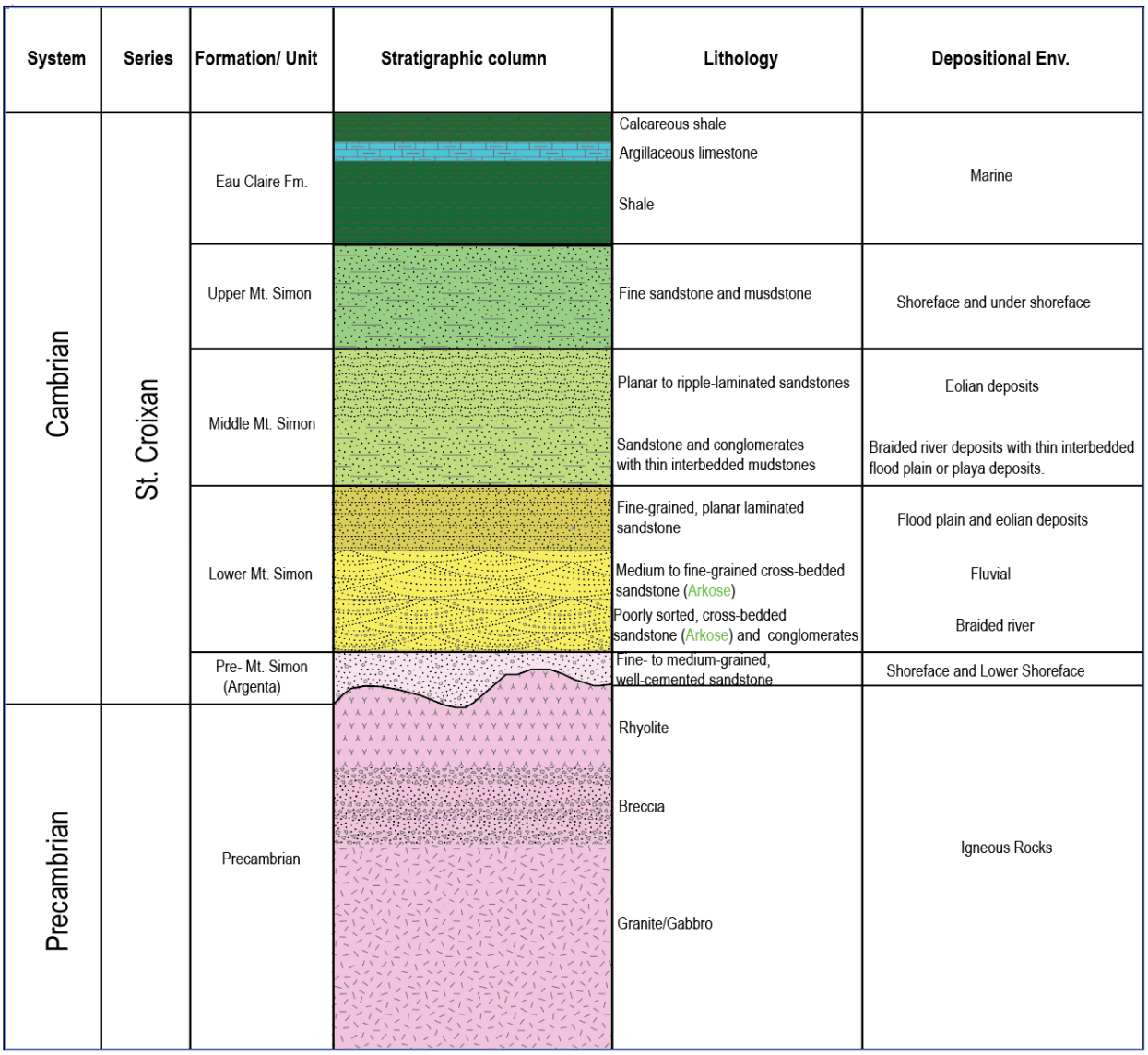

Figure 3. Stratigraphic column depicting the Precambrian crystalline basement, Argenta Formation, and Mt. Simon Sandstone at the IBDP site. The figure displays the lithology and depositional environments for each interval.

MAJOR STRUCTURAL FEATURES AND REGIONAL FAULTS IN THE ILLINOIS BASIN

The Illinois Basin, located within the interior of the North American craton, has undergone mild structural deformation as a result of mountain-building events including the Grenville, Taconic, and Acadian Orogenies that occurred within the craton (Nelson, 1995). It contains Phanerozoic sedimentary rocks that are underlain by the Precambrian crystalline basement. The Basin has several significant structural features, including the east-west-trending Rough Creek-Shawneetown and the Cottage Grove fault systems in the southern regions, the St. Genevieve Fault Zone and the Ozark Dome in west and southwestern regions, the Do Quoin Monocline and La Salle in the central and eastern regions, and the Sandwich Fault Zone and Plum River Fault Zone in the northern region.

The St. Genevieve Fault Zone has a northwest-southeast trend, formed during the Precambrian Era (Figure 4). It has a similar trend to other northwest-trending faulting and folding in Missouri, eastern Kansas, and southern Iowa (Guinness et al. 1982, Sims et al. 1987). The St. Genevieve Fault Zone is composed of high-angle normal and reverse faults and has undergone two major episodes of reactivation during the Devonian and early Pennsylvanian periods (Weller and St. Clair, 1928; Nelson and Lumm, 1985). During the Devonian Era, the fault acted as a normal fault, but it reactivated as a reverse fault during the early Pennsylvanian period (Desborough, 1961b; Nelson and Lumm, 1985).

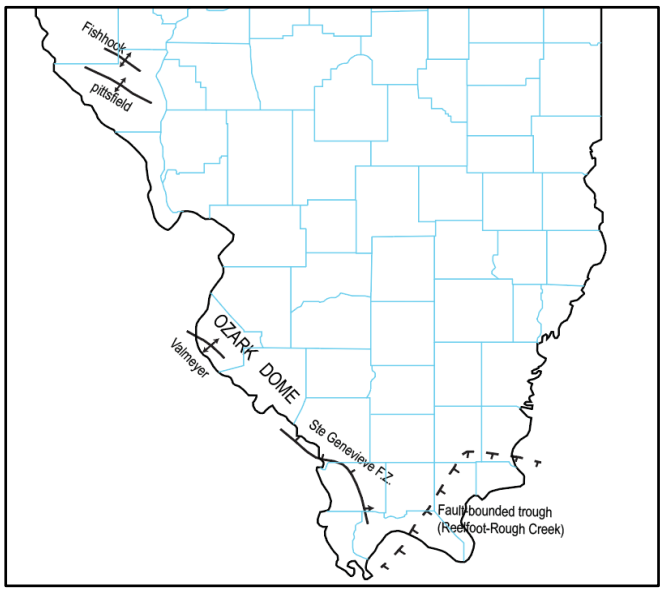

Figure 4. Major structural features of Illinois during the Precambrian (adopted from Nelson, 1995).

After Grenville Orogeny, which occurred 600 million years ago at the end of the Precambrian Era, the Laurentia continent separated from Gondwanaland, and the ocean basins formed between the continents. At that time, the Reelfoot Rift and its eastward extension, the Rough Creek Graben, developed in northeastern Arkansas, western Tennessee, and southern Illinois (Soderberg and Keller, 1981; Schwalb, 1982). During the Precambrian Era and Cambrian Period, these areas were bounded by lystric normal faults that extended into the crystalline basement (Nelson, 1995). According to geophysical seismic data indicates that the Reelfoot Rift, located at the southern part of the Illinois Basin, is a graben that trends northeast and spans 40 miles (65 km) in width and over 200 miles (320 km) in length. The displacement of the graben is over 10,000 ft (3,000 m) (Howe and Thompson 1984; COCORP, 1988). The northeastern end of the Reelfoot Rift connects with the east-trending Rough Creek Graben, which, according to seismic data, is a normal fault with displacement of over 8,000 ft (2,438 m) that primarily affected the Upper Cambrian Eau Claire Formation (Bertagne and Leising, 1991).

The regional faults in the northern part of Illinois (Figure 5) include the Sandwich Fault Zone, which has a northwest-southeast trend and the Plum River Fault Zone, which has an east-west trend. Both regional faults exhibit similar structural styles, but do not interconnect (Nelson, 1995). The Sandwich Fault Zone is nearly parallel with the La Salle Anticlinorium, indicating that they formed simultaneously into the Mississippian or Pennsylvanian periods when the crustal block between them rose (Kolata et al., 1978). The Sandwich Fault Zone is found above the crystalline basement and disappears in Pennsylvanian shales (Neslon, 1995). Quarry exposures of the Sandwich Fault Zone revealed that the faults are primarily vertical

or steeply normal with some small thrust, and reverse faults are present within the shale (Nelson, 1995). The presence of different types of faults suggests that the Sandwich Fault Zone has undergone multiple episodes of deformation under different stress regimes.

The Plum River Fault Zone is approximately 112 miles (180 km) long and has a slight east-west trend. The fault zone consists of sub-parallel to parallel high-angle faults with vertical offsets of about 500 ft (150 m) in surface rocks and up to 1,100 ft (335 m) in the Precambrian crystalline basement (Bunker et al., 1985).

Another significant structural feature affecting the Precambrian crystalline basement and Cambrian is the La Salle Anticlinorium (Figure 6). The anticlinorium comprises several sub-parallel anticlines, domes, monoclines, and synclines, aligned with the overall trend of the system. The pattern of the La Salle Anticlinorium reflects a strike-slip subsidiary fault. The trend of folds is primarily parallel to the north-northwest strike of the larger structure. The La Salle Anticlinorium is strongly asymmetrical, with west limb having a steeper dip and more significant structural relief compared to the eastern limb which has a less relief (Nelson, 1995). The La Salle Anticlinorium experienced two major uplifts before Pennsylvanian and Ordovician periods (Clegg, 1965a, 1970; Jacobson, 1985). Seismic profiles and the data of the drilled hole reveal that the uplift affected the Mt. Simon Sandstone and younger strata. Notably, the topography of the La Salle region remained unchanged despite increasing depths, as evidenced by the seismic profiles and borehole data. (Buschbach and Bond, 1974; Heigold, 1992). Seismic profiles also show high-angle reverse faulting along the western flank of domes at La Salle, which displaces seismic reflectors that are correlated with the top of the Precambrian and Cambrian intervals (Heigold, 1992).

According to drilled hole data and seismic profiles, the La Salle Anticlinorium was created due to displacements that occurred in the Mississippian and Pennsylvanian periods over faults in the crystalline basement (Nelson, 1995). Although most of these basement faults extend upward into younger strata, the faults in the La Salle can be classified as either drape folds (Stearns, 1978) or fault-propagation folds (Suppe and Medwedeff 1984) and share structural similarities with monoclines that were formed during the Laramide orogeny in the western United States (Lowell, 1985).

The southern part of the Illinois Basin is a heavily deformed region with several structural features (Figure 7), such as basement-rooted reverse, normal, and strike-slip faults, affecting the sedimentary successions. During the Mississippian period, pre-existing faults experienced recurrent movement due to different stress regimes, such as the southwest block of the St. Genevieve Fault Zone, which was a high-angle normal fault during the Precambrian to Devonian periods (Nelson and Lumm, 1985) but uplifted and acted as a reverse fault during the late Mississippian and early Pennsylvanian periods (Nelson and Lumm, 1985). Additionally, the Lusk Creek Fault Zone and Rough Creek- Shawneetown Fault System (Figure 7) have undergone multiple episodes of displacement, initially as normal faults in the Precambrian through early Cambrian periods (Soderberg and Keller, 1981; Nelson and Lumm, 1987; Bertagne and Leising, 1991) and later as high-angle reverse faults in the late Paleozoic period (Smith and Palmer, 1974). The Fluorspar Area Fault Complex (Figure 7) is composed of high-angle normal faults with a southwest-northeast trend, but some of the faults in the complex act as reverse and strike-slip faults. The Wabash Valley Fault System is composed of high-angle normal faults with up to 480 feet (145 m) of displacement (Bristol and Treworgy, 1979; Ault et al., 1980) and is believed to be Precambrian basement faults that extend up to the Pennsylvanian sediments (Pratt et al. 1989; Nelson, 1990). The Cottage Grove Fault System developed in the late Pennsylvanian to early Permian periods (Nelson and Krausse, 1981) and impacted the Precambrian crystalline basement. It is a right lateral strike-slip fault with horizontal displacement of several hundred to a few thousand feet (Nelson and Krausse, 1981). The faults affected Pennsylvanian and Chesterian strata, with maximum dip-slip displacements of approximately 200 ft (60 m).

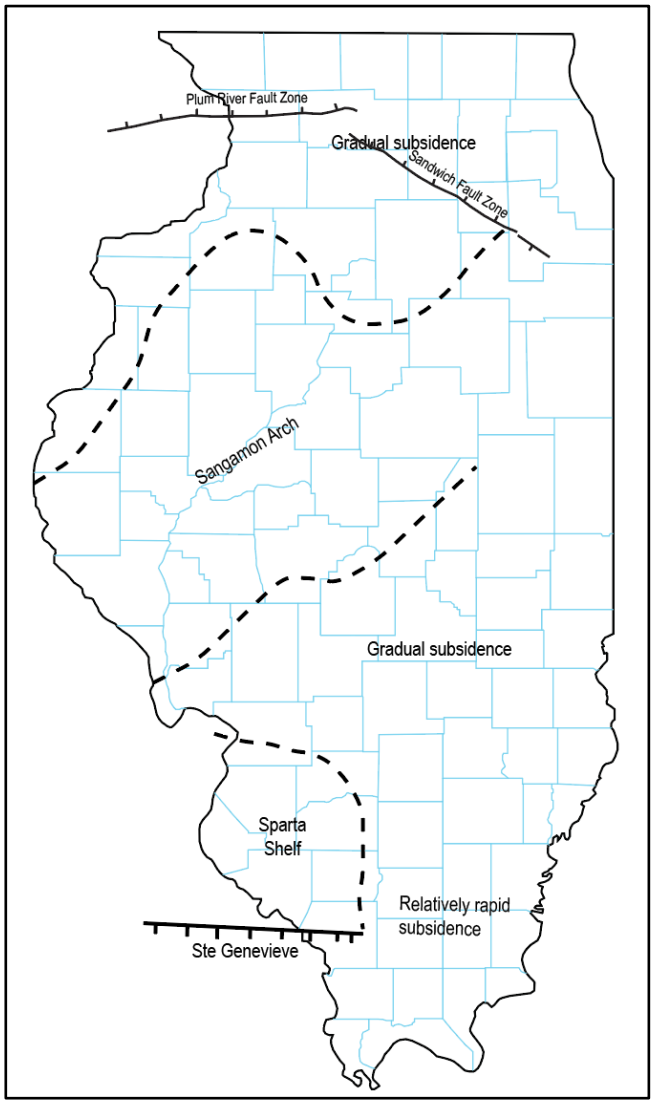

Figure 5. Major structural features in northern Illinois (adopted from Nelson, 1995).

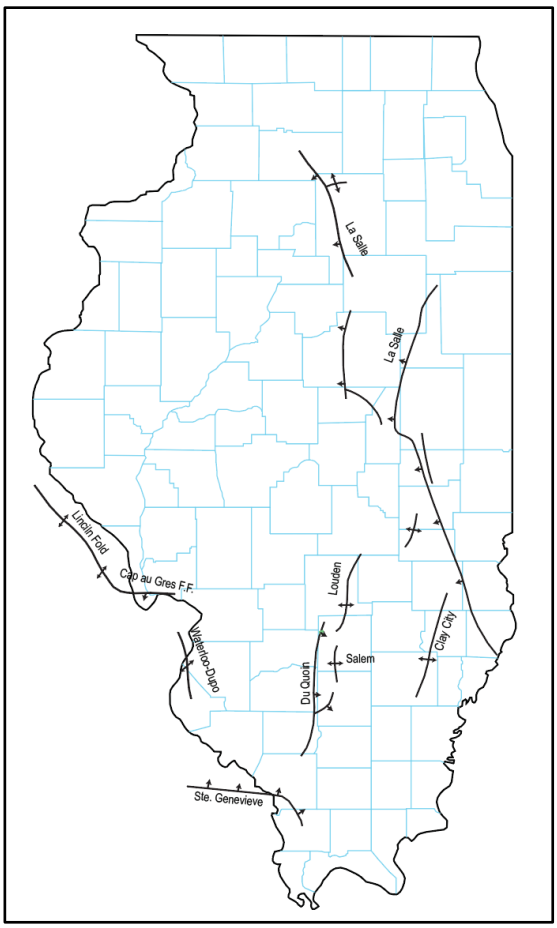

Figure 6. Active major structures during late Pennsylvanian and early Permian times in south and southeast Illinois (adopted from Nelson, 1995).

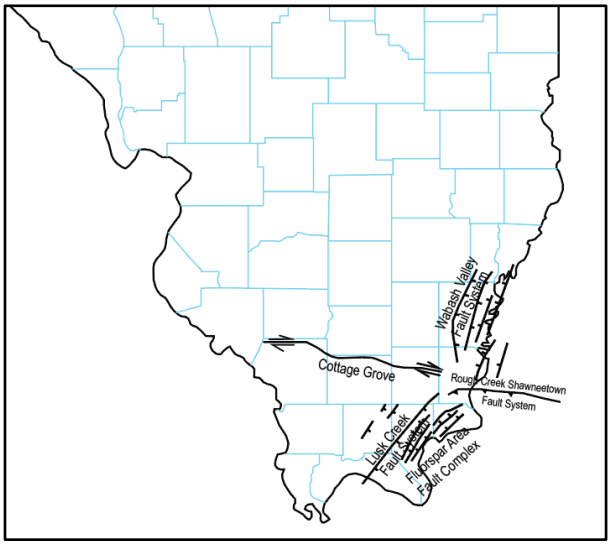

Figure 7. Structures active from late Mississippian through early Pennsylvanian periods (adopted from Nelson, 1995).

INITIAL GEOLOGIC CONCEPTUAL MODEL

The geologic conceptual model has multiple layers of crystalline basement rock, and sandstone with varying crystal and grain size. The complexity of the geology includes intrusive and extrusive igneous rock, alluvial, fluvial and eolian depositional environments These depositional environments have several orders magnitude difference in vertical permeability with continuous and discontinuous vertical flow barriers. The geologic conceptual model has faults/fault zones with and without offset in the crystalline basement and lower Mt. Simon; a network of fractures provides the permeability of the basement while intergranular connectivity provides the permeability of the clastics.

The initial conceptual model of Precambrian, Argenta, and Mt. Simon at the IBDP site was based on the lithofacies study by Leetaru and Freiburg (2014). The Precambrian crystalline basement is composed of rhyolite, breccia, granite, diorite, and gabbro. The uppermost portion of the Precambrian crystalline basement comprises weathered rhyolite with a clay-rich matrix, while the lower portion consists of granite and gabbro. Although the matrix porosity and permeability of these rocks are quite low, the upper part of the crystalline basement exhibits fracture porosity and permeability that is part of a fracture network.

A sharp unconformity exists between the Precambrian crystalline basement and the overlying Argenta Sandstone. The Argenta Sandstone primarily consists of fine-to-medium-grained sandstones deposited in lower and upper shoreface environments with varying energy conditions. The thickness of the Argenta Sandstone is related to the paleotopography of the crystalline basement, resulting in greater thickness above troughs and lesser thickness above hills. Lithologies include conglomerate and fine-to-medium-grained sandstone. The porosity and permeability of this sandstone are relatively low due to compaction and cementation diagenetic processes that occurred after the deposition of the sandstones.

The Lower Mt. Simon Sandstone, as described by Leetaru and Freiburg (2014), was deposited in a braided river system, with distinct facies representing different depositional environments, such as distal alluvial fans, ephemeral sheet flood events, and floodplains or shallow ephemeral playas. These sandstones exhibit moderate sorting and rounding of fine to medium grain sizes. The type of porosity displayed in these sandstones is intergranular, with an average porosity of 19%. The connected pore spaces contribute to a high permeability, with an average value of 200 mD. However, this section also includes very thin interbedded layers of mudstone and siltstone with significantly low porosity and permeability, which were deposited in the floodplain of the fluvial system.

The Middle Mt. Simon Sandstone comprises two depositional facies: braided river deposits with thin interbedded flood plain or playa deposits, and eolian deposits forming sand sheets, dunes, and interdune areas. Compaction and cementation processes have contributed to the destruction of primary porosity in this layer.

The Upper Mt. Simon Sandstone represents a transition from the underlying fluvial and eolian deposits of the Middle Mt. Simon Sandstone to a marine-dominated system. The upper portion features more heterogeneous, cross-bedded sandstones, indicative of deposition in tidal channels or a strandplain-barrier island system.

IBDP DATA OVERVIEW

INTRODUCTION

Induced earthquakes have been associated with CO_2 injection for enhanced oil recovery operations at the Aneth (Rutledge, 2010), Cogdell (Gan and Frohlich, 2013), and Weyburn oil fields (Whittaker et al., 2011). In the case of the Cogdell oil field, for example, events with magnitudes as large as Mw 4.4 were observed. Induced seismicity associated with dedicated CO_2 storage in saline formations has only been observed at the In Salah, Algeria, storage site (Goertz-Allmann et al., 2014; White et al., 2014) and at the IBDP CO_2 storage site (Kaven et al., 2015; Bauer et al., 2016). In both cases, event magnitudes ranged from Mw -2 to 1. Here, we focus on the IBDP site, where more than 10,000 microearthquakes have been recorded in the span of three years of CO_2 injection.

The pilot CCS program at the IBDP site has collected a comprehensive amount of data that have allowed detailed reservoir characterization of the injection interval and the units above and below it. In addition to well-log and core measurements, microseismicity monitoring during injection using borehole sensors has identified thousands of microearthquakes (Bauer et al., 2016). Previous investigations at the IBDP site have provided detailed microseismicity locations (Goertz-Allmann et al., 2017; Dando et al., 2021) and focal mechanisms analysis (Langet et al., 2020). Other authors have identified fault planes where seismicity might have occurred, using microseismicity clustering (Dichiarante et al., 2021) and active surface seismic data (Williams-Stroud et al., 2020). Well-log and core analysis have clarified in detail the stratigraphy of the injection site (Leetaru and Freiburg, 2014; Freiburg et al., 2014).

One of the main characteristics of the microseismicity at the IBDP site is its lack of clear temporal correlation with CO_2 injection rate. Additionally, detailed reservoir characterization using core and well-log data has shown that the Lower Mt. Simon formation, where injection occurs, is separated from the basement by a laterally extensive, low-porosity and permeability interval referred to as Argenta (Leetaru and Freiburg, 2014; Freiburg et al., 2014). This geological observation suggests that the Lower Mt. Simon formation is hydraulically disconnected from the basement section where the microseismicity is located, which implies that pore pressure diffusion through a stratified geological interval into the basement, by itself, cannot explain microseismicity occurrence associated with CO_2 injection.

Interpretation of surface seismic data collected at the IBDP site resulted in a complex set of non-planar 3D fault surfaces that extend from the Lower Mt. Simon into the basement interval (Williams-Stroud et al., 2020). Fault zones can hydraulically connect intervals of different depths and effectively allow pore-pressure diffusion from the injection interval to regions much further away from it (Caine et al., 1996; Faulkner et al., 2003, 2010). The extent to which pore pressure diffusion along faults can induce fault destabilization requires reservoir pressure and microseismicity monitoring that are available at the IBDP Pilot CO_2 injection site, therefore making it an excellent field-case study to investigate the hydromechanical conditions for seismicity occurrence due to CO_2 injection.

This section summarizes the data and interpretations from the IBDP project that was used as the initial geologic conceptual model and the data used to support the iterations in models used to finalize the geologic conceptual model. Early in the SoS project, it was recognized that detailed analyses of a shorter period of time and fewer induced seismicity clusters was necessary. Therefore, the IBDP operational data used was the first nine months of injection pressure, CO_2 saturation, and the two most significant seismicity clusters: #2 and #4 (Bauer et al., 2016).

GEOLOGICAL DATA

IBDP data (Bauer et al., 2016) is from various sources: petrophysical logs from four wells at the Decatur site, interpreted faults from surface seismic interpretations, and literature of regional faults and structural features in Illinois. At the Decatur site, four wells penetrate the Mt. Simon, pre-Mt. Simon (Argenta), and Precambrian crystalline basement with a full suite of well logs, including gamma ray, resistivity, porosity, photoelectric, sonic logs, and borehole image logs. The formation top and major internal markers and boundaries were picked and traced using wireline logs to build structure and thickness maps. Rock characteristics were evaluated using gamma ray, density-porosity, neutron-porosity, photoelectric, and density logs. Reservoir properties, such as porosity and permeability, were derived from wireline logs. The cross-plot of porosity was calculated by averaging density-porosity against neutron porosity. Permeability data were estimated using the Illinois State Geological Survey's (ISGS) method (Damico and Frailey, unpublished report). Borehole image logs (FMI) were analyzed in static and dynamic views to examine bed boundaries, fractures, and other geologic features. Natural fractures were interpreted as either conductive (open) or resistive (healed). Induced fractures and breakouts resulting from drilling operations were examined to determine the direction of the major and minor principal stresses.

AVAILABLE GEOCELLULAR MODEL AND CALIBRATION DATA

IBDP recorded pressure at the CCS1 injection well and multi-level monitoring VW1 well and CO_2 saturation estimates from repeat pulsed neutron capture logs, which was instrumental in geocellular model calibration/history matching. Prior to the start of the SoS project, a pressure modeling and history matching task was conducted by Schlumberger, and as such there was a static and dynamic model at the beginning of the SoS project, which was interrogated to determine if the results from the Schlumberger model could meet part of the SoS project objectives (i.e., predicting pressure results at microseismic event cluster location).

The Schlumberger model was a heterogeneous model that covered an area of 2.3 x 2.3 mi (3.7 x 3.7 km) with grid cell dimensions of 192 x 192 ft in the X and Y directions. The model comprised 132 layers and a total of 1,336,331 grid cells. It spanned from the top of the Eau Claire Formation to the top of the Precambrian crystalline basement. Furthermore, the model incorporated four faults that were interpreted from the initial version of surface seismic data. This model was calibrated to the entire 3 years of injection and 0.75 years of shut-in.

MICROSEISMIC DATA

Raw continuous microseismic data corresponding to microseismic event clusters #2 and #4 were from (1) January 14, 2012, to March 12, 2012, and (2) May 23, 2012, to August 23, 2012, respectively. Because the sample rate of continuous waveform data was changed to 2,000 Hz from 500 Hz on February 21, 2012 (Jaques et al., 2019), the waveform data was processed from February 21, 2012, for the SoS project. The total data size was ~ 5 TB of SEG2 files of 10-second windows. Each SEG2 file contained a total of 94 channels, which included eight channels from the two active CCS1 PS3 geophones (PS3-1 and PS3-2) and 86 channels from 22 geophones at geophysical monitoring well #1 (GM1). (See Jaques et al. [2019] for the detailed description of microseismic data). A total of 8,640 SEG2 files made up daily (i.e., 24 hours) recordings. The two CCS1 PS3 sensors had four channels from a tetrahedral configuration instead of the more conventional orthogonal three channels. For the SoS project, we converted the four channels of

each PS3 geophone associated with the geometric orientation of each tetrahedral channel to three orthogonal directions (V, H1, and H2), allowing us to project the contributing signal intensity of each channel onto the three directions.

TASK 2 - GEOLOGIC CONCEPTUAL AND GEOCELLULAR MODELING

METHODOLOGY

In this section, the methodology used in Task 2 is outlined, encompassing multiple steps to develop a comprehensive geocellular model from the geologic conceptual model of the study area. The subsequent paragraphs provide details on the procedures and techniques used in each step, ensuring a thorough and reliable analysis consistent with the workflow.

- Constructing the structural framework: The initial step involved constructing the structural framework for the geocellular model. This was accomplished by using depth maps derived from the interpretation of surface seismic data, which spanned from the top of the Eau Claire Shale to the base of the Precambrian crystalline basement.
- Importing petrophysical log data: Petrophysical log data from four wells (CCS1, CCS2, VW1, VW2) were incorporated into the conceptual geological model to further inform its development.
- Creating the geocellular model: A geocellular model was generated based on the conceptual geological model of the Precambrian crystalline basement, Argenta, and Mt. Simon Sandstone in the study area.
- Distributing porosity and permeability data: Porosity and permeability data from the four wells were integrated into the geocellular model using stochastic algorithms to ensure a robust representation of these key properties.
- Analyzing borehole image logs: Borehole image (FMI) logs were scrutinized to examine fractures and other geological features. Natural fractures were classified as either pen or healed, while induced fractures and breakouts were assessed to determine the orientation of major and minor principal stresses.
- Constructing the fracture model: The porosity and permeability data extracted from the image logs were used to develop a fracture model for the Precambrian crystalline basement. This model was informed by the major and minor principal stresses identified in the previous step.
- Appending porosity and permeability models: The porosity and permeability model for the Precambrian crystalline basement was combined with the models for the formations above it to create a comprehensive representation of the study area.
- Incorporating faults: A total of 28 faults, extracted from surface seismic data, were integrated into the model. Additionally, as the model progressed, new faults identified through machine learning algorithms were incorporated, resulting in an updated geocellular model.
- Updating the model through iterative feedback: The geocellular model was continuously refined based on feedback from history matching of pressure data (Task 4) and stress field model data (Task 5). This iterative process allowed for the creation of several versions of the geocellular model, each successively more accurate and representative of the study area.

This methodology provided a robust and comprehensive geocellular model for Task 2, which served as a solid foundation for further analysis and interpretation in subsequent tasks.

FMI INTERPRETATION

To support the poroelastic modeling of the Methodology (Figure 1), stress orientation was needed; additionally, to develop the Precambrian permeability model, fracture orientation was needed. Therefore, the IBDP Fullbore Formation Microimager (FMI) logs were analyzed for the Mt. Simon, Argenta, and Precambrian crystalline basement. The FMI log data were imported into the Techlog Schlumberger Software

and analyzed, resulting in static and dynamic images. The dynamic images featured a range of contrasts, allowing for enhanced views of the small features, such as vugs and fractures, bed, and layer boundaries. The use of static images allowed for the visualization of relative changes in resistivity throughout the borehole. This approach provides a better understanding of large features, such as bed boundaries, unconformities, and significant fractures, as they are presented in a single contrast. High-resistivity features, such as cements, carbonates, and sandstones, were displayed as light colors, while low-resistivity features and lithologies, including shale and water-filled open fractures, were displayed as dark colors. Fractures in the wells were characterized as induced or natural features. The natural fractures were categorized either as healed or open. The dip and azimuth of fractures were represented using both tadpole plots and stereonets. The concentration of stress around the wellbores resulted in compressive or tensile failures, which indicated the direction of maximum and minimum stresses (Bell, 1996). The orientation of borehole breakouts and drilling-induced fractures were found to be parallel to the minimum horizontal stress (S_{hmin}) and maximum horizontal stress (S_{Hmax}), respectively.

FRACTURE ANALYSIS

CCS1

The CCS1 fracture analysis shows that there were 22 open fractures and 11 healed fractures interpreted from the top of the Mt. Simon to the bottom of the hole penetrating the Precambrian crystalline basement. Additionally, the fracture analysis revealed 89 induced tensile fractures, 23 induced fractures, and 11 breakouts (Table 1). Dynamic images of breakouts, open, and healed fractures, shown in Figure 8. The distribution of dip and azimuth of the fractures were displayed in stereonets in Figure 9.

The 11 borehole breakout orientations were predominately NE-SW with azimuth of 67° and a standard deviation of 4° (Figure 9a). The breakouts were almost vertical with an average of 85° and a standard deviation of 4°. The orientation of the healed fractures was classified into two sets with azimuth of 30°-40° and 150°-170° (Figure 9b). These fractures were considered sub-vertical with a mean dip of 61° and a standard deviation of 6°. The induced fractures were considered vertical with an average dip of 84° and standard deviation of 5° (Figure 9c). These fractures displayed a NW-SE orientation with an azimuth of 337°. The open fractures did not show a predominant orientation or dip with data scattered through the stereonet (Figure 9d); however, the fracture analyses indicated that the Argenta and Precambrian fracture orientations were between 0°-50° with an average dip of 50°.

CCS2

The CCS2 fracture analysis shows that there were six healed fractures, 16 induced fractures, 26 induced tensile fractures, and 36 breakouts (Table 1) from the top of the Mt. Simon to the upper part of the Precambrian crystalline basement. Open fractures were not observed. Dynamic images of breakouts and healed fractures are shown in Figure 10. The distribution of the fracture orientations and the dip of these fractures are displayed in stereonets, shown in Figure 11.

The breakout orientations were predominantly NE-SW with an average azimuth of 65° and a standard deviation of 8° (Figure 11a). The breakouts were almost vertical with an average dip of 86°. The induced fracture orientations showed a trend of NW-SE and an average azimuth of 154° and a standard deviation of 8° (Figure 11b). The induced fractures were vertical with an average dip 87° and a standard deviation of 9°. The healed fractures do not show a predominant trend, and the data is scattered through the stereonet (Figure 11c).

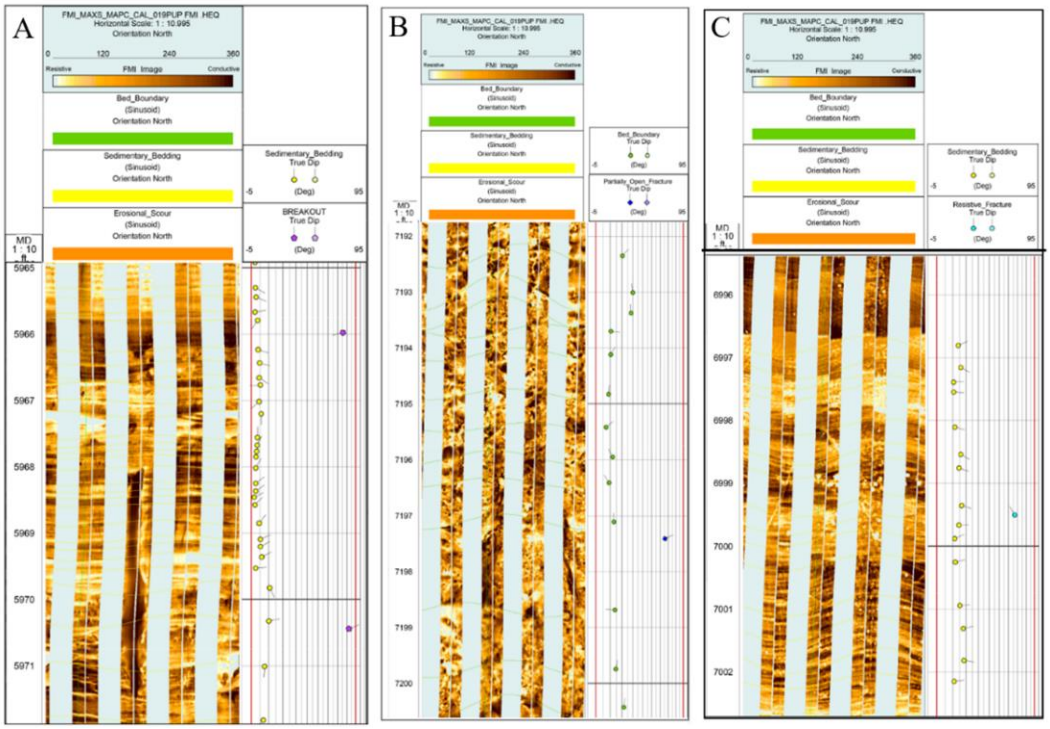

Figure 8. Interpreted FMI log of the CCS1 well at the IBDP site, showing a) breakouts, b) open fractures, and c) healed fractures.

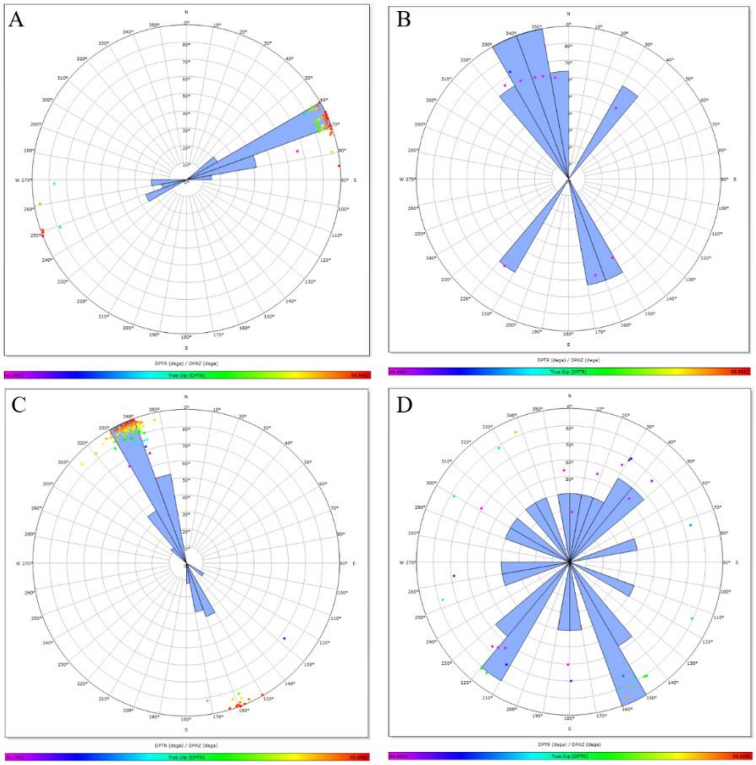

Figure 9. Bidirectional stereonet showing the density of the orientations of all fractures interpreted in the CCS1 well. a) Breakouts; b) healed fractures; c) induced fractures; d) open fractures.

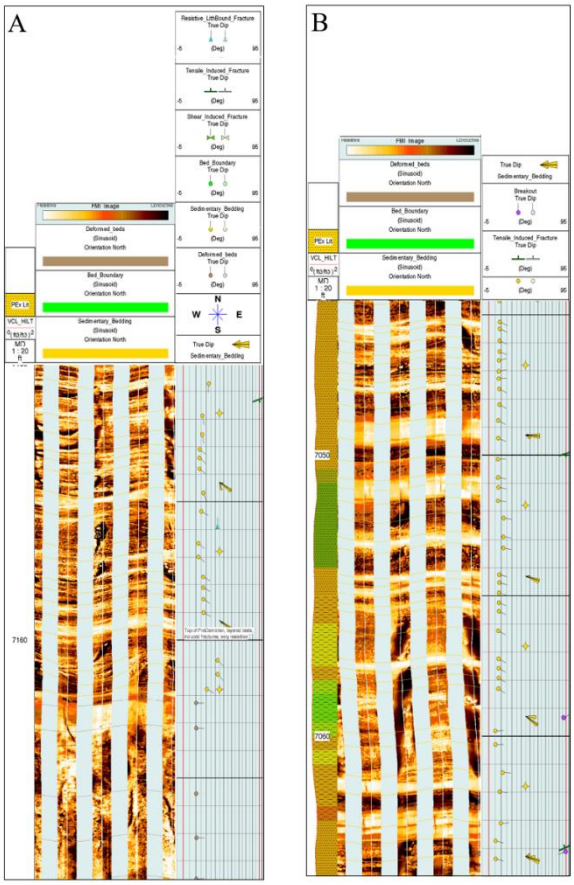

Figure 10. Interpreted FMI log of the CCS2 well at the IBDP site, showing a) healed fractures and b) breakouts.

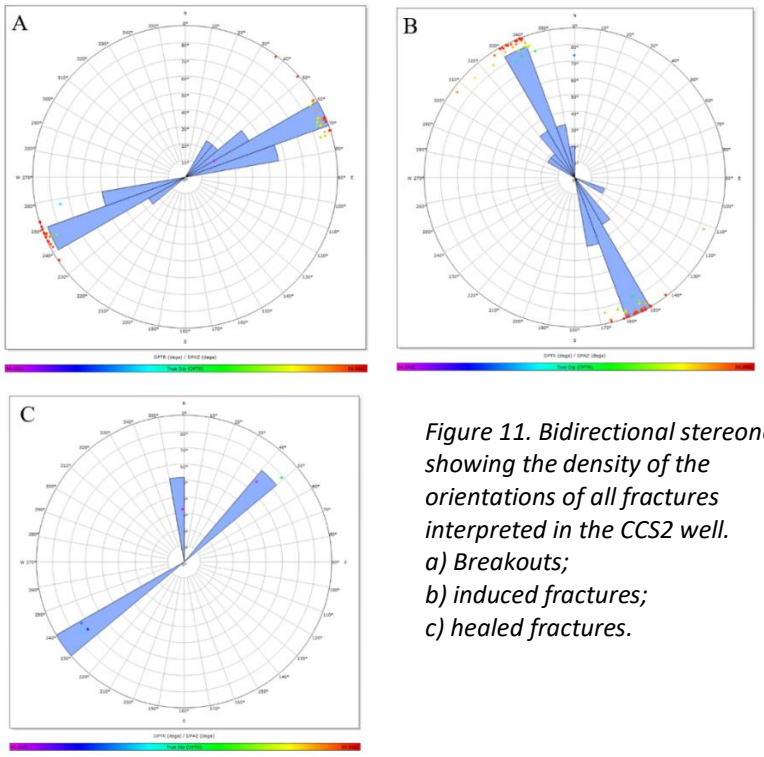

Figure 11. Bidirectional stereonets showing the density of the orientations of all fractures interpreted in the CCS2 well.
a) Breakouts;
b) induced fractures;
c) healed fractures.

VW1

The VW1 fracture analysis indicates that there were 85 open fractures and one healed fracture from the top of the Mt. Simon into the top of the crystalline basement. Furthermore, the fracture analysis revealed 32 induced tensile fractures, 41 induced fractures, and three breakouts (Table 1). Dynamic images of the open and tensile fractures are shown in Figure 12. The distribution of the orientation and the dip of these fractures are displayed in stereonets, shown in Figure 13.

The borehole breakout orientations were predominately NE-SW with an azimuth of 249° and a 2° standard deviation (Figure 13a). The breakouts were vertical with a dip of 88° and a standard deviation of less than 1°. The healed fractures were classified into two major sets, with azimuths of 80°-100° and 100°-120° (Figure 13b). The average dip of the first set is 56°, and the average for the second is 67°. The FMI analyses indicate that the induced fractures trend NW-SE with an average azimuth of 160° (Figure 13c). The open fractures do not show a predominant direction (Figure 13d).

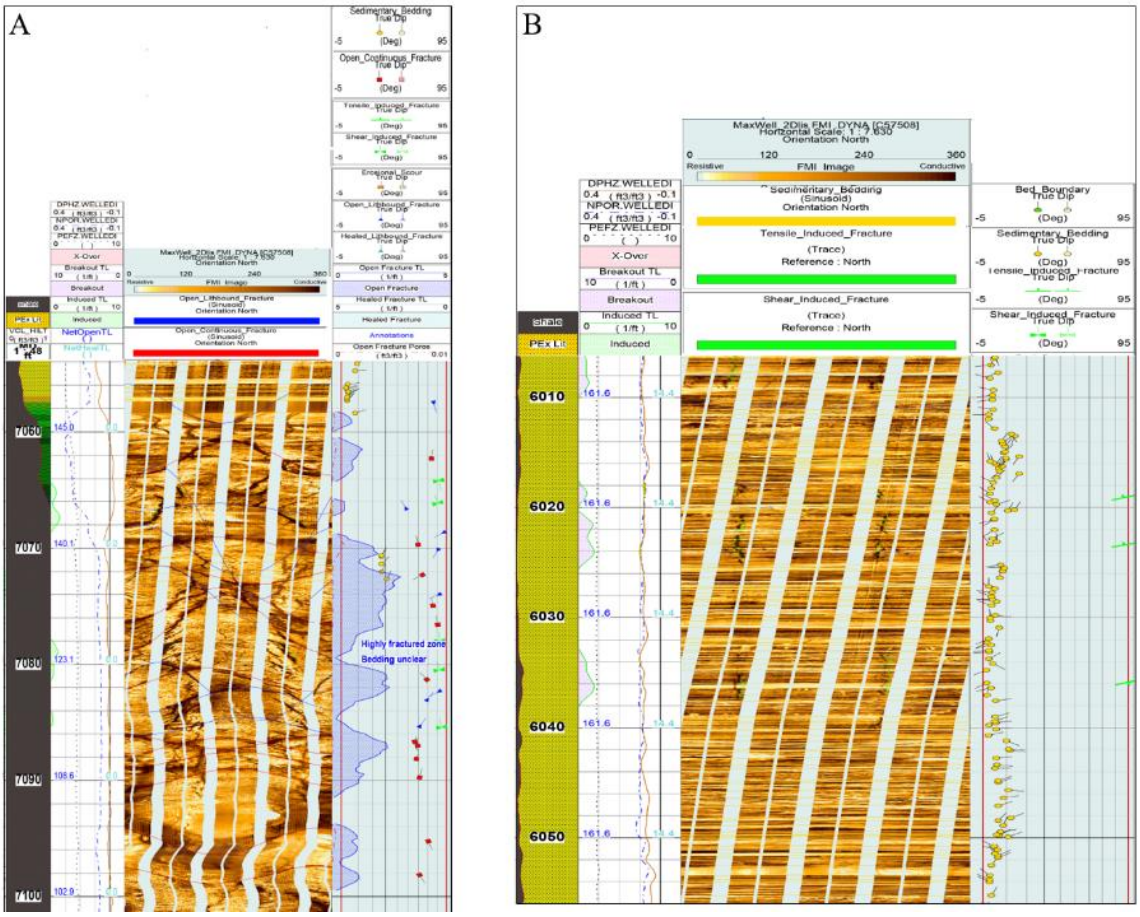

Figure 12. Interpreted FMI log of the VW1 well at the IBDP site showing a) open fractures and b) induced tensile fractures.

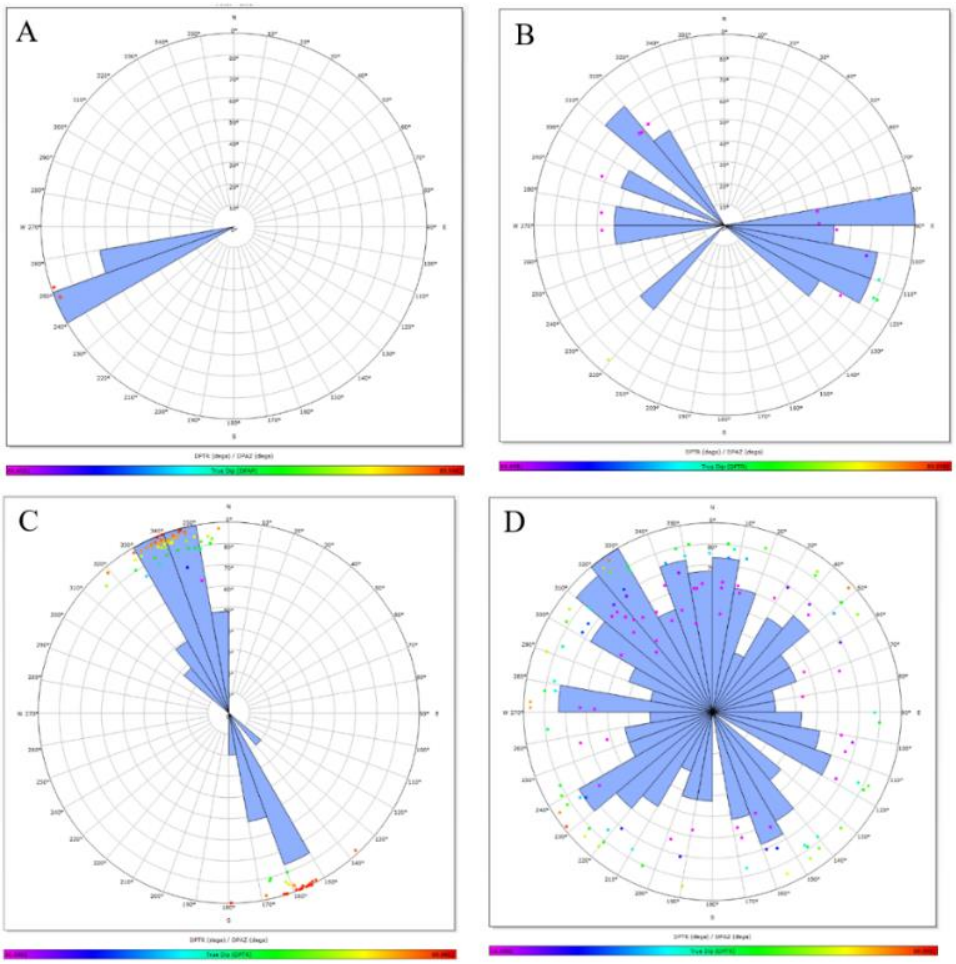

Figure 13. Bidirectional stereonets showing the density of the orientations of all fractures interpreted in the VW1 well. a) Breakouts; b) healed fractures; c) induced fractures; d) open fractures.

VW2

The VW2 borehole breakout orientations were predominantly NE-SW orientation, with an azimuth of 65° and a standard deviation of 7°, as shown in Figure 14a. The dip of the breakouts was classified into two groups, with average dips of 42° and 89°, respectively. An examination of the induced fractures revealed a trend of NW-SE, with an average azimuth of 159° and a standard deviation of 7°, as shown in Figure 14c.

Further analysis of the induced fractures revealed an average dip of 82° with a standard deviation of 5°. However, the distribution of healed and open fractures was found to be scattered throughout the stereonet, with no predominant dip or azimuth being observed, as shown in Figure 14b and 14d.

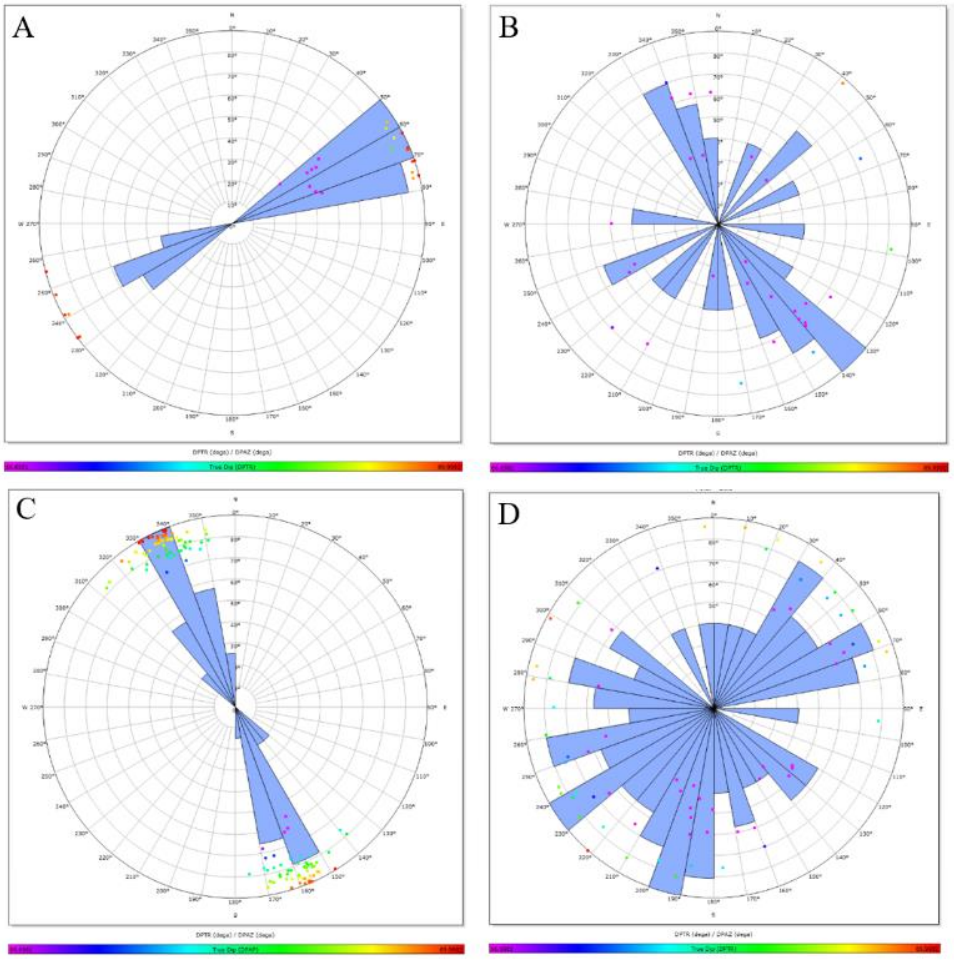

Figure 14. Bidirectional stereonets showing the density of the orientations of all fractures interpreted in the VW2 well. a) Breakouts; b) closed fractures; c) induced fractures; d) open fractures.

Table 1. Number of open fractures, healed fractures, breakouts, and drilling-induced fractures for the wells at the IBDP site.

Wells	Number of Open Fractures	Number of Healed Fractures	Number of Breakouts	Number of Drilling-Induced Fractures
CCS1	22	11	11	23
CCS2	-	6	36	16
VW1	85	1	3	41
VW2	103	14	3	68

The results of the maximum and minimum horizontal stress (S_{Hmax} and S_{hmin}) measurements from the four wells were found to be consistent with the orientations of horizontal and minimum stresses outlined in the 2008 World Stress Map (WSM) (Figure 15, in Hurd, 2012).

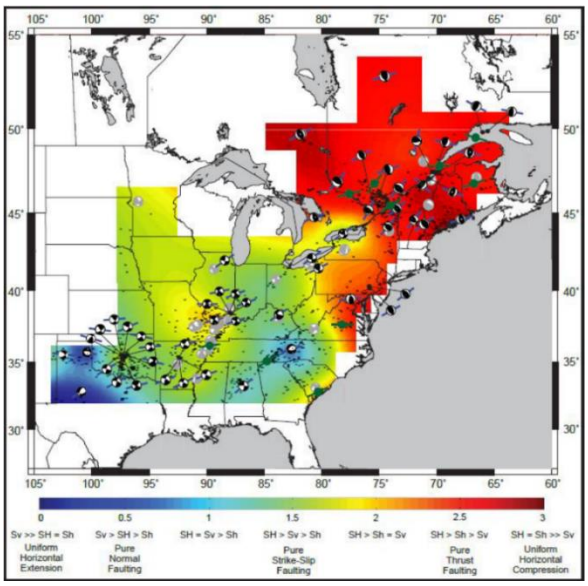

Figure 15. Spatial variation in horizontal principal stresses. Note, the Illinois Basin is located in a strike-slip region ($S_H > S_V > S_h$; 1.5, green color) with NE-SW direction of S_{Hmax} and NW-SE direction of S_{hmin}.

GEOCELLULAR MODEL

Geocellular Model Area

The model boundary encompasses an area of 5.6 × 5.6 miles (9.1 × 9.1 km) with CCS1, CCS2, VW1, and VW2 near the center of the model (Figure 16). The model comprises of 290 cells in the X direction and 290 cells in the Y direction, and 379 layers, with a grid spacing of 103 × 103 ft (31 × 31 m). The total number of cells in the geocellular model is 31,873,900.

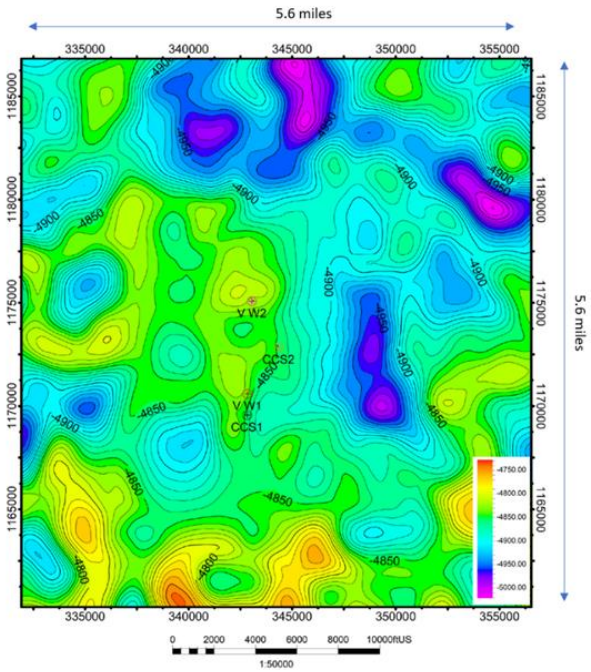

Figure 16. Dimensions of the geocellular model and the locations of wells at the IBDP site. The structure contour map shows the statistically generated top of the Mt. Simon Sandstone based on 3D surface seismic interpretation.

The structural and stratigraphic framework of the IBDP site was defined based on the surfaces and faults derived from the interpretation of the reprocessed 2019 3D seismic survey, which has a higher resolution compared to 2012 3D seismic survey. However, the seismic data only covers an area of 1.9 × 1.9 miles (3 × 3 km), which is about 10% of the size of the model. Therefore, the topography outside the seismic area were extrapolated using the Sequential Gaussian Simulation algorithm. The depth surfaces imported into the geocellular model include the surfaces of the intervals and formations from the top of the Eau Claire Formation to a depth of -10,000 ft in the Precambrian crystalline basement (Table 2).

Twenty-eight fault surfaces derived from 3D surface seismic interpretations were integrated into the static model. The interpretation of faults and depth maps was aided by tracking the seismic reflectors line by line manually and using an ant-tracking processing technique that automatically extracts fault surfaces from the 2019 IBDP Seismic Reprocessing Volume (Williams-Stroud et al., 2020). However, ant-tracking was not able to recognize small faults and strike-slip faults without vertical displacements. Using ML algorithms, nine additional faults were extracted and incorporated into the model (see Tasks 3 [Fault Identification] and 4 [Pressure and Stress Modeling]).

The Precambrian surface assessment indicates that the crystalline basement consists of several paleo-highs and troughs. Over the troughs, the thickness of the Argenta increases to about 50 ft (17.9 m), but over the hills is less than 10 ft (3.05 m). Due to the seismic resolution, it is difficult to know if the Argenta is present or not over some of the paleo-highs. Over some of the paleo-highs, the Mt. Simon directly covers the Precambrian crystalline basement or a thin interval of Argenta is present between the Mt. Simon and Precambrian crystalline basement.

The assessment of the fault heights interpreted from 3D seismic data showed the faults are across the Mt. Simon and Argenta. Since tracking the faults through the Precambrian crystalline basement is difficult, the major faults were extended into the basement. After adding the faults to the geocellular model, most of the faults have a displacement ranging from 0 to 30 ft (9.1 m), but nine faults have displacement ranging from 30 to 59 ft (9.1 to 18.0 m). Most of the interpreted faults extend into the Mt. Simon B (Table 2). Figure 17 shows the location of the faults extracted from surface seismic interpretations as well as their corresponding displacements on the surface of the Precambrian crystalline basement.

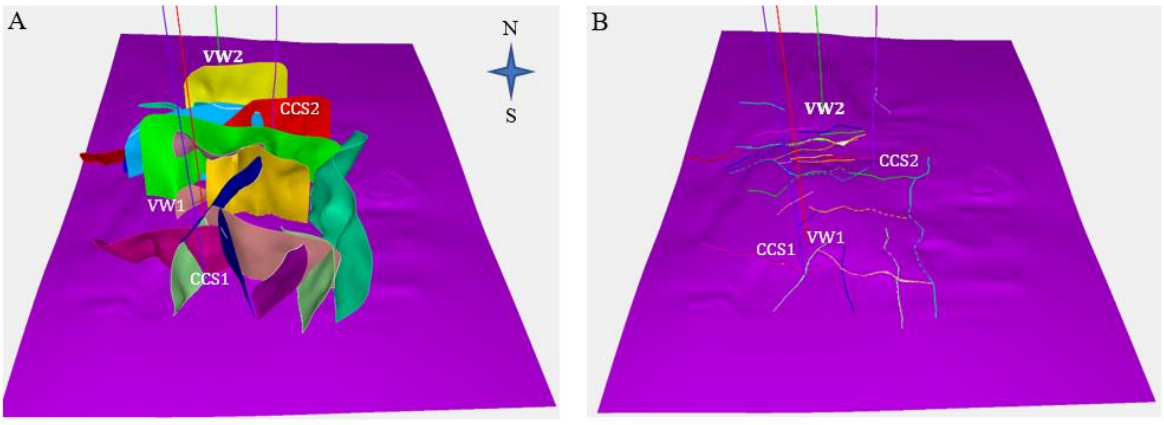

Figure 17. Map depicting the spatial distribution of faults (a) and their displacements (b) on the Precambrian surfaces, as interpreted from surface seismic data.

The correlation between interpreted faults from surface seismic data and microseismic events is observed to be low. Using ML algorithms for the interpretation of faults resulted in the identification of several small faults associated with cluster #2 and cluster #4 of microseismic events. These faults traverse

the Precambrian surface with a NE-SW trend. Most of the small faults are characterized as strike-slip and exhibit a stronger correlation with the trend of microseismic events (Figure 18).

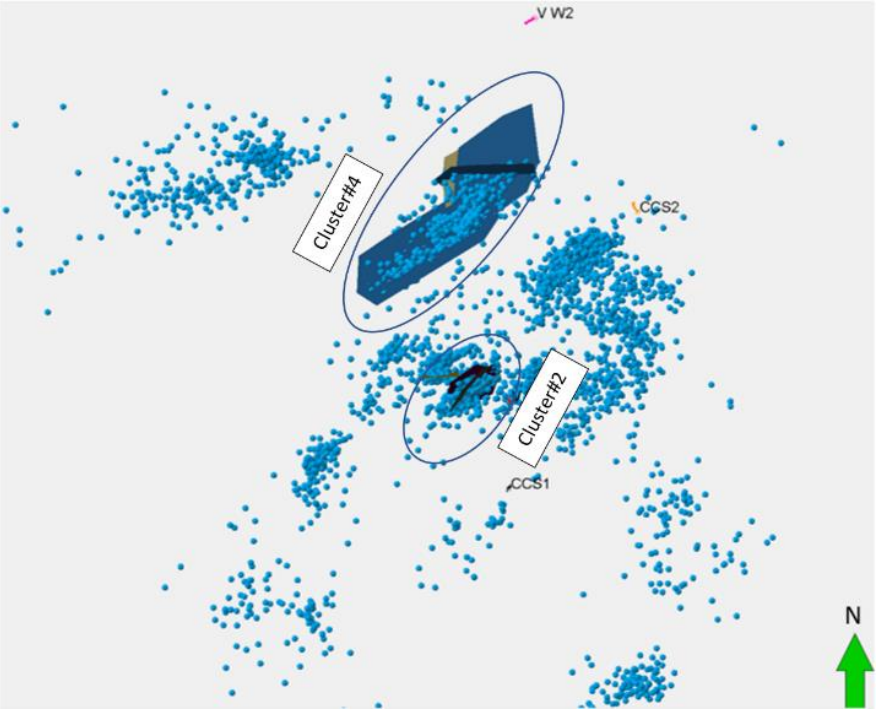

Figure 18. Map illustrating the distribution of microseismic data, wells, and faults as extracted by ML algorithms at the IBDP site.

Zone and Layering

The Lower Mt. Simon A (injection zone) and Argenta were divided into model layers, with average thicknesses from 2.3 to 3.8 ft (0.7 to 1.15 m), using the onlap layering method based on interpretations of the conceptual model (Table 2). The layer thicknesses were determined to account for contrasts in porosity and permeability in well data. The proportional layering method was used for the intervals between the top of the Lower Mt. Simon A and the top of the Mt. Simon E. To keep the overall number of cells within the model below 4 million, the zones between the top of the Mt. Simon E and the top of the Lower Mt. Simon A-Upper were divided into coarse layers in relation to the layers of the Lower Mt. Simon. The model covered the interval from the top of the Eau Claire Formation to a depth of -10,000 ft within the Precambrian crystalline basement, which is approximately 3,000 ft of the basement. Precambrian crystalline basement model layers were represented with 34.5 ft (10.5 m) thick layers. The intervals that were modeled and the thickness, average porosity, and average permeability of model layers for each interval are summarized in Table 2. Upscaling was applied to 0.5 ft resolution well logs to produce one value for each model layer. The porosity and permeability of the four wells were upscaled into the model layers. The arithmetic averaging method was selected because it matched the core porosity, while the geometric averaging method was selected to match the horizontal core permeability, and the harmonic averaging method was selected for the vertical permeability. The results of this process, including the model layers and comparison of the porosity and permeability log data to the upscaled data, are shown in Figure 19.

Table 2. Thickness, average porosity, and average permeability of model layers within the formations and intervals modeled. The intervals closer to the base of the Mt. Simon and Argenta have smaller thickness to improve resolution of predicted pressure and saturation data nearest to the locations of this data used for calibration.

Intervals and Formations	Average layer thickness (ft)	Average layer thickness (m)	Average porosity (%)	Average permeability (mD)
Mt. Simon E	44.0	13.4	10.7	9.3
Mt. Simon D	27	8.7	8.7	2.5
Mt. Simon C	16	4.8	9	2.2
Mt. Simon B	10.5	3.20	15.8	22.4
Mt. Simon A-Upper	3.5	1.1	21.9	54.9
Mt. Simon A-Middle	3.5	1.1	16	29.1
Mt. Simon A-Lower	2.3	0.7	19.4	163.8
Argenta	3.80	1.15	7.4	0.8
Precambrian	34.5	10.5	0.7[1]	1.78[2]

[1]Fracture porosity; [2]Fracture permeability

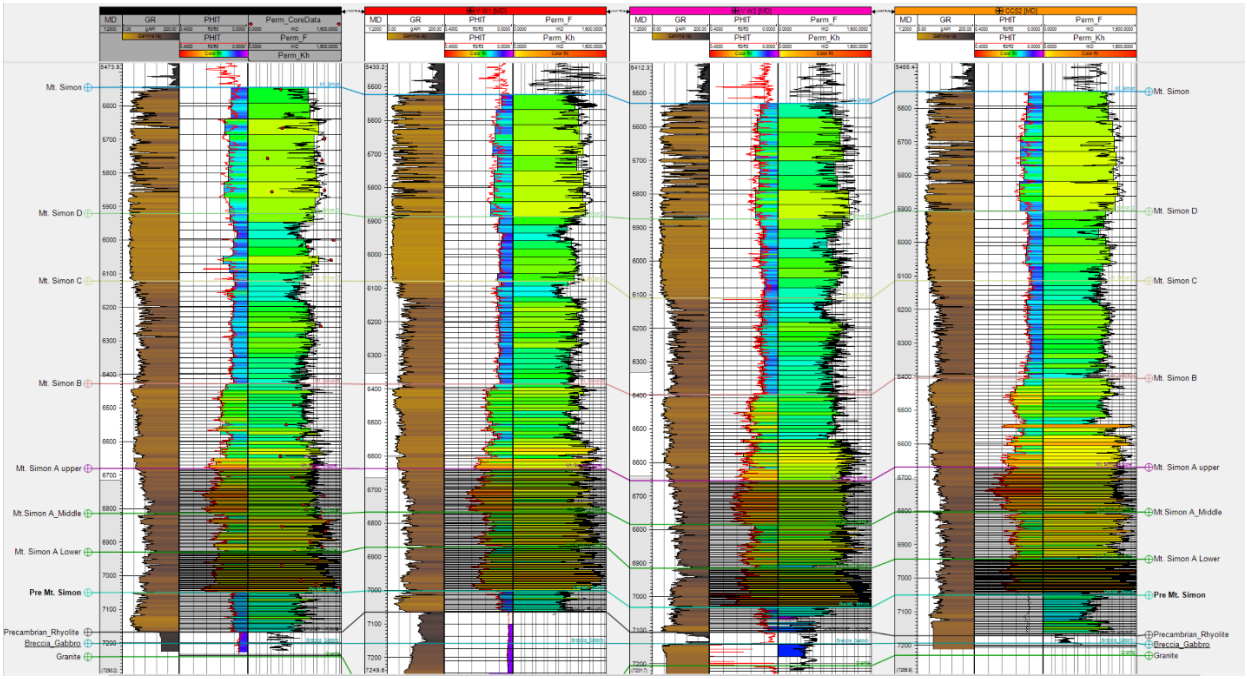

Figure 19. From left to right, well log correlation of CCS1, VW1, VW2, and CCS2. Datum is the top of the Precambrian crystalline basement. The log data includes gamma ray (GR), total porosity (PHIT), and horizontal permeabilities (Perm_F and Perm_Kh) as raw data and scaled-up data, respectively. The red dots on CCS1 log indicate the core porosity and core permeability. The layers and their thickness can be observed on the scaled-up logs. Note, there is a strong correlation between the scaled-up porosity and permeability data with their raw data.

Variogram Analysis and Petrophysical Modeling

The porosity and permeability data of the four wells was available for 0.5-ft intervals. However, there were uncertainties related to modeling the porosity and permeability values between the wells. To reduce these uncertainties and properly distribute the petrophysical data between wells, geostatistical algorithms were used in a way that distributed data represented the geologic conceptual model of the formations. To distribute the data between wells, variogram analysis was used on the porosity and permeability data, and major, minor, and vertical ranges for each interval were identified. Different methods of geostatistical algorithms were tested, and the histograms of modeled porosity and permeability were compared against the original data and upscaled log data. Finally, the distribution of data was checked against the geologic depositional setting of each interval to pick the final method. The histograms provided for each geostatistical algorithm revealed that Kriging and Sequential Gaussian Simulation (SGS) performed better in comparison to other algorithms for the distribution of interval porosity and permeabilities.

Figure 20 a-b depicts CCS1 and VW1 cross-section. CCS1 is located toward the downside of a paleo-high, where the Argenta thickness increases relative to the Argenta thickness at VW1. The intervals with high and low permeabilities are shown with warm and cold colors, respectively (Figure 20). The distribution of permeability suggests that the permeability of the sandstones at the lowermost parts of CCS1 is higher compared to equivalent intervals in VW1. However, as the stratigraphy of the Lower Mt. Simon A formation progresses upward, an increase in the thickness of the lower permeability baffles is observed at VW1. There are several thin baffles in the middle and upper parts of the Lower Mt. Simon A. While a few of the baffles are continuous, most pinch out between the wells.

Figure 20 c-d is the CCS1 and CCS2 cross section. Both wells are located on the west and east sides of a paleo-high with the same thickness as the Argenta Sandstone. The reservoir quality and thickness of Mt. Simon A-Lower are similar in both wells. However, the thickness of baffles in CCS1 is less than in CCS2.

Fracture Model

A fracture model was constructed using detailed data collected from the top of the Precambrian to the base (-10,000 ft) layer. The data collected includes FMI logs of the four wells, CCS1, CCS2, VW1, and VW2, which were used to extract natural fractures and trends, providing a comprehensive understanding of the subsurface fractures. The natural fractures, combined with the knowledge of the rock formation and tectonics of the area, enabled the model to accurately represent the distribution of fractures in the subsurface.

The permeability values of the fracture model in the X, Y, and Z axis were also determined from the FMI logs, which provides insight into the effective permeability of the reservoir in different directions. Furthermore, the porosity and permeabilities were distributed stochastically throughout the model, which allows for a more realistic representation of the subsurface rock formation.

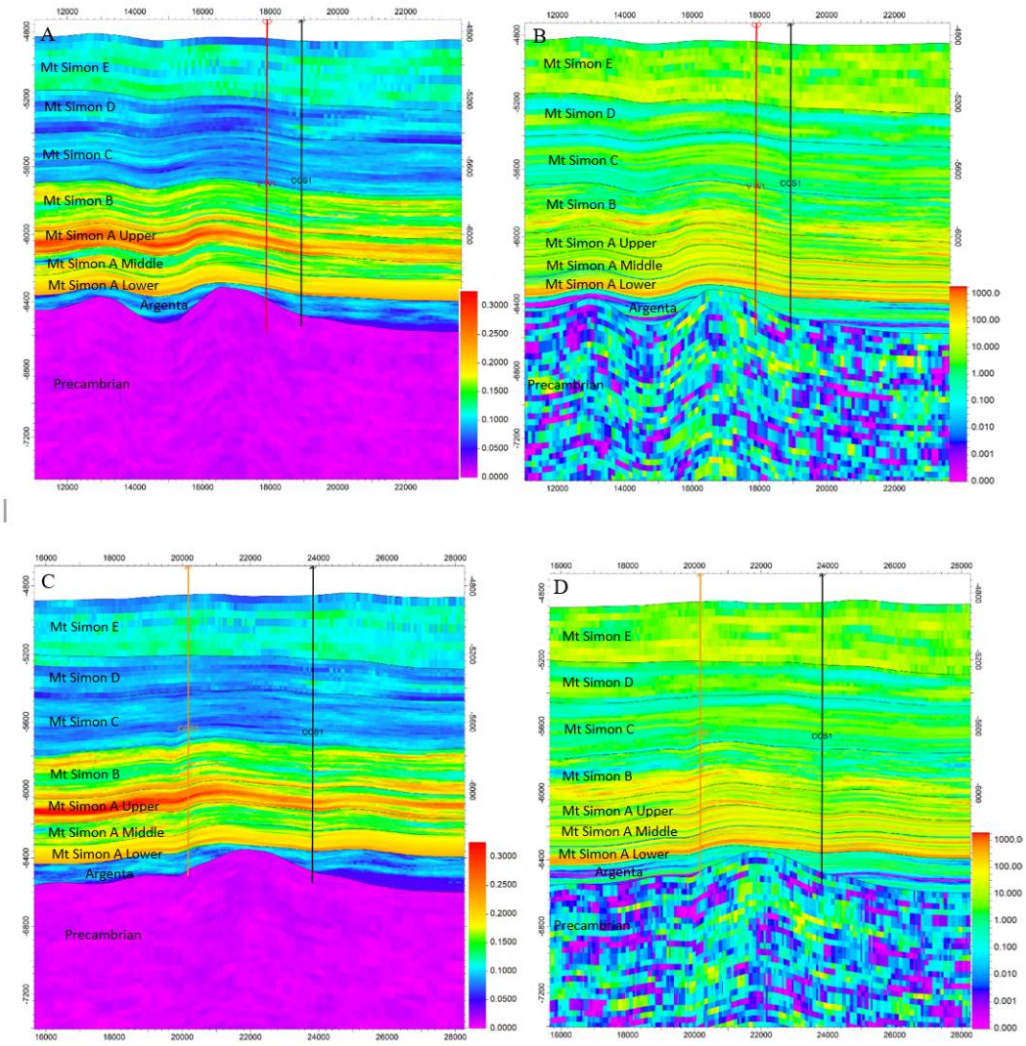

Figure 20. Cross-sections derived from the geocellular model, showing the visual representation of the distribution of porosity and permeability between the wells CCS1 and VW1 (a, b) and CCS1 and CCS2 (c, d).

DISCUSSION

Maximum and Minimum Horizontal Stress Orientations

Maximum and minimum horizontal stress orientations were determined by interpreting the directions of borehole breakouts and drilling-induced tensile fractures obtained from image logs. A total of 76 breakouts and 235 drilling-induced tensile fractures were analyzed in four wells at the IBDP site. The results of the analysis indicated that the average orientation of S_{Hmax} derived from breakouts was approximately N66°E. Additionally, the plotted data of the drilling- induced fractures also revealed an average orientation of N23°W, indicating the direction of S_{hmin} at the IBDP site. The direction of S_{hmin} can also be determined by measuring a perpendicular orientation to the S_{Hmax} of a borehole breakout, as the alignment of borehole breakout is congruent with the maximum horizontal stress. Results obtained from analyzing FMI breakouts are recognized as more accurate in determining the direction of horizontal

stresses than those obtained from drilling-induced fractures (Bell, 1996). As a result, the orientation of Shmiin calculated using the perpendicular orientation of the breakouts is N24°W.

The 2008 World Stress Map (WSM) indicates that the S_{Hmax} orientation is N65°E in nearly all foreland basins on the western side of the Appalachian Mountains (Zoback and Zoback, 1989; Zoback, 1992). The WSM shows a transition from compressional faulting regimes (i.e., strike-slip and/or reverse faulting) in eastern North America to strike-slip faulting in the mid-continent and predominantly extension in western intraplate North America, which suggests that IBDP is located in a transition zone, dominated by a strike-slip faulting regime with the S_{Hmax} direction in a NE-SW orientation. The orientation of S_{Hmax} indicates that the primary source of the horizontal stresses are forces deriving and resisting plate motion in North America (Sbar and Sykes, 1973; Yang and Aggarwal, 1981; Gough, 1984; Zoback and Zoback, 1980, 1981, 1991). Surface fracture data from outcrops in Indiana also indicate patterns of S_{Hmax} with small variation in the mean orientation of the horizontal principal stresses across the state; overall orientation of the S_{Hmax} is N60°E (Powell, 1976; Engelder, 1982; and Ault, 1989).

A small variation in the orientation of the breakouts may be related to anomalies in magnetic declination measurements by the FMI tool (Yildirim, 2014). Additionally, the presence of major and minor faults and fold contribute to small rotations (1° to 4°) in the orientation of the S_{Hmax}. Despite the presence of large structural features in Illinois, such as the Wabash Valley Fault System, La Salle Anticlinorium, Du Quoin Monocline, and the Rough Creek–Shawneetown Fault System, the orientation of S_{Hmax} does not appear to be significantly affected by these structural features, which is supported by the fact that the orientation of S_{Hmax} is equivalent to the calculated S_{Hmax} by Zoback (1992). Examination of the fault systems and the trend of the structural features in Illinois suggests that the orientation of stress regimes has changed throughout geological time due to fault movements and reactivations (Nelson, 1991). The trend and type of fault movements indicate that the orientations of stress regime were different throughout geological time relative to the contemporary stress regime. The orientations of the fractures in the crystalline basement and the Paleozoic rocks are a result of at least four compressive events (Grenville, Taconic, Acadian, and Alleghenian/Ouachita) and two tensional tectonic events (Keweenawan and Pangea rifting) (Lahann et al., 2017). The orientation of the S_{Hmax} is not significantly impacted by the large structural features present in Illinois, as it aligns with the trend of principal horizontal stresses observed in the WSM. However, the orientation of the stress regimes has undergone changes throughout geologic time, as evidenced by the presence of healed and open fractures with varying orientations.

CONCLUSION

Task 2 project conducted an examination of the major structural features and regional faults that have played a crucial role in shaping the geology and tectonics of Illinois. These major structural features were identified as the Rough Creek-Shawneetown and Cottage Grove Fault Systems in southern regions, the St. Genevieve Fault Zone and the Ozark Dome in western and southwestern regions, the Du Quoin Monocline and La Salle Anticlinorium in central and eastern regions, and the Sandwich Fault Zone and Plum River Fault Zone in the northern region. We emphasized the significance of these structural features in comprehending the subsurface rock formation and planning future drilling and injection operations. Furthermore, we provided a thorough analysis of the orientation of maximum and minimum horizontal stress at the IBDP site. This analysis was achieved by utilizing borehole breakouts and drilling-induced tensile fractures. The results of the analysis indicated that the average orientation of S_{Hmax} as inferred from borehole breakouts is approximately N66°E and the average orientation of S_{hmin} as inferred from drilling-induced fractures is approximately N24°W. Previous research on horizontal stress orientation,

such as the 2008 WSM that illustrates a transition from compressional to strike-slip faulting regimes in North America, is also referenced. The WSM suggests that the proposed injection site is in a transition zone dominated by a strike-slip faulting regime with the maximum horizontal stress direction in a NE-SW orientation. Additionally, we established a reservoir static model for the IBDP site. This model was designed to establish the structural and stratigraphic framework of the area and was created based on structure surfaces obtained from a high-resolution 3D seismic survey conducted in 2019, as well as faults that were extracted from seismic interpretation and ML algorithms. The model covered a substantial area of 5.6 x 5.6 miles and comprised various surfaces, including the top and bottom of each formation. The purpose of creating this model was to serve as a foundation for other tasks within the SoS project by providing a comprehensive understanding of the subsurface framework, and it can be used for various applications like reservoir modeling and simulation, forecasting the behavior of subsurface rock formation, and identifying potential risks for injection operations.

The geologic characterization described was developed iteratively with the fault identification aspect of Task 3 and forward modeling of Tasks 4 and 5, as designated in the methodology proposed in Figure 1. Seven unique geocellular models were made in response to these iterations. The geologic conceptual model was modified three times in support of this methodology, which concluded the relative importance of faults on the distribution of CO_2 and pressure within the Mt. Simon Sandstone and the Precambrian crystalline basement.

While updated three times, the final geologic conceptual model varied several attributes in the Argenta, Mt. Simon, and Precambrian formations (Table 3). The differences, evolved through iterations with the modeling task, were most notably the following:

- Adjusting the thickness of Argenta over the paleo-highs between the wells.
- Incorporating the discontinuous LPZs (low-permeability zones) in the model based on the conceptual characteristics of the mudstone in a fluvial system.
- Incorporating a greater number of faults in the model instead of the original four.

Table 3a. Precambrian (PC) geologic conceptual model at the beginning of the workflow and through the final iteration of the workflow.

	PC Geologic Conceptual model	
Attribute	**Initial**	**Final**
Depositional Environment	intrusive igneous, plutonic and extrusive igneous, volcanic	intrusive igneous, plutonic and extrusive igneous, volcanic
Fractures	None	Cluster of fractures, oriented with principal stresses with spacing from x to y feet and a to b length
Faults	Sparsely Faulted (4 faults), extended from top Middle Mt. Simon through Precambrian; Fault zone width x to y ft and length from a to b ft; orientation random	Intensively faulted, faults extended from Mt. Simon B to through the Precambrian; Fault zone width x to y ft and length from a to b ft; orientation with induced seismic cluster orientation and with large scale, farfield structural features
Porosity	Matrix porosity (< 1%)	Matrix and fracture porosities
Permeability horizontal	Matrix permeability (< 1 md)	Matrix and fracture permeabilities
Permeability anisotropy, horz	None	Yes, consistent with fracture orientation
Vertical permeability	<0.01 md	Yes, only in fractures.
Gross vertical height	Infinite into Earth	Infinite into Earth
Vertical height of p&p bodies	Uniform	Includes fracture p&p Upper part (Rhyolite): 30-40 ft Lower part (breccia): 20-70 ft Permeability 3 to 50 mD Porosity between 0 to 3%
Vertical height of LPZ	No LPZ	No LPZ
Horizontal dimensions p&p bodies	Infinite	2000-5000 ft x 300-800 ft
Orientation horizontal p&p bodies	N/A	p&p clusters (from fractures) with orientation of fractures
General shape of p&p bodies	None	Elongated, ellipses
Topography	Flat, surround area Near wells up to about 150 ft 3500 width of near circular topography; high surrounded by mostly lows and no other high in about 2 x 2 miles	Flat, surround area extended to simulate the near well area. Near wells up to about 150 ft 3500 width of near circular topography; 6 x 6 miles area about 6 highs somewhat evenly distributed with lows. Lows and highs relatively connected laterally, but some highs are isolated. Lows are wide features up to 6000 ft
Dip	Except topography, relative flat	Except topography, relative flat
Lateral continuity	N/A	Relatively isolated with low perm matrix surrounding the fracture clusters (0.0005-1 md)

Table 3b. Argenta geologic conceptual model at the beginning of the workflow and through the final iteration of the workflow.

	Argenta Geologic Conceptual model	
Attribute	**Initial**	**Final**
Depositional Environment	lower and upper shoreface environments with varying energy conditions	lower and upper shoreface environments with varying energy conditions
Fractures	None	None
Faults	Yes, same as PC	Yes, same as PC
Porosity	Intergranular, average 8%	Intergranular, average 8%
Permeability horizontal	0.8 md average	0.08 md average
Permeability anisotropy, horz	Yes, upper shore face higher perm than lower shore face	Yes, upper shore face higher perm than lower shore face
Vertical permeability	0.03 md average	0.003 md average
Gross vertical height	greater thickness above PC troughs and lesser thickness above PC hills (100-150 and 20-60 ft, respectively.)	greater thickness above PC troughs and lesser thickness above PC hills (100-150 and 20-60 ft, respectively.)
Vertical height of p&p bodies	Mostly uniform with gross thickness	Mostly uniform with gross thickness
Vertical height of LPZ	No layering or baffling	No layering or baffling
Horizontal dimensions p&p bodies	No bodies; uniform p&p	No bodies; uniform p&p
Orientation horizontal p&p bodies	N/A	N/A
General shape of p&p bodies	N/A	N/A
Topography	Similar to PC, but troughs filled, so a little less. Lack of knowledge regarding the thickness of Argenta in areas without wells.	Similar to PC, but troughs filled, so a little less. Thickness of Argenta reaches to less than 3 feet over the pleo-highs.
Dip	Except topography, relative flat	Except topography, relative flat
Lateral continuity	High, no isolated bodies	High, no isolated bodies

Table 3c. Arkose (Mt. Simon A) geologic conceptual model at the beginning of the workflow and through the final iteration of the workflow.

	Arkose (Mt. Simon A) Geologic Conceptual model	
Attribute	**Initial**	**Final**
Depositional Environment	Braided River, Fluvial, Eolian	Braided River, Fluvial, Eolian
Fractures	None	None
Faults	Same as PC initial	Same as PC final
Porosity	total = effective ϕ Intergranular, average 19% Injection interval (7025-7050) 7-32.5 % (avg 19.4 %)	total = effective ϕ Intergranular, average 19% Injection interval (7035-7050) 7-32.5 % (avg 19.4 %)
Permeability horizontal	62 md average Injection interval (7025-7050) 163 md (0.02-1920 md)	96 md average Injection interval decreased 10 ft (7035-7050)
Permeability anisotropy, horz	No, relative uniform	No, relative uniform
Vertical permeability	31 md average include LPZ	31 md average include LPZ
Gross vertical height	The gross thickness ranges from 350 ft to 375 ft above the Argenta.	The gross thickness ranges from 350 ft to 375 ft above the Argenta.
Vertical height of p&p bodies	In each interval of 20-30 ft of sandstone, there is a separation by mudstone and siltstone with low porosity and permeability.	In each interval of 20-30 ft of sandstone, there is a separation by mudstone and siltstone with low porosity and permeability.
Horizontal extension of LPZ	Continuous layers with low p&p	discontinuous layers with low p&p
Vertical height of LPZ	1 to 4 feet	1 to 4 feet
Horizontal dimensions p&p bodies	Infinite (at variable thickness) over 50x50 miles in central IL	Infinite (at variable thickness) over 50x50 miles in central IL
Orientation horizontal p&p bodies	N/A	N/A
General shape of p&p bodies	Uniform-sheet with cross bedding	Uniform-sheet with cross bedding
Topography	Yes, Similar to Argenta, but troughs filled, so a little less	Yes, Similar to Argenta, but troughs filled, so a little less
Dip	Except topography, relative flat (2.6°)	Except topography, relative flat (2.6°)
Lateral continuity	The sand bodies are continuous, but the siltstones are not.	The sand bodies are continuous, but the siltstones are not.

TASK 3 - FAULT IDENTIFICATION

INTRODUCTION

Quantifying in-situ subsurface conditions and understanding slip mechanisms along faults are critical to reducing the risk of induced seismicity and improving modern energy activities in the subsurface. In Task 3 (Sandia/MIT), we present both supervised and unsupervised ML methods to process and characterize microseismic data obtained at the IBDP site. During subsurface injection activities, there is a risk of activating hidden or unknown faults with stress and pore pressure changes associated with the injection.

Machine learning for fault detection and interpretation of microseismic wave fields has increasingly developed over the past five years (Perol et al., 2018; Zhu and Beroza, 2019; Mousavi et al., 2020; Münchmeyer et al., 2022). A recent deep-learning (DL) success to identify seismic phases from microseismic events and their wave patterns can be attributed to the DL method's ability to extract salient features in the data set from big training data. However, most DL methods require large training (i.e., labelled) data to train the model properly, which is not typical for geologic CO_2 storage sites.

At the IBDP site, CO_2 injection was maintained below fracture pressure, meaning that induced activities generally developed at natural, pre-existing zones of mechanical weakness. Thus, the low-magnitude (< ~1.5) microseismic data may reveal hidden or unknown faults that are prone to changes in stress and pore pressure. From previous interpretations of surface seismic data, there were indications of faults at the IBDP site. However, we hypothesized that waveform characteristics to identify events could be extracted through an ML feature extraction process with proper data-preprocessing and simple neural architecture to accommodate the limit in the training data. The latter is an important aspect since most geologic carbon storage sites experience a small number of events compared to large earthquake events. The proper feature extraction process can be enhanced by incorporating physical properties of waveforms in ML architecture. With ML, focal mechanism analysis of events, and inverse analyses of the microseismic data, characteristics of faults can be identified rapidly, which need to be corroborated by the geologic conceptual model.

In Task 3 (Sandia/MIT), we first implemented four supervised ML approaches for detection, phase picking, and source location of microseismic waveform data induced by CO_2 injection at the IBDP site using a small number of located event data (~600 events) over a period from February to March 2012 (cluster #2) in the catalog. For the first approach, we used a set of preprocessing and data augmentation techniques to feed waveform time-frequency information to a convolutional neural network (CNN) to accurately detect true events. For the second approach, we implemented the transfer-learning method to re-train the original PhaseNet architecture, which was developed based on conventional seismic data, such that it adapted to microseismic-level events to accurately obtain p-and s-arrival times. In both cases, we achieved a higher true event detection rate compared to the original catalog (manual picks). For source location identification, we used Wasserstein generative adversarial network (WGAN) to generate new synthetic waveform data that have properties similar to those in the catalog. With the increased number of waveform data as training

data, the last CNN-based model was constructed to estimate the source locations for newly detected events by the first CNN model.

Next, an unsupervised ML approach was developed as a fingerprint-based clustering approach (Hoffman et al., 2018) to classify waveform characteristics resulting from different zones of mechanical weakness. We used a Short Time Fourier Transform (STFT) to reduce dimensionality and highlight rupture motion, followed by the Nonnegative Matrix Factorization (NMF) and the Hidden Markov Model (HMM) to construct a time-dependent probabilistic architecture. The resulting spatio-temporal patterns were taken as fingerprints of waveform characteristics. Unsupervised clustering was performed on the fingerprints to identify similarities and reveal time-dependent patterns of the microseismic data associated with hidden and unknown faults. We presented how the spatio-temporal patterns were related to changes in pore pressure and stress caused by CO_2 injection, and we also compared clustering results with the focal mechanism solutions of the microseismic data. This ML approach improved characterizing seismic waveforms and detected low-magnitude seismic events leading to the discovery of hidden fault/fracture systems.

METHODOLOGY

Data Preprocessing of Raw Continuous Microseismic Data

Raw continuous microseismic data at IBDP was processed for event detection and waveform characteristics. The raw data was originally saved as 10-second windows at 2 kHz sampling rate with traces between 84 and 94. A two-WellWatcher-PS3-geophone array in a CO_2 injection well (CCS1) had four-channel data from a four-component passive seismic sensing system; the geophysical monitoring well (GM1) had three-channel data per each geophone from a 31-level array of three-component geophones (Bauer et al., 2016). One example of waveform with a total number of 94 traces is shown in Figure 21. The detailed description of microseismic data acquisition and processing is reported in Will et al. (2016).

In the catalog of microseismic events at IBDP, as briefly described in Will et al. (2016), there are two types of events: (1) detected events selected by simple triggering algorithms (e.g., a combination of filters and short-time-average/long-time-average [STA/LTA] thresholding) and (2) located events, which have source locations estimated by additional constrains of directional waveform information derived from hodograms.

For ML applications in Task 3 (Sandia/MIT), four-channel data in the raw continuous microseismic data from two PS3 geophones (i.e., PS3-1 and PS3-2) were converted to three-directional waveform data (V, H1, H2). The continuous waveform was stored in separate 10-second files (total of 8,640 files) that make up the 24-hour recording and converted to an MSEED file. Both raw and processed waveform data are shown as examples in Figure 22.

We focused on two microseismic event clusters (#2 and #4) to characterize events detected at the IBDP site that occurred in the Precambrian basement, as opposed to those that occurred in the Mt. Simon Sandstone. The microseismic event locations are shown in Figure 23.

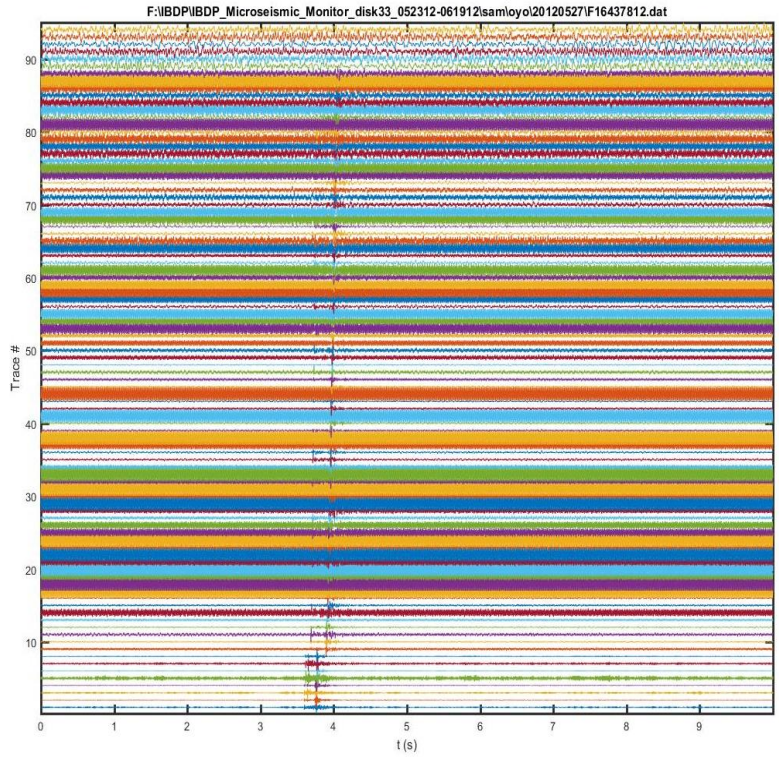

Figure 21. An example of raw continuous 10-second window waveform event data from two PS3 geophones and GM1 geophones.

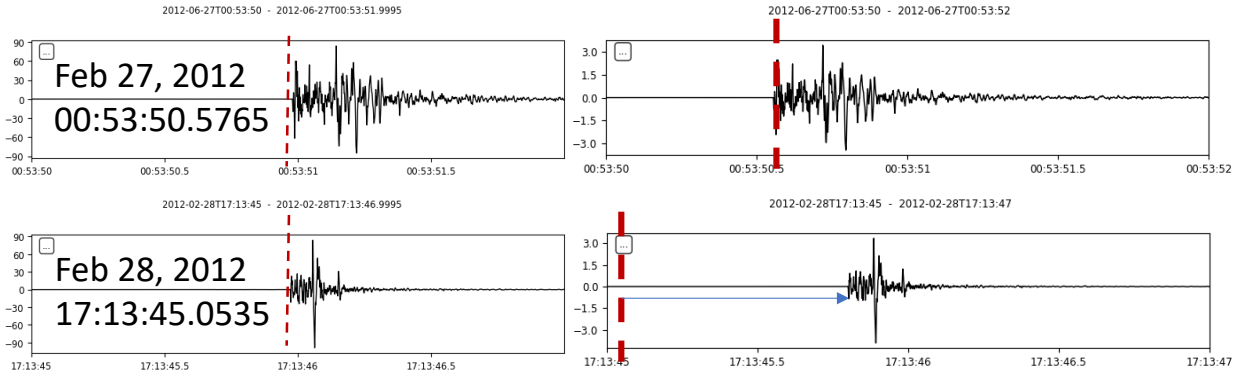

Figure 22. Examples of waveform (vertical channel) from the located event catalog (left) and raw continuous data (right). Dashed red lines represent event times in the catalog. Note that the waveform in the catalog is after filtering, hence they are different from the raw continuous data. The red dashed line on the raw data (right) is the same as the catalog to highlight the data shift between the original raw and processed catalog data. This also shows that the data shift is consistent.

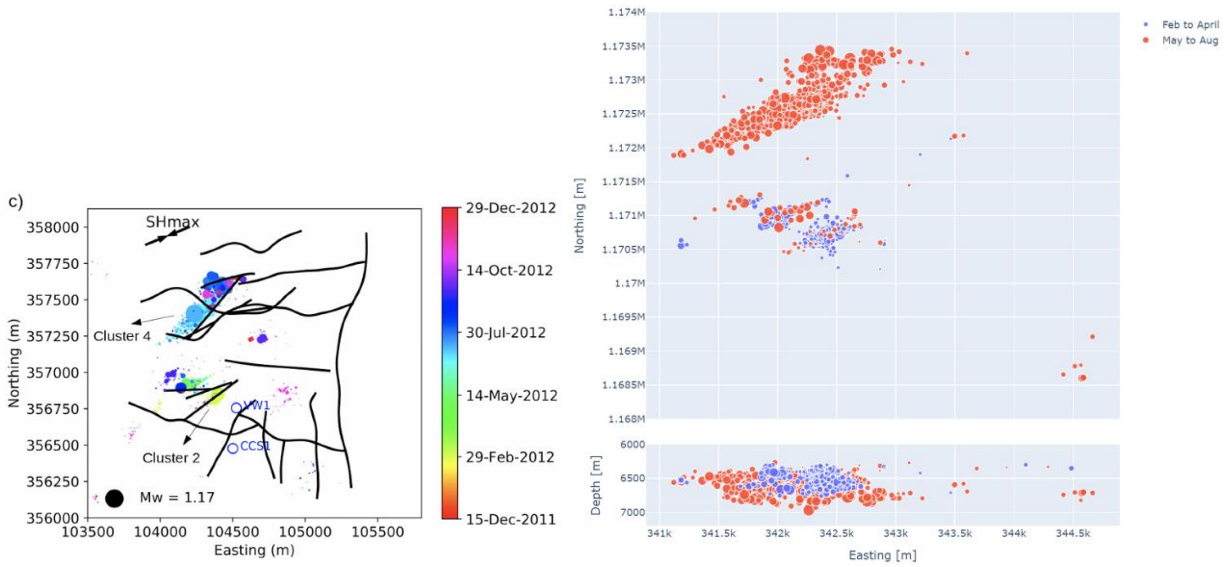

Figure 23. (Left) Microseismic event locations from the beginning to the end of 2012 at the IBDP site. The solid lines represent faults constructed from seismic survey. (Right) Microseismic event location from clusters #2 (February-April 2012) and #4 (May-August 2012) at the IBDP site.

For event detection, phase arrival-time estimation, and fingerprint methods for waveform characterization, we focused on data recorded at PS3-1 and PS3-2, which have better signal to noise ratio and are collected from the two deepest geophones near the injection depth. Figure 24 presents the frequency of recorded events between February 27, 2012, and March 3, 2012, when there was a significant increase in seismic activity in cluster #2. This period accounts for more than 80% of the located events over the 15 days (most of cluster #2's active period). Seismic event origins of this period were mainly concentrated in cluster #2, which was located 1,161 ft (354 m) away from the CCS1 injection well, as shown in Figure 23. This active period was then followed by a few days of minimal seismic records, which we will call a transition period, since we discovered changing waveform characteristics in both periods.

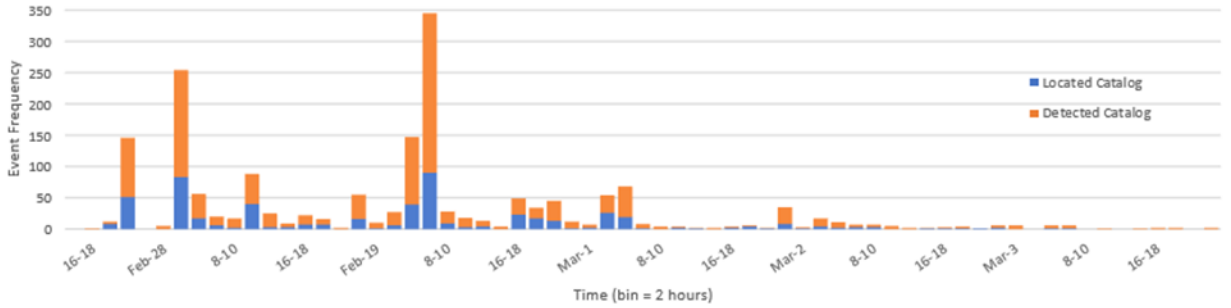

Figure 24. Reduced period of event frequency of occurrence within chronological 2-hour bins over February 27, 2012, to March 3, 2012. The located catalog is superimposed on top of the detected catalog. The active period of cluster #2 is from February 27, 2012, to March 1, 2012, which is followed by the transition period of cluster #2.

Data Processing and Training Data Generation for Event Detection and Phase Arrival Times

Event data preparation: We implemented ConvNetQuake's window selection strategy (Perol et al., 2018) by using the catalog to find samples. For the case of events, this strategy assumes the catalog reports an onset time of each event and its origin coordinates to estimate and find the events in the continuous records when given an average wave-travel velocity. To prepare the event windows, the continuous raw waveform data must be preprocessed, since the located event data in the catalog at the IBDP site (Will et al., 2016) contains the time information as the onset of seismic wave arrival to the sensors. Additionally, the two-second window of the event waveform is processed so that the arrival time of the waveform from PS3-1 is aligned slightly earlier than the center of the two-second window. Hence, the event data must be extracted from raw continuous waveform data using information in the catalog to pinpoint the event occurrence. To do this, the start of the sampling window is offset to about two seconds behind the reported event time in the catalog and a travel speed of ~16,000 ft per second is added, ensuring that the 0.2−0.5-second interval of event is captured within the two-second window. For this work, we used waveform data from both PS3-1 and PS3-2 sensors for event data.

Noise data preparation: We looked for windows of seismic noise in between the cataloged events to ensure that the noise data could be captured randomly. We implemented ConvNetQuake's window selection strategy by using the catalog to find events or noise samples. We also added a threshold value (0.01 amplitude) to prevent non-cataloged true events from integrating into the noise-training dataset. As a result, one noise data was selected every 100 seconds for 15 days, resulting in a total of ~13,191 noise data from PS3-1 & PS3-2.

The event times in the catalog were used to search for the start of a seismic event within raw continuous waveform, and we extracted 2-second windows of waveform for event detection using convolutional neural network (CNN) and 1.5-second windows for phase arrival times using PhaseNet (Zhu and Beroza, 2019). Figure 25 shows the overall workflow for both the CNN model and PhaseNet, respectively, starting from this window extraction.

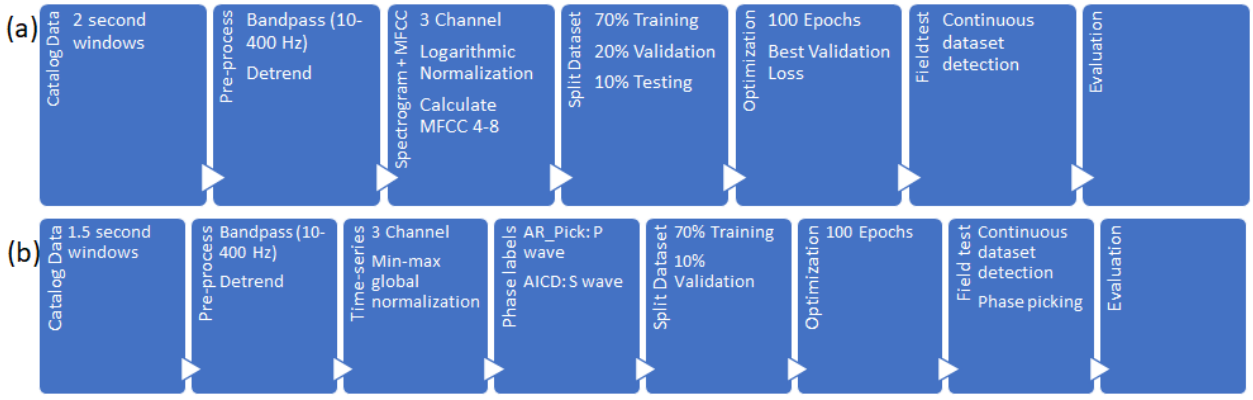

Figure 25. Workflow for (a) event detections using convolutional neural network (CNN) and (b) arrival-time estimation (i.e., phase picking) using PhaseNet.

***Data preparation for event detection*:** Waveform samples were preprocessed prior to training CNN models. Inspection of time-frequency of multiple raw data samples suggested seismic event energy to be predominant between 10-400 Hz. First, a bandpass filter of 10-400 Hz and a simple data detrend was applied to the waveforms. We transformed the sample's time-series information into an augmented input information in the form of time-frequency to provide our ML approach with additional and sufficient

information to achieve the best detection-accuracy performance. Short Time Fourier Transform (STFT) with a window size of 64 ms (i.e., 128 points) was used to convert the independent channels of the 2-second waveform samples into 60 x 60 spectrogram images. These images were then normalized to adjust the distribution of the data values, leaning towards Gaussian. We implemented a normalization preprocessing similar to one in sound signal spectrograms (Dennis, Tran, and Li, 2010) to improve our CNN model results. This preprocessing incorporated the log-scaling of the spectrogram images to adjust the sample data distribution using the following log-power transformation:

$$S(k,t) = \log(X(t, k)+c), \quad \text{(Eq. 1)}$$

where X(t, k) is the Fourier Transform of the time bin t with the frequency bin k, and c is a constant value to avoid infinity values in the calculation (i.e., $1x10^{-22}$). All three-channel spectrogram images of each event window were then stacked into 3D input, resulting in 60 x 60 x 3 input samples. Figure 26 shows a spectrogram example prior to corrections (A) and after corrections (C) with their respective histograms (B and D).

The new log-scaled time-frequency images were further normalized to [0,1] using a min-max function over the entire waveform data set (i.e., global min and mix values), which is suitable for the rectified linear unit (ReLu) activation function.

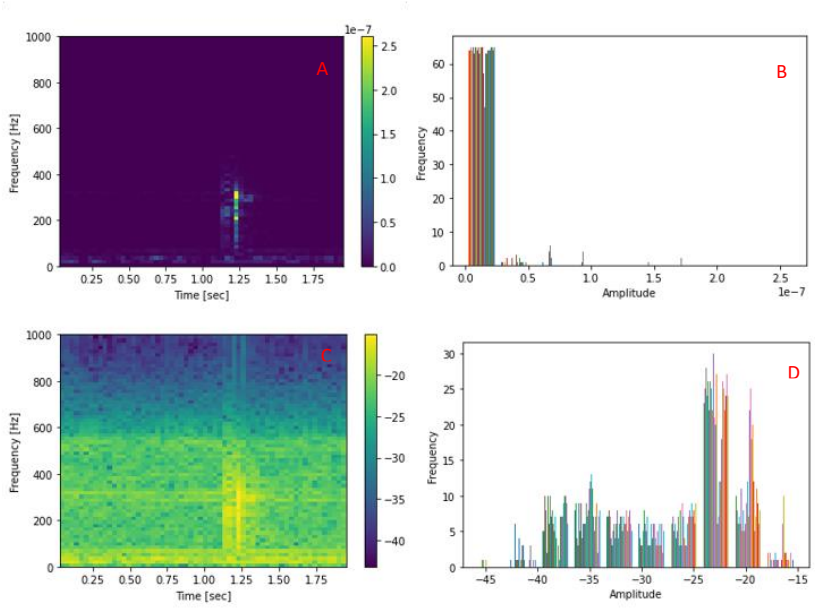

Figure 26. Input data preparation for CNN before data remapping. (A) Generated spectrogram example for a single-channel seismic event. (B) Histogram of spectrogram prior to rescaling. (C) Spectrogram after logarithmic rescaling. (D) Histogram of spectrogram after rescaling.

Data preparation for phase picking: Preprocessing of the dataset for PhaseNet included applying a 10-400 Hz bandpass filter, data detrend, per channel normalization, and determination of phase arrival times for each waveform. Two traditional phase-picking methods were used to estimate the p- and s-wave arrival times of raw continuous waveform data corresponding to the cataloged events. First, AR-picker method implemented in the Obspy package (Beyreuther et al., 2010) used an Auto Regression – Akaike Information Criterion (AR-AIC) method and the STA/LTA ratio, and PhasePaPy (Chen and Holland, 2016) used the derivative of the AIC function (i.e., AICD picker). For generating training data for p- and s-wave arrival times, AR-picker and PhasePaPy were used to estimate the arrival times, and the best results

of these methods were evaluated manually to finalize the training data sets. For the cluster #2 events, we focused on the waveform data over a period of February 27 to March 12, 2012. Based on manual comparison for selected cases (see Figure 27), the p-arrival times using the AICD-picker were generally more accurate and consistent than those of the AR-picker, while the s-arrival times using the AR-picker were consistently reasonable. We also noted that the general p- and s-arrival time difference for cataloged waveforms was between 0.065-0.08 seconds for the cluster #2 data, which was also used as a guide to evaluate automatic-picking accuracy.

The precision of this labeled data was approximate but not as optimal as would be preferred for a deep learning (DL) model, but transfer learning (TL) easily overcame this to make even more precise picks. These picks were later inspected for a final screening to remove incorrect labels, resulting in 419 labeled training samples to be used in PhaseNet.

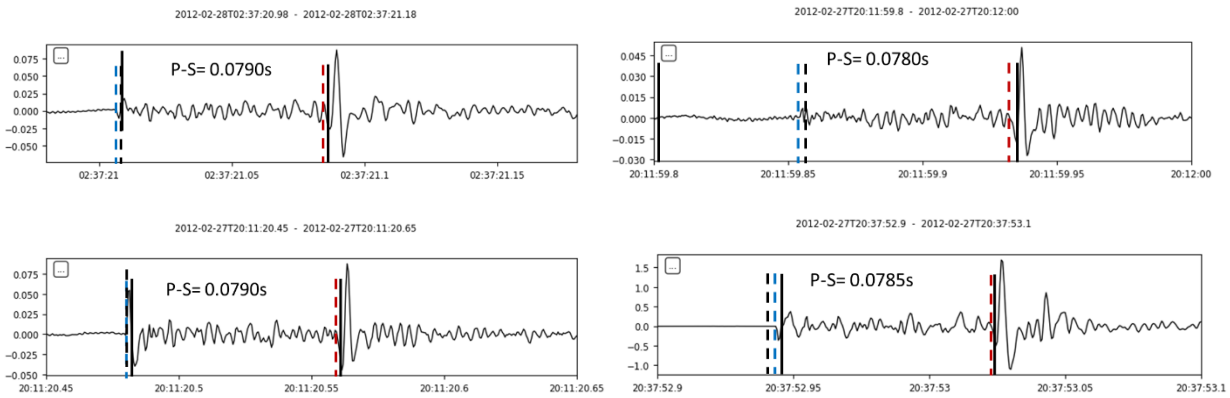

Figure 27. Sample phase picks from manual picks and parameter-based auto pickers. Human p-arrival picks are shown with a blue dashed line, and s-arrival picks by a red dashed line. The p- and s-arrival obtained by AR-pick are shown by solid black lines. AICD p-arrival picks are shown by dashed black lines. Data-specific, optimized AR-picker performs well at predicting s-arrivals but is outperformed by the optimized AICD model at predicting p-arrivals.

Data augmentation for source location estimation: To enhance the accuracy of source location estimation and overcome a limited number of events (i.e., 400-500 events in cluster #2) for ML training data, we explored a data augmentation approach. It is noted that the DL methods for source locations in the literature have typically been trained with tens to hundreds of thousands of event data (Münchmeyer et al., 2022). In this work, we generated additional training data by training generative DL models. An open source SeismoML (Mancini et al., 2021) was used to learn the relationships between source locations (3D coordinates and distance) and waveform data. Here we used Wasserstein generative adversarial networks (WGAN)−Gradient Penalty from SeismoML. As in the original model, input includes x, y, z coordinates of source locations and distance between source and geophone locations, while output is a seismogram of a single channel. Detailed description of the method is available in Mancini et al. (2021) and references therein. Once the WGAN-GP model was trained with located event data in the catalog, the trained generative model was applied for generating synthetic event data at a range of locations to increase overall training data.

Figure 28 shows examples of generated synthetic waveform data with waveform of the located events in the catalog. We applied a bandpass filter (10-400 Hz) to dampen the noise level of the generated waveform. Overall, the generated waveform had very similar p- and s-arrival times to the located events.

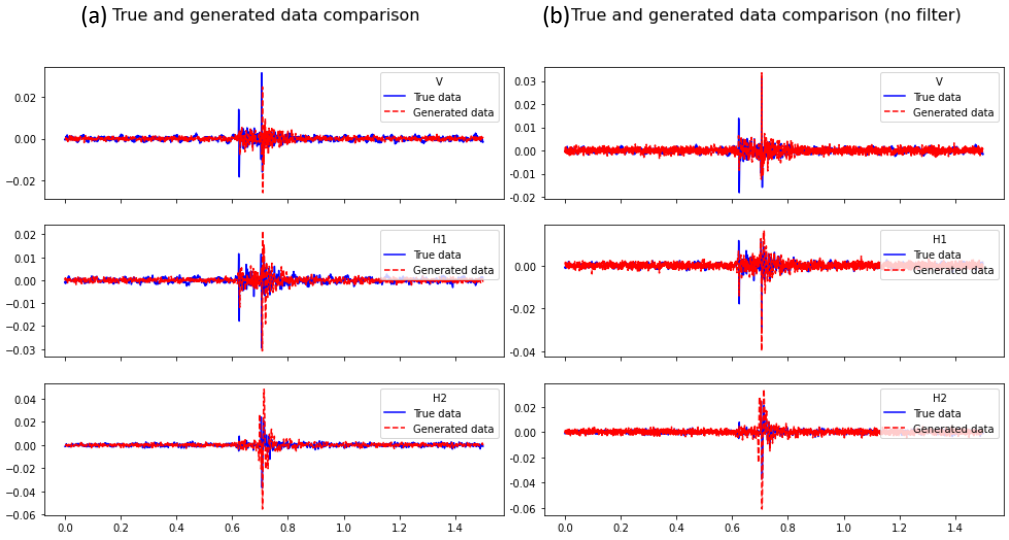

Figure 28. Comparison of generated waveform using WGAN and waveform in the catalog ("true"). a) Bandpass filter and b) no bandpass filter. V, H1, and H2 represent three-directional channels.

Deep Learning Methods for Event Detection, Phase Arrival-time Picking, and Source Location Estimation

***Event detection*:** We developed a convolutional neural network (CNN) model to detect microseismic events from the continuous waveform data at the IBDP site. The CNN model consisted of four convolution layers with each layer followed by max pooling, batch normalization, and dropout, as shown in Figure 29. As described in the data preprocessing, a three-channel waveform spectrogram was used as input to the CNN. A ReLu activation function was used in each layer, excluding the final classification layer, which used a Softmax activation for event classification. The loss was computed using binary cross entropy by comparing each of the predicted probabilities to actual class output (event or noise).

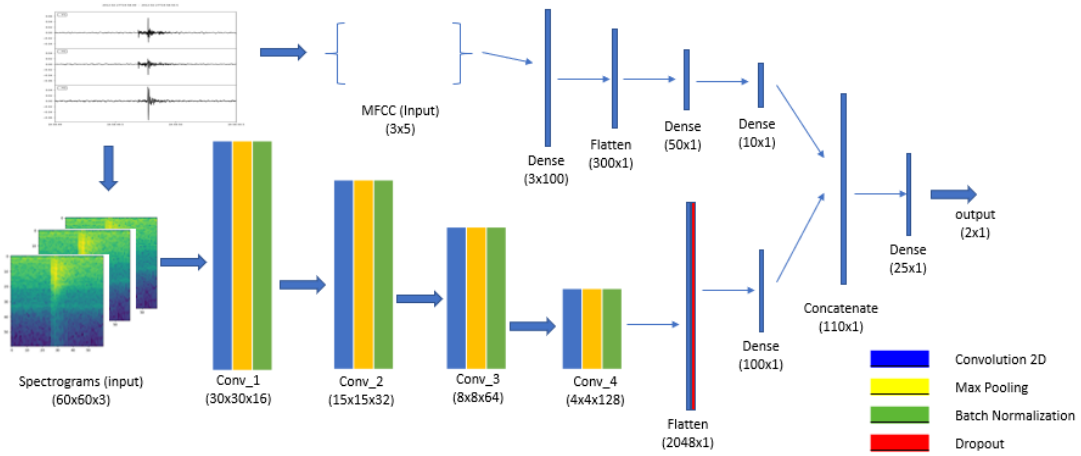

Figure 29. Schematic of CNN and MLP (multi-layer perceptron) architecture for event detection. The inputs are three-channel spectrogram images for the CNN and MFCC coefficients for the MLP. Features extracted by both models are concatenated before entering a final dense layer leading to the final prediction output.

We considered presenting multiple input information to the DL model to improve DL performance, especially by using additional physics-based information (e.g., Yoon et al., 2020). For additional physical quantity, Mel-Frequency Cepstrum Coefficients (MFCCs) were extracted from each channel time-series to serve as the input to a multilayer perceptron (MLP) to improve detection accuracy. The MFCCs represented a short-term power spectrum of sound as perceived by human hearing, representing energy-related information of waveform. For the CNN + MLP model, the output of MLP was concatenated with that of the final dense layer from the CNN, which was followed by a dense layer before the classification output.

For training event detection CNN models, the data set was split into 70% of samples for training, 20% for validation, and 10% for testing. Due to the significant imbalance in the number of event and noise samples for training, we avoided the use of batch shuffling and decided to stack the training set such that there would be an event sample after every eight noise samples, ensuring there would be at least a few numbers of events in every batch during training.

***Phase picking for p- and s-arrival times*:** PhaseNet (Zhu and Beroza, 2019), which is a deep neural network designed for automatic phase picking through data segmentation, was used. PhaseNet is a U-Net variant architecture, designed for 1D time series inputs and outputs three probabilities corresponding to p-arrival, s-arrival, and noise. PhaseNet was originally trained on three-component data from the Northern California Earthquake Data Center Catalog with more than 700,000 local earthquake event data recorded at 100 KHz. These events contain very distinct characteristics in the waveform, compared to the IBDP microseismic data, in terms of seismic magnitude, sampling rate, and total samples. The IBDP data consists of microseismic recordings at 2,000 Hz with fewer than 20,000 detected events over ~3 years in the catalog. To improve the accuracy of model performance, we studied the retraining of PhaseNet using the IBDP dataset. This transfer learning approach was evaluated by retraining PhaseNet with initialization using the pre-trained model weights of the original PhaseNet, followed by training the model with our distinct waveform characteristic training samples. The new PhaseNet model adjusted to the temporal resolution of our data, as well as the signal amplitudes and aleatory artifact noise, which were all different from the dataset used for the original PhaseNet.

We used the same procedure with PhaseNet but with 1.5-second windows instead and no overlap. Since the output of PhaseNet is the prediction probability of events for all possible waveform points, a two-step approach was used to finalize the event detection. First, all 1.5-second waveform windows that did not have p-wave and s-wave prediction were eliminated. Second, for the remaining windows, a threshold on the prediction probability in both p-wave and s-wave detection was applied to separate event windows from noise windows. Our visual inspection indicated the probability that a threshold of 0.9 tends to detect events better than that of 0.8 in terms of false positive detection. Hence, we evaluated the performance of PhaseNet with a threshold of 0.9.

Fingerprint Method of Waveform Data for Waveform Clustering

Our first stage of unsupervised learning involved identification procedures of the hidden Markov Model (HMM). A stochastic matrix is a square matrix used to describe the transitions of a Markov Chain such that each entry is a real, non-negative number that represents a probability. To achieve this requirement, we implemented the non-negative matrix factorization (NMF), which processes observations to generate non-negative estimated parameters for the HMM.

We performed the NMF such that each spectrogram was reconstructed to a product of two matrices: the first matrix being the dictionary of frequency components, or W matrix, and the second

matrix being the activation coefficients, or H matrix. This resulted in dimensionality reduction, where columns of the original spectrogram were mapped into smaller dimensions. The W matrix focused on the features within the spectrogram and specifically highlighted the amplitude of the signal. The H matrix focused on the patterns within the spectrogram and specifically highlighted when the signal changed significantly. We tested and learned the HMM on both matrices separately and compared the results. Examples are shown in Figure 30.

To calculate the NMF for each spectrogram, we utilized a Python library known as NIMFA (Zitnik and Zupan, 2012). NIMFA includes several different factorization methods for the NMF and supports both dense and sparse matrices. We implemented the standard NMF, which uses simple multiplicative updates based on Euclidean distance. We specified the objective function to be the standard Frobenius distance cost function, and to reduce dimensionality, we selected the number components that can be used in the NMF. This type of NMF is a powerful method for identifying distinct patterns within the signal.

In this work, we began by learning our HMM on the NMF H or W matrix, which further isolated and removed commonalities between signals and reduced dimensionality. We focused specifically on temporal patterns as a sequence of hidden states in time. These states are defined as patterns of frequency components that tend to happen together. In this case, we used what is known as a first-order Markov Chain. With an HMM, the output of a time step is also dependent on the hidden, imaginary state corresponding to the observation. After the HMM algorithm converges, the learned distributions are used to find the final values for the states (Holtzman et al., 2018).

In this work, HMM analysis was performed using a Python package of Pomegranate (Schreiber, 2018). Pomegranate assumes that all probabilistic models can be seen as probability distributions, meaning they all result in probability estimates for the samples. Since compositional models can be viewed as probability distributions, a mixture of Bayesian Networks or Hidden Markov Model Bayes' Classifiers can be built to make predictions over sequences. After HMM analysis of the hidden state of the waveform signals, k-means clustering was performed to clusters based on the fingerprint of the hidden state change. A detailed description of the method used in this work can be found in Willis (2020).

For IBDP data, the waveform data were converted to the spectrogram using short-time Fourier transform (STFT) as shown in Figure 30. For the HMM application for the fingerprint identification of the waveform signal, the most basic NMF was employed. We built the HMM model such that the model learned the transition matrix, emission distribution, and start probabilities for each state. We specified for this method to use an exponential distribution for the emission distribution of the components of the model. Exponential distributions are generally used to model the time for a process to occur at a constant average rate, which is what results from the STFT, making it an appropriate distribution to use.

Using k-means clustering, we clustered the HMM predictions into three distinct clusters and analyzed the spatio-temporal relationship within these clusters. This clustering and analysis resulted in a sequence of outputs for each signal and a transition matrix representing the probability of a certain state following a previous state. We used the transition matrices to create a fingerprint for each signal. Our final stage of unsupervised learning involved testing different clustering methods with every signal's fingerprint. We tested and compared k-means clustering and t-distributed stochastic neighbor embedding (t-sne) clustering. We focused our study on two event clusters: cluster #2 (698 events), which occurred between February 21 and April 3, 2012, and cluster #4 (745 events), which occurred between May 16 and August 12, 2012. Each waveform data was processed with a Butterworth Bandpass Filter, and we transformed the waveforms into event spectrograms using STFT to reduce dimensionality and improve pattern recognition.

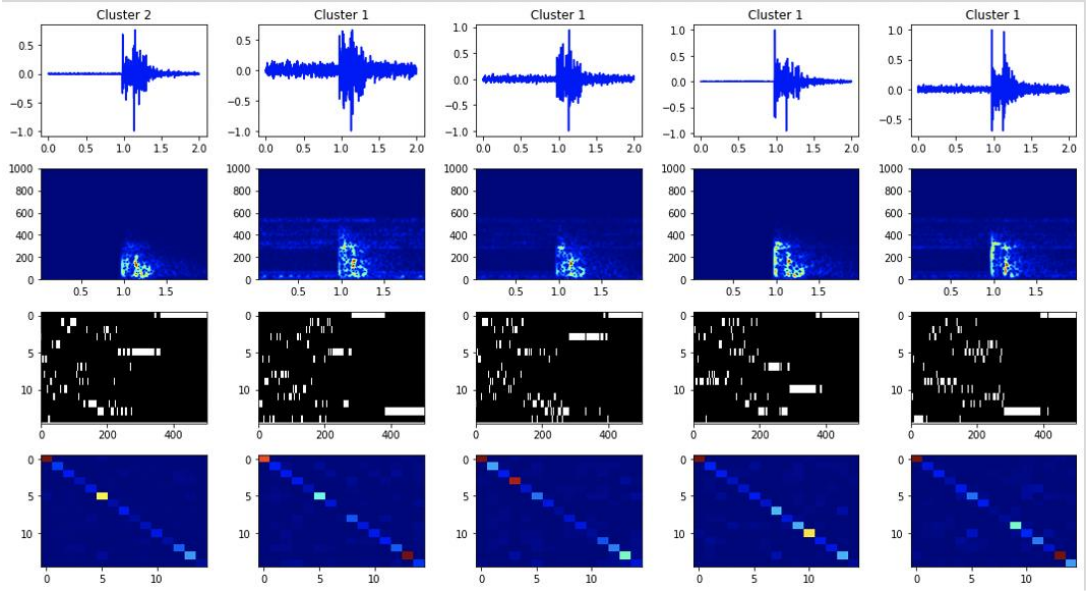

Figure 30. Application of the fingerprint method for the microseismic waveform data at the IBDP. The top row is the three-channel event waveform data of two-second window; the second row is the corresponding spectrogram; the third row shows the hidden state change over time based on the HMM analysis; the bottom row is the fingerprint map of the hidden state change. A total of three clusters were used for clustering, and clusters #1 and #2 examples are shown.

Focal Mechanism Analysis

Microseismic waveforms contain rich information about the source and medium properties along the path of propagation. Focal mechanisms can be used to determine the orientation and slip of a fault. Seismic-phase polarity is the most straight-forward way to calculate the focal mechanism of a seismic event. With microseismic data, the determination of seismic-phase polarity can be difficult due to emergent phases and low signal-to-noise ratio (SNR). Estimation of p- and s-arrival times helps when determining seismic-phase polarity. Although p- and s-waves can be observed in induced microseismicity, surface waves are often absent from the waveforms, making it harder to identify the s-wave. For cluster #2 events, we estimated that the s-wave would arrive between 0.076 and 0.079 seconds after the p-wave. With these estimates, we identified the seismic-phase polarity for microseismic data. Then, using recent developments in earthquake analysis, we computed stable and accurate focal mechanism solutions for microseismic data. By picking arrival times and polarities of the p-and s-waves, we computed the focal mechanisms with the implementation of HASH (Hardebeck and Shearer, 2002, 2003) in SEISAN, which is an open-source earthquake analysis software. HASH is also an open-source software from the USGS that finds the best-fitting, double-couple mechanism for each event.

HASH is a method for determining focal mechanism solutions with first-motion p-wave polarities. The main difference between HASH and previous methods, such as FPFIT, is that HASH considers possible errors in the source location, velocity model, and polarity observations. A set of acceptable focal mechanism solutions, including those with up to a given fraction of misfit polarities, is found for each event. Due to the complexity and poorly understood effects of source location and velocity models on focal mechanism, multiple combinations of these parameters are used when determining the focal mechanism solution. A set of acceptable solutions is considered stable if the solutions are tightly

clustered. Once the set of acceptable solutions is considered stable, an average solution is computed to find the preferred focal mechanism (Hardebeck and Shearer, 2002, 2003).

In focal mechanism analysis, the best solutions are generally found using one seismic event recorded by several seismic stations that are distributed evenly around the epicenter of the event. However, stations at the IBDP only differ in location by depth since the seismic network is a string of receivers in injection and GM wells. This limitation greatly affects the accuracy of the focal mechanism solutions. We selected five to nine three-component stations with the highest SNR to help achieve more accurate focal mechanism solutions.

RESULTS

Detection of Microseismic Events

Figure 31 shows that the CNN model was accurately trained, and the best model selected had a loss value at an order of ~1×10^{-6} for validation dataset. However, the CNN + MLP model improved the validation loss value by nearly one order of magnitude at ~1×10^{-7} within the same number of epochs. The CNN + MLP model with reduced MFCC parameters (six key-feature MCFF components) achieved only slightly lower results than the simple CNN model but showed a similar trend to all MFCC models, which suggested models with MFCCs would keep improving as they underwent more epochs.

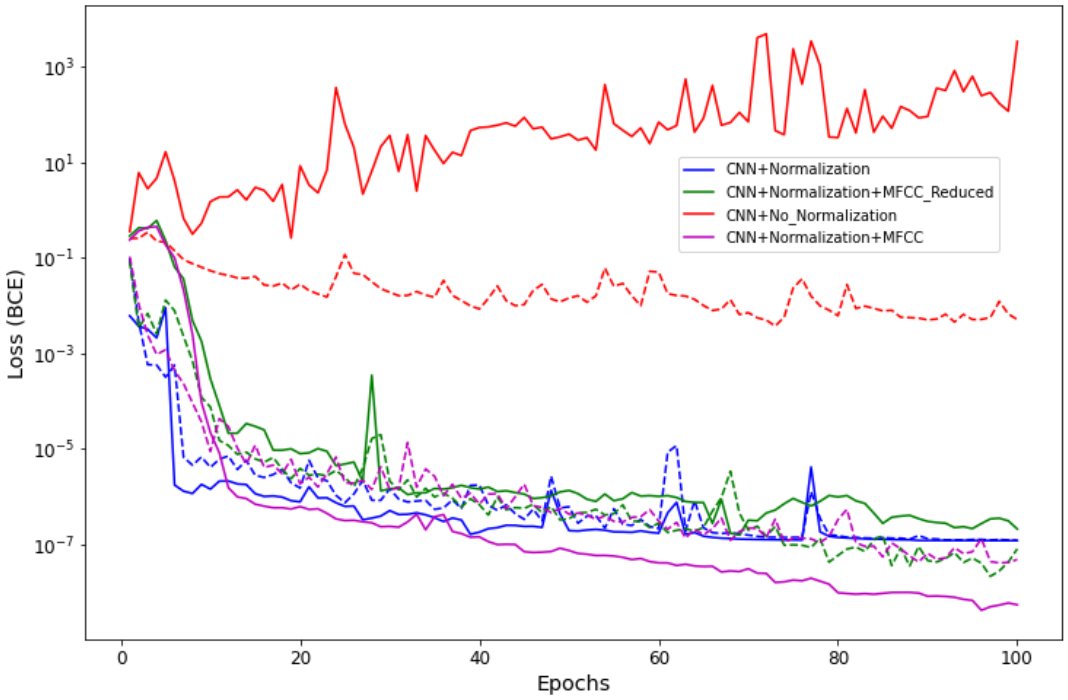

Figure 31. Model loss versus epoch for multiple CNN model variations. Individual model losses are shown as dashed lines, and the individual model validation losses are shown by the solid lines of the respective model color line identified in the legend. Properly normalized data models significantly improve performance and minimize overfitting, compared to simply using raw data.

Properly normalizing the spectrograms allowed the frequency of the waveform data to be distributed over the range of amplitude more evenly (Figure 26, b and d). Figure 31 shows that validation

loss results with normalization perform better than those without normalization. Therefore, proper data-preprocessing reduced model overfitting and identified new waveforms of interest.

Comparison of detection rates over an active period of the cluster #2 period in Figure 32 indicates that the CNN model detected more events than those reported by the standard triggering algorithm in the detected catalog. Specifically, the CNN detection rate was similar to the triggering algorithm (STA/LTA) during the active and post periods but exceled at detecting event waveform characteristics during the transition period (depicted by the yellow zone in Figure 32), revealing a new set of events to enhance the catalog information. Because the CNN model extracted more complex features from site-specific samples, we expected higher-confidence-level pickings than with the triggering algorithm. Visual inspection of image windows corresponding to CNN detections confirmed that most of these events revealed at least one phase arrival onset. To show the effectiveness of this model, we detected more than double events of interest than using PhaseNet alone over continuous data.

We also compared the number of recorded events with clear microseismic characteristics obtained from the PhaseNet model and the located catalog. PhaseNet detected almost double the number of events having evident p- and s- wave features (more than 90% probability) compared to those initially reported in the located catalog.

Detection rate comparison over cluster #4 in Figure 32 shows a similar trend during a period of high event density. The standard triggering algorithm detected slightly more potential microseismic events during an active period compared to the CNN model.

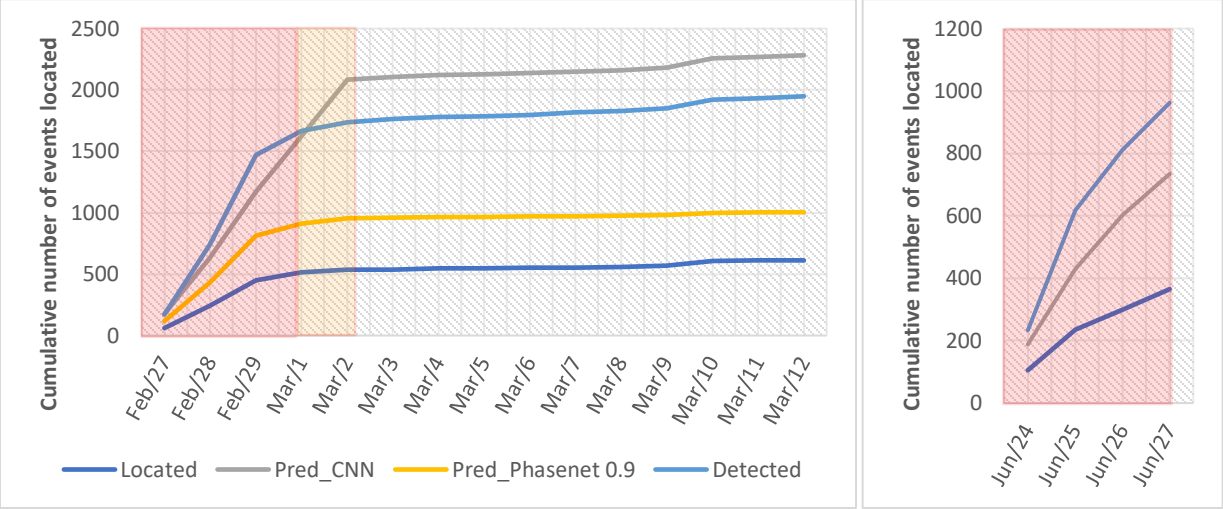

Figure 32. Cumulative number of detected events through the CNN (Pred_CNN) and PhaseNet (Pred_Phasenet 0.9) models in comparison to the located and detected events in the catalog. Cluster active region is represented by the red-shaded area in the plots, and the yellow-shaded area represents the transition period. (a) Cluster #2 and (b) a short period of cluster #4.

Most detected events (Figure 33a) showed major similarities with events in the located catalog, which generally had short duration (0.25 seconds) and very distinct phase onset and p-s arrival difference between 0.065-0.08 seconds. This waveform characteristic is represented well within the training data, resulting in excellent feature extraction by the CNN model. In contrast, we also detected activity not represented in the catalog, consisting of events around one second in duration and very distinct p-wave arrival but no notable s-wave arrival (Figure 33b). Therefore, the characteristic of no distinct s-wave arrival events shared more characteristics with slow slip physics compared to the fast slip of the first group of

waveforms. The third group of detected events consisted of overlapping slow slip events spanning the full window, making it difficult to identify individual p- and s-wave arrivals, shown in Figure 33c. This type of waveform is known to be challenging for most parametric-based methods and is consequently usually discarded as a non-event. However, we found that these events, stacked together with subsequent detections, behaved as a single event of long duration that could range from 30 seconds to 30 minutes.

The last group in Figure 33d consisted of detected waveforms from cluster #4. At first glance, they looked similar to the first group's waveforms, but in fact, they showed subtle dissimilarities, which were consistent with our knowledge of cluster #4. In general, their arrival-time difference was significantly larger than the first group's, which is consistent with the larger travel time required by cluster #4 events to reach the sensors and our knowledge that p-waves move faster than s-waves. Due to this arrival-time difference, the duration of the events was also larger, between 0.4-0.5 seconds. Cluster #4 also had lower SNR event signals in PS3-1 than cluster #2, despite being reported in the located catalog as higher magnitude events.

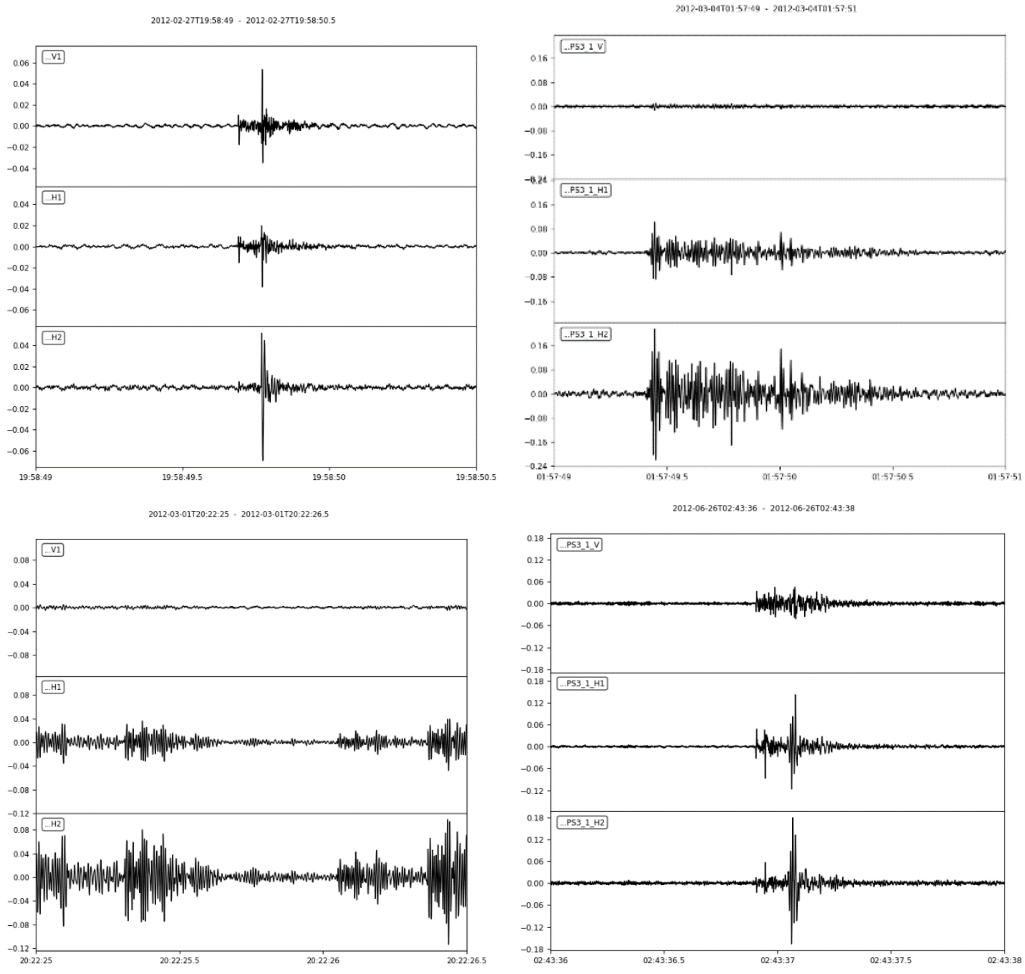

Figure 33. Examples of event characteristics in cluster #2 (a-c) and cluster #4 (d) captured by the CNN model. Three channels from PS3-1 are shown.

Microseismic Event Clustering

We performed k-means clustering of fingerprint output from the NMF-HMM process with three-channel components of cluster #2 and cluster #4 microseismic events, separately. The vertical span of the sensors benefited the ability to detect differences in vertical component and allowed for more depth locations. Horizontal components of waveform highlight shear wave characteristics more clearly. As presented, we chose to use the HMM on the activation coefficient matrix of frequency components from the NMF. For clustering, we needed to determine the input of waveform data and the number of clusters to optimally characterize the waveform patterns. In this work, we used three channels (V, H1, and H2) of waveform as input to NMF to extract fingerprints of each waveform event. An example of these maps is shown in Figure 34. For clustering waveform events, we tested clusters (or groups) from 3 to 10. To clarify the feature maps, we used t-sne to visualize high-dimensional data in a two-dimensional map (Figure 35). Figure 35 shows that three groups tended to cluster the events better than the higher number of groups. Figure 35b also shows that group 0 represents dominantly high-magnitude events, group 1 represents intermediate-magnitude events, and group 2 represents low-magnitude events. From this relation, we speculated that group 0 represents the main slip events or those that occurred along the main fault plane, while events in groups 1 and 2 represent small-scale slip events or those that occurred along the fracture network.

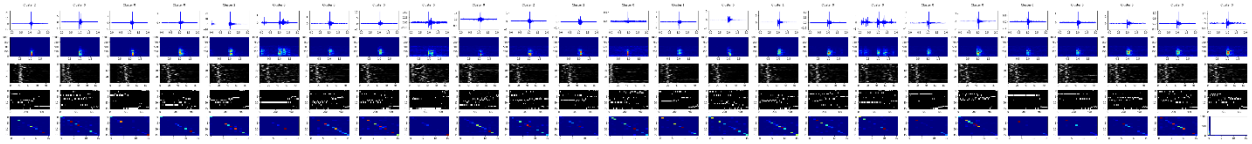

Figure 34. Example of clustering results with the vertical channel waveform data and a total number of three clusters. The order of rows follows the vertical waveform of event, seismogram, activity coefficients of NMF output, state sequence of HMM output, and fingerprint of waveform data.

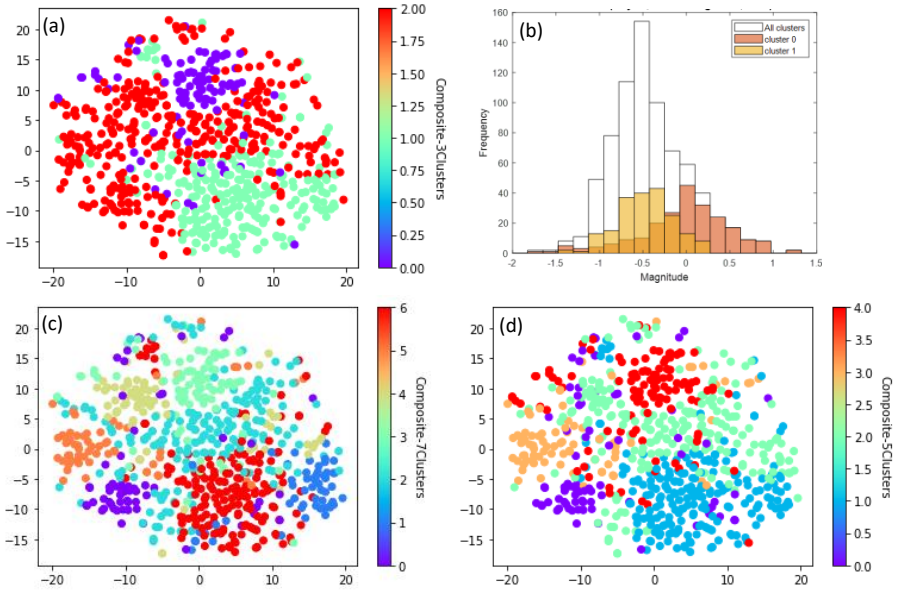

Figure 35. (a, c, d) For different number of clusters (3, 5, and 7) t-distributed stochastic neighbor embedding (t-sne) is a statistical method for visualizing high-dimensional data by giving each datapoint a location in a two- or three-dimensional map. (b) Distribution of the magnitude of events for three clusters (0, 1, and all three clusters).

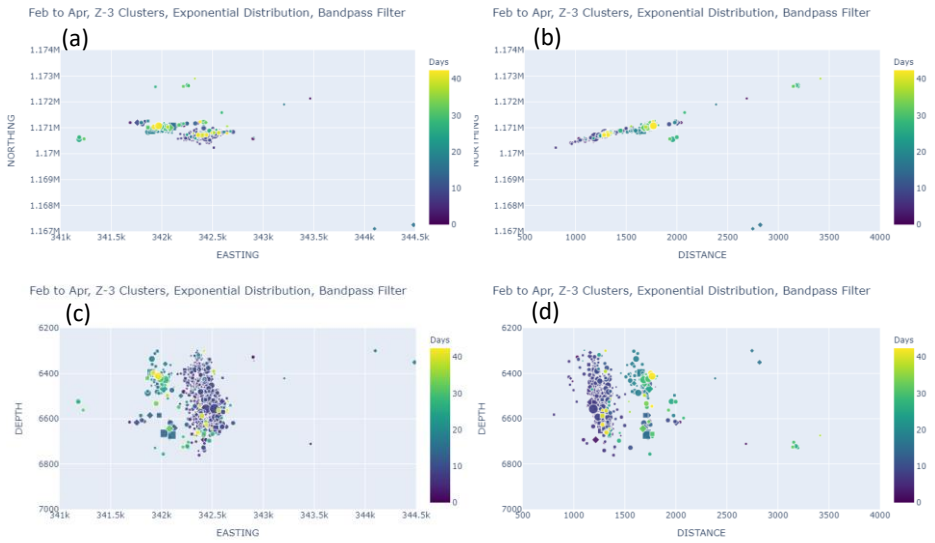

Figure 36. Spatial distribution of three groups (or clusters) from fingerprint-based clustering of microseismic cluster #2 between February 21, 2012, and April 1, 2012. Circle = group 0; square = group 1; diamond = group 2. The size of the symbols represents the magnitude of events, and the color represents the time from 00:00:00, February 21, 2012.

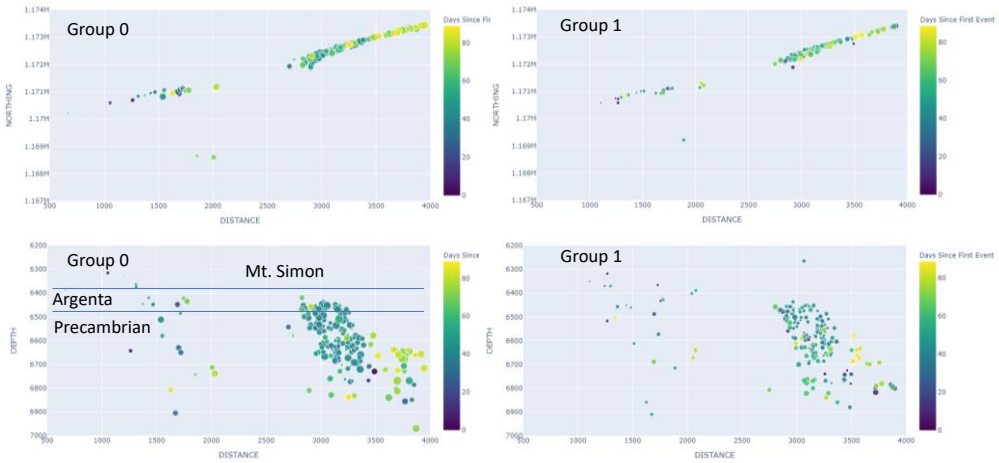

Figure 37. Spatial distribution of three groups from fingerprint-based clustering of microseismic cluster #4 between May 16, 2012, and August 6, 2012. Only groups 0 and 1 are shown. The size of the symbols represents the magnitude of events, and the color represents the time from 00:00:00, May 16, 2012.

Figure 36 shows the spatial distribution of three groups based on fingerprint-based clustering of NMF-HMM. All three groups tended to be overlapped in space and time. It is noted that one of the bigger sub-groups of cluster #2 (i.e., early concentrated events in Figure 37) occurred over three days from February 27, 2012, to March 1, 2012, which indicates that short-period microseismic events would be driven by direct pore diffusion through connected fault-zone architecture.

Figure 37 shows that in the spatio-temporal relations of group 0 in cluster #4, we found one distinct accumulation of events stretching from the Argenta formation into the Precambrian, which

occurred midway through the time series, and a second accumulation of events in the Precambrian, which occurred at the end of the time series. We believe these two sets of events represent the two primary mechanisms associated with CO_2 injection-induced seismicity, direct pressure diffusion and indirect stress transfer. As pressure propagates through highly permeable material, it can hit a fault directly, increasing the possibility of a fast slip event, or it can hit the fault indirectly (through slow pore pressure diffusion and/or stress transfer), which causes the material to compress the fault, making slip events be overlapped and/or longer in duration. The accumulation of earlier events that are connected to the reservoir, specifically the Argenta, are most likely a result of direct pressure diffusion, while the later events in the Precambrian region are more likely a result of indirect stress transfer.

Fault Plane Analysis Using Located Events in the Catalog

Microseismic clusters reveal concentrated trends, which suggests the presence of faults or pre-existing zones of weakness. In previous studies, extensive analysis was performed on the seismic data to find evidence of structural features responsible for the linear trends. No such features were found, suggesting that the responsible features were either sub-seismic or the result of more complex interactions in the sub-surface (Will et al., 2016). In this work, we used NMF-HMM fingerprint-based clustering to characterize sub-seismic features of microseismic patterns. As suggested previously, group 0 represents the main slip events or events that occurred along the main fault plane, while groups 1 and 2 represent small-scale slip events or events that occurred along the fracture network. To construct main faults corresponding to IBDP microseismic clusters, we used group 0 featured with higher magnitude events to reconstruct a hidden/undetected fault plane (Figure 38). As shown, clustering-based fault plane (Figure 38b) had steeper projection of fault plane than that constructed with the entire microseismic data (Figure 38a).

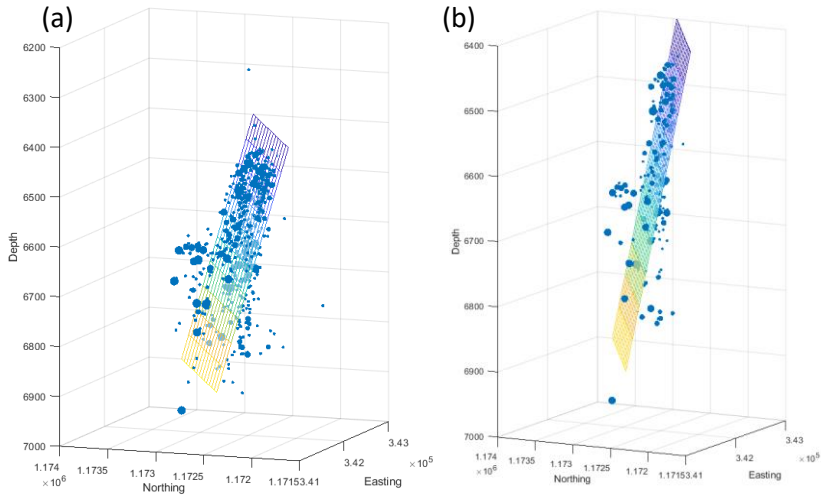

Figure 38. Reconstructed fault plane using (a) entire microseismic events and (b) microseismic events from group 0 from fingerprint-based clustering. This data is from IBDP microseismic cluster #4. The size of each event point represents a magnitude (Mw) of events.

Characteristics of Microseismic Events

Long-period long-duration pattern of waveform data

Many events detected during the transition period in cluster #2 are grouped together to be a single event of long duration, which could last from 30 seconds to 30 minutes, as shown in Figure 39.

Kumar et al. (2017) recognized these events as long period long duration (LPLD) events, which are known for their low amplitude compared to typical detectable (micro-)seismic events and emergent waveforms with no distinctive p- and s-wave arrivals (making it difficult to perform phase picking and source location). Despite their low amplitude, LPLD events are known to release energy orders of magnitude higher than regular microseismic events due to the comparable longevity of the event. Das and Zoback (2013) suggest that LPLD events tend to be observed around faults large enough to produce a sequence of overlapping slow-slip events, and these locations are associated with high natural fracture density, likely caused by the increase in pore pressure and/or the presence of high clay (>40%) contents (i.e., low permeability). LPLD observation at IBDP cluster #2 indicates that fault architecture in cluster #2 contains dense fracture networks or a large damage zone, and a sequence of slow shear slip may be triggered by pore pressure increase from CO_2 injection. This observation needs to be used to parameterize the thickness of fault zone in inverse modeling. Furthermore, the higher amplitude detected at PS3-2 (upper geophone) during LPLD events shows that wave attenuation and propagation is different than during the active period.

These LPLDs may be associated with the energy accumulated during the high event succession of the active period. However, these waveforms were not observed in cluster #4's active period, possibly due to wave propagation obstacles associated with the region. Since LPLDs are generally not events of high magnitude but rather of low magnitude with long duration, an LPLD occurring in the region of cluster #4 would be gravely attenuated before reaching the geophone sensors of the IBDP or no LPLD-type events.

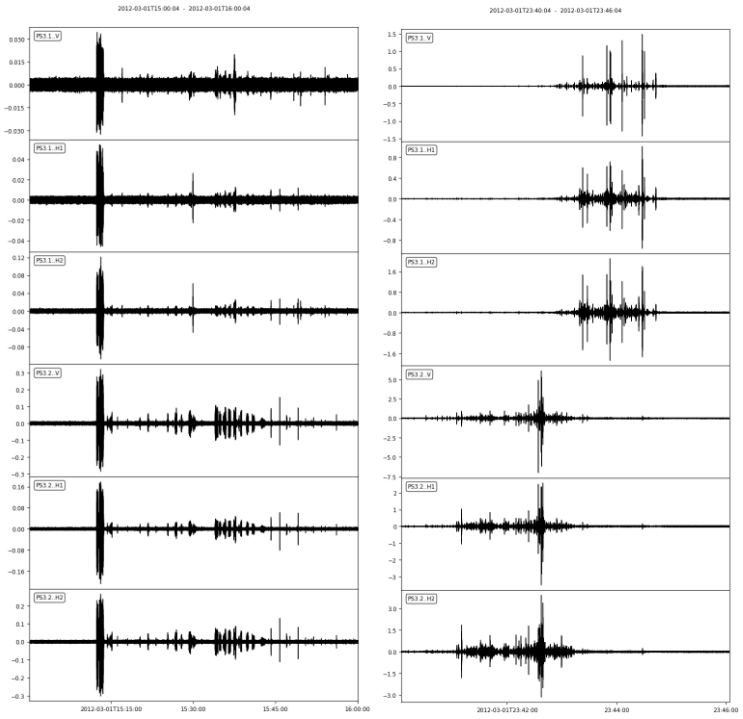

Figure 39. Examples of long-period long-duration (LPLD) events with different duration. The left window interval is one hour, and the right window interval is six minutes.

Phase arrival-time estimation

The retrained PhaseNet model in this work reported promising validation results and reflected improved consistency in accuracy compared to the performance of AR-picker or PhasePaPy packages. The model reported a p- and s-arrival pick precision of 0.906 and 0.942, respectively, with the validation data. These are very similar results to the retrained model from Chai et al. (2020). Figure 40 represents observations of differences and similarities regarding phase picking using PhaseNet (right) and parameter-based pickers (left). We applied the AR-picker and AICD method to the very windows where PhaseNet detected both phase arrivals to see the difference in picking accuracy between these methods. The examples A and B in Figure 40 show that both methods generally produced phase picks close to actual onset. However, close inspection shows PhaseNet was more consistent and precise in its phase picking placement, highly comparable to a manual picking, despite the variability of waveform characteristics. This consistency is even more evident in examples (Figure 40 d and f) where the parameter-based picks mistook the p-arrival with an s-arrival. It is very interesting to see how PhaseNet outperformed the traditional methods used to label and re-train the DL model. One possible explanation is that the model retained the most important feature information gathered from the well-trained original model and simply adjusted weights to adapt to the IBDP signal strength and frequency, along with other unique waveform characteristics.

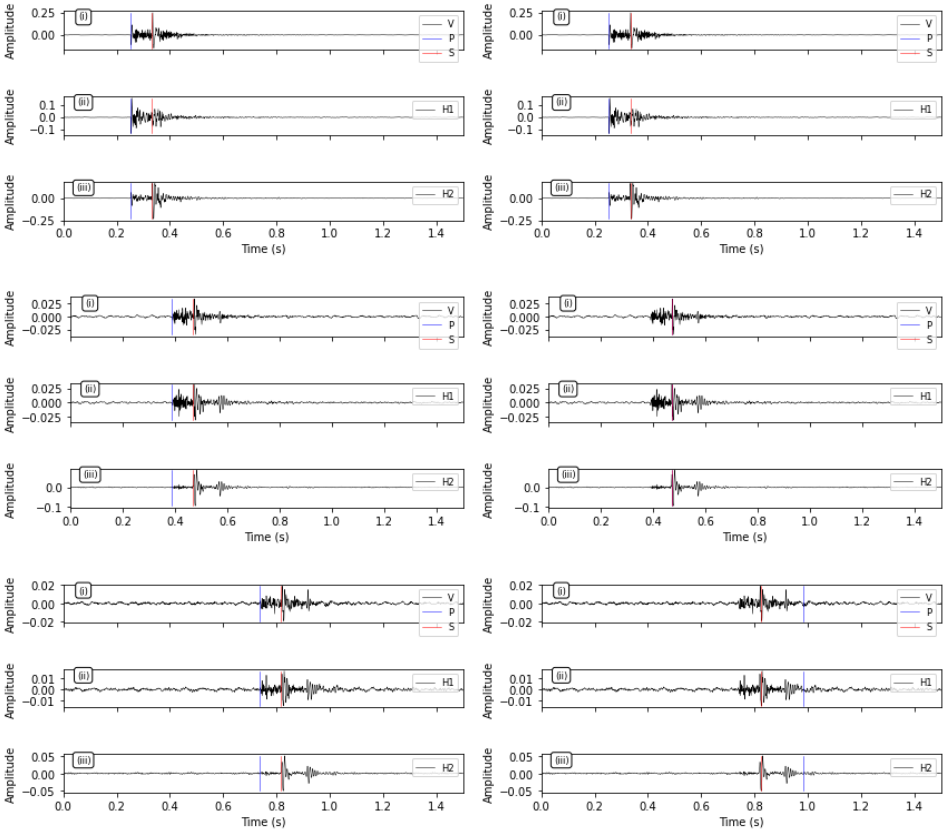

Figure 40. PhaseNet picking accuracy over continuous dataset. On the right, parameter-based automatic pickers applied on the same windows for accuracy comparison. Row 1 shows both PhaseNet and the parameter-based pickers predicting nearly identical arrival-time picks. Rows 2 and 3 show how PhaseNet maintains picking consistency, while parameter-based pickers make mistakes, demonstrating the superior accuracy and consistency of PhaseNet.

Focal Mechanism Results

In this analysis, we focus on the most active time periods during IBDP clusters #2 and #4 to account for slip mechanisms during the active periods. As with fingerprint-based clustering, we used t-sne for deciding an optimal number of clusters needed for k-means clustering through visualization. Figure 41 shows the t-sne projection of k-means clustering results with three, five, and seven clusters. This visualization suggests that three and five clusters work well with focal mechanisms.

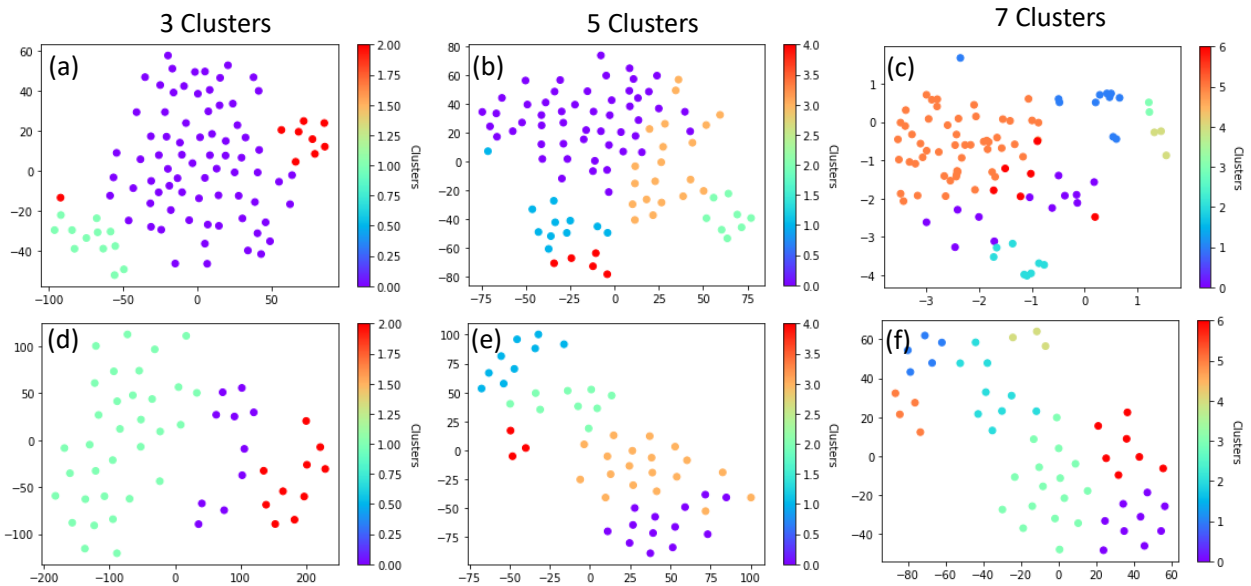

Figure 41. T-sne projection of waveform data from NMF-HMM k-means clustering used for focal mechanism analysis. (a-c) IDBP microseismic cluster #2 and (d-f) IDBP microseismic cluster #4.

The goal of this clustering of focal mechanism results is to evaluate if k-means clustering is classifying the microseismic events based on different focal mechanisms. In our focal mechanism analysis, we have shown that we may be able to estimate location and type of slip associated with fault planes in the area. Here we evaluate if our clustering results are related to the type of focal mechanisms.

Figure 42 shows that most events are assigned to group 0 and the majority of group 0 is associated with Normal Right Lateral Oblique (NRLO), Reverse Right Lateral Oblique (RRLO), and Right Lateral Strike Slip (RLSS). In previous analysis, we have also seen that group 0 is associated with larger magnitude events than groups 1 and 2. In the focal mechanism analysis, we showed that the main focal planes associated with clusters #2 and #4 are RRLO, RLSS, and NRLO. These are also the focal mechanisms associated with group 0. Since group 0 is associated with larger magnitude events and the focal mechanisms that create the main focal planes, it seems that group 0 represents events that occur along the focal plane, and groups 1 and 2 represent events that occur separate of the focal plane.

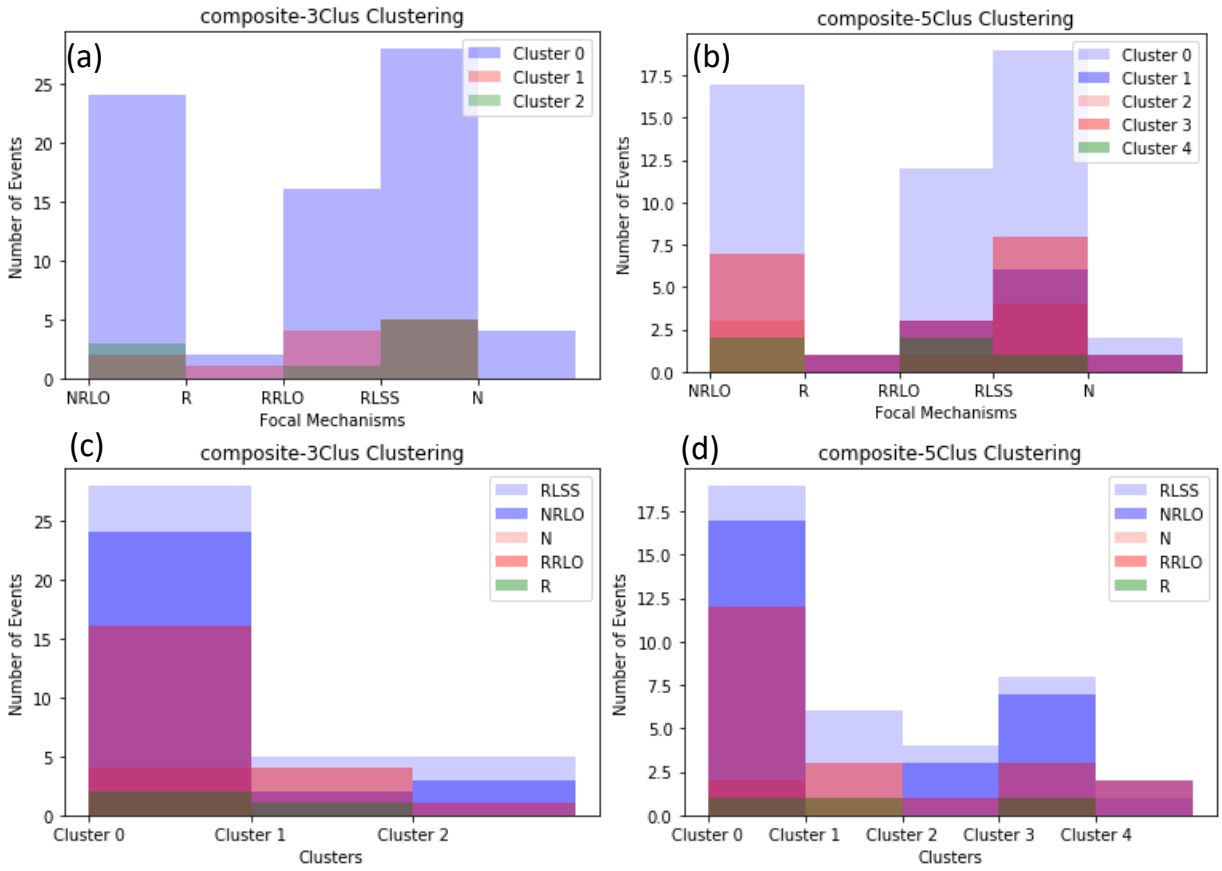

Figure 42. Clustering results of focal mechanism results for cluster #2 (a-b) and for cluster #4 (c-d). Focal mechanisms: NRLO = Normal Right Lateral Oblique, R = Reverse, RRLO = Reverse Right Lateral Oblique, RLSS = Right Lateral Strike Slip, and N = Normal.

Source Location Identification of Microseismic Events and Rapid Recognition of the Presence of Faults

We used WGAN-GP as a generative model to improve source location identification. For demonstration purposes, we focused on events over February 27, 2012 – March 3, 2012, corresponding to the active period of cluster #2. As mentioned earlier, supervised ML models, such as the CNN model in this work, require enough training data to extract features of event data. Figure 43 shows comparison of CNN model performance between event data in the catalog only and synthetic waveform data in addition to catalog data. The WGAN-GP model was constructed using the full waveform information and four quantities (latitude, longitude, depth, and distance) from events in the catalog. The trained WGAN-GP model was then used to generate synthetic microseismic events over a range of four quantities (latitude, longitude, depth, and distance) at different locations from the catalog events.

With event data only from the catalog, the CNN model was well trained with training data. However, the trained model performed poorly with validation data (Figure 43, a and b). For all four quantities (latitude, longitude, depth, and distance), the prediction showed narrow values rather than along a one-to-one line. With synthetically generated event data, the number of events increased from 419 to ~2,500, which improved prediction of source locations, especially with validation data (Figure 43, c and d). All four quantities were well predicted with a few points off from one-to-one line. Overall, this

result demonstrated a significant improvement of source location identification using two different DL models (i.e., WGAN-GP for synthetic data generation and the CNN model for source location prediction). As described in detail by Spurio Mancini et al. (2021), the DL models developed in this work can be also used to perform Bayesian source location inversions of microseismic events.

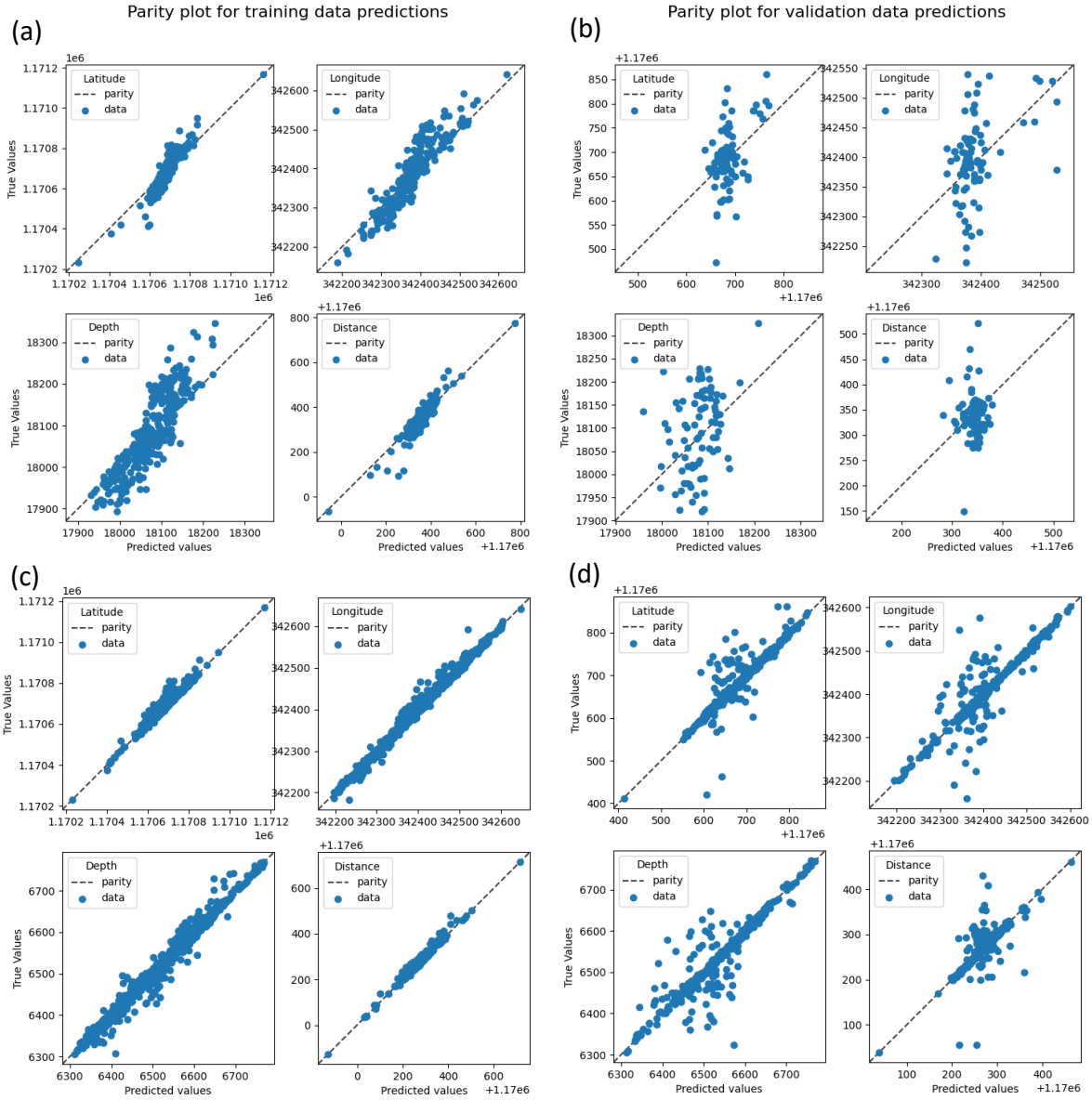

Figure 43. CNN model performance of source location coordinates (latitude, longitude, depth, and distance). Parity plots of training and validation data from (a, b) 419 events in the catalog and (c, d) 419 events in the catalog and 2,100 events with synthetic data.

Rapid recognition of the presence of faults can be achieved by integrating four ML models presented in this task. These four ML models include the CNN model for event detection from continuous waveform data, PhaseNet for phase picking of detected events, WGAN-GP for generating synthetic data using outcomes from the CNN model and PhaseNet, and another CNN model to predict source locations.

Once source locations are identified, a fault plane can be constructed to evaluate the presence of (hidden) faults. In this case, we can perform a projection method as a rapid tool to construct fault planes with or without a clustering method, as shown in Figure 38. The execution of all four ML models is very fast, at seconds per event, hence the rapid recognition can be achieved compared to traditional standard methods.

CONCLUSION

We designed and compared multiple DL models for the rapid recognition of faults based on microseismic waveform data. With time-frequency feature extraction capabilities, automated microseismic event detection using the CNN model was drastically improved by the augmentation of the data time series into a time-frequency domain and a proper normalization strategy for the input information. We also demonstrated that inclusion of additional physical properties, such as MFCCs as an indicator for energy term of waveform, improves event detection. The increase in detected events and long-duration and long-period type events using DL method compared to the catalogue suggests there is more microseismic events of interest unidentified in the IBDP repository. With phase estimates of newly detected events using PhaseNet, source locations were identified using another CNN model that was improved with data augmentation using the generative model (i.e., WGAN-GP). WGAN-GP was trained with full waveform data and location information, generating new synthetic data at various locations different from the located events. Overall, these four DL models can be integrated to perform rapid fault identification.

Many ML applications to seismic data involve detection of events with the use of supervised methods, in which a model is learned and predicts an output corresponding to a given input. However, supervised ML methods need intensive labelling of training data, which is sometimes challenging and requires a certain knowledge. Here, we also used an unsupervised approach to classify the signals and make clusters based on the hidden features. An unsupervised learning approach does not require labeled data for model training; instead, it learns features in latent space through data analysis itself.

By identifying fractures and faults from microseismic event locations, we are better able to identify the potential of induced seismicity. The spatial distribution of these faults/fractures helps us to understand fluid migration and/or stress transfer within or around the reservoir, providing insight into the behavior of the injected CO_2, the reservoir, and the risk of seismic hazard. Moreover, the microseismic events have the potential to reveal small-scale fractures that are below the resolution of active seismic imaging.

TASK 4 - PRESSURE AND STRESS MODELING

INTRODUCTION

The purpose of the pressure and stress modeling was to fully understand and identify the geologic features that controlled pressure transmission between the injection interval of CCS1 and the clusters of induced seismicity events (clusters #2 and #4). Because stress (i.e., poroelastic) modeling is more computationally intense, relatively coarser grid cells would be necessary in comparison to pressure modeling only. Because grid cells represent average geologic features, smaller grid cells are able to represent smaller geologic features. Therefore, a rigorous calibration to IBDP data was only attempted with the pressure modeling, and the rigorously calibrated geocellular model was upscaled for poroelastic modeling. The poroelastic model predicted pressure and stress distribution in the Mt. Simon and Precambrian, but specifically in the microseismic clusters #2 and #4. Additionally, poroelastic modeling helped understand how pressure was transmitted from the injection interval to the clusters' locations.

The calibration to the IBDP pressure and saturation using pressure modeling was explored by identifying geologic features of varying scales and simulating these features in geocellular models. The effort was to understand the effect, if any, faults, if present, may have on the calibration. The poroelastic modeling was expected to require relatively coarser model cells compared to the pressure modeling; consequently, the geocellular model used for poroelastic modeling was upscaled from the model used for pressure modeling and was not rigorously calibrated to the IBDP data.

The coupled multiphase flow and geomechanics provided a geologically consistent mechanistic explanation for microseismicity occurrence at the IBDP site. Our work focused on leveraging the upscaled geocellular model calibrated from the pressure modeling effort that provides an in-depth understanding of the fault system associated with the microseismicity. By using an integrated approach combining advanced computational modeling with accurate geological structures (Figure 1), we aimed to understand the hydraulic and geomechanical conditions that resulted in the microseismicity occurrence.

PRESSURE MODELING

Grid Design and Settings for Geocellular Model (ISGS model version 6; 2020-2022)

At the beginning of the SoS project (2019-2020), the pressure modeling effort initially used the geocellular model (ISGS version 1). Because SoS pressure modeling efforts failed to get a good match (i.e., with field data) of the first six to nine months of IBDP injection, seven unique geocellular models were constructed. (The development of version 7 is discussed in Task 2 section of this report.)

To limit pressure modeling run time, the grid of geocellular model version 6, which comprised of nine geologic formations and subintervals (Table 2) (i.e., Precambrian, Argenta, Mt. Simon A-Lower, Mt. Simon A-Middle, Mt. Simon A-Upper, Mt. Simon B, Mt. Simon C, Mt. Simon D, and Mt. Simon E), was redesigned in Petrel such that it would have a reduced number of grid cells. The number of grid cells in the model was initially cut down to ~12.5 million by reducing the volume of the constructed geocellular model to ~21,758 x 21,861 x 2,172 ft (~4.1 x 4.1 x 0.4 mile). This reduction included the exclusion of the Precambrian zone from the model. To further reduce the number of grid cells, the central area of the model [Figure 44; red box (~10,453 x 10,453 ft; ~2 x 2 mi)] was refined to make the grid cell within this area 100 x 100 ft. This refinement effected changes to the lateral dimension of grid cells on the outer sides of the model domain (i.e., outside the red box in Figure 44), which resulted in grid cell sizes ranging from ~100 x 900 ft to ~900 x 900 ft. (Version 7 used the version 6 geocellular model of the Mt. Simon.)

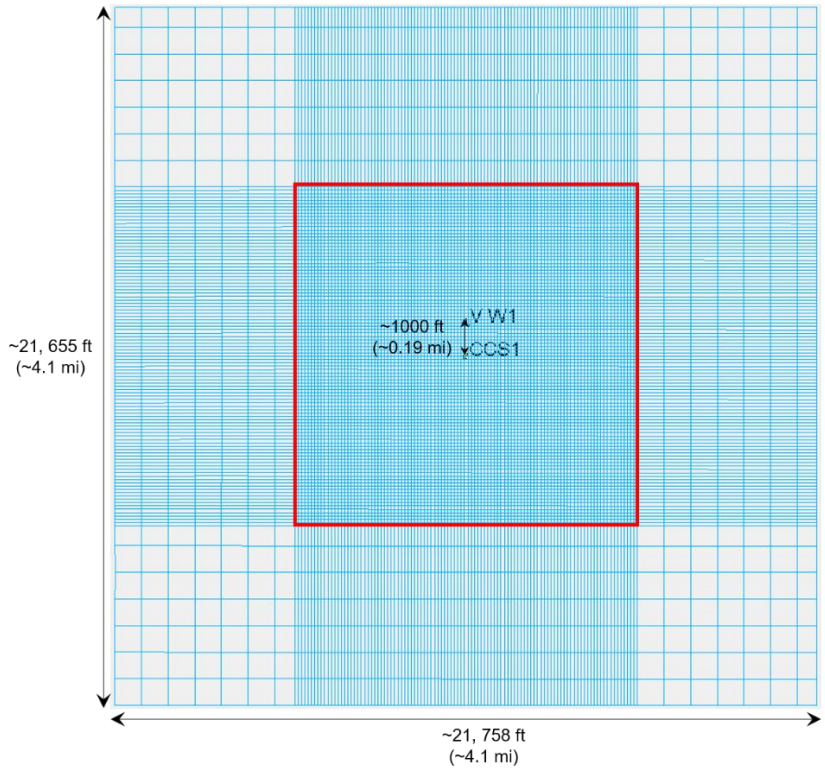

Figure 44. Map view of the geocellular model area. The red box indicates the area with grid cell dimension of 100 x 100 ft.

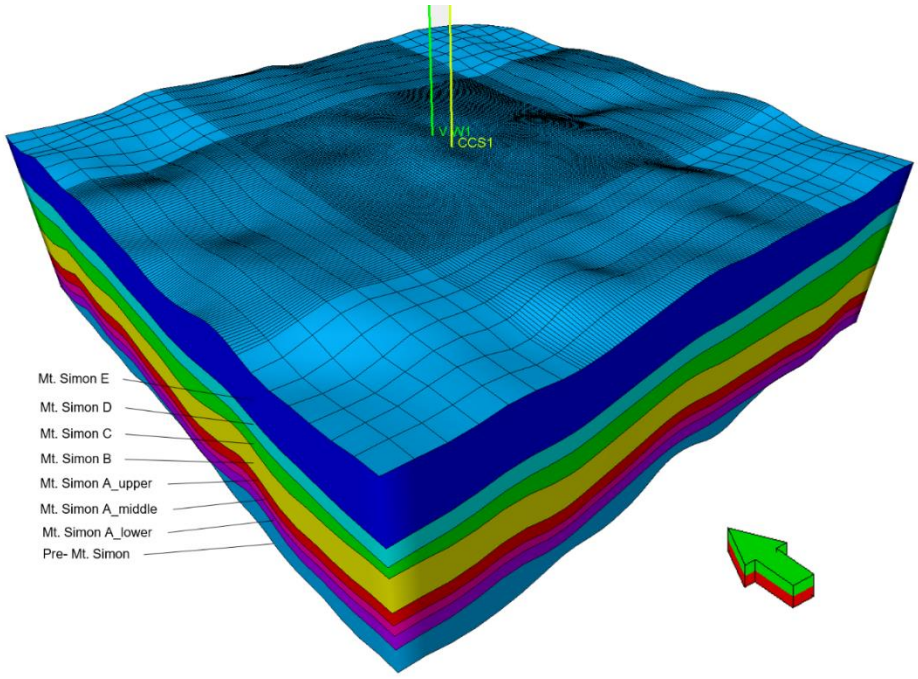

Figure 45. Geocellular model showing structure, different geologic zones, and gridding (vertically exaggerated 4x).

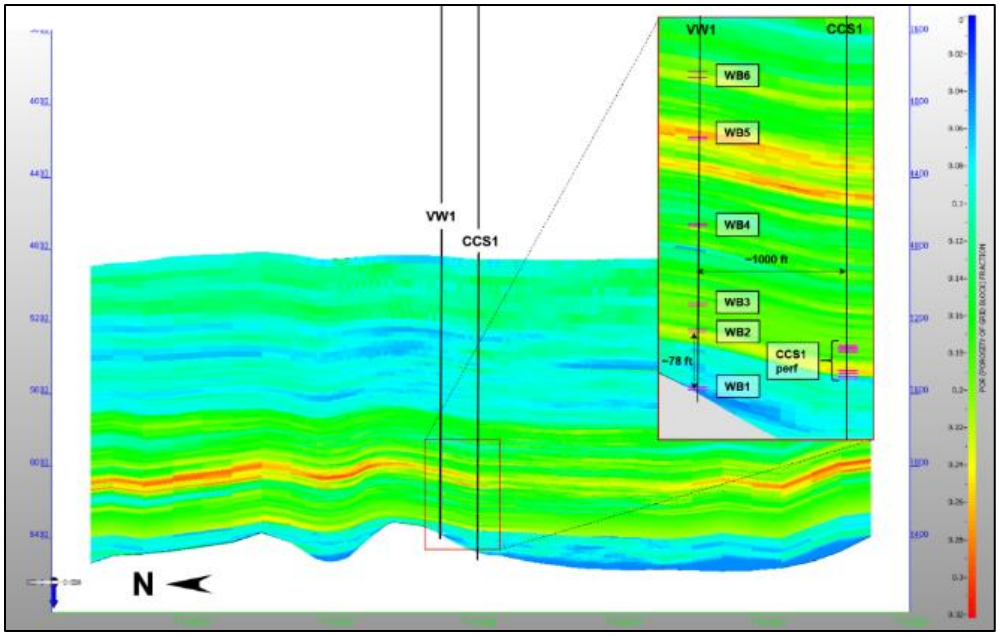

Figure 46. Cross-section across CCS1 and VW1 showing location of the CCS1 perforation, VW1 Westbay perforations (WB 1–6), and the porosity distribution (vertically exaggerated 4x).

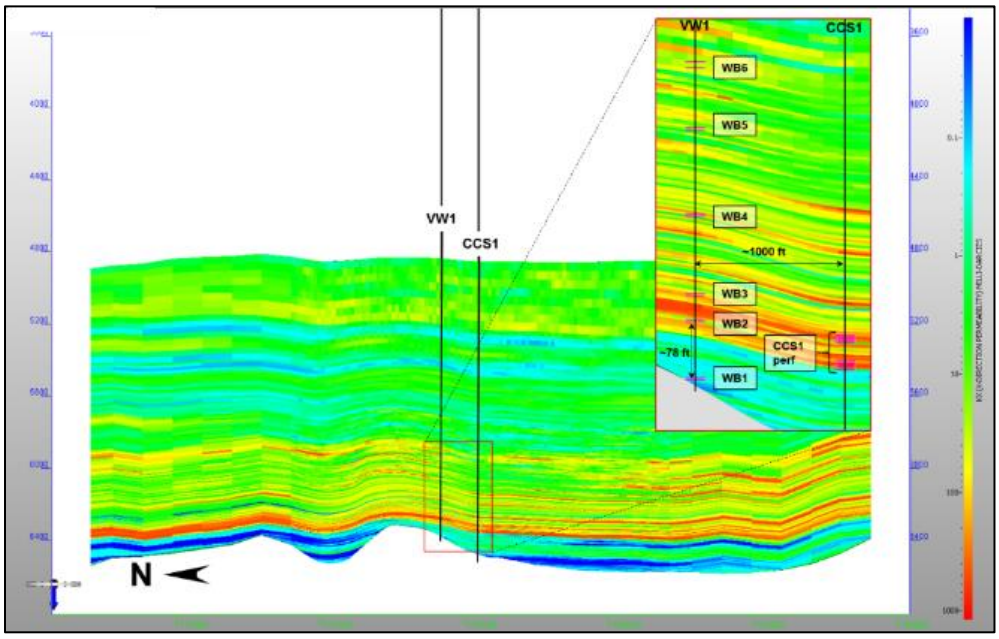

Figure 417. Cross-section across CCS1 and VW1, showing location of the CCS1 perforation, VW1 Westbay perforations (WB 1–6), and the porosity distribution (vertically exaggerated 4x).

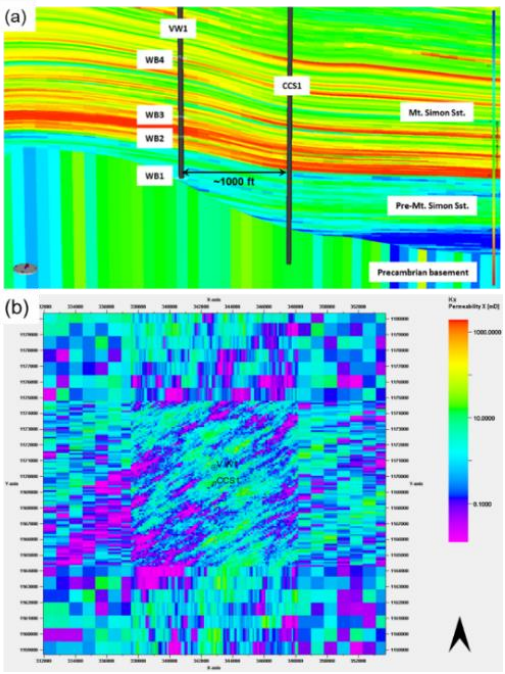

Figure 48. Geocellular model version 7 after merging Mt. Simon, Argenta, and Precambrian model; a) Cross-section through the CCS1 and VW1 within the permeability model, showing part of the Mt. Simon Sandstone and Precambrian (only the first layer out of 8-layer zone) zones and b) Map view, showing permeability distribution at the top of the Precambrian model.

Grid Design and Settings for Later Version of Geocellular Model (ISGS model version 7; late 2022)

In late 2022, the geocellular model described above was modified to include the fractured Precambrian crystalline basement (PCB). A model for the fractured PCB was attached to the base of the Mt. Simon geocellular model, which increased the number of model layers. The unification of both models increased the geocellular model from 117 x 116 x 276 (~3.8 million) grid cells to 117 x 116 x 286 (~3.9 million) grid cells. Afterwards, the finalized property model (ISGS model version 7) was transferred into Nexus Desktop. A cross-section view of the revised model showing the PCB zone is shown in Figure 48. Note that the relatively high vertical cell thickness used within the PCB zone, compared to Mt. Simon Sandstone zones, was to reduce computational time of the pressure modeling. Reducing vertical cell thickness within the PCB zone will mostly increase the vertical resolution of dynamically modeled results within this zone and will not have much effect on the overlying zones, which is of interest for the pressure modeling effort.

Faults

Faults at the IBDP site were interpreted on 3D seismic data (Williams-Stroud et al., 2020) and inferred from microseismic data (Dichiarante et al., 2021). A total of 14 fault planes were interpreted from 3D seismic data. In Task 3, three fault planes were inferred from microseismic cluster #4 (around CCS1; Bauer et al., 2022). The grid cells through which these fault planes cut through were determined in Petrel and defined in VIP simulator by I, J, and K cell index/location. Because of limited information about the faults, transmissibility multipliers between cells or hydraulic properties of cells representing the faults were assumed. Additional discussion on how these properties were varied is provided below under the section titled "Major Modifications to Geocellular Models." The geometry of the seismically interpreted fault planes within the geocellular model is shown in Figure 49.

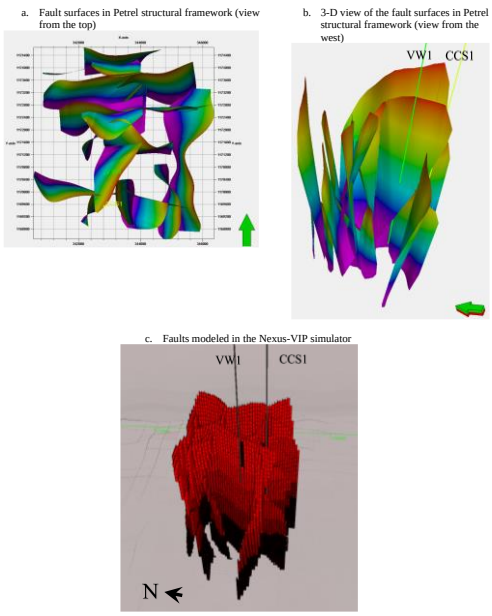

Figure 49. Fault planes incorporated into the models.

Model Set-up/Initialization

In Nexus Desktop 5000.4.14, the geocellular model was initialized using VIP-COMP simulator (Mirzaei et al., 2004). VIP-COMP simulates the flow of oil, gas, and water through subsurface reservoir and predicts the behavior of all associated production or injection wells, while considering that fluid properties and phase behavior can vary strongly with fluid composition. Because the goal of the modeling work was to calibrate the reservoir model using predictions of reservoir pressure response to IBDP CO_2 injection, gas-water fluid system was used to simulate the in-situ brine and the injected CO_2. Estimated fluid and reservoir properties listed in Table 4 were used as model parameterization and initialization. The estimated initial pressure at reference elevation depth (sea level, 0 ft) based on measured hydrostatic pressure and brine properties was 326.27 psia. The relative permeability curve used for simulation was based on generalizations from the literature. Assuming laterally continuous geologic units, infinite-acting boundaries (i.e., aquifer functions) were attached on the sides of the model to eliminate reservoir pressure build-up at boundaries.

Table 4. Fluid and reservoir properties used for pressure modeling.

Properties	**Value**
Brine density (g/cc)	1.051
Formation volume factor (rb/stb)	1.00
Viscosity (cp)	1.1297
Water compressibility (1/psia)	2.76e-06
Rock compressibility (1/psia)	2.74e-06
Reservoir temperature (°F)	116
Standard temperature (°F)	60
Standard Pressure (psia)	14.5

Model Calibration

To calibrate the geocellular model to the recorded dynamic data (i.e., field data) at IBDP (Senel et al., 2014), the process involved conducting various refinements to the stochastically distributed reservoir properties and structural characteristics and fluid flow properties of faults incorporated into the geocellular model. The history matching effort focused on matching CCS1 and VW1 multi-level bottom-hole pressure (BHP) data and the time-lapse CO_2 saturation logs. Deviation of the modeled pressure and saturation profiles from the field data were used as the basis to investigate, determine, and refine the geologic conceptual and geocellular model via reservoir and flow properties that were most influential to the calibrate with field data. Figure 50 shows the weekly averaged BHP and injection rate data between 11/04/2011 and 12/11/2012; Figure 51 shows the time-lapse CO_2 saturation profiles at the IBDP site. Note that the time interval between when injection began (November 2011) and the March 2012 saturation profile is four months, hence this time interval was used as the basis for calibrating the saturation profile.

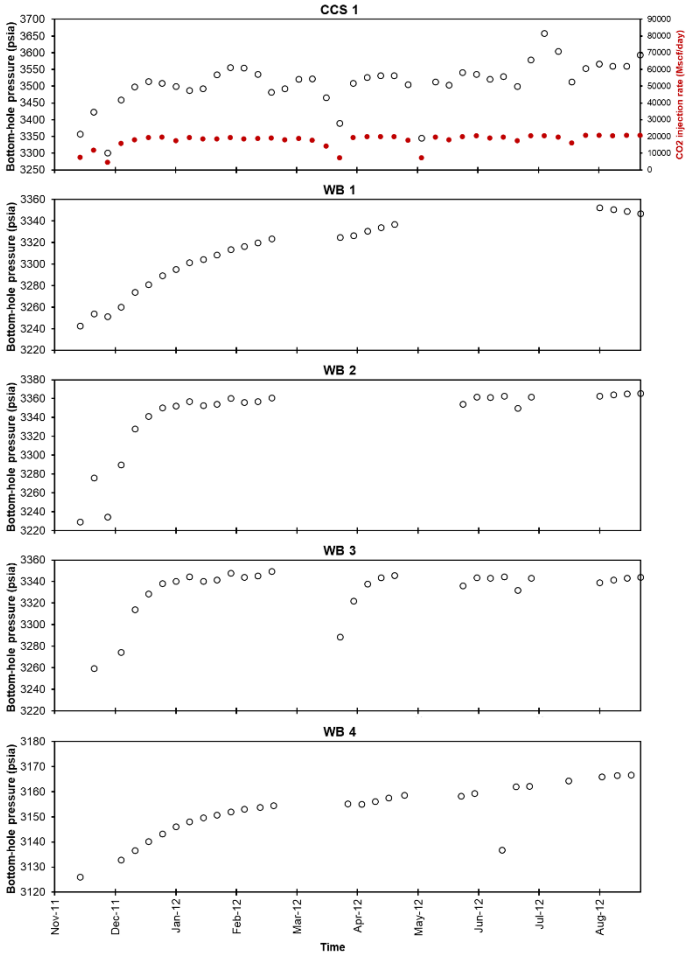

Figure 50. Plots of dynamic bottom-hole pressure (weekly average at CCS1, VW1-WB1, VW1-WB2, VW1-WB3, VW1-WB4) and injection rate (weekly average at CCS1) between 11/04/2011 and 12/11/2012.

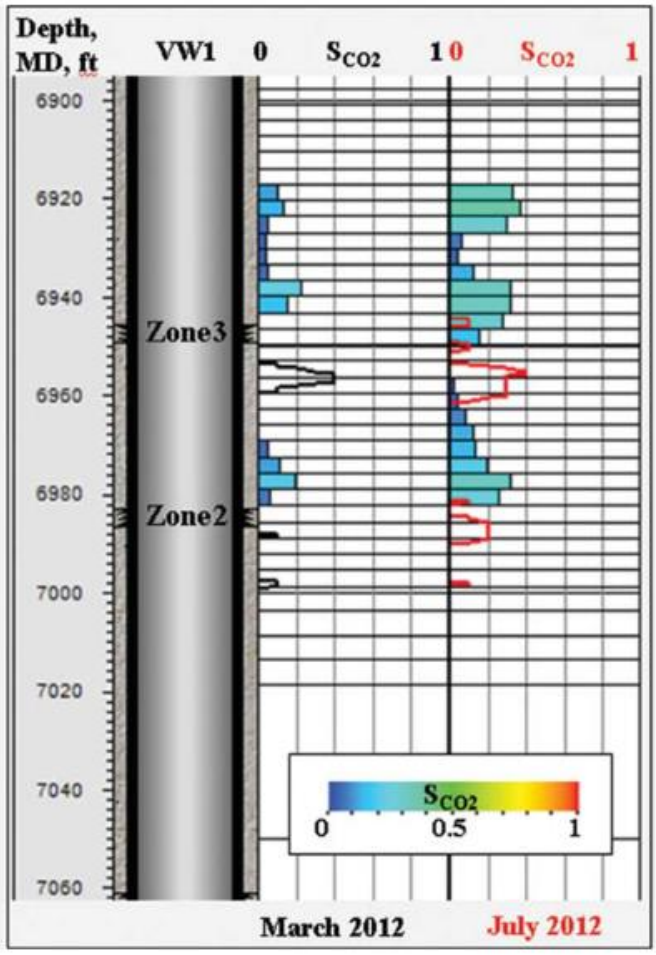

Figure 51. Time-lapse CO_2 saturation profiles around VW1 (from Senel et al., 2014). Zones 2 and 3 shown in the borehole track (track 1) illustrate the levels of WB2 and WB3 pressure gauges. The black and red lines shown in tracks 2 and 3, respectively, illustrate the measured CO_2 saturation in March 2012 and July 2012, respectively. The colored bars in tracks 2 and 3 are CO_2 saturation results from Senel et al., 2014.

Variation of Geologic Features and Reservoir Properties

Three primary variables in the model were the focus of refinement in the calibration process. The variables were 1) permeability distribution (vertical and horizontal) within the model domain. This included permeability of some layers [referred to as low permeability zones (LPZs)] and the Mt. Simon Sandstone, Argenta, and Precambrian zones, 2) the vertical extent of portion of the perforation interval that was open to CO_2 injection, and 3) structural and fluid flow properties of faults, which were interpreted from 3D seismic data and inferred from the microseismic clusters.

These variables were modified independently or concurrently during the simulation process to build on preceding simulation results and achieve the desired calibration. For example, a preceding simulation result required a decrease in the pressure observed at WB1 (i.e., at the representative grid cell) only. To build on this particular result, a subsequent simulation required reducing the permeability of either the Argenta or the fault by using a multiplier for the Argenta zone or assigning a permeability value to a section of the fault. This example modification was made to minimize vertical pressure migration into Argenta and its base and, as such, the observed pressure at WB1. An additional example is that a preceding simulation result may have shown lower pressure level at the grid cells of WB2 and WB3 (i.e.,

within the middle Mt. Simon Sandstone) compared to observed field pressures. Such a result required either independently or concurrently increasing the permeability of the Mt. Simon Sandstone (in a reasonable manner) or modifying the transmissibility of an incorporated fault to enable faster pressure communication between CCS1 and the WB systems and a higher pressure to be achieved at WB2 and WB3 grid cells. Separately, variations of LPZ permeability, thickness and later distribution were varied to improve calibration to WB2 and WB3.

Model Iterations

The model calibration process was started by using the geocellular model developed by Schlumberger as an input into Nexus. However, the result obtained from simulating the first nine months using this model did not result in an acceptable calibration with IBDP pressure and saturation data. Consequently, different sensitivities were applied to the geocellular model by varying the petrophysical properties of the model in order to improve the calibration. Despite the refinements that were applied to the petrophysical properties, the pressure modeling did not improve the calibration. This led to the need to rebuild the geocellular model that was developed for IBDP. The geocellular model was re-built, and several iterations of the model were generated through the progression of the calibration process according to the project methodology (Figure 1). The accepted models by the geology team, as close representation of the geology at the IBDP site, were then further used as inputs into subsequent pressure modeling work.

Furthermore, several refinements were carried out on the geocellular models to get the simulated result to match the observed data. High-level descriptions of the refinements made on this newly built geocellular model are provided below.

Major Refinements/Modifications to Geocellular Models

- **Perforation interval that is in hydraulic communication with the rock matrix:** For the CCS1 injection, three intervals were perforated. The first and second perforated depths were for injection purposes, and the third perforated depth was for a vertical interference test (VIT). The presence of these three perforations brought about the uncertainty of where fluid was going in the CCS1 well. However, based on a spinner log test of CCS1 80% of the CO_2 was going into the first perforation, it was concluded during the simulation process that only part of the first perforation is in hydraulic communication with the rock matrix. Nevertheless, before this conclusion was made, the perforation intervals that were opened to b the rock matrix were varied in simulations. The depths for the perforations were:
    - Measured depth (MD) for the lowermost/first perforation was 7,025-7,050 ft [Subsea (SS) depth: 6,335 – 6,360 ft]. This is a 25 ft interval.
    - MD for the uppermost/second perforation was 6,985-7,015 ft (MD) (SS depth: 6,295-6,325 ft). This is a 30 ft interval.
    - MD for the third perforation was 6,286-6,288 ft. The purpose for the third perforation was an attempt at VIT with brine injection before CO_2 injection operation commenced.

  Modifications made with the perforations during the various simulations included:
    - Inclusion of all perforation intervals.
    - Inclusion of the first and second perforation interval.

- Inclusion of parts of the first and second perforation (e.g., 10 ft of first perforation interval and 5 ft of second perforation interval).
- Inclusion of only part of the first perforation (e.g., 10 or 15 ft only).

- **Addition of a hypothetical fault plane into the geocellular model:** Because the acquired seismic data did not fully cover the area south of the CCS1, there was uncertainty about the presence of geologic structures south of CCS1. This uncertainty formed the basis to test the hypothesis that unimaged structures present within the south of CCS1 have influence on the observed field pressure data. This hypothesis was tested by:
  - Adding a hypothetical 4,000-ft-long fault that is vertical (i.e., with 90° dip angle) and strikes east to west. The fault was added 400 ft south of CCS1.
  - The petrophysical properties (i.e., the permeability) of the fault were also varied to assess the influence of the fault on the predicted result.

- **Incorporation of interpreted fault planes from 3D seismic and microseismic data into the geocellular model:** Fault planes that were structurally interpreted from 3D seismic data and inferred from microseismic cluster were incorporated into the geocellular model (Figures 49 and 52). The planes were represented by using the grid cells, which intersect within the model domain. (Faults represented by grid cells of x-y dimensions relatively larger than a fault plane were representing a fault zone.) The faults had distinct structural characteristics, i.e., length, strike, and dip direction. Different hypotheses, relating to the fault transmissibility/fault properties, were also tested after the incorporation of the faults to determine how sensitive the simulation results were to a specific fault property or the location of a fault. The hypotheses tested included:
  - The transmissibility of the faults depends on its characteristics, specifically its strike. Based on this hypothesis, the strike of fault plane was estimated, and a transmissibility value was assigned to each group of grid cells, i.e., a fault zone.
  - Like the hypothesis above, the transmissibility of a fault depends on the slip potential of the fault. Based on this, fault slip potential of each fault was calculated. This resulted in different fault slip potential values for each grid cell that a fault plane cuts through. The calculated value was equated to the transmissibility multiplier value and further used for the pressure modeling.
  - The faults that have vertical offset (>5 ft) are less transmissible when compared to faults with little to no vertical offset (<5ft). Based on these criteria, some faults were designed to be invisible (i.e., have permeability like that of the rock matrix), while others were assigned with low transmissibility multipliers. For example, an interpreted fault located between CCS1 and VW1 is expected to be invisible (i.e., flow across is not impeded) because of the early pressure response observed at VW1 gauge systems.

  Other modifications carried out on the faults included:
  - Varying the transmissibility multipliers of faults that were expected to influence the predicted result.
  - Truncating the height of faults using a reference surface.

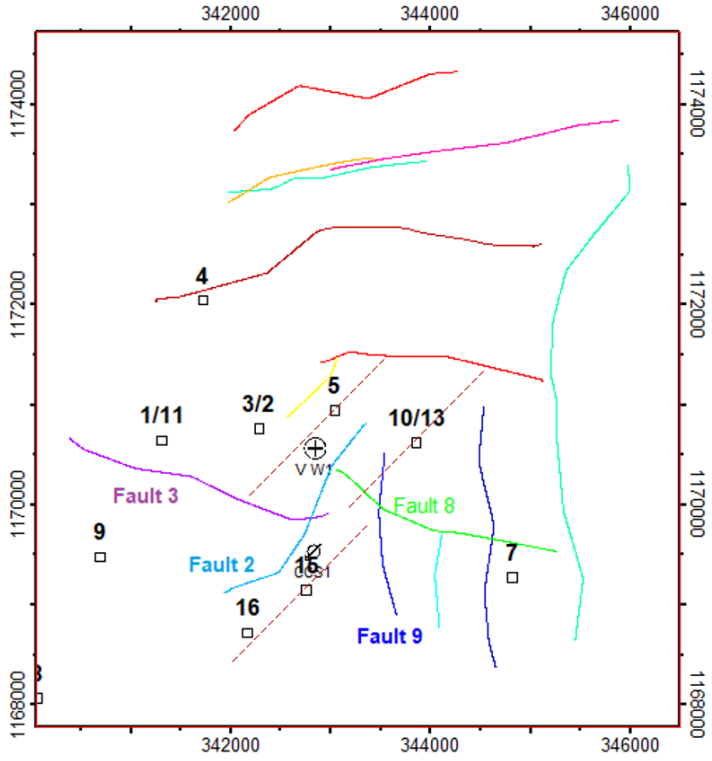

Figure 52. Map view of the interpreted faults (colored lines show the top of the faults) from 3D seismic data and approximate centers of the different microseismic clusters (the numbered, black-open squares) that were recorded during the IBDP injection period. The numbered faults are indicated here because they are listed as part of Appendix C headings, hence it is worth showing their locations relative to the CCS1 injection well. The dashed red lines show fault traces inferred from microseismic cluster locations, which were incorporated into some of the simulated cases listed in Appendix C.

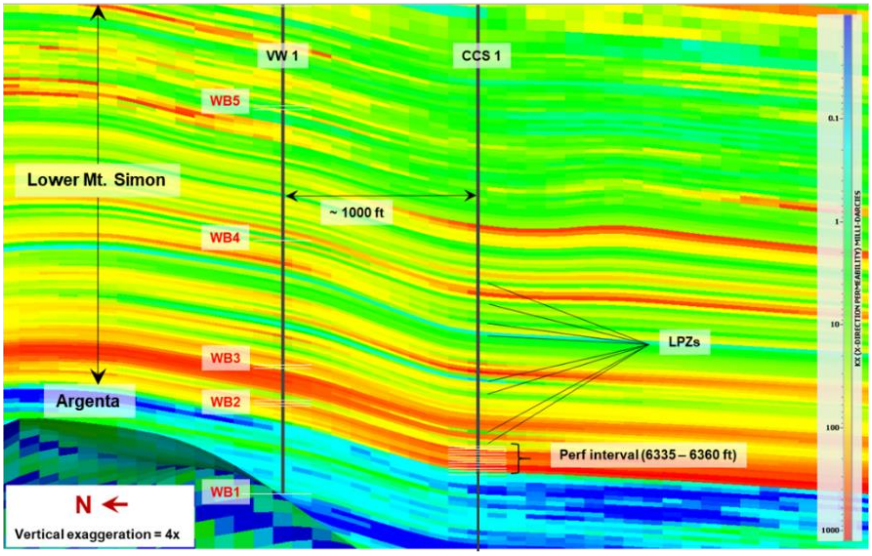

Figure 53. Permeability cross-section showing the layers referred to as low permeability zones (LPZs).

- **Refining the permeability model:**
    - Identifying and modifying permeability of layers around CCS1 and VW1, which have permeability less than ~5 mD. These layers were informally referred to as low permeability zones (LPZs) (Figure 53).
    - Modifying the permeability (vertical and horizontal) of the entire model domain.
    - Modifying permeability structure observed south of CCS1.

In the appendix of the report, two logs of simulated cases are presented. Appendix B provides a log of cases (including description of modifications applied to the geocellular models) that were simulated from the time a new geocellular model was generated to October 2022. The log also provides, in most cases, an approximate difference between observed average BHP and simulated average BHP. Appendix C provides a log of cases (including details of the different variables present in each case) that were simulated using the October 2022 geocellular model. It is worth noting that in between the time of running these simulations, the newly generated geocellular model by ISGS was constantly evolving to include new geologic features or zones suggested by ISGS geologists.

Pressure Modeling Results

For most of the simulated cases, an acceptable calibration between field and simulated BHP and saturation data was not achieved. Specifically, getting a result showing an early pressure response at WB2 and WB3 that was similar to the observed field pressures and a nearly constant (i.e., flat) pressure trend after the first month of injection proved unachievable. In this section of the report, the result of a selected case that best matches the historical pressure and saturation data is documented.

The selected case is SOS_110922_33 (Appendix C). For this case, the following modification was applied to the newly built geocellular model:

- The LPZs (Figure 53), which include model layers 102, 112, 124, 131, 134, 137, 151, 156, 159, 170, and 173 were multiplied by 0.3.
- A total number of 17 fault planes (14 faults interpreted on 3D seismic data and three faults inferred from microseismicity cluster #5, #10, and #15) were incorporated into the geocellular model.
- All faults were truncated around the level of WB3 (layer 163).
- For faults 2, 3, 8, and 9 (Figure 52) and faults inferred from microseismicity cluster (i.e., clusters #5, #10, #13, and #15 [Bauer et al., 2016]): 1) the Mt. Simon part of the fault zone was assigned with along-fault (i.e., along-strike) permeability of 2,000 mD and across-fault permeability equal to the rock matrix permeability, and 2) the Argenta and Precambrian basement parts of the fault zone were assigned with along-fault permeability of 0.1 mD and across fault permeability equal to the rock matrix permeability.
- Other faults within the model were assumed to be impermeable, thus a transmissibility multiplier of 1e-05 was applied to the set of cells representing these faults.
- The perforated interval used at CCS1 injection point was 15 ft.
- Simulated CCS1 BHP was set to the actual CCS1 BHP so that the injection pressure at CCS1 was causing with the VW1 WB calibration pressure data. (To this end CCS1 injection rate become a calibration data trend.)

Figure 54 shows a plot of observed (open circles) and simulated (solid line) BHP at CCS1 and WB1-4 pressure gauges. Also shown in Figure 54 is the field and simulated injection rate. At CCS1 pressure

gauge level, it is evident that the field and simulated BHPs matched accurately, mainly due to the constant CCS1 BHP constraint that was applied. With this constraint and the 15-ft perforation interval used for injection, the match between simulated injection rate and actual injected CO_2 rate was good. Except over short time periods around January 2012 and June 2012, the match between the injection rates was generally good over the nine-month period.

At WB1 pressure gauge level within the model, the match between field and simulated BHPs was also relatively good over the simulated period, although the simulated pressure overshoots by ~10 psi around January-February 2012 and August 2012, compared to the observed pressure response. Generally, throughout the simulated period, the result showed good agreement with field data. The maximum difference between observed field pressure and simulated pressure was <10 psi.

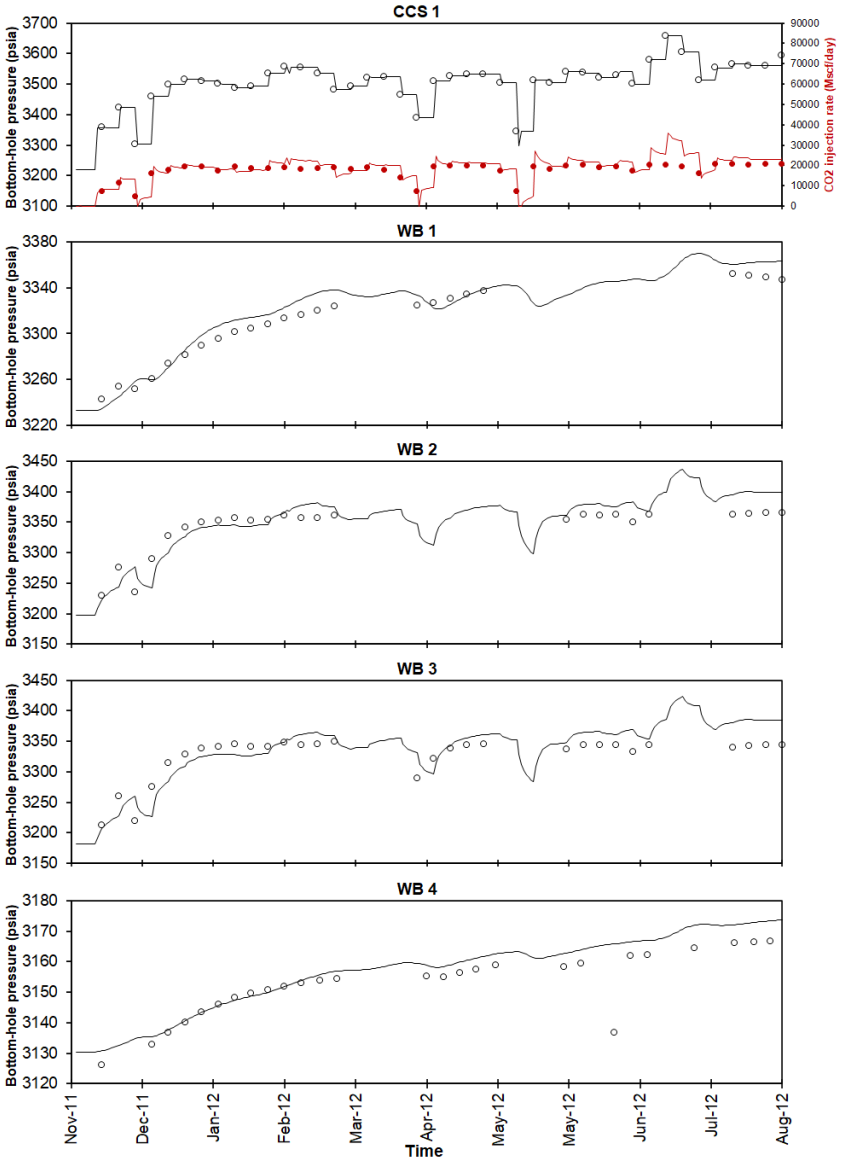

Figure 54. Plots of observed BHP and injection CO_2 rate from field data (open circles) and simulated BHP and injection rate (solid line).

At WB2 and WB3 pressure gauge levels, the match between field and simulated BHPs was relatively good over the first six to seven months, with a maximum difference <10 psi. After this period (i.e., around June 2012), a separation between the two BHP curves was observed. A maximum pressure difference of ~25 psi was observed around the ninth month (August 2012). Between WB2 and WB3 levels, gas saturation at ~120 days (Figure 55) was also observed to have matched the measured gas saturation profiles (Figured 51). Throughout the process of performing model iterations and pressure modeling, it was a challenge to get the pressure level at these two pressure gauge levels to stay constant after the first two months. It was only through the addition of a permeable fault zone between the two wells could the relative rapid, early pressure increase occur followed by a relatively flat pressure trend.

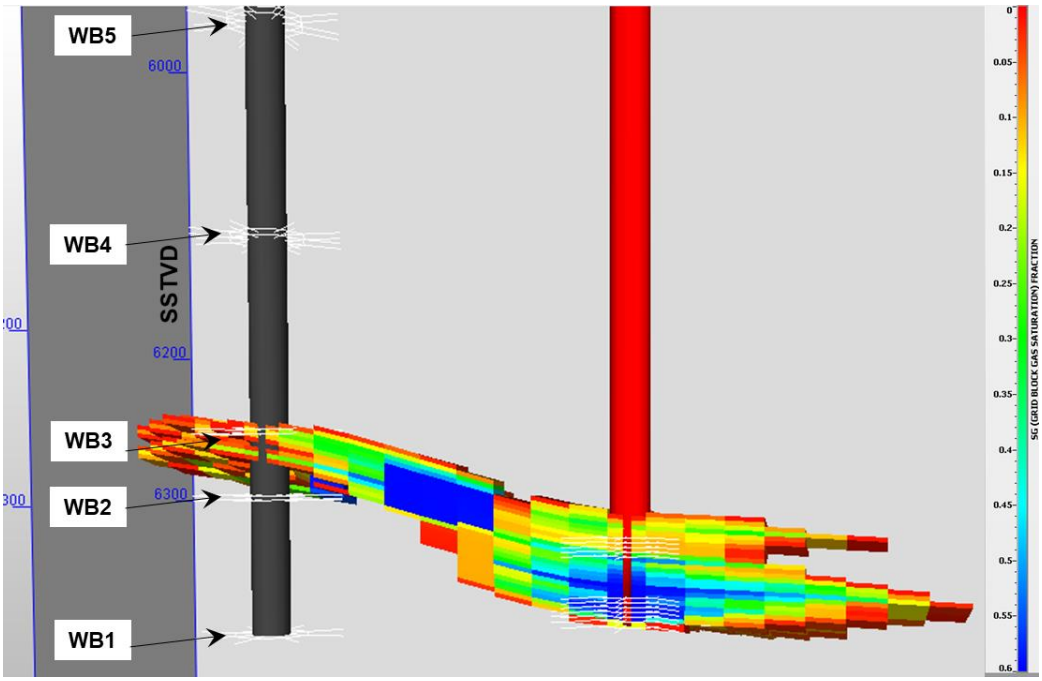

Figure 55. Cross-section simulated CO_2 saturation between CCS1 (black-left) an VW1 (red-right)

POROELASTIC MODELING

Geological Model

For the coupled flow and geomechanics modeling, we used a simplified stratigraphic representation of the injection interval. Specifically, we divided the storage interval into six main zones, defined based on changes in reservoir properties and layer thickness (Figure 56). To make the problem computationally tractable, our stratigraphic model did not include thin layers, such as the Argenta and the Mudstone baffles, and instead we chose to represent those layers using transmissibility multipliers in the flow model. The Lower Mt. Simon interval, where CO_2 injection occurs, is represented by Layer 5 in our stratigraphic interval, the Precambrian basement is represented by Layer 6, and the overburden above the Mt. Simon interval is represented by Layer 1 (Figure 56).

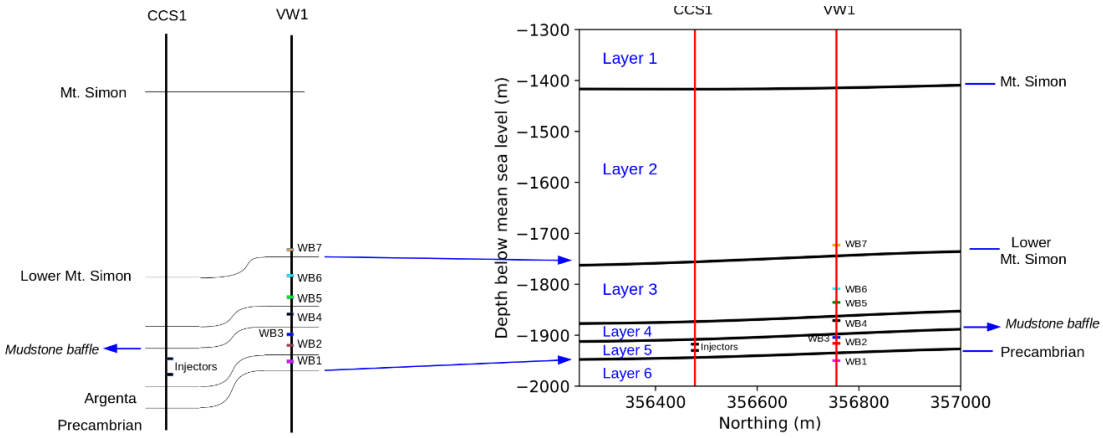

Figure 56. (Left) Schematic view of the location of the different pressure gouges in the VW1 well with respect to the injection ports in the CCS1 well. In this schematic, we also show the key stratigraphic horizons that control pressure compartmentalization in the vertical directions, namely the Mudstone baffle and the Argenta formation. (Right) View of stratigraphic intervals used in our model. We divided the Mt. Simon interval according to the depth of the different pressure gouges at the VW1 well. Due to their low thicknesses, we accounted for the Argenta formation and the Mudstone baffle using transmissibility multipliers at those interfaces. Layer 1 corresponds to an impermeable overburden, Layers 2 to 5 are the Mt. Simon sections where injection occurs. Layer 6 is the Precambrian basement.

A key feature of our geological model is that we included a set of non-planar faults, interpreted based on 3D surface seismic data and microseismicity locations. The shallowest portions of the faults are located halfway into the Mt. Simon formation, at a depth of about 4,921 ft (1,500 m), and the deepest portions penetrate as much as 1,312 ft (400 m) into the Precambrian basement where the microseismicity is located, reaching a depth of about 8,202 ft (2,500 m) (Figure 57). We note that the largest faults in our model were interpreted using 3D surface seismic data, whereas the smaller fault planes were inferred based on the microseismicity locations, since these faults were not visible in the 3D surface seismic interpretation.

Computational Mesh

We used the geological model, including all horizons and fault surfaces, to build a unified computational mesh for the flow and geomechanics simulations. The complex geometry furnished by the presence of many non-planar faults intersecting each other required the use of an unstructured mesh. To achieve this goal, we performed spatial discretization using tetrahedral elements that were set to be smaller near the faults and in the injection interval (~90 ft; ~30 m) and progressively larger away from these areas. The final computational mesh is composed of 2.67 million tetrahedral elements that conform to all faults and horizons in our model (Figure 58).

Reservoir and Fluid Properties

We populated our computational mesh with reservoir properties upscaled from a geocellular model constructed based on well-log and core data. A notable feature of the reservoir model is that the Precambrian basement is heavily fractured, which was modeled using an effective medium approach by setting anisotropic permeability values. Specifically, in the Precambrian interval, $k_{yy} = 0.1k_{xx}$ and $k_{zz} = 0.79k_{xx}$. The Lower Mt. Simon interval has isotropic horizontal permeability and a vertical permeability that is 10 times less than the horizontal permeability. In Figure 59, we show the Precambrian permeability and histograms of permeability and porosity for the basement and the Lower Mt. Simon.

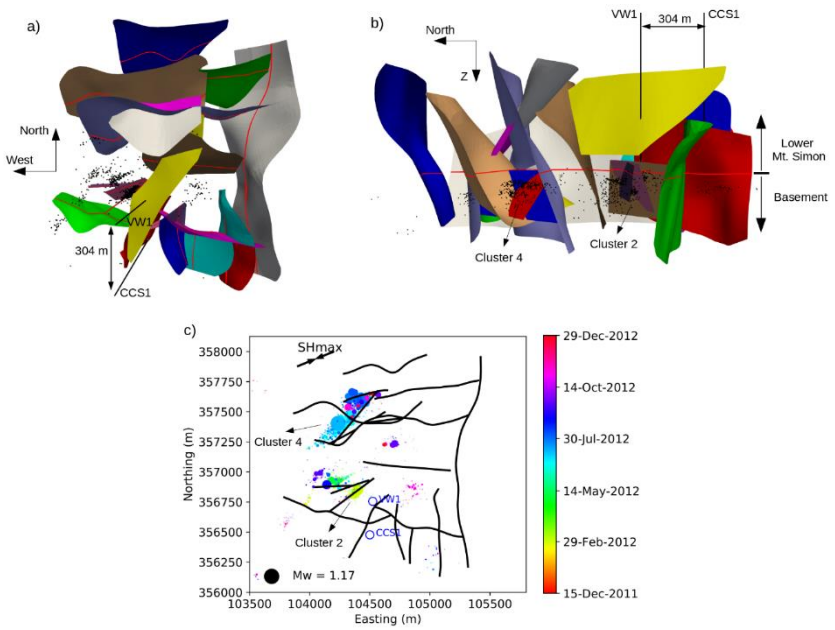

Figure 57. Fault geometry and microseismicity locations. a) View from the top showing all the faults included in our model. The fault surfaces are assigned random colors to improve visualization. Microseismicity locations are shown by the black dots. Solid red lines indicate the intersection of the basement surface (Precambrian) with the fault surfaces. b) View from the west of the fault surfaces shown in a). The location of clusters #2 and #4 are indicated as well as the fault intersection with the Precambrian surface (solid red lines). c) Map view of the fault locations and microseismicity. The solid black lines are the intersection of the fault planes with the Precambrian surface [shown by the red lines in a) and b)]. Circles are proportional to event magnitude and colored by time.

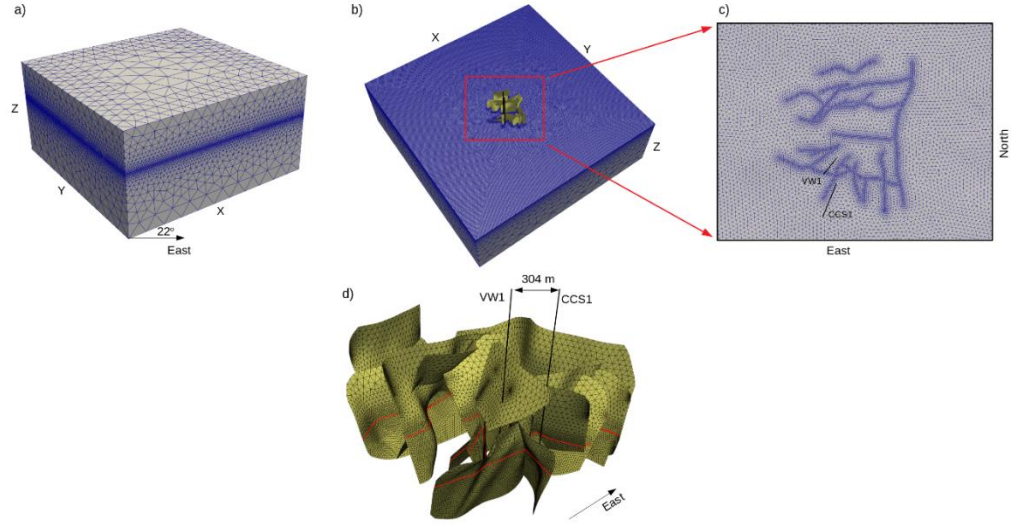

Figure 58. Model geometry and computational mesh used in our simulations. a) Perspective view of the entire domain showing the computational mesh. The domain X direction is parallel to the maximum horizontal stress direction (N68E). The domain size is 10 km x 10 km x 5 km. b) View of the computational mesh at the top of the Precambrian surface, showing the faults included in our model. c) View from the top showing the mesh around the faults and the CCS1 and VW1 wells. Note the imprint of the fault locations on the unstructured mesh conforming to all fault planes. d) View of the computational mesh at the fault planes included in our model. The solid red lines indicate the intersection of the Precambrian top with the faults. Our computational mesh contains 2.67 million tetrahedral elements that conform to the input horizons and fault surfaces.

We defined the flow properties using empirical correlations from the literature. At the depth where CO_2 is injected (~2,000 m), CO_2 is in supercritical state. We used the thermodynamic model from Duan and Sun (2003) and Hassanzadeh et al. (2008) to compute the CO_2 and brine properties for pressure, temperature, and salinity conditions of the Lower Mt. Simon, assuming isothermal conditions. We defined relative permeability curves consistent with previous flow simulations at the Lower Mt. Simon (Senel et al., 2014; Strandli et al., 2014), where we set the irreducible water saturation to be $S_{w,irr} = 0.6$. For flow boundary conditions, we multiplied the pore volumes at the edge of the domain by 10,000 to model a strong aquifer support. In our simulations, we neglected capillary pressure and CO_2 dissolution in brine, therefore focusing only on two-phase immiscible reservoir simulation. In Figure 60, we show the CO_2 and brine density variation with pressure and the relative permeability curves that we used.

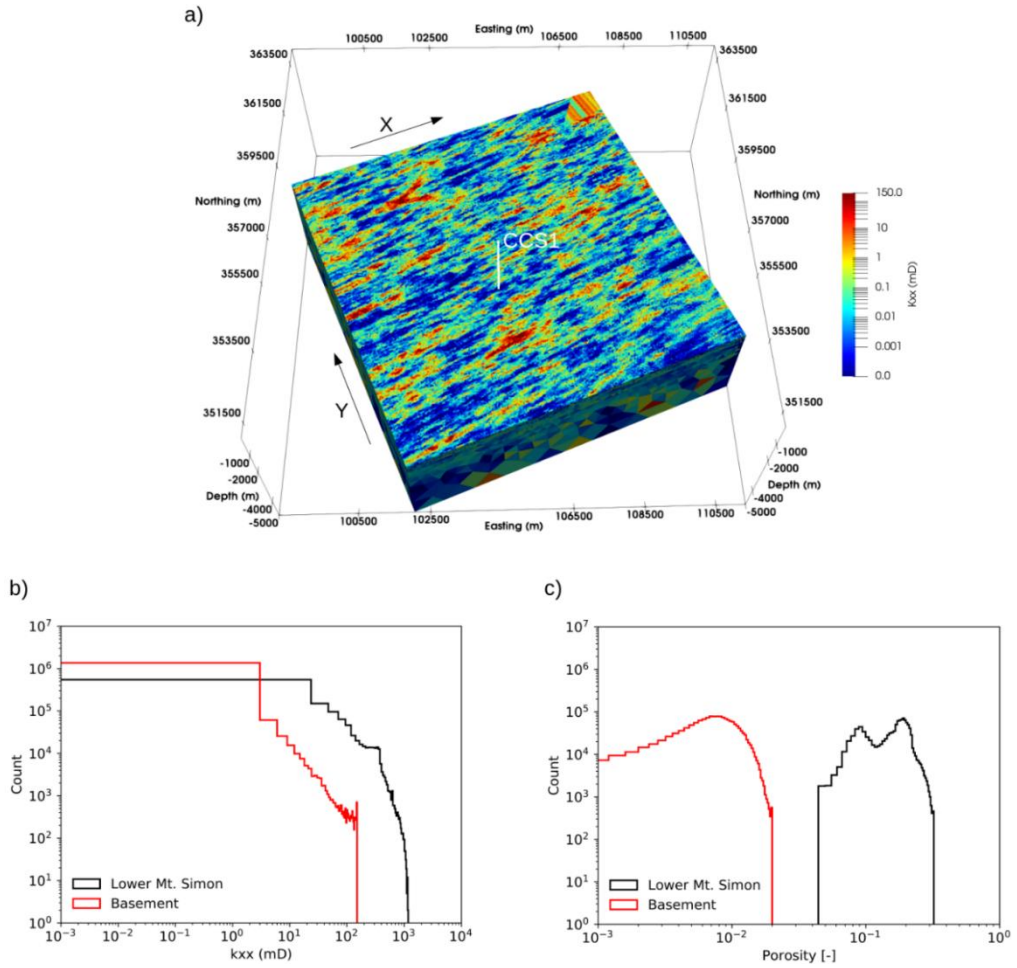

Figure 59. Reservoir properties used in the flow simulations. a) Perspective view of the spatial variation of the k_{xx} permeability component for the Precambrian basement. The other components of the permeability tensor for the Precambrian basement were $k_{yy} = 0.1k_{xx}$ and $k_{zz} = 0.79k_{xx}$. For the Lower Mt. Simon interval, $k_{xx} = k_{yy}$ and $k_{zz} \approx 0.1k_{xx}$. b) Histogram comparing permeability values for the Precambrian basement and the Lower Mt. Simon interval. c) Same as b) but for porosity.

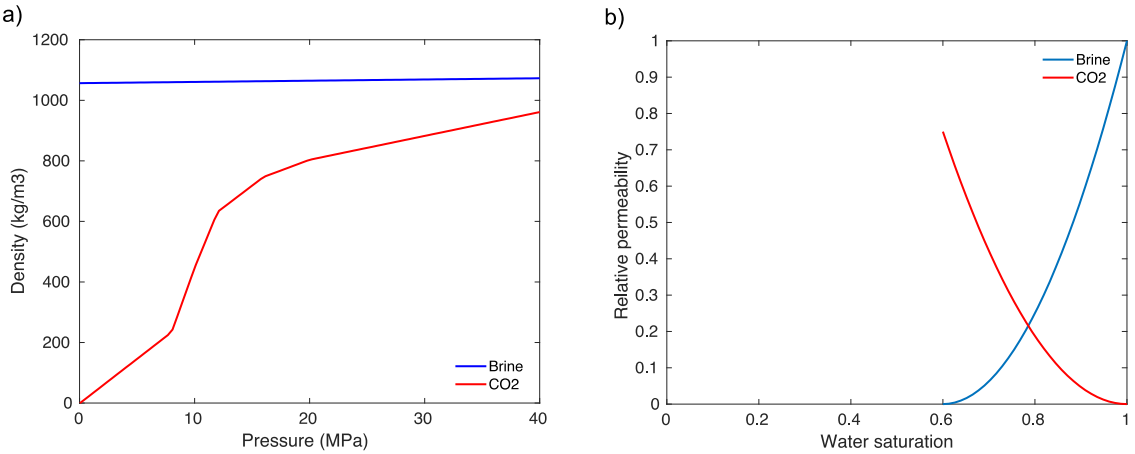

Figure 60. Fluid properties used in the flow simulations. a) Fluid density variation with pressure for the brine and CO_2; b) Relative permeability curves.

Fault Properties

In our coupled flow and geomechanics modeling, faults were modeled as 2D planes with an assigned thickness (Karimi-Fard et al., 2004), which allowed us to define permeability across and along the faults such that faults contribute actively to pressure diffusion and CO_2 transport.

We defined the along-fault permeability to be much larger in the Precambrian section than the fault locations intersecting the Mt. Simon interval. This modeling choice was intended to account for field observations showing that faulting in crystalline basement rocks tends to be accompanied by a fault zone that is much more permeable than the surrounding rock matrix (Faulkner et al., 2003; Chester et al., 2005; Mitchell and Faulkner, 2009). In sedimentary sections where faulting occurs, the fault zone is likely to be filled with fine-grained material that significantly reduces its permeability. To account for these observations, we set the along-fault permeability in the fault areas within the Lower Mt. Simon to be 1 mD, whereas the fault locations in the Precambrian basement have permeability as large as 1,000 mD (Figure *62*61).

We define fault zone thickness to be the zone where significant permeability alteration occurs due to frictional processes, causing it to be differentiated from the host rock where faulting occurred. In the absence of outcrops, empirical correlations are used that relate fault zone thickness to the amount of clay content in the fault zone and the amount of fault displacement. Here, we use the empirical correlation proposed by Sperrevik et al. (2002) to define the fault zone thickness:

$$b = D(0.06 \cdot (\mathrm{SGR})^2) - \ 0.12 \cdot \mathrm{SGR} + 0.0659) \qquad \text{(Eq. 2)}$$

where b is the fault zone thickness, D is the fault throw, and SGR is the shale gouge ratio, which quantifies the amount of clay content at the fault zone. The SGR is related to the clay content of the formation as:

$$\mathrm{SGR} = \ \sum_{i=1}^{N} Vcl_i h_i D^{-1}, \qquad \text{(Eq. 3)}$$

where Vcl_i is the fractional clay volume for each zone crossed by the fault, $h_i$is the thickness of the offset layer, and D is the cumulative or total fault slip. The Lower Mt. Simon contains, on average, 5% clay (Freiburg et al., 2014) with an average thickness of ~1,640 ft (~500 m). We assumed an average fault displacement of 65 m, which we justified by noting that smaller fault throws would not be visible in the 3D surface seismic data. Therefore, we found that the average fault zone thickness is ~3 ft (~1 m).

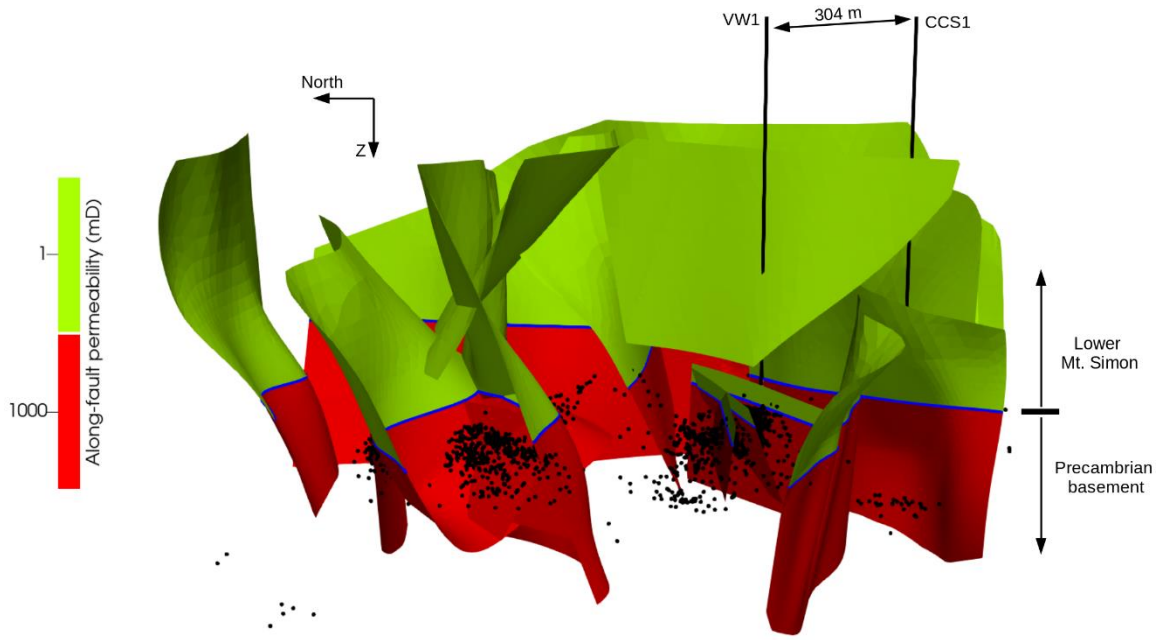

Figure 621. View from the west of the fault properties. Here we show the along-fault permeability. We divide the fault in two regions and assign constant fault properties within each region. The regions are defined as follows: the upper region (green colors) within the Lower Mt. Simon and a lower region (red colors) within the Precambrian basement interval. The solid blue line is the intersection of the fault planes with the Precambrian basement.

Model Calibration

We performed history matching to model the observed pressures at the VW1 well. We used transmissibility multipliers to adjust the degree of pore pressure diffusion from the injection interval to the pressure sensors located above the injection zone. Reservoir pressure data indicated that the Lower Mt. Simon is compartmentalized, with pressure diffusion in the vertical direction significantly limited, presumably because of the mudstone baffles identified in well logs and core data. The distinctive character of the observed pressure at the WB1 sensor indicated that pressure diffusion into the basement is likely occurring; however, core data analysis showed the presence of a very low permeability (< 1 md) and low porosity (<10%) sandstone (Argenta formation) separating the Lower Mt. Simon from the Precambrian basement. It is unclear if the Argenta formation is laterally continuous or if it thins in some areas to hydraulically connect the Lower Mt. Simon to the Precambrian basement. Here, we assumed that the Argenta formation hydraulically disconnects the Lower Mt. Simon from the Precambrian basement, an assumption that we enforced by assigning zero transmissibility multiplier for the interface between these two zones. Therefore, in our hydraulic model, the only way that pore pressure could diffuse from the Lower Mt. Simon into the basement was along the pre-existing faults shown in Figure 57.

Consequently, in our flow simulations, we identified the along-fault permeability as the key hydraulic parameter controlling the match between the observed and modeled pressures at the VW1 well. The along-fault permeability controls the degree of pore pressure diffusion into the basement section, which impacts the modeled pressure at the WB1 sensor, given that this sensor is located at the transition zone between the Lower Mt. Simon and the Precambrian basement. Our flow model results indicated that an along-fault permeability of above 10 mD is necessary to match the observed data (Figure

62). We noted that the along-fault permeability controls the degree that pore pressure diffuses along the faults into the basement, whereas the basement fractured model shown in Figure 59 controls the extent that pressure diffusion occurs between the faults and the VW1 well.

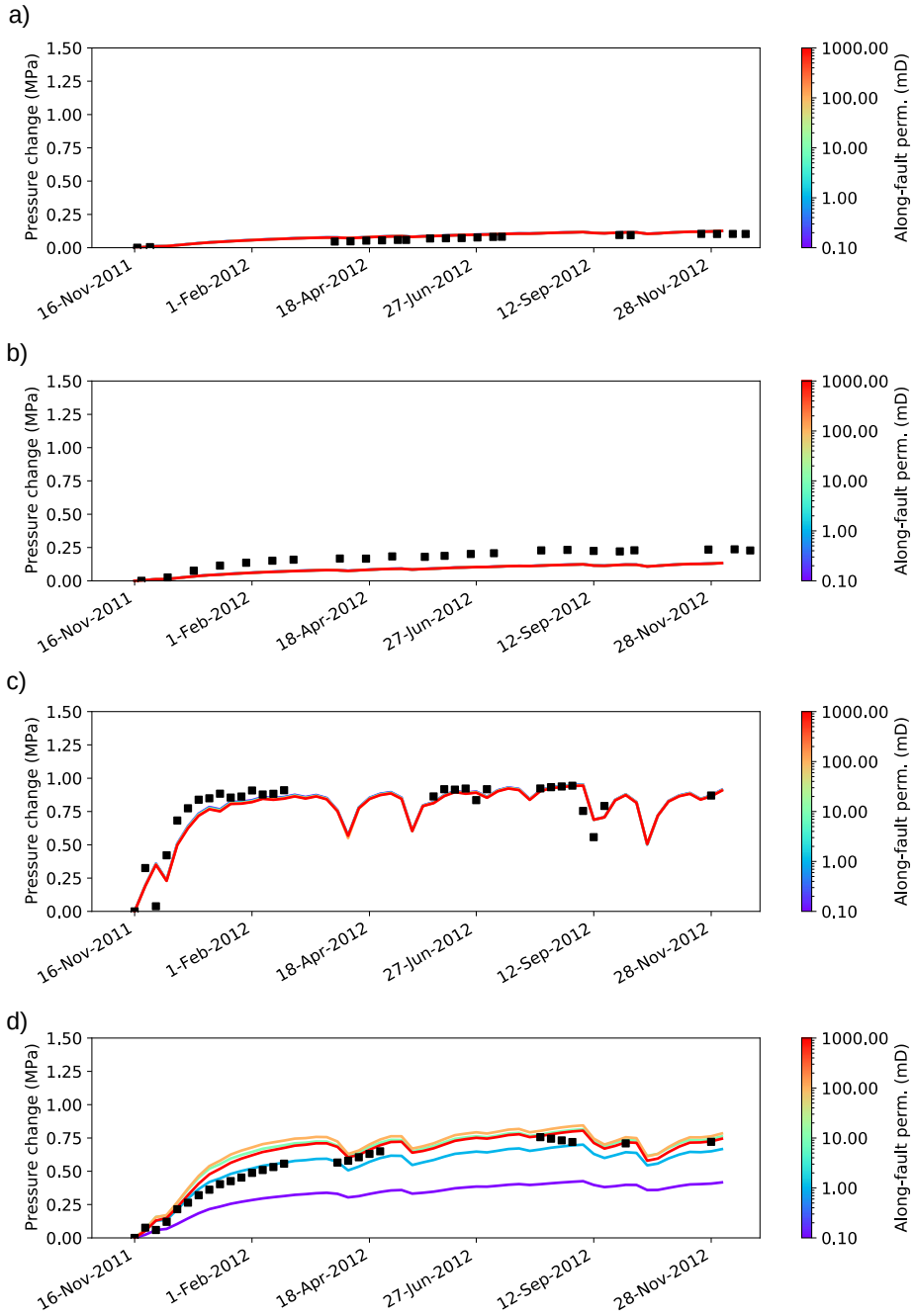

Figure 62. Comparison between modeled and observed pressures at the VW1 well for different along-fault permeability values. a) WB5 sensor, b) WB4 sensor, c) WB2 sensor, d) WB1 sensor.

Methodology

We modeled the coupling between subsurface flow and deformation using the theory of poroelasticity (Biot, 1941). The equations governing the coupling between flow and deformation are the

balance of linear moment and the fluid mass balance equation, with the effective stress linking pore pressure changes to deformation.

For an isotropic material, assuming infinitesimal deformation at isothermal conditions, the balance of linear momentum under quasi-static deformation is given as:

$$\nabla \cdot \boldsymbol{\sigma} + \rho_b \boldsymbol{g} = \mathbf{0} \quad \text{(Eq. 4)}$$

where $\boldsymbol{\sigma}$ is the Cauchy total stress tensor, $\boldsymbol{g}$ is the gravitational acceleration vector, $\rho_b = (1-\phi)\rho_s + \phi\rho_f$ is the bulk density, $\rho_f$is the fluid density, ρ_s is the solid grain density and ϕ is the porosity of the porous medium.

The fluid mass balance equation for a non-reactive multiphase flow system is given as (Coussy, 1995):

$$\frac{dm_\alpha}{dt} + \nabla \cdot \boldsymbol{\omega}_\alpha = \rho_\alpha f_\alpha \quad \text{(Eq. 5)}$$

where $m_\alpha$is the fluid mass content of phase α, $\boldsymbol{\omega}_\alpha$ is the mass flux of fluid phase α relative to the solid skeleton, ρ_α is the density of fluid phase α, where the total fluid density is given as $\rho_f = \sum_{\beta=1}^{\eta_{\text{phase}}} \rho_\beta S_\beta$, with ρ_β and $S_\beta$being the density and saturation of phase β, and η_{phase} is the total number of phases.

We assumed that the fluid phases are immiscible, and thus the fluid mass flux of phase α is given as $\boldsymbol{\omega}_\alpha = \rho_\alpha \boldsymbol{v}$, where $\boldsymbol{v}_\alpha$ is the Darcy velocity, which for a multiphase system is given as (Bear, 1972):

$$\boldsymbol{v}_\alpha = -\frac{\boldsymbol{k} k_{r\alpha}}{\eta_\alpha}(\nabla p_\alpha - \rho_\alpha \boldsymbol{g}) \quad \text{(Eq. 6)}$$

where η_α and $k_{r\alpha}$ are the dynamic viscosity and the relative permeability of phase α, and p_α is the fluid pressure of phase α. Here, we neglect capillary pressure, and thus $p_\alpha = p$ for all phases α.

The porous medium deformation results from effective stresses are given as (Coussy, 1995):

$$\boldsymbol{\sigma}' = \boldsymbol{\sigma} + bp\mathbf{1} \quad \text{(Eq. 7)}$$

where $\boldsymbol{\sigma}'$ is the effective stress tensor, b is the Biot coefficient (Coussy, 1995) and **1** is the unit tensor. We adopt the sign convention that tensile stresses are positive. Finally, the constitutive equation governing deformation in a poroelastic medium is:

$$\nabla \cdot (\sigma' - bp\mathbf{1}) + \rho_b \boldsymbol{g} = \mathbf{0} \quad \text{(Eq. 8)}$$

In our model implementation, due to the small strains associated with CO_2 injection, we performed a one-way coupled flow and geomechanics modeling, where pore pressure was used to drive deformation only, without the reverse coupling (pore pressure changes induced by the deformation). We first solved the flow problem to obtain pore pressure and saturation changes, which were then used in the solution of the mechanics problem. We solved the flow problem using the finite volume simulator Matlab Reservoir Simulator Toolbox (MRST) (Lie, 2019). We solved the mechanics problem using the finite element mechanical simulator PyLith (Aagaard et al., 2013). We avoided interpolation of the pore pressure field by using the same computational mesh, shown in Figure 58, in both simulators.

We investigated the impact of CO_2 injection on the fault stability behavior using the Coulomb Failure Function, CFF, defined as (Reasenberg and Simpson, 1992; King et al., 1994):

$$\mathrm{CFF} = |\tau| + \mu\sigma' \quad \text{(Eq. 9)}$$

We fixed the fault friction coefficient at $\mu = 0.6$. Additionally, τ is the shear stress magnitude computed from the horizontal and vertical shear stresses.

We quantified the impact of CO_2 injection on fault stability using changes in CFF, DCFF, relative to a reference state of stress:

$$\mathrm{DCFF}(t) = \mathrm{CFF}(t) - \mathrm{CFF}(t_0) \quad \text{(Eq. 10)}$$

where $\mathrm{CFF}(t_0)$ is the Coulomb stress prior to the beginning of the injection. In our sign convention, where tensile stresses are positive, fault destabilization occurs when DCFF > 0, whereas fault stabilization occurs when DCFF < 0.

Additionally, we investigated the combined effects of fault destabilization caused by pore pressure diffusion and by poroelastic stresses by expanding the DCFF as:

$$\mathrm{DCFF}(t) = \mathrm{CFF}(t) - \mathrm{CFF}(t_0) = \Delta|\tau| + \mu\Delta\sigma_n + \mu\Delta p \quad \text{(Eq. 11)}$$

The term $\Delta|\tau| + \mu\Delta\sigma_n$ is often referred to as "poroelastic stress" since it is the result of poromechanical coupling only.

Because the IBDP project included geocellular modeling, the SoS project started with the model available at that time (2018/2019 geocellular model). This IBDP model was calibrated to the three years of injection. In the first six months of the SoS project, it was necessary to limit the analyses of seismicity data to two major clusters (#2 and #4) that developed in the first nine months following injection startup. Hence, the SoS model calibration effort was limited to nine months. Unfortunately, the 2018/2019 geocellular model did not match the first nine months as well as it appeared to match the entire three years of CCS1 and VW1 pressure and saturation data. Therefore, a new geocellular model was developed earlier in the SoS project than was originally planned. In the process of following the iterative methodology of integrating modeling results (Figure 1), seven unique geocellular models were required and over 300 modifications to these geocellular models to calibrate rigorously the geocellular to the IBDP pressure and saturation data. Dozens of these modifications occurred between development of the next geocellular model in order to test geologic features that might be present and improve the calibration before requestioning the next geocellular model.

Flow Model Results

Pore pressure diffusion in the basement section due to CO_2 injection is shown in Figure 63. Due to the relatively large along-fault permeability values (> 10 mD along all faults compared with < 10 mD in the basement matrix), pore pressure diffusion was initially localized near the faults in our models. Over time, pressure diffusion into the fractured basement caused pressure to increase away from the faults in a NE-SW direction that followed the fracture orientation determined by the anisotropic permeability field (Figure 59). Between March and July 2012, the pore-pressure change at cluster #2 was as large as 0.5 MPa (5 bar).

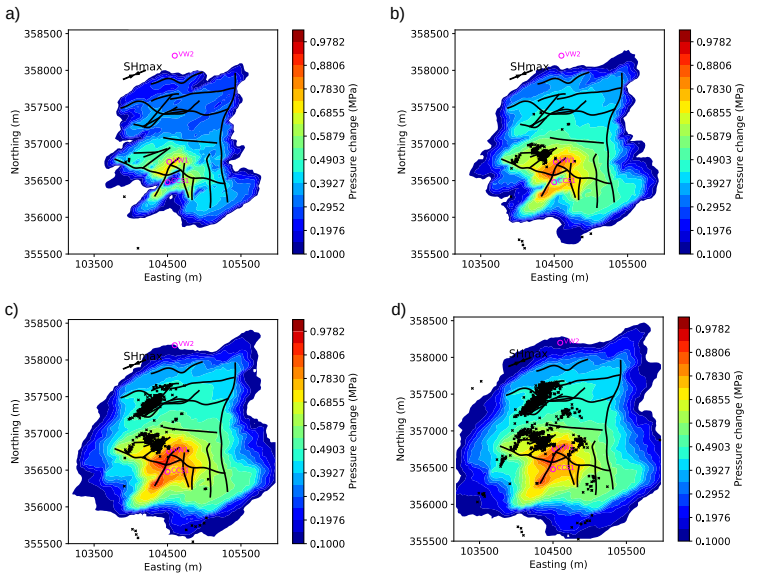

Figure 63. Modeled pore pressure spatial distribution at the top of the Precambrian basement at different times. a) January 2012, prior to seismicity occurrence. b) March 2012, when microseismicity at cluster #2 occurred. c) July 2012, when microseismicity at cluster #4 occurred. d) December 2012.

A key modeling result from our flow simulations was that the pore pressure along the faults in our model increased significantly in the basement section compared with the regions in the Mt. Simon interval. This simulation result was derived directly from our along-fault permeability definition shown in Figure 61, where regions in the basement interval have much larger permeability than in the sedimentary sections.

In the regions surrounding cluster #2 and cluster #4, pore pressure changes were as large as 0.7 MPa and 0.4 MPa, respectively. We noted that without flow along faults, pressure diffusion to regions where microseismicity occurred would be constrained by the hydraulic properties of the Argenta formation and the Precambrian basement.

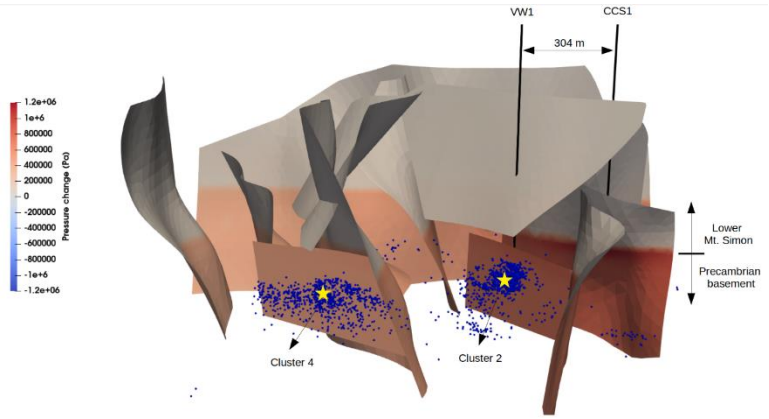

Figure 64. Spatial distribution of pore pressure at the faults in our model for July 2012, when cluster #4 of seismicity occurred. Yellow stars denote fault locations that will have the fault traction and pore pressure analyzed in the following figures. Here we used an along-fault permeability of 100 mD.

Finally, Figure 65 compares the breakthrough time for the modeled CO_2 saturation at the VW1 well with the observed data. The data shows that CO_2 plume arrived at the VW1 well around March 2012, which agrees with our model results. CO_2 saturation was confined to the injection interval, and no CO_2 leakage to the shallower formations occurred due to flow along the faults.

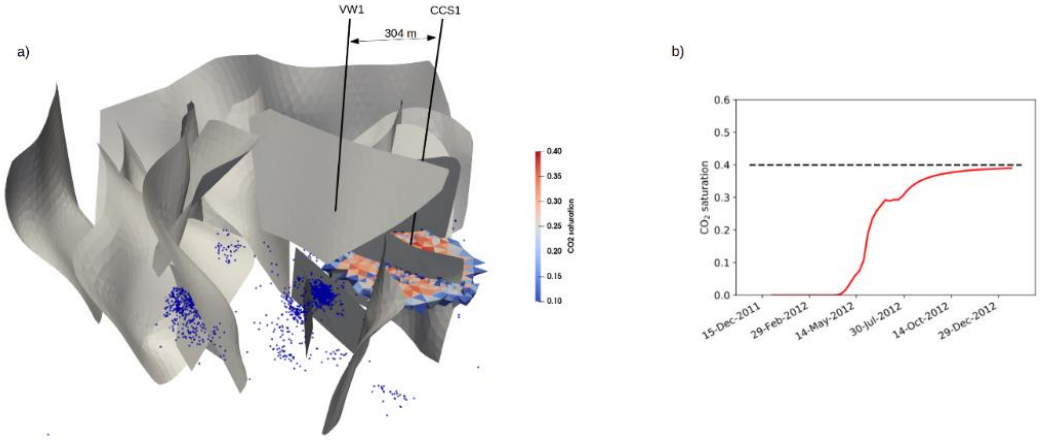

Figure 65. Spatial distribution of CO_2 saturation after one year of injection. a) 3D perspective view showing CO_2 plume with respect to all faults in the model. Blue dots indicate microseismicity location. b) Temporal evolution of the modeled CO_2 saturation at the VW1 well (solid red line). Dashed black line indicates the maximum CO_2 saturation observed at the VW1 well location.

Elastic and Poroelastic Properties Used in the Geomechanical Model

In Table 5, we show the elastic and poroelastic properties used in our geomechanical model. For each layer, we defined constant average values estimated from well-log measurements at the IBDP site.

Table 5. Summary of elastic and poroelastic properties used for each layer in our model. Within each layer, values are assumed to be constant.

		E (GPa)	ν	ρ_b (g/cm3)	b
Layer 1	Overburden	40	0.30	2550	0.7
Layer 2	Mt. Simon	41	0.29	2550	0.7
Layer 3	Lower Mt. Simon	29	0.30	2430	0.7
Layer 4	Lower Mt. Simon	27	0.30	2320	0.7
Layer 5	Lower Mt. Simon	25	0.33	2390	0.7
Layer 6	Basement	39	0.25	2700	0.7

State of Stress at the IBDP Site

At the IBDP site, interpretation of wellbore breakouts and drilling-induced tensile fractures using FMI logs indicate an average maximum horizontal stress orientation of N68E (Babarinde et al., 2021), a value that is in agreement with contemporary S_{Hmax} orientation in the eastern and central U.S (Lund et al, 2020) and consistent with six in-situ stress measurements within 37 to 62 miles (60 to 100 km) away of the IBDP site (Bauer et al., 2016; Lahann et al., 2017). Focal mechanism analysis of several microseismic

events at IBDP has consistently shown a strike-slip stress regime with events happening on fault planes oriented within 30° from the S_{Hmax} direction (N68E) (Kaven et al., 2015; Langet et al., 2020), suggesting that seismicity occurred on critically stressed faults.

We estimated the vertical stress magnitude by integrating the density values corresponding to each zone in our model (Table 5), resulting in a vertical stress gradient of 24.8 MPa/km. At the IBDP site, the magnitude of the minimum horizontal stress, S_{hmin}, was measured at two different depths using mini-frac tests (Bauer et al., 2016; Babarinde et al., 2021). No measurements of S_{Hmax} magnitude were available at the IBDP site; however, stress magnitude measurements available for a site ~100 km away showed that S_{Hmax} gradients vary between 28 MPa/km to 43 MPa/km (Lahann et al., 2017). Figure 66 shows the stress measurements at the IBDP site and 100 km away from it for different S_{hmin}/S_v and S_{Hmax}/S_v gradients. The stress ratio that agrees best with the S_{hmin} measurements at the IBDP site are on the range $S_{hmin}/S_v \approx 0.6$ to 0.9, whereas ratios for S_{Hmax}/S_v vary from 1.1 to 2.5.

Our geomechanical model was initialized with pre-stresses corresponding to one of the stress gradients shown in Figure 66. For boundary conditions, we disallowed displacement perpendicular to all sides and the bottom of the domain (no displacement boundary conditions), leaving the top of the domain as a free surface.

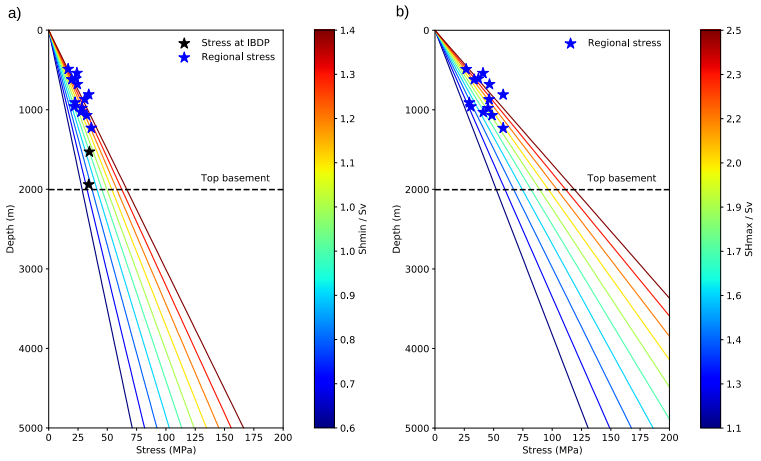

Figure 66. Initial stress variation with depth for the geomechanics simulations. a) Minimum horizontal stress, S_{hmin}. Colored lines indicate different S_{hmin} / S_v ratios. Blue stars correspond to stress measurements 95 km away from the IBDP site (Lahann et al., 2017). Black stars are minimum horizontal stress measurements at the IBDP site. The average depth of the basement at the CCS1 well is shown by the dashed black line. b) Same as a) but for the maximum horizontal stress, S_{Hmax}. Note that no data are available for S_{Hmax} at the IBDP site.

Geomechanical Model Results

Impact of uncertainty on initial pre-stresses

We investigated the impact of uncertainty in the initial pre-stresses assigned to our domain by measuring the slip tendency, T_s, at selected faults in our model. Assuming that faults have zero cohesion, the slip tendency is defined as the ratio of the shear to effective normal stress (Morris et al., 1996; Lisle and Srivastava, 2004):

$$\mathrm{Ts} = \frac{|\tau|}{-\sigma'} \qquad \text{(Eq. 12)}$$

where τ is the shear stress magnitude and σ′ is the effective normal stress.

Figure 67 shows slip tendency values at the center of the fault "F.333", located at cluster #4, for different initial pre-stress scenarios corresponding to different S_{Hmax}/S_v and S_{hmin}/S_v stress ratios in Figure 66. For fault "F.333", slip tendency values are as low as 0.2 and as high as 1.2 for S_{hmin}/S_v between 0.6 to 0.9 and S_{Hmax}/S_v between 1.2 and 2. Our preferred scenario is defined by the ratio $S_{hmin}/S_v = 0.6$ and $S_{Hmax}/S_v = 1.1$. However, other pre-stress ratios would yield similar results (e.g., $S_{hmin}/S_v = 0.9$ and $S_{Hmax}/S_v = 1.97$). Additional measurements of S_{Hmax} at the IBDP site are required to resolve the precise ratio of S_{Hmax}/S_v.

For different pre-stress ratios, we show in Figure 67b,c,d the spatial variation of the slip tendency at the fault locations intersecting the basement horizon. Overall, our model initialization results indicated that the faults near clusters #2 and #4 have T_s ~ 0.55 to T_s ~ 0.7 and, therefore, are critically stressed. Other fault locations are also critically stressed but do not show any apparent seismicity — a result that can be an indication of local stress magnitude variation, uncertainty in fault geometry, or that fault slip occurred aseismically. In fact, Figure 67 shows that small changes in fault strike orientation, with respect to the S_{Hmax} orientation, cause significant differences on the fault proximity to failure, which stresses the connection between fault geometry in subsurface and seismic hazards.

Impact of along-fault permeability on the stability of basement faults

For different values of the along-fault permeability, we show in Figure 68 the temporal evolution of changes in pore pressure (Δp) and fault tractions at clusters #2 and #4 for the spatial locations that are shown by the yellow stars in Figure 67. As expected, Δp at clusters #2 and #4 decreases with decreasing along-fault permeability. For along-fault permeability equal to 1 Darcy, Δp is as large as 0.75 MPa in April 2012 (Figure 69a), when cluster #2 of seismicity occurred, and 0.5 MPa in July 2012, when cluster #4 of seismicity occurred (Figure 69b). Similarly, for along-fault permeability equal to 0.01 mD, pore Δp at clusters #2 and #4, respectively, are $\Delta p \approx 0.15$ MPa in April 2012 and $\Delta p \approx 0.2$ MPa in July 2012.

Pore pressure increase in the fractured basement (Figure 63) results in poroelastic stresses that increase compression at the fault surfaces, resulting in an increase in total normal stress that leads to fault stabilization at clusters #2 and #4 (Figure 68c,d). Similar to the behavior of pore pressure, along-fault permeability controls the extent of fault normal stress increases. The effective normal stress, $\sigma' = \sigma_n + bp$, however, shows a decrease in compression, indicating that pore pressure changes outweigh the increase in compressive normal stress and resulting in fault destabilization (Figure 68e,f). Our model results also indicated that the shear stress magnitude is one order of magnitude smaller than the effective normal stress changes (Figure 68g,h); therefore, the poroelastic stress changes are dominated by changes in the total normal stress at the fault planes (Figure 68I,j). In agreement with the total normal stress variations, poroelastic stress changes are negative, indicating that, in absence of pore pressure changes at the fault locations, basement faults would be stabilized due to CO_2 injection at the CCS1 well. These results point out the importance of along-fault pore pressure diffusion to explain the destabilization of basement faults.

We quantified the impact of poroelastic stresses and pore pressure on the fault stability using changes in the Coulomb Failure Function (DCFF) (Eq. 10). The temporal evolution of DCFF indicated that for along-fault permeability equal to 1 Darcy, DCFF ≈ 0.3 MPa at cluster #2 (March 2012) and DCFF ≈ 0.2 MPa at cluster #4 (July 2012). Likewise, for along-fault permeability equal to 0.01 mD, DCFF ≈ 0.05 MPa at cluster #2 (March 2012) and DCFF ≈ 0.1 MPa at cluster #4 (July 2012) (Figure 68a,b; Figure 69a,b). Our model results showed that DCFF is always positive, indicating that the faults are being moved toward destabilization due to the increase in pore pressure (Figure 68a,b). Similar to DCFF variations, the fault slip tendency, T_s, also

depends on the along-fault permeability — with larger values of along-fault permeability increasing T_s. For both clusters #2 and #4, T_s increased slightly (≈ 3%) with respect to its initial value.

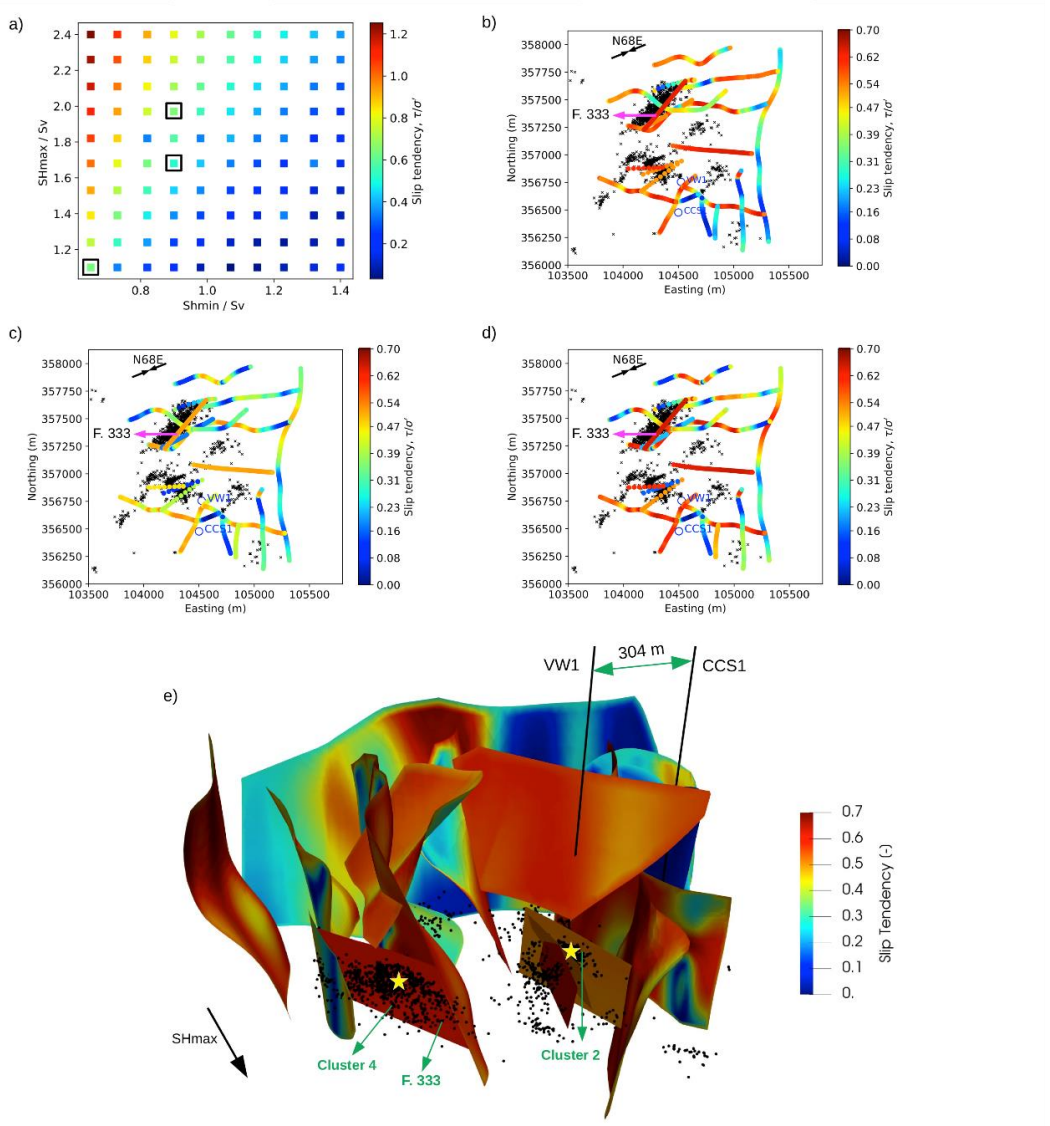

Figure 67. Variation of slip tendency with initial stresses and fault location. a) Slip tendency, $T_s = \tau/\sigma'$, corresponding to different initial stresses shown in Figure 63. Here we show T_s for fault 333, which is indicated in b, c, and d as "F. 333". Black open squares indicate the initial stresses shown in b, c, and d. b) Slip tendency for all faults in our model. Here we show the slip tendency computed at the fault locations that intersect with the basement surface. In this case, the slip tendencies were computed using an initial stress of $S_{Hmax}/S_v = 1.1$ and $S_{hmin}/S_v = 0.65$. c) Same as b but for an initial stress of $S_{Hmax}/S_v = 1.68$ and $S_{hmin}/S_v = 0.9$. d) Same as b but for an initial stress of $S_{Hmax}/S_v = 1.97$ and $S_{hmin}/S_v = 0.9$. e) 3D perspective view of T_s for an initial stress of $S_{Hmax}/S_v = 1.1$ and $S_{hmin}/S_v = 0.65$. The yellow stars indicate fault locations where temporal evolution of fault tractions and pore pressure will be analyzed.

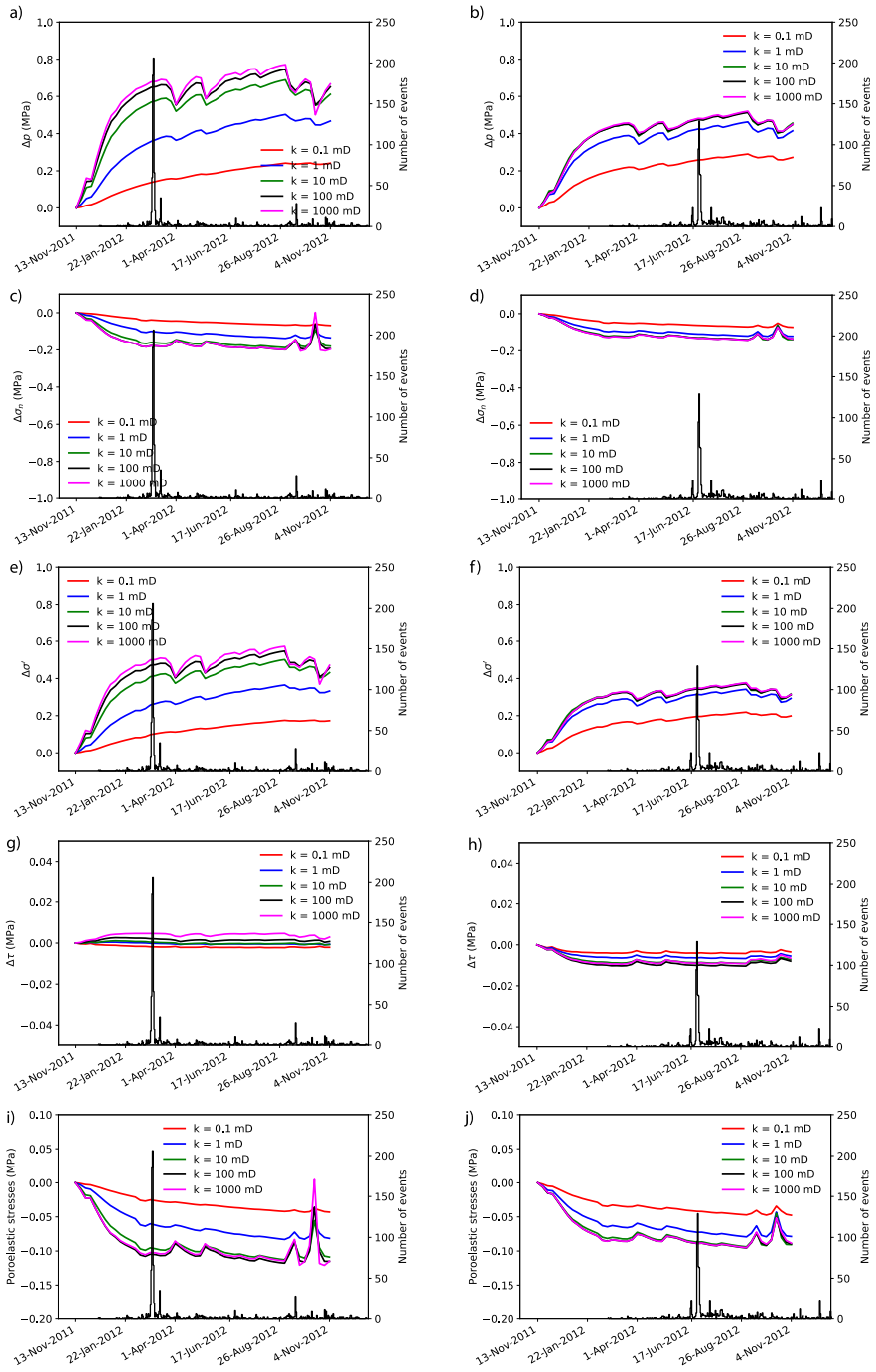

Figure 68. Temporal evolution of fault pore pressure and stress changes for different along-fault permeability values. The left and right columns are clusters #2 and #4, respectively. a, b) Pore pressure changes (positive means increase in pore pressure). c, d) Changes in normal stress (negative means increase in compression). e, f) Changes in effective normal stress (positive means decrease in compression). g, h) Changes in shear stress magnitude (positive means increase in shear stress magnitude). i, j) Poroelastic stress changes (negative means decrease in poroelastic stress). All changes are relative to the beginning of the injection. The histogram of earthquakes for each cluster is given by the black lines. All plots correspond to the fault locations shown in Figure 67.

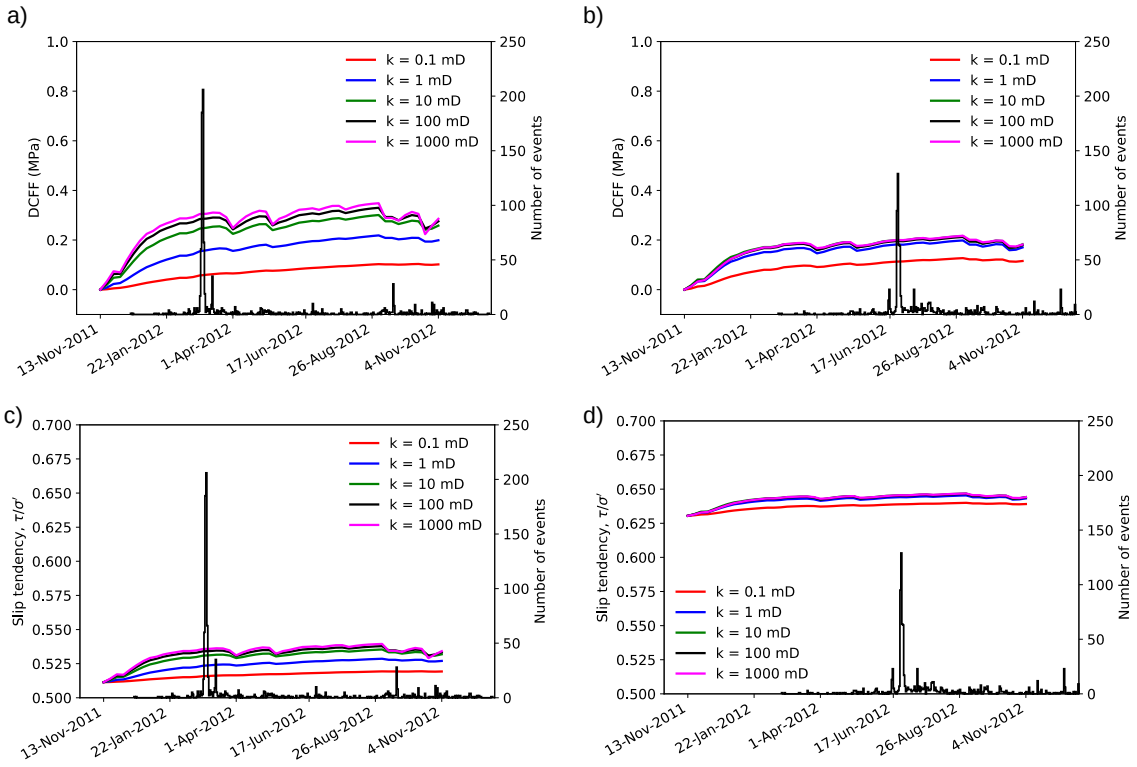

Figure 693. Temporal evolution of DCFF and slip tendency, Ts = τ/σ', for clusters #2 and #4. Colored lines correspond to different along-fault permeability values. a) DCFF for cluster #2. b) DCFF for cluster #4. c) Slip tendency for cluster #2. d) Slip tendency for cluster #4. The fault location shown here is indicated by the yellow star in Figure 67.

DISCUSSION

Fault geometry has a significant impact on the fault proximity to failure (Figure 67) and points out the importance of using accurate subsurface fault representations to investigate earthquake hazards. Despite our dense fault model based on detailed interpretation of 3D surface seismic reflection data, the fault planes where the microseismicity cluster occurred were below the seismic resolution and invisible a priori to seismicity occurrence. This observation indicates the challenges of earthquake hazard prediction prior to injection and that, even with detailed fault mapping using state-of-the-art seismic reflection data, smaller faults are likely to be characterized only after seismicity occurs.

Building accurate geological models of the subsurface requires detailed reservoir characterization using all available data. In the case of the IBDP site, reservoir pressure measurements at the VW1 well combined with well-log and core information were essential to constrain the extent that the Lower Mt. Simon formation is hydraulically connected to the Precambrian crystalline basement. The absence of pore pressure diffusion along-faults, in combination with the low porosity and low permeability of the Argenta interval, would compartmentalize reservoir pressure increase to the Lower Mt. Simon only, which is incompatible with seismicity occurrence in the basement section. Our model results showed that along-fault pore pressure diffusion is an important mechanism to explain the destabilization of basement faults due to injection in shallower sedimentary sections at the IBDP site.

In our hydraulic model, along-fault permeability was the main parameter controlling the degree of pore pressure diffusion from the Lower Mt. Simon into the Precambrian basement. Presumably, high values of the along-fault permeability correspond to highly fractured fault zones surrounding the fault

core. There are extensive field observations of how fractures enhance permeability of fault zones (Faulkner et al., 2003; Sperrevik et al., 2002), but the exact fracture density at the IBDP site warrants additional study. There is also uncertainty with respect to the degree that such fractures are filled with fine-grained clay particles, causing reduction in their permeability. Here, we have used empirical equations derived for siliciclastic rocks only. Additional work is required to investigate fault zone permeability for transitional zones between sedimentary and crystalline rocks, such as the location of the IBDP site.

Our model results indicated that poroelastic stress changes alone would stabilize the basement faults where seismicity occurred due to normal stress increase at the fault planes. This increase in normal stress occurs due to elastic deformation of the basement associated with pore pressure diffusion from the faults to the fractured basement, which explains the dependency of the poroelastic stress changes on the along-fault permeability.

Our model results did not indicate a clear correlation between DCFF temporal variation for clusters #2 and #4 and the seismicity rate (Figure *693*69). We hypothesize that this lack of temporal correlation is attributed to heterogeneity in the along-fault permeability or in the fault frictional properties, uncertainty in the initial stress magnitudes, and the presence of additional faults that can significantly impact pore pressure diffusion behavior. Further studies using rate and state models (Dieterich, 1994) could be used to investigate the seismicity rate associated with our DCFF variation and its dependency on the fault hydraulic and frictional properties.

CONCLUSION

We have shown that pore pressure diffusion along pre-existing faults connecting the Lower Mt. Simon and the Precambrian crystalline basement is the main mechanism for the occurrence of induced seismicity associated with CO_2 injection at the IBDP. For a fault zone thickness of 6 ft (1.88 m) and along-fault permeability of 1 Darcy, we find that pore pressure changes at faults can be as high as $\Delta p \approx 0.75$ in basement regions away from the injection well where microseismicity occurred.

We also found that poroelastic stresses alone tend to stabilize the basement faults, counteracting the destabilizing pore pressure effects and causing an overall decrease in the DCFF at the microseismicity locations. These results indicate the importance of pore pressure diffusion along faults connecting sedimentary sections and the crystalline basement as a mechanism for microseismicity occurrence at the IBDP site and in other geologically similar locations. Slip tendency analysis showed that fault strike variation relative to the maximum horizontal stress direction plays a major role on the proximity of faults to failure. Fault planes interpreted based on the microseismicity locations were found to be critically stressed and showed slip tendency ranging from $T_s \approx 0.55$ to ≈ 0.7 prior to injection.

Our model results highlighted the importance of accurate subsurface characterization to understand the hydraulic and geomechanical factors that lead to induced seismicity associated with CO_2 injection and other subsurface injection activities, such as subsurface wastewater disposal operations.

TASK 5 - INJECTION-INDUCED SEISMICITY MODELING

INTRODUCTION

Several mechanisms have been proposed to explain induced seismicity, including fault weakening through pore pressure perturbation, increased fault loading due to poroelastic coupling, and rock properties alteration due to chemical effective from reactive fluids. While the mechanisms are broadly understood, the details are site specific. Furthermore, the role of fault network complexity, fault friction heterogeneity, and rock inelasticity remain largely unexplored. These specific details may play a significant role in controlling the spatio-temporal distribution of injection-induced seismicity in any site. This work focused on elucidating the role of these details on the mechanics of induced seismicity in general and the seismicity patterns observed in the IBDP site in particular.

OVERVIEW AND BACKGROUND

Figure 70 shows a schematic of geologically identified fault systems at the IBDP site together with the recorded microseismicity. Mapped faults did not coincide with the microseismicity locations in clusters #2 and #4. Accordingly, new fault surfaces were suggested by Task 3 (Sandia/MIT) to fit the recorded seismicity.

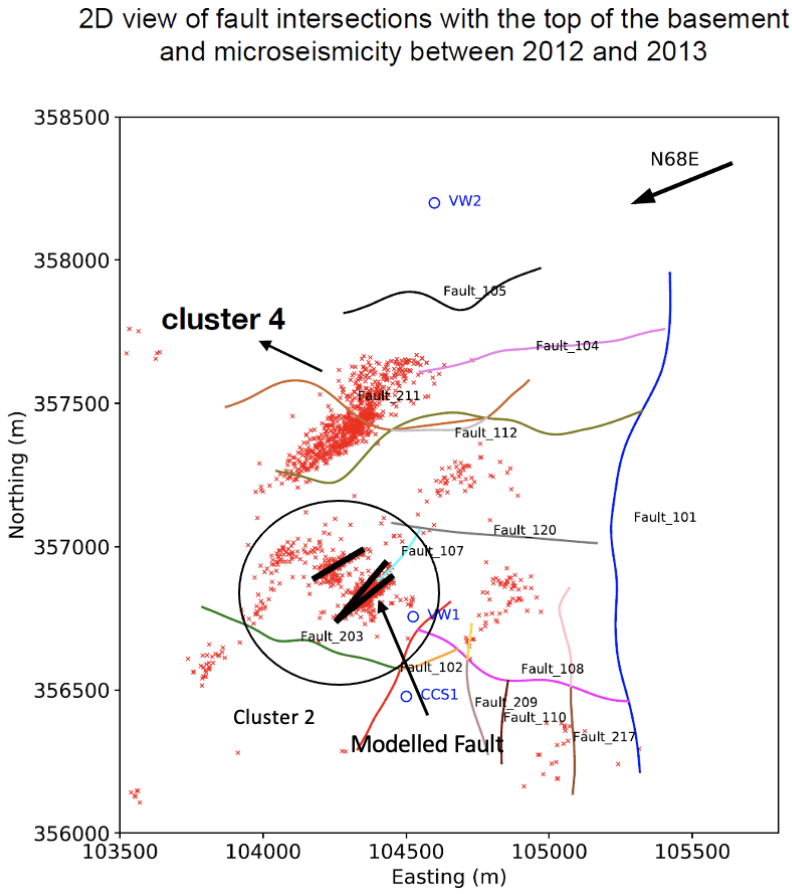

Figure 70. Schematic of a geologically identified fault system in the Decatur basin together with the recorded microseismcity.

In our work, Task 5 (UIUC) had four questions of interest:

- What controls the spatio-temporal distribution of seismicity in Decatur?
- Is there a correlation between the magnitude of the pore pressure perturbation due to injection and the timing or magnitude of the seismic events?
- How do the characteristics of the injection influence the spatio-temporal distribution of seismicity?
- Is it possible to control seismicity through varying the injection characteristics?

We addressed these questions through a series of hypotheses, which were tested using computational models that simulate fault response over different spatial and temporal scales to external stimuli. The hypotheses are as follows:

- The spatio-temporal evolution of microseismicity on the mapped fault for cluster #2 is governed by heterogeneous rate and state frictional properties.
- An active fault zone is home to a plethora of complex structural and geometric features that are expected to affect earthquake rupture nucleation, propagation, and arrest, as well as inter-seismic deformation. These complexities can affect the seismicity on the main fault even if they accommodate only a small fraction of the seismic moment. The feedback between structural heterogeneities, stress evolution, and earthquake mechanics are thus important to consider for both natural and induced seismicity.
- Fault response is governed by friction law, which relates the tangential component of stress (fault strength) with the normal stress acting on the fault. Fluid injection increases the pore pressure, which results in a reduction in effective normal stress acting on the fault. Therefore, injection pressure and its spatio-temporal diffusion lead to heterogeneous distribution of effective normal stress. The reduced heterogeneous effective normal stress makes the fault susceptible to slip and results in different patterns with respect to number of seismic events, inter-seismic timing, presence of slow slip, and aperiodic cycles with or without spatio-temporal clustering. We hypothesized that the seismicity pattern is controlled not only by the injection protocol but also by the fault and bulk properties.

State of the Art

Modeling injection-induced seismicity is largely done using a quasi-static approach based on Mohr-Coulomb criteria. Susceptibility for induced seismicity is evaluated based on the state of the stress resolved on an optimally oriented fault surface. If the resolved stress is high enough to exceed the fault strength, the fault is expected to slip. However, this picture is an oversimplification due to the complex nature of fault friction and prevalence of stress and material heterogeneities at different scales. Specifically, the Mohr-Coulomb criterion is a necessary but not sufficient condition for fault slip. For the slip to nucleate, the stress must be high enough not only at a single point but also over a large enough region, called the nucleation region, for the slip to start. The size of the nucleation region depends on both the fault friction and the elastic properties of the surrounding material. Furthermore, the final event size and the magnitude of seismic hazard depend on the distribution of frictional properties and stresses on the fault surface. While these concepts are well-established in the area of mechanics of natural earthquakes, they are not widely discussed in the state-of-the-art simulations of induced seismicity. This is in part due to the multiscale nature of nucleation and propagation of seismic events, which pose significant computational challenges. Here we use a unique and highly efficient computational scheme to address this gap and simulate the long-term history of seismicity in complex fault zones subjected to

external stress and pore pressure perturbations spanning multiple cycles of both slow inter-seismic deformation to fast earthquake rupture propagation.

Challenges

The challenges faced by our task may be summarized as follows:

- Quantifying uncertainty associated with field and lab data related to rock properties, fault geometry, and fault frictional properties. To address this, we generated different stochastic realizations that were consistent with field and lab observations and used these realizations to generate sequence of seismic events that approximate observed records.
- Multiscale nature of earthquake processes. A seismic event may take only a fraction of a second. However, processes leading up to seismicity can take from days to years. Furthermore, a microseismic event may propagate over only tens of meters. However, the region over which extreme changes in stress and deformations occur near the rupture front, and which must be resolved computationally to ensure convergence, may only extend over sub-millimeter scale. To address this conundrum of spatial and temporal scales, we developed an in-house computational scheme, FEBE, that combines finite element and spectral boundary integral equation methods. The technique used adaptive time steeping to alternate between quasidynamic during slow deformations and fully dynamic integration schemes during rapid earthquake rupture propagation. This enabled us to simulate sequences of induced events accounting for full inertia effects as well as nonlinear material response in the near-fault region.

SINGLE FAULT RESPONSE

We considered cluster #2's seismicity and focused on one of the faults that was suggested to fit the microseismic event spatial distribution.

Methodology

We used FEBE, a hybrid finite element spectral boundary integral equation method, to simulate a sequence of earthquakes and aseismic slip on a planar fault with alternating patches of rate-weakening and rate-strengthening frictional properties embedded in a homogeneous linear elastic medium. The details of the method have been outlined in Ma et al. (2018), Abdelmeguid et al. (2019), and Abdelmeguid and Elbanna (2022).

Geometry

Figure 71a shows a schematic of the planar fault surface, highlighting the rheological heterogeneities. This fault surface represents a mid-depth horizontal section through one of the mapped faults, as shown in Figure 71b. We assumed 2D plane strain conditions.

Friction

We used a rate and state friction formulation in which the frictional strength was proportional to the effective normal stress, and the coefficient of friction depended on the fault slip rate as well as variables that described the contact history, such as microscale fault roughness. The nature of the steady state frictional response depended on two experimentally identified parameters, a and b. If $a-b > 0$, the frictional response was rate-strengthening—an increase in the slip rate leads to an increase in frictional resistance. Such response is characteristic of creeping fault segments. Rate-strengthening response suppressed nucleation of frictional instabilities in the creeping segments and resisted ensued propagation

of dynamic rupture, leading to their arrest. If a-b < 0, the frictional response was rate-weakening—an increase in the slip rate led to a decrease in frictional resistance. Such response is characteristic of locked fault segments. Rate-weakening response favors nucleation of frictional instabilities and promotes earthquake rupture propagation.

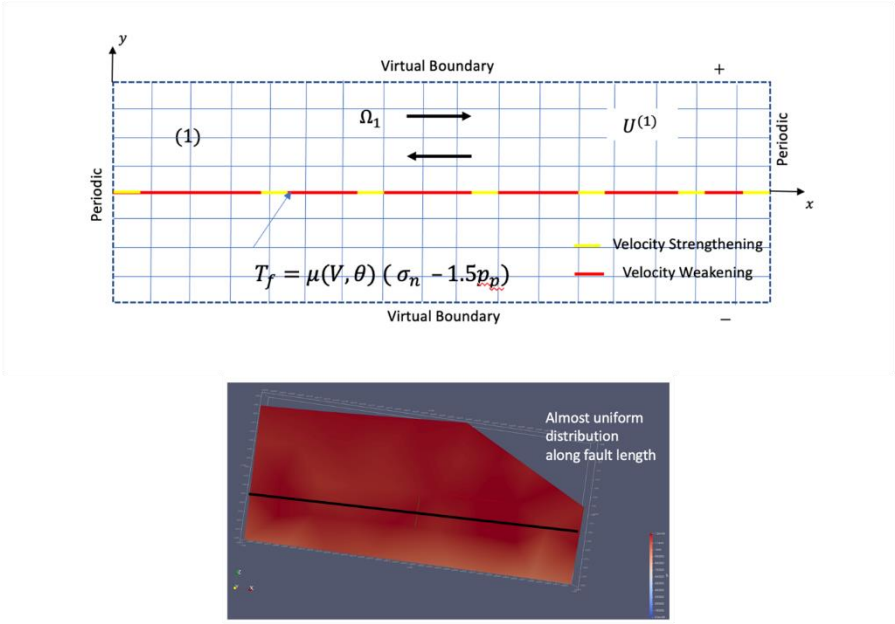

Figure 71. Model geometry. a) Schematic of a planar fault surface with heterogeneous rheology embedded in a homogeneous bulk. Region highlighted with yellow represents velocity-strengthening patches that are substantiable to unstable slip, while regions highlighted with red represent velocity-weakening patches that are stably creeping. b) The pore pressure distribution over the fault surface is approximately spatially uniform.

Effective Normal Stress

We used Terzaghi's effective stress principle and computed the effective normal stress on the fault surface as the difference between the total normal stress and the pore pressure. The pore pressure distribution on the fault surface was obtained from the geomechanical numerical simulations conducted by Task 4 (MIT/ISGS). The geomechanical analysis from Task 3 (Sandia/MIT) found that the spatial distribution of the pore pressure over the fault surface is approximately uniform, as shown in Figure 71b. The time evolution of the pore pressure with injection is shown in Figure 72.

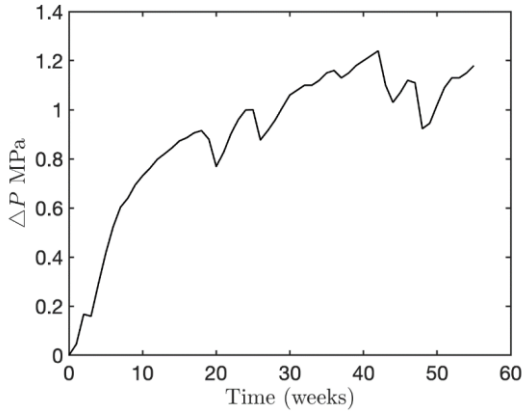

Figure 72. Time history of the pore pressure perturbation, computed by geomechanical numerical simulations (courtesy of Ruben Juanes, MIT).

Results

The spatio-temporal distribution of simulated seismic events is shown in Figure 73. The horizontal axis represents the position along the fault. The vertical axis gives the simulated time in units of time steps. The contours represent the slip velocity on the fault—how fast one side of the fault moves relative to the other side. The velocity ranges from sub-nanometer per second (dark blue) to several centimeters per second (dark red), covering the full range from slow aseismic deformation to fast seismic motion. The nucleation location of each event is marked by a white circle. Four observations follow:

- Events of different sizes (extent along the fault) are generated. The inter-event times are also non-uniform.
- Events nucleate within a velocity-weakening segment of the fault or at the boundary between a velocity-weakening segment and a velocity-strengthening segment. Most of the events propagate bilaterally from the nucleation location.
- Most events arrest when they reach a velocity-strengthening segment, leading to small events whose sizes are controlled by the length of the velocity-weakening segment. However, an event may occasionally be energetic enough to penetrate through the full velocity-strengthening segment and into a neighboring velocity-weakening segment. As a result, these events grow bigger.
- Both post-seismic and pre-seismic slip are observed. However, the deformation is slow enough that it may not be possible to detect on the surface using geodetic tools.

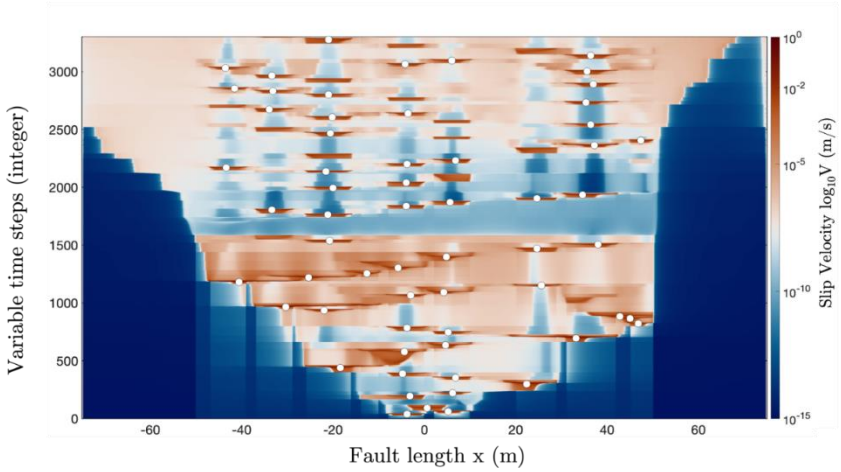

Figure 73. Spatio-temporal evolution of the slip rate on the fault subjected to pressure perturbation due to fluid injections. As fluid is injected, the unstable velocity-weakening patches start to slip in a heterogeneous manner with non-uniform recurrence pattern. Pore pressure perturbation is a catalyst that destabilizes the initially creeping velocity-strengthening patches.

Quantitative Comparison with Cluster #2

In the following figures, we compare the patterns of simulated seismic events with the recorded microseismicity. The nucleation zones of the simulated events are highlighted with a yellow star, the recorded microseismicity is highlighted with blue dots, and the microseismic events that occur during a given time interval are highlighted by red triangles.

We observe a good agreement between the location and timing of simulated events and recorded microseismicity for the time period between 02/23 and 02/28. Events nucleate near the center of the fault and remain, for the most part, clustered in this region.

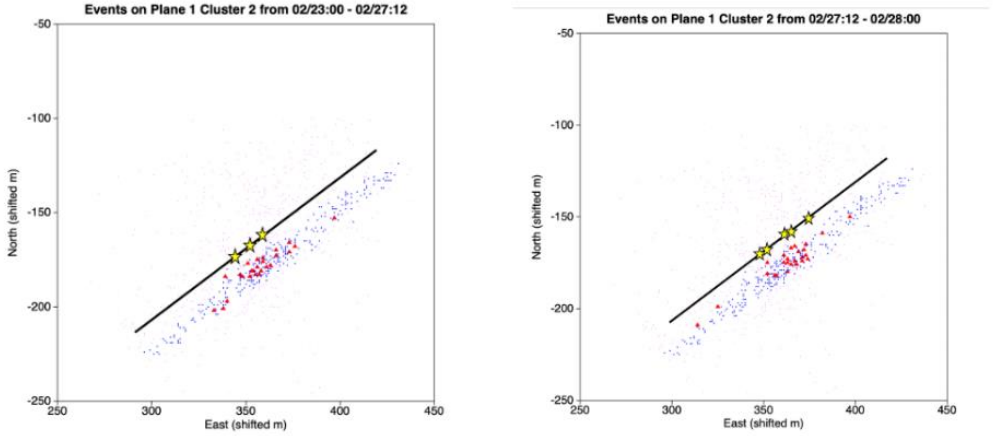

Figure 74. Seismic record comparison with numerical simulation of heterogeneous fault rheology for the time period from 02/23 to 02/28. The black line represents the fault surface, and yellow stars represent hypocenters of microseismicity. The red triangles are the seismically recorded events.

For the time period between 02/28:06 and 02/29:00, we observe some discrepancy. While we match the event clusters near the center of the fault as well as those events occurring toward the north-east end, we also generate more events in the south-west direction that were not observed during that particular time period.

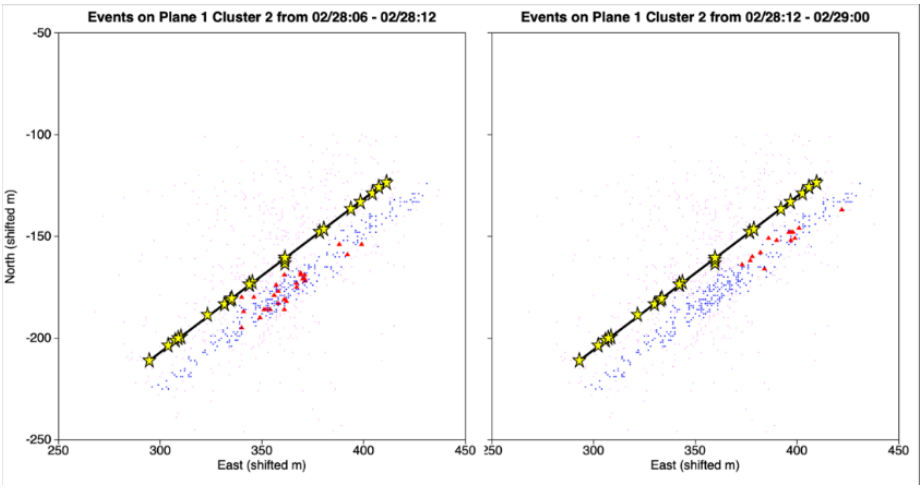

Figure 75. Seismic record comparison with numerical simulation of heterogeneous fault rheology for the time period from 02/28 to 02/29. The black line represents the fault surface, and yellow stars represent hypocenters of microseismicity. The red triangles are the seismically recorded events.

However, when considering the time period between 02/29 and 02/29:12, we observe a burst in microseismic event activity on the south-west portion of the fault consistent with the earlier simulation. While we continue to observe simulated events on the south-west half of the fault during this time interval, the results suggest that the naturally occurring microseismic events have occurred a few hours later than expected. Despite the good agreement, this difference in timing may point to smaller-scale heterogeneities in fault friction or bulk properties that have not been included in our model.

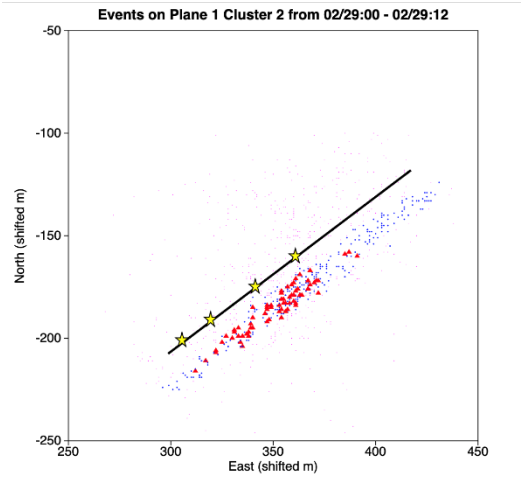

Figure 746. Seismic record comparison with numerical simulation of heterogeneous fault rheology for the time period from 02/29 to 02/29:12. The black line represents the fault surface, and yellow stars represent hypocenters of microseismicity. The red triangles are the seismically recorded events.

Finally, for the time period between 02/29:12 and 03/02, the microseismicity trend generally agrees with the simulated catalog, showing more clustering toward the north-east parts of the fault. However, differences exist where simulated events also occur on the south-west end while microseismicity is absent. This gap may be filled later by a swarm of events, as was discussed earlier.

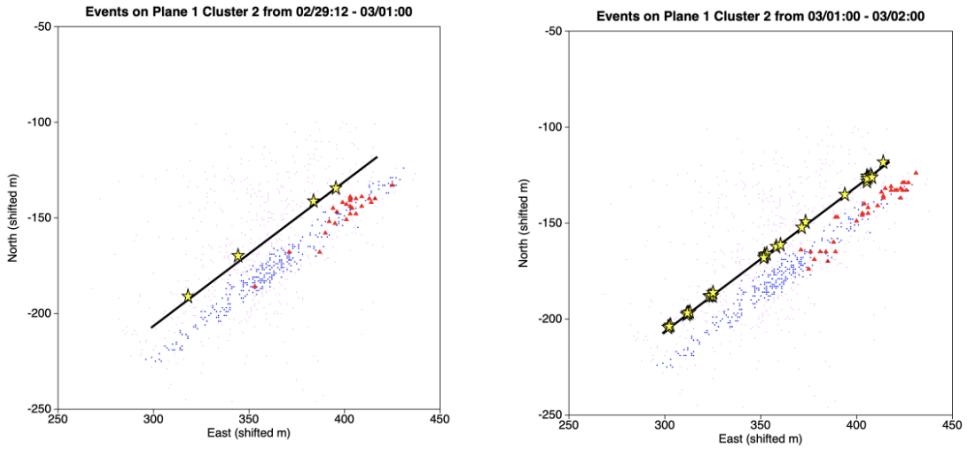

Figure 77. Seismic record comparison with numerical simulation of heterogeneous fault rheology for the time period from 02/29:12 to 03/02. The black line represents the fault surface, and yellow stars represent hypocenters of microseismicity. The red triangles are the seismically recorded events.

These observations are summarized in Figure 78, where the simulated events form three distinct clusters consistent with natural observations. One cluster spanned 02/24-02/25, another cluster was centered around 02/28, and the third cluster was centered around 03/01.

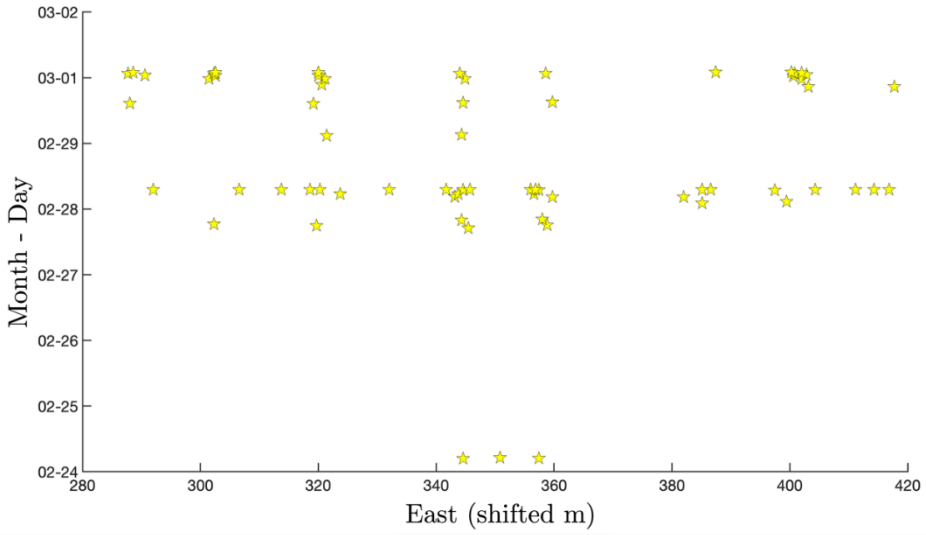

Figure 78. Time history of event occurrences. Yellow stars represent hypocenters of microseismic events starting on the fault surface. Earthquakes occur with an irregular occurrence interval.

Conclusions

Heterogeneous frictional rheology of geological faults potentially explains the spatio-temporal distribution of the recorded microseismicity. Results indicate good agreement with the observed trends from the seismic record in terms of temporal clustering as well as general spatial distribution of nucleation sites for the time period from 02/23 to 03/02 (Figures 74-77). The migration pattern and sequence of events show similar trends to the recorded catalog. The matching may be improved by incorporating finer-scale heterogeneities in the frictional properties and the bulk elastic properties. However, these smaller-scale variations would be hard to constrain from field observations. In the next section, we examine how some small-scale heterogeneities, beyond the observation limit, further influence the fault behavior.

FAULT SYSTEM RESPONSE

Hypothesis

An active fault zone is home to a plethora of complex structural and geometric features that are expected to affect earthquake rupture nucleation, propagation, and arrest, as well as inter-seismic deformation. These complexities can significantly affect the seismicity on the main fault even if they accommodate only a small fraction of the seismic moment. The feedback between structural heterogeneities, stress evolution, and earthquake mechanics are thus important to consider for both natural and induced seismicity.

Model Setup

We considered our fault system to exist in an infinite medium. A planar horizontal main fault was placed in the middle of the domain with secondary fault branches explicitly modeled as shown in Figure 79. The main fault was right lateral, and the secondary faults were placed on one side of the main fault (on the tension side), away from the nucleation zone. This minimized the effect of the secondary fault

branches on the rupture nucleation. The secondary faults were distributed over a finite length along the main fault and not throughout the whole fault length, so that we could explore features of the main fault rupture after it exited the region with the branches. The angle between the secondary faults and main fault varied, and a range of values were explored. The secondary faults had constant spacing along the fault strike. The length of each secondary fault was chosen to be equal to the length scale of frictional weakening so that they would be considered small when compared to other dimensions of the problem. This "smallness" is critical for the current investigation as it could prompt neglecting these features or render them hard to observe.

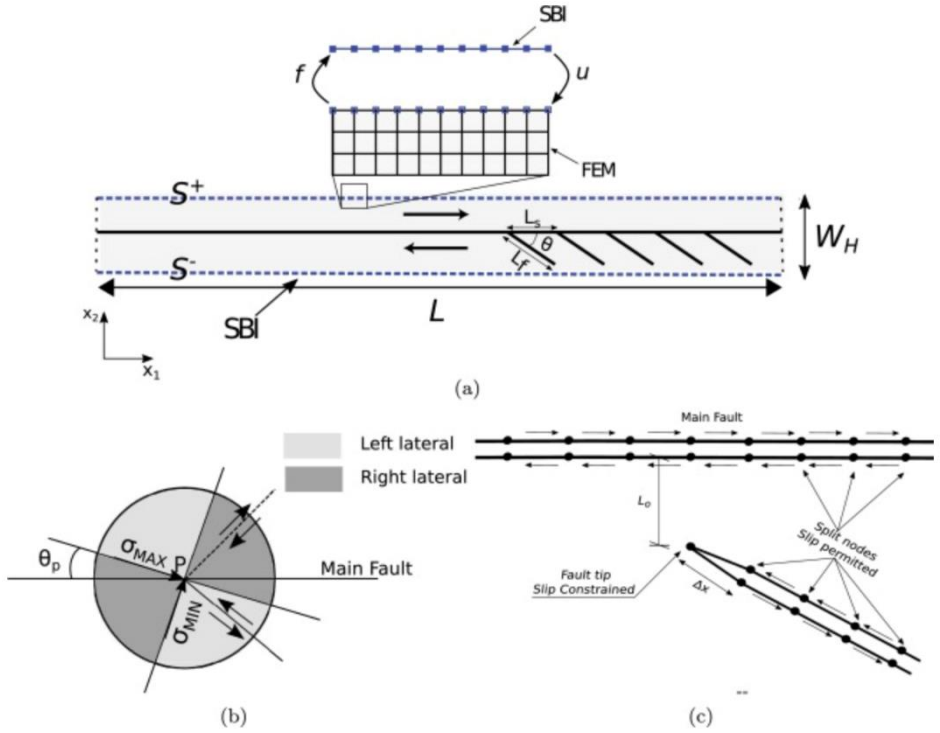

Figure 79. Model setup. a) Schematic of the complex fault zone structure considered in this report. The main fault lies horizontally in the middle of the domain, and the secondary fault branches are located in a limited region on one side of the fault (tension side). Following Poliakov et al. (2002), we call this setup a fish bone structure. All secondary faults are contained in a narrow, virtual strip of dimensions L × W that is discretized using the Finite Element Method (FEM). On the upper and lower edges, S^+ and S^-, the FEM is coupled with the Spectral Boundary Integral Equation, which models the exterior homogeneous elastic half-spaces. Tractions and displacements are consistently exchanged between the two methods at the shared nodes. The details of the coupling are outlined in the text. σ_{max} and σ_{min} represent the maximum and minimum principal stresses, respectively. θ_p is the angle between the maximum principal stress and the main fault parallel direction. L_s is the spacing between the secondary faults. θ is the angle between the secondary fault and the main fault. L_f is the secondary fault length. b) The orientation of the principal stresses for the assumed background stress state. The maximum principal stress makes an angle θ_p = 19.33° clockwise with the main fault. Also shown is the sense of motion for the secondary faulting consistent with this state of stress. Faults oriented in the dark grey quadrants have a right lateral shear, while those oriented in the light grey quadrants have left lateral shear. For the faults considered here, the main fault is right lateral, while the branches are left lateral. c) Sketch of the discretization for the main and secondary faults using split nodes. Arrows represent the sense of shear. The secondary fault is shifted L_o away from the main fault. The slip is constrained to be zero at the tips of the secondary fault.

Methodology

We used a highly efficient novel hybrid finite element-spectral boundary integral equation scheme to investigate the dynamics of fault zones with small-scale, pre-existing branches as a first step toward explicit representation of anisotropic damage features in fault zones. The hybrid computational scheme enabled exact near-field truncation of the elasto-dynamic field, allowing us to use high-resolution finite element discretization in a narrow region surrounding the fault zone that encompasses the small-scale branches while remaining computationally efficient. The details of the computational algorithm are outlined in Ma et al. (2018) and Ma and Elbanna (2019).

Results

Effect of short branches on rupture characteristics

Figure 80 shows the slip, slip rate, and post-rupture normal and shear stress distributions on the main fault with and without short branches. The fault with branches resembles a fish bone; thus, we will refer to it as a fish bone system. As expected, the presence of the short branches delayed the rupture propagation on the main fault and lead to accumulation of less slip at the same period of time. This is explained by the fact that the slip on the secondary branches increased the frictional dissipation and lead to slowing down of the rupture. Furthermore, the presence of these branches lead to fluctuations in the slip rate profile behind the rupture tip, a feature that was not observed in the case of rupture propagating on a fault in a homogeneous medium. Moreover, there was significant heterogeneity in the fault normal and shear stress in the case of the fish bone system. While the final normal and shear stress distributions, behind the rupture tip, on the fault surface in the homogeneous medium were uniform, the distributions in the case of the fish bone were heterogeneous since the slip on each branch produced a force dipole on the main surface, leading to strong, localized perturbations in the normal and shear stress. These perturbations could potentially grow, leading to fault-opening or slip in an opposite direction to the overall sense of shear in the domain.

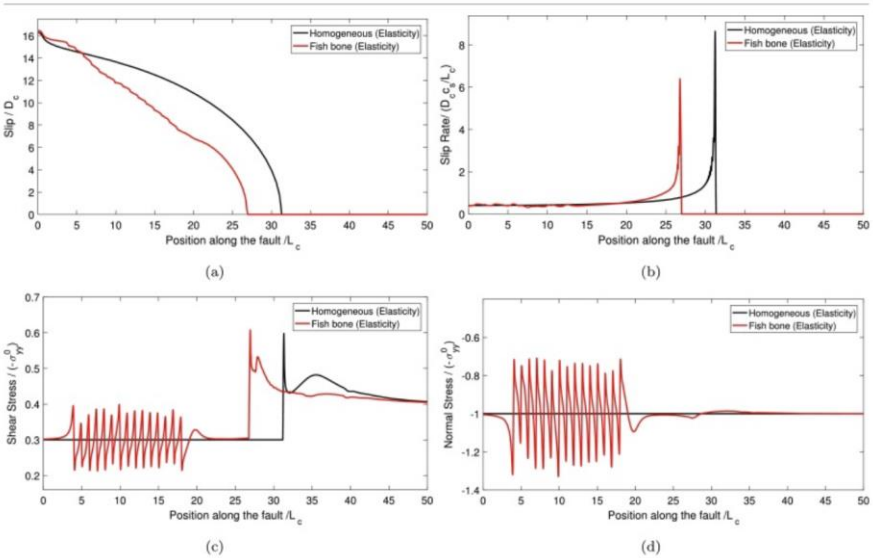

Figure 80. Slip, slip rate, shear stress, and normal stress distributions on the main fault, at the same point in time, with and without secondary fault branches for the elastic material case. a) Slip, b) slip rate, c) shear stress distribution, and d) normal stress distribution. Overall, the fish bone system shows significant post-event stress heterogeneities as well as reduced slip, maximum slip rate, and rupture speed.

The influence of secondary branches on the high-frequency generation in the bulk

Figure 81 shows the near-field particle velocity for both cases with and without the secondary branches. For the homogeneous medium, the wave field is smooth almost everywhere, with a concentration of high frequencies near the rupture tips. On the other hand, for the medium with branches, we observe coherent wave fronts that are propagating away from the tips and spaced apart periodically, consistent with the periodic distribution of the secondary branches. These coherent fronts are generated due to the constructive interference of seismic radiation from the secondary faults. The acceleration spectrum plotted in Figure 82 further proves this point. The fault with small branches has a spectrum that is richer in high-frequency content and shows an almost flat spectrum in the frequency range of 2-20 Hz. This is consistent with observations in Chen (1995) and Wald and Heaton (1994) and similar to the results from dynamic rupture simulation on rough faults in Dunham et al. (2011b). This suggests that small-scale fault branches may explain near-field radiation characteristics of active faults.

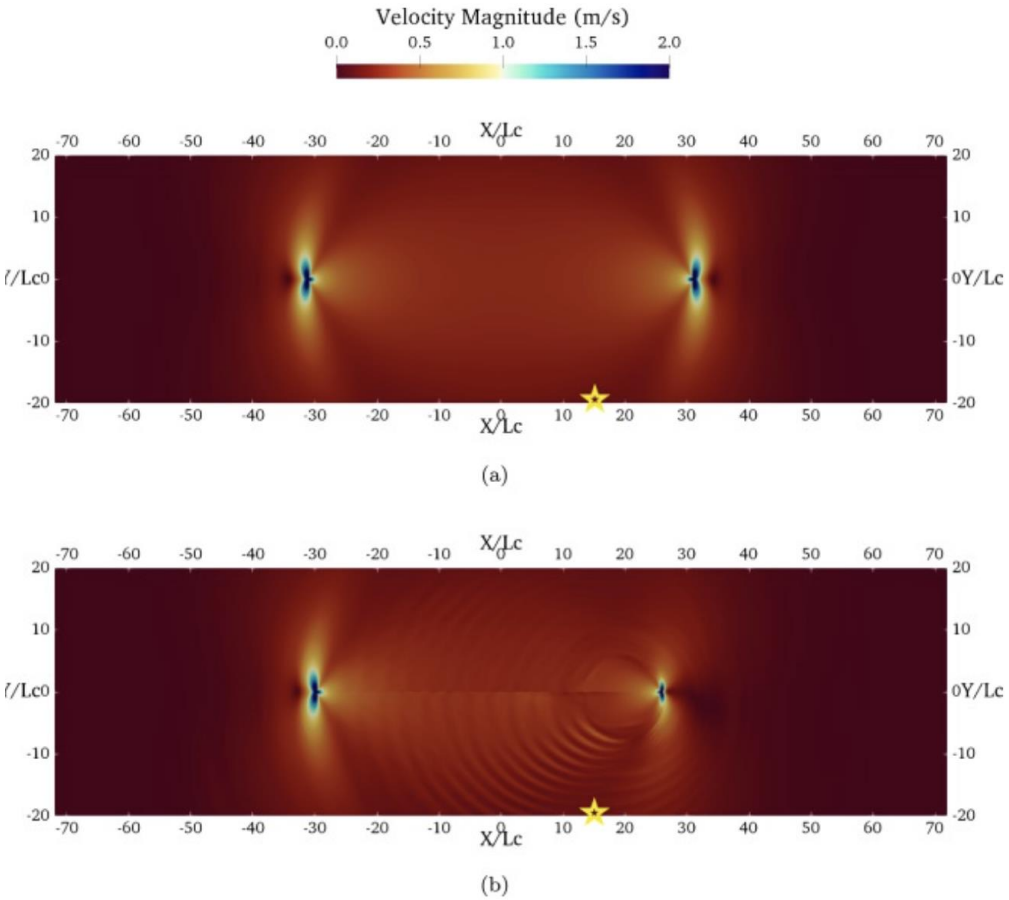

Figure 81. Contours of the bulk velocity field. a) Homogeneous medium. b) Domain with fish bone structure. Coherent high-frequency generation emerges in the case of the fault with secondary branches (fish bone structure) and propagates away from the fault plane as concentric fringes. These high-frequency waves are generated as a result of the constructive interference between the waves emitted by the secondary branches. In the homogeneous case, the high-frequency wave field is localized near the rupture fronts.

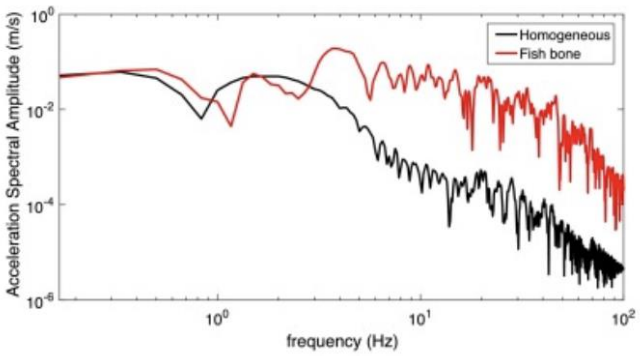

Figure 82. Fault-normal acceleration spectral amplitude at station $x^* = 15L_c$ and $y^* = -20L_c$.

Effect of branch length

Figure 83 shows the distribution of maximum slip on the secondary faults for different secondary fault lengths. The results suggest that as the secondary fault length increases, a crack shielding effect emerges. The slip distribution along the secondary faults is non-uniform in the sense that as one secondary fault accumulates large slip, the following one or two accumulates smaller slip; then comes another secondary fault with large slip, and the pattern continues. The non-uniformity in slip, which increases as the secondary fault length increases, leads to non-monotonicity in the stress peaks on the main fault with some peaks smaller than others. This crack shielding-like phenomenon (also referred to as stress shadowing phenomenon) has been observed in the experimental work by Ngo et al. (2012) for tensile cracks, numerical simulation results using finite-discrete element method by Klinger et al. (2018), and other studies modeling spontaneous crack branching (Ando and Yamashita, 2007) and off-fault plasticity (Templeton and Rice, 2008).

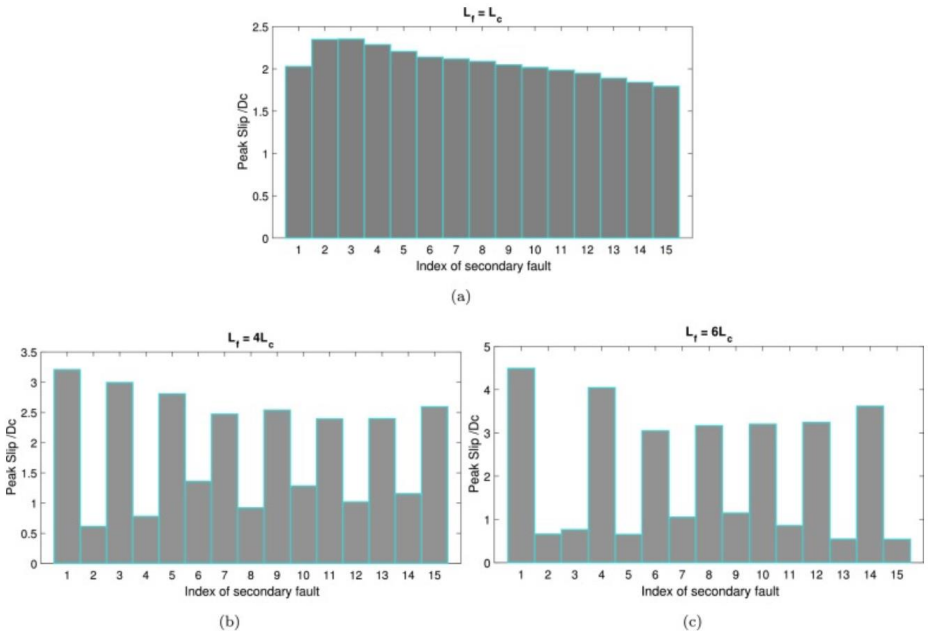

Figure 83. Peak slip distribution on the secondary faults with different lengths $L_f = L_c$, $L_f = 4L_c$, and $L_f = 6L_c$. The crack shielding effect is more significant in the presence of longer secondary faults.

Effect of spacing between the branches

Figure 84 shows a snapshot of slip, slip rate, shear stress, and normal stress distribution on the main fault at a given instant of time for three cases of secondary fault spacing. As shown in Figure 84c and d, as the spacing between the secondary faults increases, the amplitude of perturbations in the shear and normal stresses on the main fault increases, since each secondary fault accumulates more slip on average than in the case of smaller spacing. With smaller spacing between the secondary faults, the secondary faults are more effective in decelerating the rupture on the main fault. The insert in Figure 84b shows that with the increased spacing, the oscillations in the slip rate are spaced at a larger distance, but their amplitude increases.

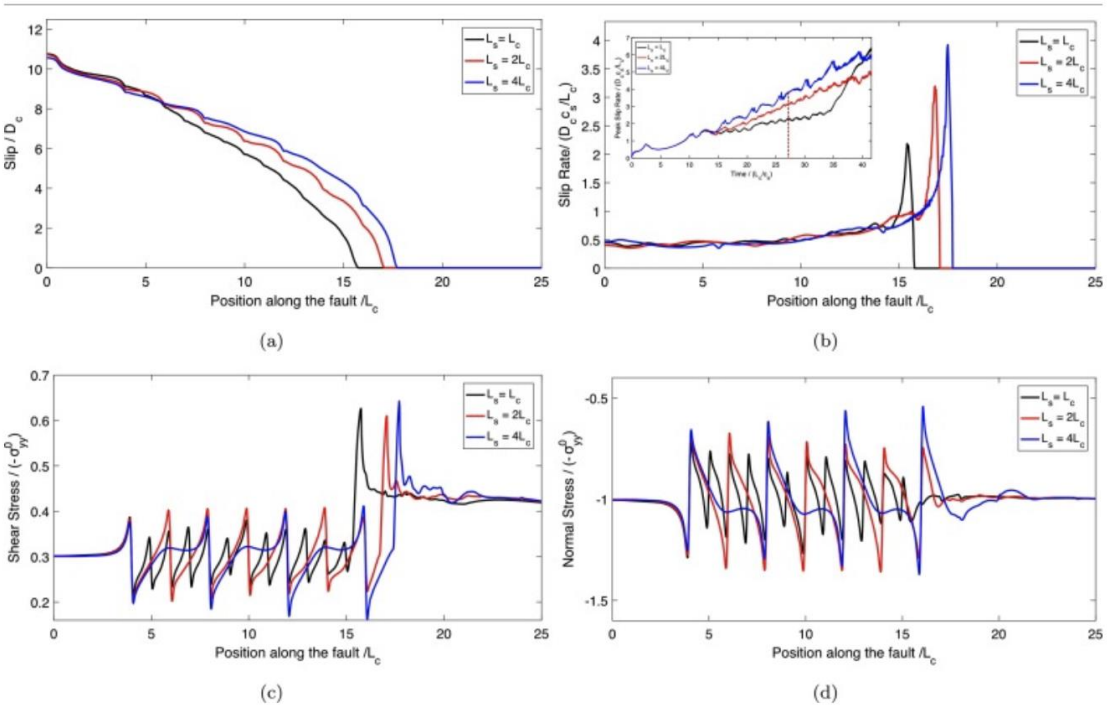

Figure 84. Slip, slip rate, shear stress, and normal stress distributions on the main fault, at the same point in time, with different spacing between the secondary faults $L_s = L_c$, $2L_c$, $4L_c$ for the elastic material case. a) Slip, b) slip rate, c) shear stress distribution, and d) normal stress distribution. Larger spacing between secondary faults promotes stronger perturbations in the stress and slip rate on the main fault.

Effect of branch orientation

While the angle that a secondary fault makes with the main fault is arbitrary, we explored different secondary fault orientations that varied around the direction of optimally oriented shear plane, computed using the background tectonic stress field and a Mohr-Coulomb failure criterion.

For the parameters used in this study, the direction of optimally oriented shear plane made approximately a 50° angle clockwise with the direction of the main fault. Accordingly, we considered four cases of orientation of the branching faults, 50°, 60°, and 70°, in addition to the default case discussed above. By investigating the slip evolution on the main fault (Figure 85), we found that the main fault rupture transitioned into supershear mode when the branch angles were 50° and 60°, while it remained subshear in all the other cases (30°, 40°, and 70°). The resulting slip distribution across the secondary faults for the different branch angles are given by the histograms in Figure 86. The average slip on the

secondary faults increased as the branch angle moved toward the optimal orientation (i.e., from 30° to 40°), which was consistent with the increase in the amplitude of stress perturbations on the main fault. Surprisingly, the average slip on the secondary faults was lower at 50° (the optimal orientation, according to the background stress state) and 60°. The reduction in slip on the secondary faults in these cases, despite favorable orientation, was hypothesized to be due to the supershear transition on the main fault which led to 1) the amplification of slip on the main fault and 2) rapid exit of the main fault rupture tip from the fish bone region, reducing the exposure time of the secondary faults to the impulsive dynamic loading from the main fault rupture tip. This was accompanied by a reduction in the amplitude of stress perturbations on the main fault compared to the case of 40°. Finally, as the branch angle further increased (e.g., 70°), the resolved shear stress started to decrease, while the resolved normal stress continued to increase, making it difficult to trigger slip on the secondary branches. Indeed, the case for 70° had much smaller average slip value (almost an order of magnitude less) than all the other cases. As a result, the stress perturbations on the main fault in this case were also the smallest.

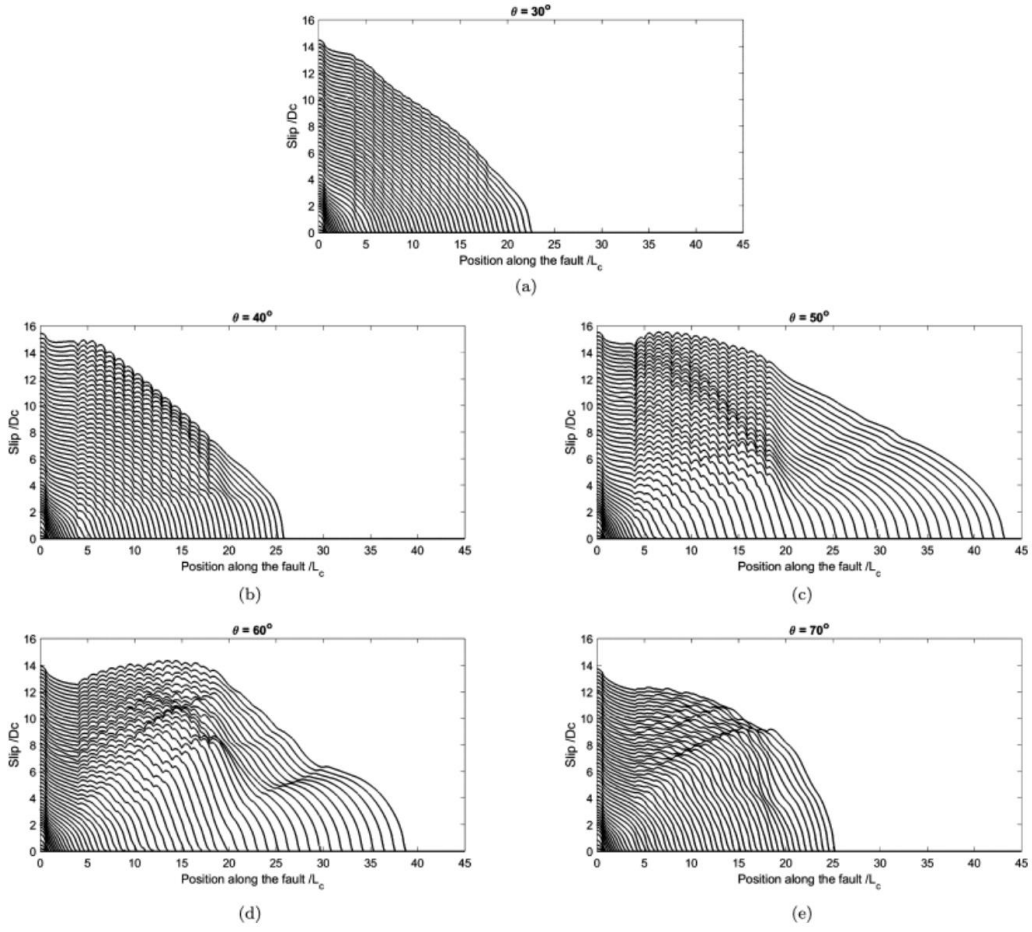

Figure 85. Slip line plotted every 0.1 s up to t = 6 s on the main fault with secondary faults of different angles ϑ = 30°, 40°, 50°, 60°, 70°. Note that the rupture has traversed a much longer distance for cases ϑ = 50° and 60° than the other cases, suggesting that a supershear transition has occurred. The rupture speed in the case with secondary faults ϑ = 50° was found to be 0.92c_p.

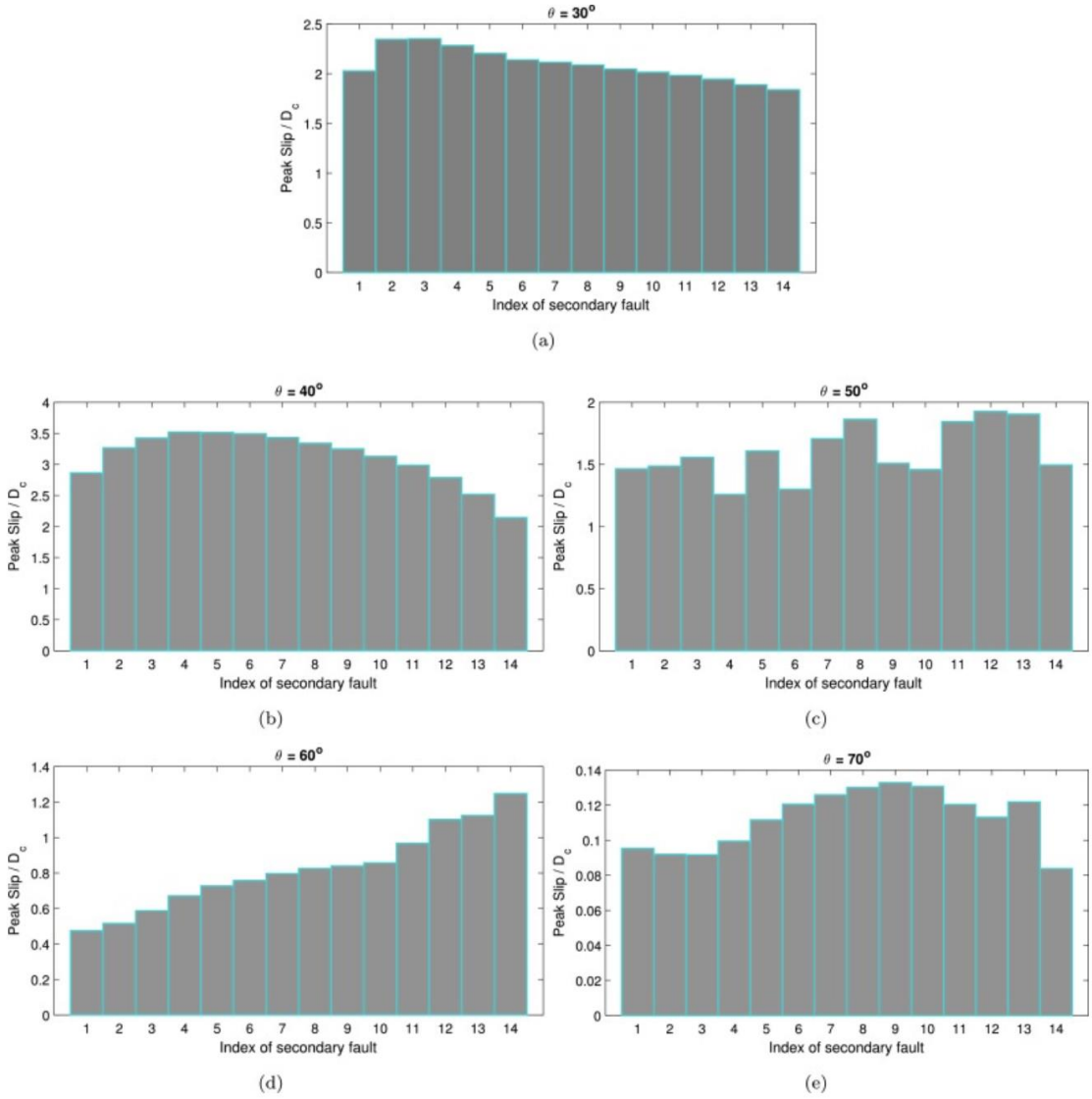

Figure 86. Peak slip distribution on the secondary faults with different angles ϑ = 30°, 40°, 50°, 60°, 70°.

Conclusions

Fault zone complexity is a dominant factor in controlling slip and stress distributions on primary fault surfaces. Small-scale branches or small-scale variations in the orientation of the fault strike may lead to significant stress heterogeneity and complex rupture dynamics and enhance high-frequency radiation that may affect infrastructure. In injection projects, the presence of small-scale geometric complexities, such as branches and non-planar fault geometry, may bring segments of the fault closer to failure than what the average strike of a planar fault may suggest. Accordingly, it is imperative to enrich models of induced seismicity with fault zone heterogeneities, including rheological heterogeneities and structural complexities.

CONCEPTUAL MODEL FOR SEISMICITY

Modeling Sequence of Earthquake and Aseismic Slip (SEAS), including injection-induced pore pressure perturbation, plays a key role in understanding the spatio-temporal evolution of induced seismicity. We conducted case studies through numerical simulation to investigate how long-term pattern of seismicity could be influenced by several factors associated with fluid injection and fault friction. These factors included injection location with respect to fault rheology, background tectonic loading, injection pressure magnitude, permeability evolution, and off-fault inelastic response.

Hypothesis

Fault response is governed by friction law, which relates the tangential component of stress (fault strength) with the normal stress acting on the fault. Fluid injection increases the pore pressure, which results in a reduction in effective normal stress acting on the fault. Therefore, injection pressure and its spatio-temporal diffusion lead to heterogeneous distribution of effective normal stress. The reduced heterogeneous effective normal stress makes the fault susceptible to slip and results in different patterns with respect to number of seismic events, inter-seismic timing, presence of slow slip, and aperiodic cycles with or without spatio-temporal clustering. We hypothesized that the seismicity pattern is controlled not only by the injection protocol but also by the fault and bulk properties.

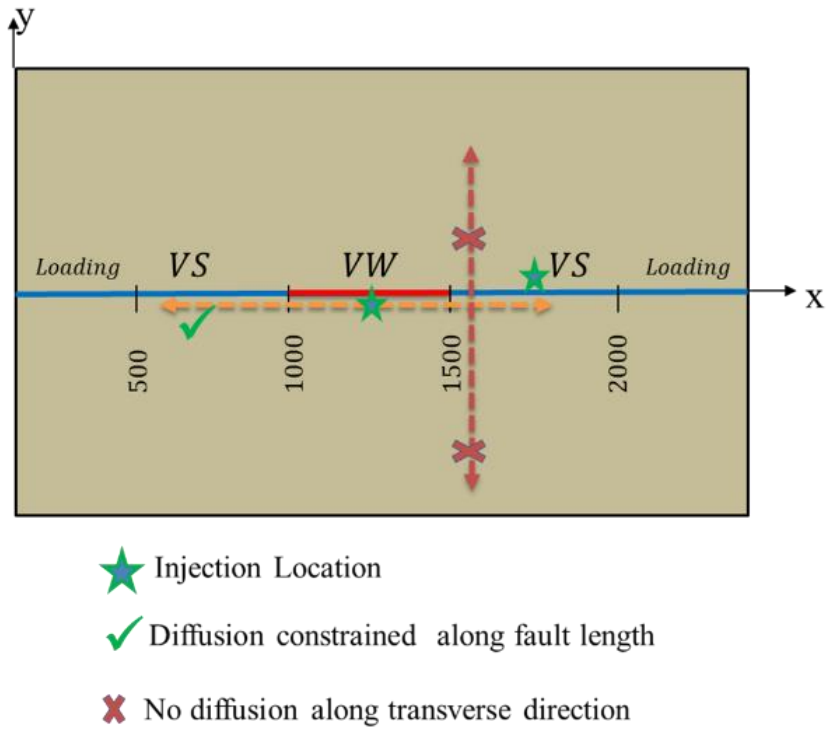

Figure 87. Model set-up for simulating sequence of injection-induced earthquakes and aseismic slip.

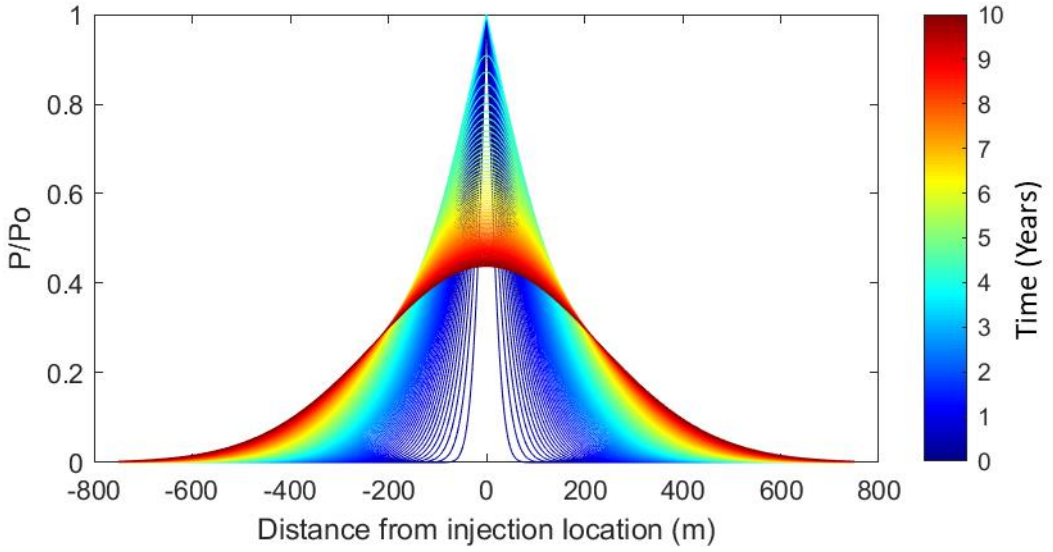

Figure 88. One-dimensional diffusion of pore pressure. Constant injection pressure is maintained at the injection location, and it follows free diffusion after injection shut-off.

Model Set-up

The model geometry is shown in Figure 87. We considered a 2D anti-plane rate-and-state fault having a velocity-weakening (VW) and velocity strengthening (VS) patch. The off-fault material is considered homogeneous linear elastic unless mentioned otherwise. Injection is assumed to happen directly in the fault core. Pressure diffusion is allowed only along the fault, which assumes higher permeability along the fault. Evolution of pore pressure for one-dimensional diffusion is shown in Figure 88. We also model a separate case, with uniform pore pressure perturbation, considering almost impermeable fault core and off-fault plasticity, presented at the end of this section.

Methodology

The simulation of SEAS is carried out using a hybrid finite-element spectral boundary integral scheme. An alternating quasi-dynamic and dynamic solver is used to account full inertia effect during rapid seismic rupture and approximating inertia through radiation damping during aseismic slow deformation (Abdelmeguid et al., 2019; Mia et al., 2022).

Results

Role of injection location

As shown in the model geometry, the fault has a central VW patch and VS patch on both sides. We simulated two cases: injection within VW and injection within VS. In both cases, the injection pressure was 20% of the background normal stress, and the background tectonic plate rate was 35 mm/year. Usually, the VW patch remained locked during the aseismic phase and got destabilized occasionally with seismic rupture. On the other hand, the VS patch slowly crept, following the background tectonic loading. Before starts of injection, the seismic cycle was found periodic. In both cases, the periodic pattern was broken due to injection. As shown in Figure 89, injection started at 20 years and ended at 24 years. During this interval, one seismic event was supposed to happen if there was no injection. For injection within the VW, there was one additional event during the injection. The nucleation site for the first event during

injection was shifted toward the injection location (Figure 89). For the case of injection within the VS, there was no additional seismic event during injection. However, the event timing was changed through seismic events happening earlier than expected. The seismicity pattern was influenced by accelerated aseismic slip near the injection location (Figure 90).

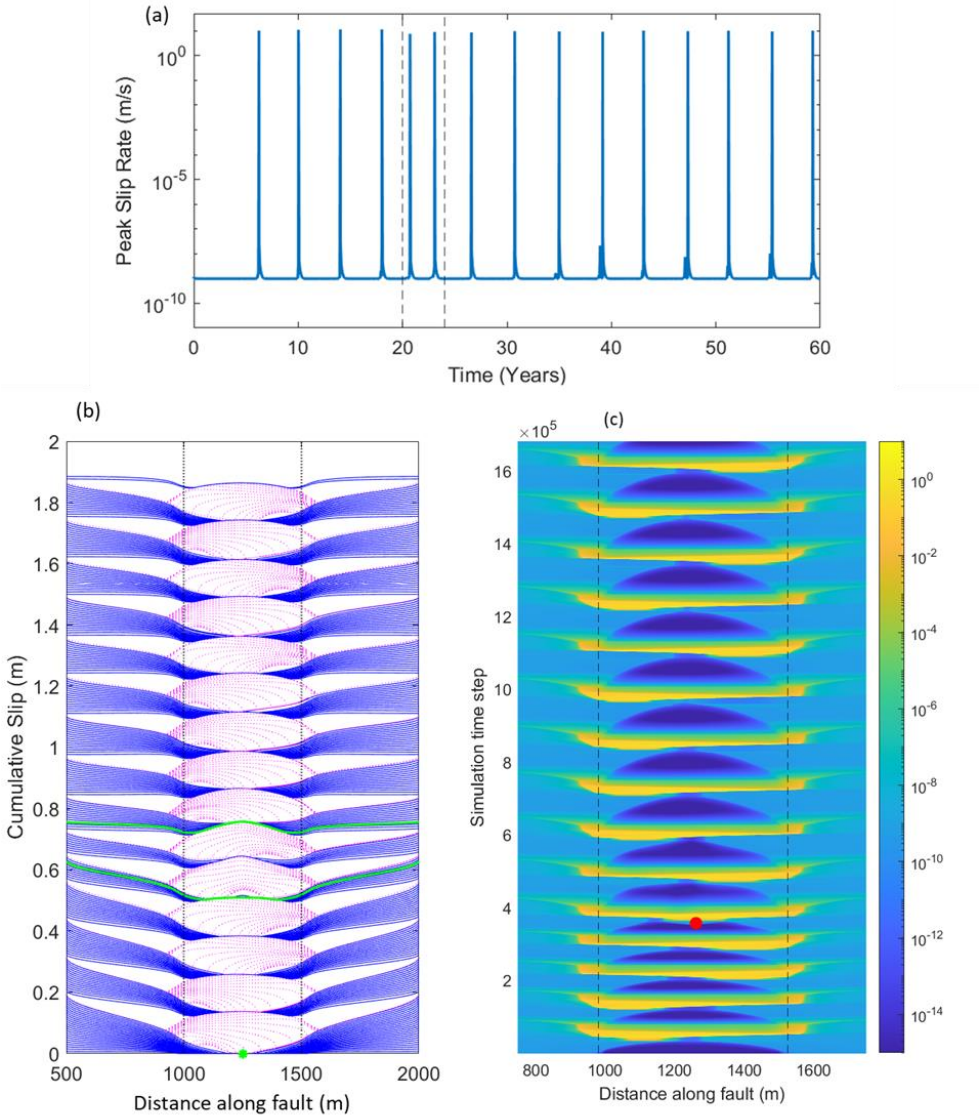

Figure 89. Injection within the velocity-weakening (VW) patch. a) Peak slip rate history shows the break in the pre-injection periodic pattern through reduced interevent time during injection. Vertical dashed lines at 20 and 24 years indicate the duration of injection. b) Cumulative slip plot shows additional events during injection. The region between vertical dotted lines indicates the VW patch. Green dot indicates the injection location at the center of the VW patch. Solid blue lines are plotted at an interval of three months during aseismic slip, and dotted magenta lines are plotted at every ~20 milliseconds during dynamic rupture when peak slip rate is above 0.01 m/s. Green slip lines correspond to the beginning and end of injection. c) Spatial evolution of slip rate is shown with respect to the simulation time step. The VW patch remains locked during aseismic phase and slides with higher slip rate during seismic rupture. Red dot indicates the nucleation site shifts to the injection location.

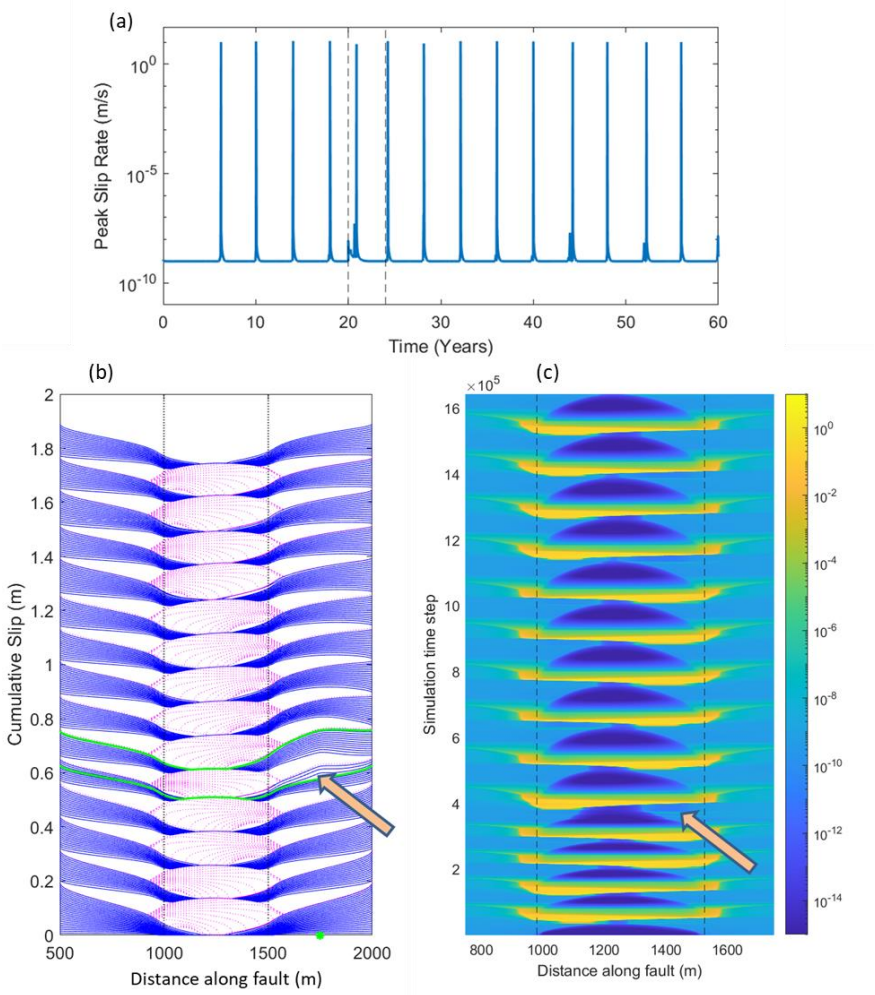

Figure 90. Injection within the velocity-strengthening (VS) patch. a) Peak slip rate history. Vertical dashed lines at 20 and 24 years indicate the duration of injection. b) Cumulative slip plot shows accelerated aseismic slip due to injection as indicated by the arrow. The region between vertical dotted lines indicates the VW patch. Green dot indicates the injection location is at the center of the VS patch. Solid blue lines are plotted at an interval of three months during aseismic slip, and dotted magenta lines are plotted at every ~20 milliseconds during dynamic rupture when peak slip rate is above 0.01 m/s. Green slip lines correspond to the beginning and end of injection. c) Spatial evolution of slip rate is shown with respect to the simulation time step. Accelerated aseismic slip appears as higher slip rate (indicated by the arrow) than the background plate rate (35 mm/year).

Role of background tectonic loading

To investigate the effect of injection in a region where seismicity is less frequently observed, background tectonic loading was chosen one order of magnitude lower. Here the background plate rate was 3.5 mm/year, as opposed to the previous cases where it was 35 mm/year. This lower plate rate generated periodic seismic cycles with an inter-event time of around 50 years. The peak slip rate history for no injection showed that this low plate loading rate value was not supposed to generate seismic events from 200-250 years. When injection was made for four years starting at 220 years and ending at 224 years, a seismic event was observed during the injection (Figure 91). Also, after the injection shut-off, temporal clustering of seismic events was found with inter-event time in order of months. In the later phases, the cycle tended to restore the original pre-injection pattern. The seismic pattern, including post-seismic complexity, is shown in Figures 92 and 93 through cumulative slip plot and spatio-temporal evolution of

slip rate, respectively. Segmentation in the spatio-temporal evolution of slip rate indicates the seismic complexity in terms of rupture arrest and multiple events.

In this background tectonic plate rate, injection within the VS patch (Figure 94) also generated a seismic event during injection. Before the seismic event, the fault slip rate history showed the signature of a slow-slip event, as indicated by the peak slip rate reaching around $10^{-6}\frac{m}{s}$, which is three orders of magnitude higher than the background tectonic plate rate. To understand how injection within the VS patch contributed to generating a seismic event during injection, we plotted the history of slip accumulation for chosen points near the injection location. As shown in Figure 95, slip accumulation accelerated once the injection started, and it continued to accumulate aseismic slip through an injection-induced slow-slip event. Near the end of the injection, the slip accumulation became steeper due to the seismic event.

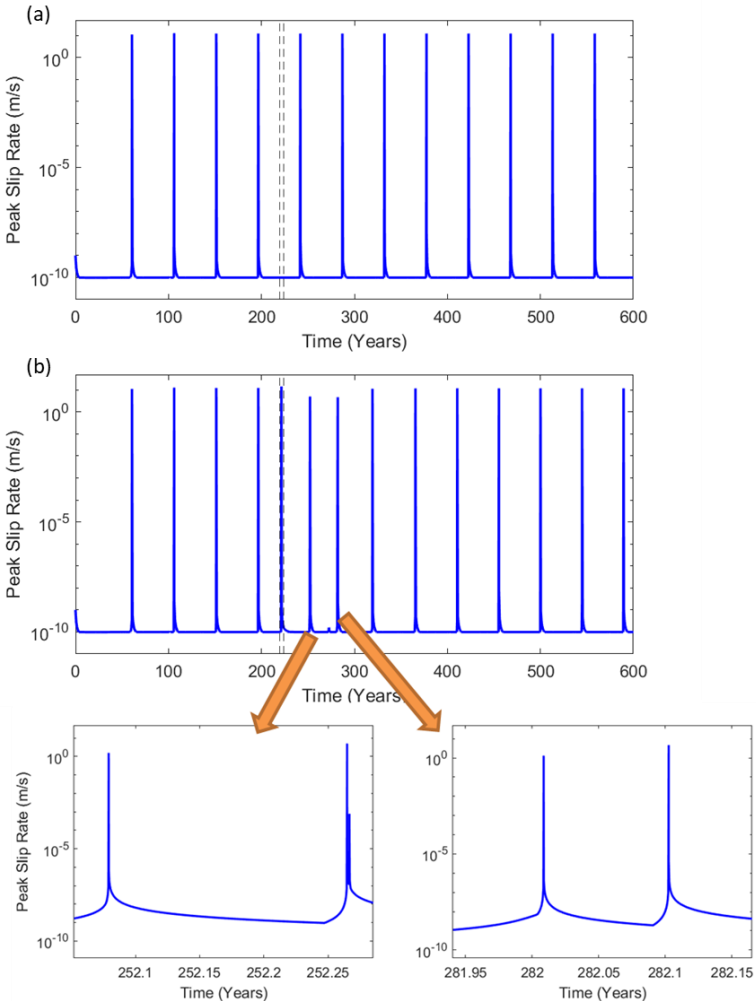

Figure 91. Peak slip rate history for injection within the VW patch and background plate rate of 3.5 mm/year. a) No-injection case showing periodic pattern of seismicity with inter-event time ~ 50 years. b) Injection within the VW patch with a duration of four years marked by vertical dashed lines. Injection pressure is 20% of the background normal stress. Pre-injection periodicity is broken through seismic events during injection. Post-injection temporal clustering of events is observed with seismic events within months.

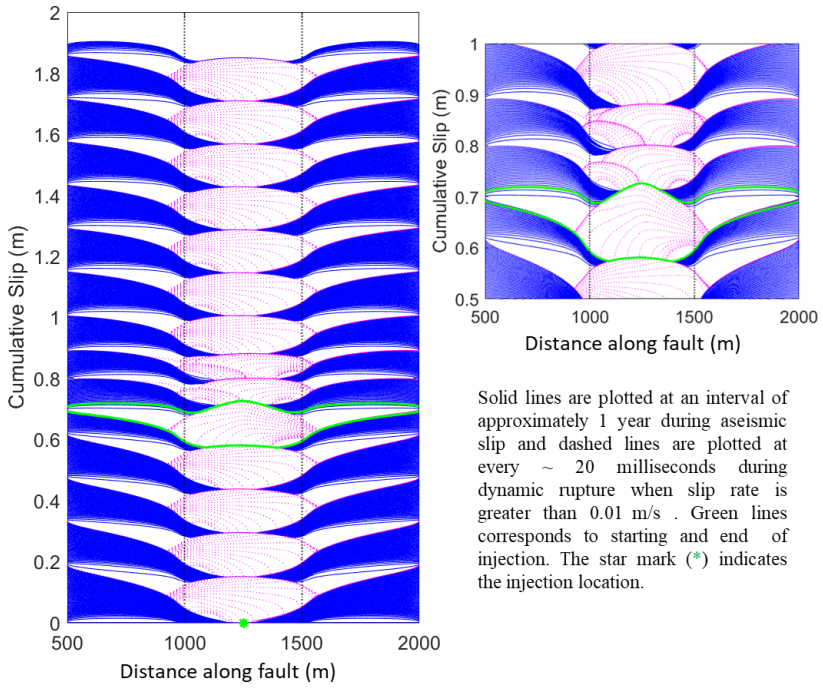

Figure 92. Cumulative slip plot for background plate rate of 3.5 mm/yr. Seismic event occurs during injection (between the green lines). Post-seismic complexity with rupture arrest and multiple events is shown in the zoomed-in view.

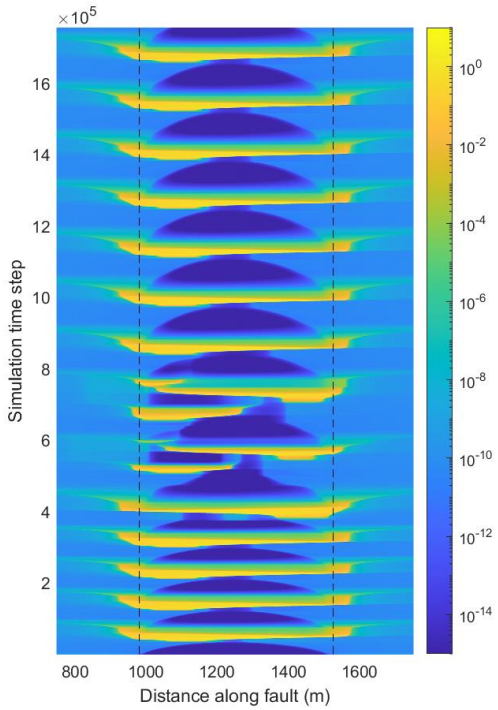

Figure 93. Spatio-temporal evolution of slip rate for background plate rate of 3.5 mm/year. Injection pressure is 20% of the background normal stress. Injection is made within the VW patch. Segmentation in the slip rate contour indicates the post-injection seismic clustering.

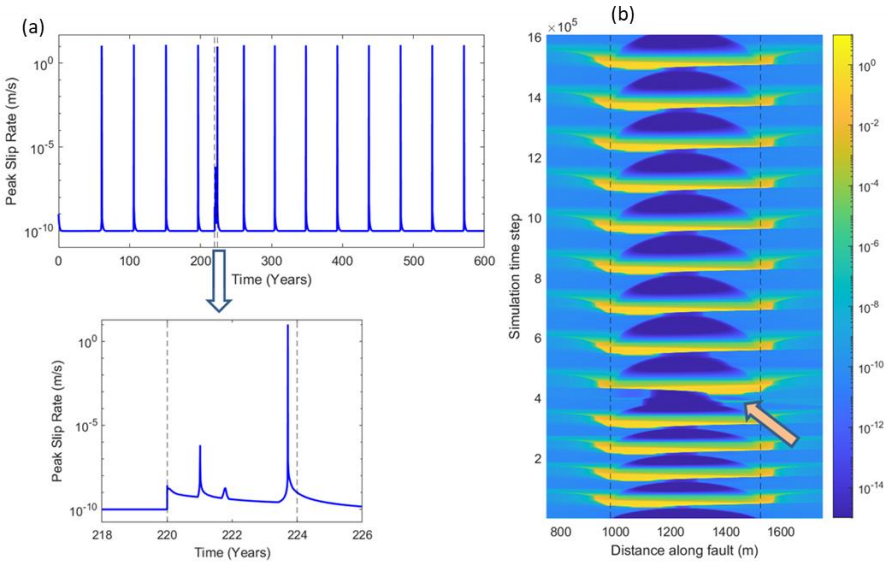

Figure 94. Injection within the VS patch for background plate rate of 3.5 mm/year. Injection pressure is 20% of the background normal stress. a) Peak slip rate history shows seismic event during injection; b) Spatio-temporal evolution of slip rate, indicating signature of slow slip event before the seismic event during injection.

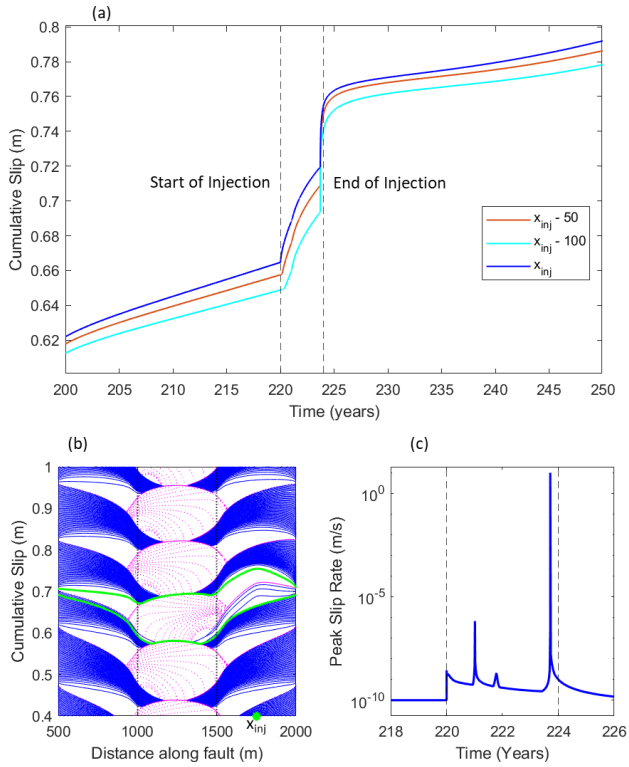

Figure 95. Accelerated aseismic slip due to injection into the VS patch with plate rate of 3.5 mm/year. Injection pressure is 20% of the background normal stress. a) History of slip accumulation at different points near the injection location. b) Zoomed-in view of cumulative slip, where injection location is indicated by x_{inj}. Solid blue lines are plotted at an interval of approximately one year during aseismic slip, and dotted magenta lines are plotted at every ~20 milliseconds during dynamic rupture when peak slip rate is above 0.01 m/s. Green slip lines correspond to the beginning and end of injection. Increased spacing between the cumulative slip lines during injection indicates

accelerated aseismic slip due to injection. c) Peak slip rate history during injection, showing a slow slip event and a seismic event.

Role of injection pressure magnitude

We modeled three different injection pressures (P) as a percentage of initial normal stress (σ_n) acting on the fault: $P = 0.02\ \sigma_n$; $P = 0.1\ \sigma_n$; $P = 0.2\ \sigma_n$. The shape of the slip lines for $P = 0.2\ \sigma_n$ in Figure 96 indicates the rupture was driven by the fluid pressure, and the nucleation site for the first seismic event during injection was near the injection location. The lower pressure cases did not show this feature. We observed that higher injection pressure leads to increased number of seismic events during injection both for a background plate rate of 35 mm/year (Figures 96-97) and 3.5 mm/year (Figures 98-99).

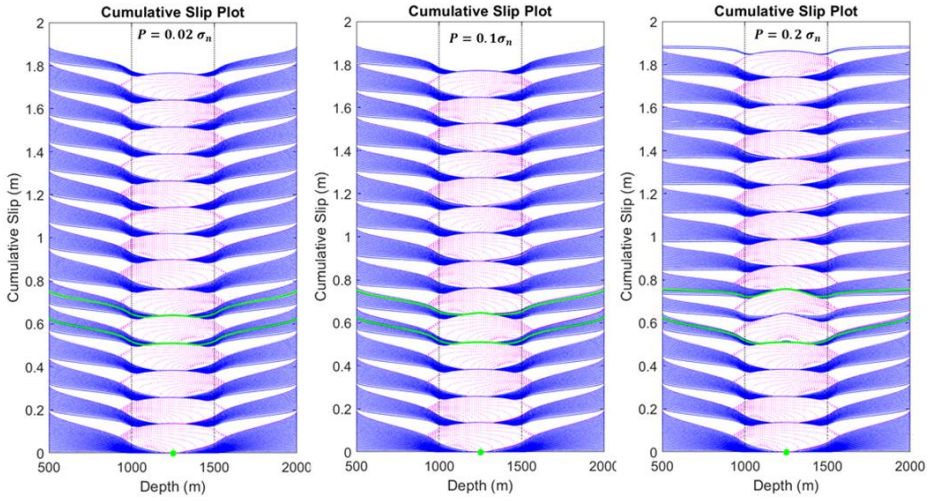

Figure 96. Effect of injection pressure. Cumulative slip plot for three different injection pressures: $P = 0.02\ \sigma_n$, $P = 0.1\ \sigma_n, and\ \ P = 0.2\ \sigma_n$. Solid blue lines are plotted at an interval of three months during aseismic slip, and dotted magenta lines are plotted at every ~20 milliseconds during dynamic rupture when the peak slip rate is above 0.01 m/s. Fluid is injected at the center of the fault, indicated by the green dot. The green lines mark the slip lines at the beginning and end of injection. Additional seismic event is observed during injection for higher injection pressure.

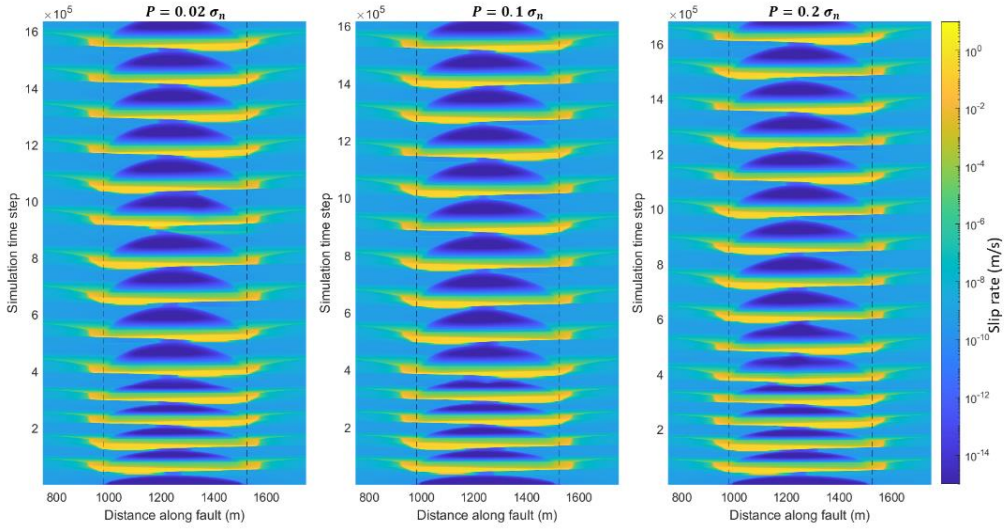

Figure 97. Effect of injection pressure. Spatio-temporal evolution of slip rate for different injection pressures.

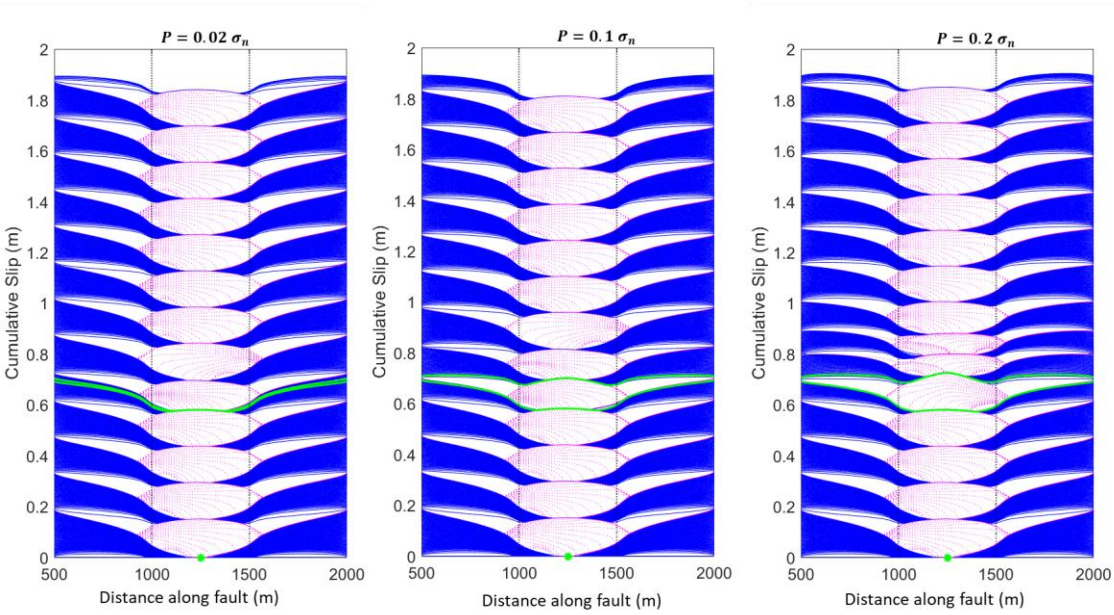

Figure 98. Effect of injection pressure for a tectonic loading rate of 3.5 mm/year. Cumulative slip plot for three different injection pressures: $P = 0.02\ \sigma_n$, $P = 0.1\ \sigma_n, and\ \ P = 0.2\ \sigma_n$. Solid blue lines are plotted at an interval of one year during aseismic slip, and dotted magenta lines are plotted at every ~ 20 milliseconds during dynamic rupture when peak slip rate is above 0.01 m/s. Fluid is injected at the center of the fault, indicated by the green dot. The green lines mark the slip lines at the beginning and end of injection. Additional seismic event is observed during injection for higher injection pressure.

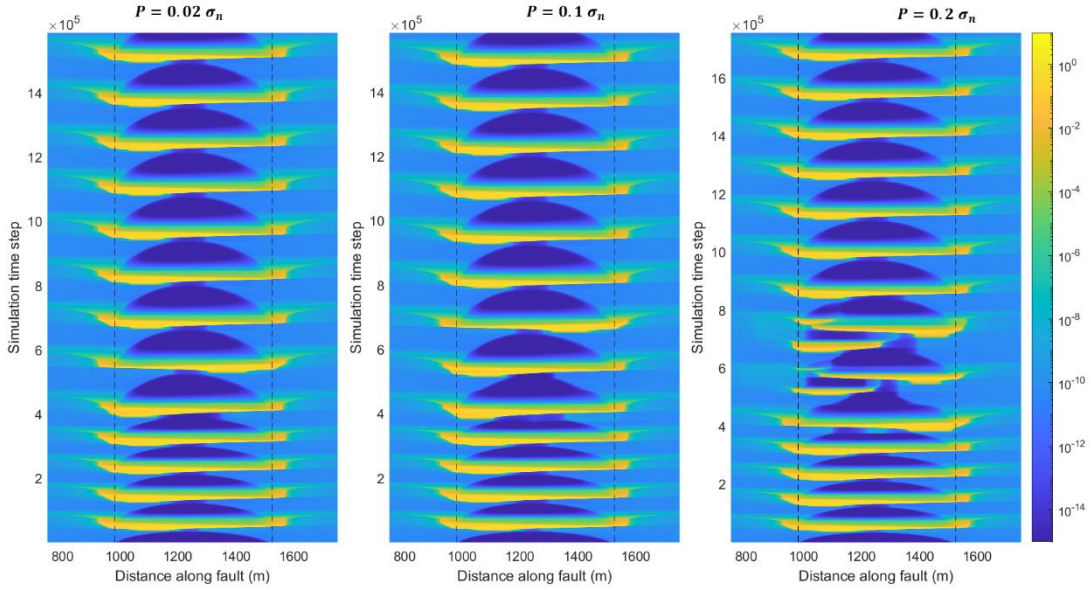

Figure 99. Effect of injection pressure for a tectonic loading rate of 3.5 mm/year. Spatio-temporal evolution of slip rate for different injection pressures: $P = 0.02\ \sigma_n$, $P = 0.1\ \sigma_n, and\ \ P = 0.2\ \sigma_n$. The lower injection pressure generates events that rupture the whole VW patch. The higher injection pressure shows post-injection seismic complexity, as indicated by the segmentation of slip rate contour for $P = 0.2\ \sigma_n$.

Role of permeability evolution

In the previous sections, we have considered constant permeability. However, permeability can evolve, depending on effective normal stress and, hence, pore pressure (Rice, 1992; Yang et al., 2021). The pressure sensitivity of permeability evolution influences the pore pressure diffusion, which in turn influences the seismic cycles. Figure 100 shows the peak slip history comparing the fixed permeability with the variable permeability case. It shows that in both cases, there was one additional event during injection compared to the case of no injection. The timing for seismic events was earlier with variable permeability than fixed permeability. The effect of variable permeability became more pronounced when the pressure sensitivity parameter (σ^*) was changed from 15 MPa to 5 MPa, as shown in Figure 101. The inter-event time for the no-injection case was almost constant after a few initial events. Variable permeability showed reduced inter-event time during injection. After injection shut-off, the cycle tended to regain the unform pre-injection state; however, this takes longer time to settle at periodic pattern compared to the no-permeability evolution case.

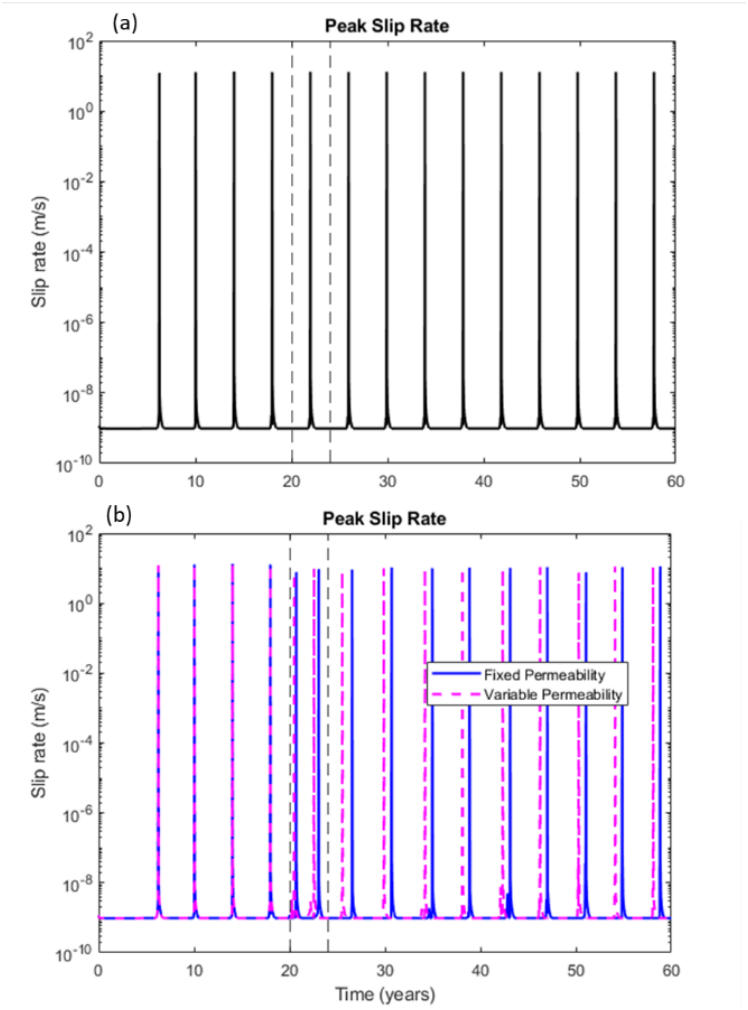

Figure 100. Comparison of seismic cycle for pressure-dependent permeability evolution with constant permeability.

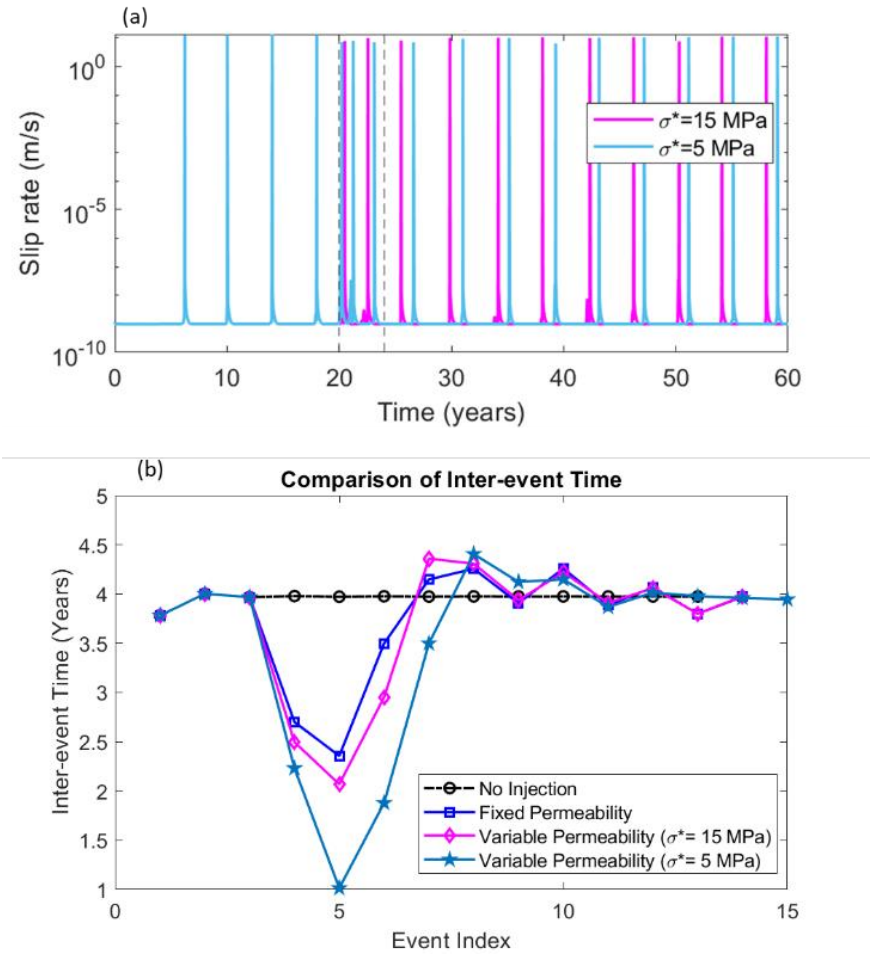

Figure 101. Comparison of inter-event time for variable and constant permeability. Variable permeability shows reduced inter-event time compared to constant permeability.

Role of fault core permeability and off-fault plasticity

Instead of along-fault pore pressure diffusion, there could be situations where pore pressure diffuses quicker in the bulk than the fault. Also, injection at a distant location can make the pressure front reach the fault region with almost uniform pressure. To simulate such a situation, we consider an impermeable fault core and allow the step change in pore pressure in the off-fault bulk, which allows the bulk effective normal stress to decrease. Since the off-fault bulk yield strength depends on the effective normal stress, yield strength decreases when pore pressure perturbation is introduced. In Figure 102, spatio-temporal evolution of slip rate is shown for a cycle simulation with off-fault plasticity. Periodic system spanning rupture is shown before the start of pore pressure perturbation, and spatio-temporal clustering of seismicity is observed after the pore pressure perturbation is applied. Pore pressure perturbation of 5 MPa (10% of normal stress) is introduced, which reduces the effective normal stress from 50 MPa to 45 MPa and corresponding yield strength reduces from 40 MPa to 37 MPa. It allows to move in the phase diagram shown in Figure 103 due to the change in yield strength. Depending on the bulk inelastic properties like yield strength and viscosity, the seismic cycle may attain periodic, complex, or intermediate quasi-complex pattern.

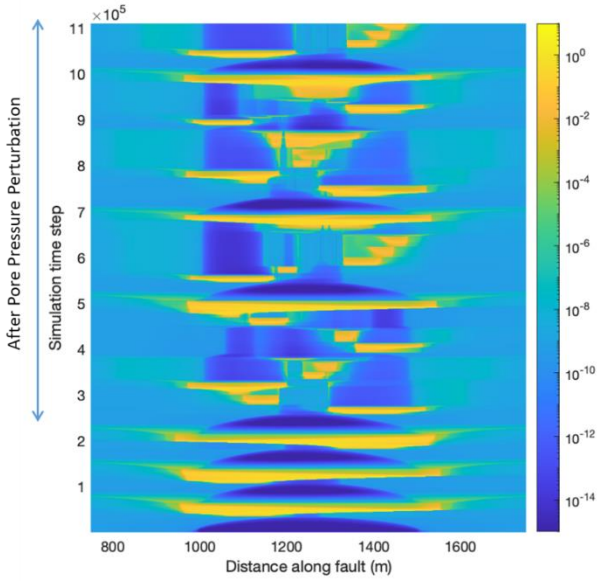

Figure 102. Effect of pore pressure perturbation for off-fault plasticity. Spatio-temporal evolution of slip rate shows system-spanning periodic events before pore pressure perturbation. Spatio-temporal clustering of seismicity is observed when pore pressure in the bulk increases.

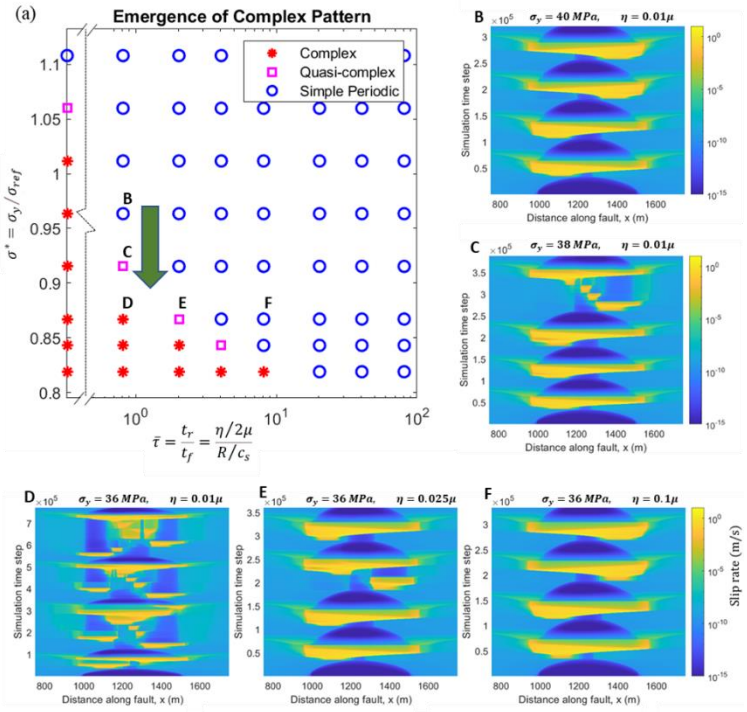

Figure 103. Emergence of complex seismic pattern depending on yield strength (σ_y) and viscosity (η). a) Summary of seismicity patterns generated by varying yield strength and viscosity. Yield strength (σ_y) is normalized by a reference stress, $\sigma_{ref} = \sigma_n[f_0 + a\ ln(V_{seismic}/V_p)] \approx 41.5\ MPa$, which is an estimation of peak stress for elastic case accounting direct effect in rate-and-state friction. Relaxation time is normalized by time-scale associated with frictional weakening within the process zone, $t_f = R/c_s = 0.0062\ s$. Complex patterns are found for lower yield

strength and lower range of viscosity. For a particular viscosity, a decrease in yield strength leads to transition from periodic to quasi-complex and complex pattern (as shown in B, C, and D). For a particular yield strength, a decrease in viscosity leads to the emergence of spatio-temporal clustering as shown in D, E, and F. Rate-independent plasticity also shows transition from periodic to complex pattern when yield strength is decreased.

Conclusion

Interplay between fault friction and several factors, including injection location with respect to fault rheology, background tectonic loading, injection pressure magnitude, permeability evolution, and off-fault inelastic response, contribute to the sequence of injection-induced earthquakes and aseismic slip. Injection within the VW patch can destabilize the locked fault and introduce seismic events. Injection within the VS patch accelerates the aseismic slip and influences the seismic cycle through slow-slip event or by changing the event timing. Higher injection pressure and variable permeability pronounced the effects through additional seismic events with reduced inter-event time. Off-fault inelastic material behavior also plays a role in changing the seismicity pattern from simple periodic to spatio-temporal clustering, depending on the increase in pore pressure and consequent reduction in yield strength.

SUMMARY OF TASK CONCLUSIONS

After comprehensive discussion of the major structural features in the ILB and their significance in comprehending the subsurface rock formation, as well as a thorough analysis of the orientation of maximum and minimum horizontal stress at the IBDP site, Task 2 developed a geocellular model for the IBDP site that was designed to establish the structural and stratigraphic framework of the area. The model was enhanced iteratively to improve the calibration to the IBDP data with the forward modeling results as designed in the proposed methodology (Figure 1). At various stages of development, the geocellular model served as a foundation for other tasks within the project by providing a comprehensive understanding of the subsurface geologic framework.

In Task 3, we designed and compared multiple deep learning (DL) models for the rapid recognition of faults based on microseismic waveform data. It was found that automated microseismic event detection using our convolutional neural network (CNN) model was improved by the augmentation of the data time series into a time-frequency domain and a proper normalization strategy for the input information. We also found that including physical properties, such as Mel-Frequency Cepstrum Coefficients (MFCCs) as an indicator for energy term of waveform, into the CNN model improved event detection. The increase in detected events and long-duration and long-period type events using the DL method suggested there were more microseismic events of interest unidentified in the IBDP repository. With phase estimates of newly detected events using PhaseNet, source locations were identified using another CNN model that was improved with data augmentation using the generative model (i.e., WGAN-GP). WGAN-GP was trained with full waveform data and location information, generating new synthetic data at locations different from the located events. Overall, these four DL models can be integrated to perform rapid fault identification.

In Task 4, we showed that pore pressure diffusion along pre-existing faults connecting the Lower Mt. Simon and the Precambrian crystalline basement is the main mechanism for the occurrence of induced seismicity associated with CO_2 injection at IBDP. For a fault zone thickness of 6 ft (1.88 m) and along-fault permeability of 1 Darcy, we found that pore pressure changes at faults can be as high as $\Delta p \approx$ 0.75 MPa in basement regions away from the injection well where microseismicity occurred.

We also found that poroelastic stresses alone tend to stabilize the basement faults, counteracting the destabilizing pore pressure effects and causing an overall decrease in the DCFF at the microseismicity locations. These results demonstrate the importance of pore pressure diffusion along faults connecting sedimentary sections and the crystalline basement as a mechanism for microseismicity occurrence at the IBDP site and in other geologically similar locations. Slip tendency analysis showed that fault strike variation relative to the maximum horizontal stress direction plays a major role on the proximity of faults to failure. Fault planes interpreted based on the microseismicity locations were found to be critically stressed and showed slip tendency ranging from $T_s \approx 0.55$ to ≈ 0.7 prior to injection.

In Task 5, we showed that fault zone complexity is a dominant factor in controlling slip and stress distributions on primary fault surfaces. Small-scale branches or small-scale variations in the orientation of the fault strike can lead to significant stress heterogeneity and complex rupture dynamics and enhance high-frequency radiation that affects infrastructure. In injection projects, the presence of small-scale geometric complexities, such as branches and non-planar fault geometry, can bring segments of the fault closer to failure than what the average strike of a planar fault suggests. Accordingly, it is imperative to enrich models of induced seismicity with fault zone heterogeneities, including rheological heterogeneities and structural complexities.

PROJECT CONCLUSIONS

Usage of the proposed methodology (Figure 1), the iterative development of the final geologic conceptual model represented by the final geocellular model as determined by calibrating three forward models' simulation results, identified faults/faults zones as the geologic features present that are most likely controlling microseismicity at IBDP.

Over 200 simulations of non-faulted variations of the geocellular model within the bounds of the geologic conceptual model (which is bound by core and log data, depositional environment, and established regional geology) resulted in no acceptable calibration to the IBDP pressure and saturation data of CCS1 an VW1. Only after this exhaustive, comprehensive, and methodical search for a calibration without faults/fault zones present in the geocellular model were faults introduced for the pressure modeling.

On the basis of an updated interpretation of the reprocessed 3D surface seismic survey (10 km^2or 3.9 square miles), 28 faults/fault zones are present at the IBDP site that originate deep into the Precambrian, pass through the Argenta, and extend upward into the lower part of the Mt. Simon. (These faults were interpreted based solely on offset of seismic reflectors which are indicative of revers, normal, and oblique faults) Two of the faults/faults zones were between CCS1 and VW1, and parts of three additional faults/fault zones were within < 500 ft of at least one of the two wells. At most 1-2 of these faults could be approximated to coincide with long axis of the elliptical shaped microseismic clusters. Consequently, the faults identified through surface seismic had no to minimal recorded and located seismic activity.

It is commonly accepted that the most likely source of injection induced seismicity is within fault and faults zones where rock surfaces are passing each other and releasing seismic energy. The area defined be individual microseismic clusters at IBDP had no faults interpreted from 3D seismic. So, at IBDP faults interpreted from 3D seismic had no induced seismicity, and faults with induced seismicity were not identifiable from 3D seismic. Therefore, the faults present within the seismic clusters are likely strike-slip faults.

Injection induced seismicity is a risk to developing a CO_2 storage project. If traditional approaches of identifying faults do not identify faults that are susceptible to injection induced seismicity, it will be challenging to adequately address injection induced seismicity before a CO_2 injection begins.

Consistency between all models' results highlighted the importance of representative subsurface characterization to understand the hydraulic and geomechanical factors that lead to induced seismicity associated with CO_2 injection and, more generally, other subsurface injection operations.

PROJECT RECOMMENDATIONS

After thorough review of regional geology, specifically of large structural features, faults with orientation similar to those identified at IBDP were found such that, a priori, faults could be assumed at IBDP with knowledge of regional faults to more fully define injection induced seismic risk to a project. In particular, fault orientations that coincide with the maximum principal should be of particular interest for seismicity; however, the faults with different orientations may be the means of transmitting pressure and of equal importance.

The proposed workflow was proven to identify the presence unique geologic features by integrating results of pressure, stress, and seismic modeling. Integrated use of these models is recommended as part of site selection process and assessment of seismic risk to a project.

While not a direct part of this research, brine injection should be further explored to intentionally attempt to induce seismicity within the projected estimates of injection pressure required for CO_2 injection. This could better characterize a site before final decisions are made to inject and store CO_2 at a site and a perforated interval.

REFERENCES

Aagaard, B. T., Knepley, M. G., and Williams, C. A. (2013). A domain decomposition approach to implementing fault slip in finite-element models of quasi-static and dynamic crustal deformation. *Journal of Geophysical Research-Solid Earth*, 118(6), 3059–3079.

Abdelmeguid, M., Ma, X., and Elbanna, A. E. (2019). A novel hybrid finite element-spectral boundary integral scheme for modeling earthquake cycles: Application to rate and state faults with low-velocity zones. *Journal of Geophysical Research: Solid Earth*, *124*(12), 12854-12881.

Alghannam, M. and Juanes, R. (2020). Understanding rate effects in injection-induced earthquakes. *Nature Communications*, 11(1), 3053.

Atekwana, E. A. (1996). Precambrian basement beneath the central Midcontinent United States as interpreted from potential field imagery, in B. A. van der Pluijm and P. A. Catacosinos, eds., Basement and basins of eastern North America. *Geological Society of America Special Paper*, 308, p. 33–44.

Ault, C. H. (1989). Map of Indiana showing directions of bedrock jointing. Indiana Geological Survey, Miscellaneous Map 52, scale 1:380,160, 1 sheet.

Babarinde, O., Okwen, R., Frailey, S., Yang, F., Whittaker, S., and Sweet, D. (2021). A workflow to assess the efficacy of brine extraction for managing injection-induced seismicity potential using data from a CO_2 injection site near Decatur, Illinois. *International Journal of Greenhouse Gas Control*, 109, 103393.

Bauer, R. A., Carney, M., and Finley, R. J. (2016). Overview of microseismic response to CO_2 injection into the Mt. Simon saline reservoir at the Illinois Basin – Decatur Project. *International Journal of Greenhouse Gas Control*, 54, 378–388.

Bauer, R., Will, R., E. Greenberg, S., & Whittaker, S. (2019). Illinois Basin–Decatur Project. In T. Davis, M. Landrø, & M. Wilson (Eds.), *Geophysics and Geosequestration* (pp. 339-370). Cambridge: Cambridge University Press. doi:10.1017/9781316480724.020

Bauer, R. A., Will, R., El-Kaseeh, G., Jaques, P., Greenberg, S., and Carney, M. (2022). Microseismic Monitoring, Event Location, and Focal Mechanisms at the Illinois Basin–Decatur Project, Decatur, Illinois, USA. *Geophysical Monitoring for Geologic Carbon Storage*, 321-341.

Bauer, R. A., Will, R. E., Greenberg, S., and Whittaker, S. G. (2019). Illinois Basin – Decatur Project, *Cambridge University Press*, 339–370.

Bear, J. (1972). *Dynamics of Fluids in Porous Media*. John Wiley, New York, N.Y.

Bear, G. W., Rupp, J. A., and Rudman, A. R. (1997). Seismic interpretation of the deep structure of the Wabash Valley Fault System, *Seismological Research Letters*.

Bell, J. S. (1996). In situ stresses in sedimentary rocks (part 1): measurement techniques. *Geoscience Canada*, 23, 85–100.

Bell, J. S. and Gough, D.I. (1979). Northeast–southwest compressive stress in Alberta: evidence from oil wells: Earth Planet. *Science Letters*, 45, 475–482.

Benson, S. M. and Cole, D. R. (2008). CO_2 sequestration in deep sedimentary formations, *Elements*, v. 4, no. 5, 325–331.

Bertagne, A. J. and Leising, T. C. (1990). Interpretation of seismic data from the Rough Creek Graben of western Kentucky and southern Illinois, in Interior Cratonic Basins, M.W. Leighton, D.R. Kolata, D.E Oltz, and J.J. Eidel, eds., *American Association of Petroleum Geologists Memoir*, 51, 199-208.

Bickford, M. E., Van Schmus, W. R., and Zietz, I. (1986). Proterozoic history of the mid-continent region of North America. *Geology*, 14, 492–496. doi: 10.1130/0091-7613 (1986)14<492:PHOTMR>2.0.CO;2

Biot, M. A. (1941). General theory of three-dimensional consolidation. *Journal of Applied Physics*, 12(2), 155–164.

Birkholzer, J. T. and Zhou, Q. (2009). Basin-scale hydrogeologic impacts of CO_2 storage: Capacity and regulatory implications. *International Journal of Greenhouse Gas Control*, 3, 745–756.

Bradbury, J. C., and Atherton, E. (1965). The Precambrian basement of Illinois. *Illinois State Geological Survey Circular,* 382, 13 p.

Buschbach, T. C. and Kolata, D. R. (1991). Regional setting of Illinois Basin, in Leighton, M.W., et al., eds., Interior Cratonic Basins. *American Association of Petroleum Geologists Memoir*, 51, 29–55.

Caine, J. S., Evans, J. P., and Forster, C. B. (1996). Fault zone architecture and permeability structure. *Geology*, 24(11), 1025–1028.

Cesca, S., Grigoli, F., Heimann, S., Gonzalez, A., Buforn, E., Maghsoudi, S., Blanch, E., and Dahm, T. (2014). The 2013 September–October seismic sequence offshore Spain: a case of seismicity triggered by gas injection. *Geophysical Journal International*, 198, 941–953.

Chester, J. S., Chester, F. M., and Kronenberg, A. K. (2005). Fracture surface energy of the Punchbowl fault, San Andreas system. *Nature*, 437(7055), 133–136.

Collinson, C., Sargent, M. L., and Jennings, J. R. (1988). Illinois Basin region. Sedimentary Cover—North American Craton. US: Geological Society of America. *The Geology of North America*, 2, 383-426.

Coussy, O. (1995). *Mechanics of Porous Continua*. John Wiley, Chichester, U.K.

Dando, B. D. E., Goertz-Allmann, B. P., Kuhn, D., Langet, N., Dichiarante, A. M., and Oye, V. (2021). Relocating microseismicity from downhole monitoring of the Decatur CCS site using a modified double-difference algorithm. *Geophysical Journal International*, 227(2), 1094–1122.

Dean, S. L. and Baranoski, M. T. (2002). A look at western Ohio's Precambrian tectonic setting. *Oil & Gas Journal*, 100, 34–37.

Deichmann, N. and Giardini, D. (2009). Earthquakes induced by the stimulation of an enhanced geothermal system below Basel (Switzerland). *Seismological Research Letters*, 80(5), 784–798.

Denison, R. E., Lidiak, E. G., Bickford, M. E., and Kisvarsanyi, E. B. (1984). Geology and geochronology of Precambrian rocks in the Central Interior region of the United States: U.S. G.P.O. Professional Paper USGS Numbered Series 1241–C. http://pubs.er.usgs.gov/publication/pp1241C (accessed June 2017).

Dichiarante, A. M., Langet, N., Bauer, R. A., Goertz-Allmann, B. P., Williams-Stroud, S. C., Kühn, D., and Dando, B. D. E. (2021). Identifying geological structures through microseismic cluster and burst analyses complementing active seismic interpretation. *Tectonophysics*, 820, 229107.

Dieterich, J. (1994). A constitutive law for rate of earthquake production and its application to earthquake clustering. *Journal of Geophysical Research: Solid Earth*, 99(B2), 2601–2618.

Dost, B. and Haak, H. W. (2007). Natural and induced seismicity. In T. E. Wong, D. A. J. Batjes, and J. de Jager, eds, *Geology of the Netherlands*, 223–229. Royal Netherlands Academy of Arts and Sciences.

Duan, Z. and Sun, R. (2003). An improved model calculating CO_2 solubility in pure water and aqueous NaCl solutions from 273 to 533 k and from 0 to 2000 bar. *Chemical Geology*, 193(3), 257–271.

Ellsworth, W. L., Giardini, D., Townend, J., Ge, S., and Shimamoto, T. (2019). Triggering of the Pohang, Korea, earthquake (Mw 5.5) by enhanced geothermal system stimulation. *Seismological Research Letters*, 90(5), 1844–1858.

Engelder, T. (1982). Is there a genetic relationship between selected regional joints and contemporary stress within the lithosphere of North America? *Tectonics*, v. 1, no. 2, 161–177.

Eyre, T. S., Eaton, D. W., Garagash, D. I., Zecevic, M., Venieri, M., Weir, R., and Lawton, D. C. (2019). The role of aseismic slip in hydraulic fracturing-induced seismicity. *Science Advances*, 5(8), eaav7172.

Faulkner, D., Jackson, C., Lunn, R., Schlische, R., Shipton, Z., Wibberley, C., and Withjack, M. (2010). A review of recent developments concerning the structure, mechanics and fluid flow properties of fault zones. *Journal of Structural Geology*, 32(11), 1557–1575.

Faulkner, D. R., Lewis, A. C., and Rutter, E. H. (2003). On the internal structure and mechanics of large strike-slip fault zones: Field observations of the Carboneras fault in southeastern Spain. *Tectonophysics*, 367(3), 235–251.

Fehler, M., House, L., and Kaieda, H. (1987). Determining planes along which earthquakes occur: Method and application to earthquakes accompanying hydraulic fracturing. *Journal of Geophysical Research: Solid Earth*, 92(B9), 9407–9414.

Finley, R. J. (2014). An overview of the Illinois Basin – Decatur Project. *Greenhouse Gases: Science and Technology*, 4(5), 571–579.

Freiburg, J. T., McBride, J. H., Malone, D. H., and Leetaru, H. E. (2020). Petrology, geochronology, and geophysical characterization of Mesoproterozoic rocks in central Illinois, USA. *Geoscience Frontiers*, 11(2), 581-596.

Freiburg, J. T., McBride, J. H., Malone, D. H., and Leetaru, H. E. (2020). Petrology, geochronology, and geophysical characterization of Mesoproterozoic rocks in central Illinois, USA. *Geoscience Frontiers*, 11(2), 581–596.

Freiburg, J. T., Morse, D. G., Leetaru, H. E., Hoss, R. P., and Yan, Q. (2014). A depositional and diagenetic characterization of the Mt. Simon sandstone at the Illinois Basin-Decatur Project carbon capture and storage site, Decatur, Illinois, USA. *Illinois State Geological Survey Circular*, Technical Report 583. available at http://hdl.handle.net/2142/55338 (accessed December 2021).

Gaillot, P., Brewer, T., Pezard, P., and En-Chao, Y. (2007). Borehole imaging tools-principles and applications. *Scientific Drilling,* 5, 1–5.

Galis, M., Ampuero, J. P., Mai, P. M., and Cappa, F. (2017). Induced seismicity provides insight into why earthquake ruptures stop. *Science Advances*, 3(12), doi:10.1126/sciadv.aap7528.

Gan, W. and Frohlich, C. (2013). Gas injection may have triggered earthquakes in the Cogdell oil field, Texas. *Proceedings of the National Academy of Sciences*, 110(47), 18786–18791.

Goertz-Allmann, B. P., Gibbons, S. J., Oye, V., Bauer, R., and Will, R. (2017). Characterization of induced seismicity patterns derived from internal structure in event clusters. *Journal of Geophysical Research: Solid Earth*, 122(5), 3875–3894.

Goertz-Allmann, B. P., Ku¨hn, D., Oye, V., Bohloli, B., and Aker, E. (2014). Combining microseismic and geomechanical observations to interpret storage integrity at the In Salah CCS site. *Geophysical Journal International*, 198(1), 447–461.

Gough, D.I. (1984). Mantle upflow under North America and plate dynamics. *Nature*, 311(5985), 428-433.

Hajarolasvadi, S., and Elbanna, A. E. (2017). A new hybrid numerical scheme for modelling elastodynamics in unbounded media with near-source heterogeneities. *Geophysical Journal International*, 211(2), 851–864.

Hassanzadeh, H., Pooladi-Darvish, M., Elsharkawy, A. M., Keith, D. W., and Leonenko, Y. (2008). Predicting PVT data for CO_2-brine mixtures for black-oil simulation of CO_2 geological storage. *International Journal of Greenhouse Gas Control*, 2(1), 65–77.

Heigold, P. C. and Oltz, D. E. (1990). Seismic expression of the stratigraphic succession, in Interior Cratonic Basins, M.W. Leighton, D.R. Kolata, D.E Oltz, and J.J. Eidel, eds., *American Association of Petroleum Geologists Memoir*, 51, 169-178.

Hincks, Thea, et al. "Oklahoma's induced seismicity strongly linked to wastewater injection depth." Science 359.6381 (2018): 1251-1255.

IEAGHG. (2013). Induced seismicity and its implications for CO_2 storage risk. Technical Report No. 2013-09.

Jaques, P., Bauer, R. A., and Malkewicz N. W. (2019). Monitoring: Geophones, Arrays, Procedures, Velocity Models, Chronology, Catalogue and Notes on Data.

Jha, B., and Juanes, R. (2014). Coupled multiphase flow and poromechanics: A computational model of pore pressure effects on fault slip and earthquake triggering. *Water Resources Research*, 50(5), 3776-3808.

Juanes, R., Hager, B. H., and Herzog, H. J. (2012). No geologic evidence that seismicity causes fault leakage that would render large-scale carbon capture and storage unsuccessful. *Proceedings of the National Academy of Sciences*, 109(52), E3623–E3623.

Kanamori H., and Brodsky, E. E. (2001). The physics of earthquakes. *Physics Today*, 54, 34–40.

Karimi-Fard, M., Durlofsky, L. J., and Aziz, K. (2004). An efficient discrete-fracture model applicable for general-purpose reservoir simulators. *SPE Journal*, 9(02), 227–236.

Kaven, J. O., Hickman, S. H., McGarr, A. F., and Ellsworth, W. L. (2015). Surface monitoring of microseismicity at the Decatur, Illinois, CO_2 sequestration demonstration site. *Seismological Research Letters*, 86, 1096–1101. https://doi.org/10.1785/0220150062.

Keranen, K. M. and Weingarten, M. (2018). Induced seismicity. *Annual Review of Earth and Planetary Sciences*, 46(1), 149–174.

King, G. C. P., Stein, R. S., and Lin, J. (1994). Static stress changes and the triggering of earthquakes. *Bulletin of the Seismological Society of America*, 84(3), 935–953.

Kumar, A., Zorn, E., Hammack, R. and Harbert, W. (2017). Long-period, long-duration seismicity observed during hydraulic fracturing of the Marcellus Shale in Greene County, Pennsylvania. *The Leading Edge*, 36(7), 580-587.

Lahann, R. W., Rupp, J. A., Medina, C. R., Carlson, G., and Johnson, K. M. (2017). State of stress in the Illinois Basin and constraints on inducing failure. *Environmental Geosciences*, 24(3), 123–150.

Langet, N., Goertz-Allmann, B., Oye, V., Bauer, R. A., Williams-Stroud, S., Dichiarante, A. M., and Greenberg, S. E. (2020). Joint focal mechanism inversion using downhole and surface monitoring at the Decatur, Illinois, CO_2 injection site. *Bulletin of the Seismological Society of America*, 110(5), 2168–2187.

Leetaru, H. E., Frailey, S. M., Morse, D., Finley, R. J., Rupp, J. A., Drahozval, J. A., and McBride, J. H. (2009). Carbon sequestration in the Mt. Simon Sandstone saline reservoir, in M. Grobe, J. C. Pashin, and R. L. Dodge, eds., Carbon dioxide sequestration in geological media—State of the science. *AAPG Studies in Geology*, 59, 261–277.

Leetaru, H. E. and Freiburg, J. T. (2014). Lithofacies and reservoir characterization of the Mt. Simon Sandstone at the Illinois Basin–Decatur Project. *Greenhouse Gases: Science and Technology*, 4, 580–595.

Leetaru, H. E. and McBride, J. H. (2009). Reservoir uncertainty, Precambrian topography, and carbon sequestration in the Mt. Simon Sandstone, Illinois Basin. *Environmental Geoscience*, 16, 235–243. doi: 10.1306 /eg.04210909006.

Lidiak, E. G. (1996). Geochemistry of subsurface Proterozoic rocks in the eastern midcontinent of the United States: Further evidence for a within-plate tectonic setting, in van der Pluijm, B. A. and Catacosinos, P. A., eds., Basement and basins of eastern North America. *Geological Society of America Special Paper*, 308, 45–66. doi: 10.1130 /0-8137-2308-6.45.

Lie, K.A. (2019). *An Introduction to Reservoir Simulation Using MATLAB/GNU Octave: User Guide for the MATLAB Reservoir Simulation Toolbox (MRST).* Cambridge University Press.

Lisle, R. J. and Srivastava, D. C. (2004). Test of the frictional reactivation theory for faults and validity of fault-slip analysis. *Geology*, 32(7), 569–572.

Lowell, J. D. (1985). Structural Styles in Petroleum Exploration: Oil and Gas Consultants International, Inc., Tulsa, Oklahoma, 477 p.

Lund Snee, J. E. and Zoback, M. D. (2020). Multiscale variations of the crustal stress field throughout North America. *Nature Communications*, 11(1), 1951.

Makhnenko, R. Y., Bondarenko, N. B., Kim, K., and S. Whittaker. "Laboratory Modeling of Induced Microseismicity in the Illinois Basin." Paper presented at the 54th U.S. Rock Mechanics/Geomechanics Symposium, physical event cancelled, June 2020.

McBride, J. H., KeachII, R. W., Leetaru, H. E., and Smith, K. M. (2018). Visualizing Precambrian basement tectonics beneath a carbon capture and storage site, Illinois Basin. *Interpretation*, 6(2), T257–T270.

McBride, J. H. and Kolata, D. R. (1999). Upper crust beneath the central Illinois Basin, United States. *Geological Society of America Bulletin*, 111, 375–394. doi: 10 .1130 /0016 -7606 (1999)111 <0375: UCBTCI>2 .3 .CO;2.

McBride, J. H., Kolata, D. R., and Hildenbrand, T.G. (2003). Geophysical constraints on understanding the origin of the Paleozoic Illinois Basin and the Proterozoic eastern granite-rhyolite province, USA. *Tectonophysics*, 363, 45–78. doi: 10 .1016 /S0040 -1951 (02)00653 -4.

McBride, J. H., Leetaru, H. E., Keach, R. W., and McBride, E. I. (2016). Fine-scale structure of the Precambrian beneath the Illinois Basin. *Geosphere*, 12, 585–606. https://doi.org/10.1130/GES01286.1

McBride, J. H. and Nelson, W. J. (1999). Style and origin of mid-Carboniferous deformation in the Illinois Basin, USA—Ancestral Rockies deformation. *Tectonophysics*, 305, 249–273. doi: 10 .1016 /S0040 -1951 (99)00015 -3.

McGarr, A. (2014). Maximum magnitude earthquakes induced by fluid injection. *Journal of Geophysical Research,* 119, 1008–1019.

Mia, M. S., Abdelmeguid, M., and Elbanna, A. E. (2022). Spatio-Temporal Clustering of Seismicity Enabled by Off-Fault Plasticity. *Geophysical Research Letters*, *49*(8), e2021GL097601.

Mirzaei, M., Khamehchi, E., and P. J. Clifford. "Study of Compositional Processes in Oil Recovery from Andrew Field due to Submiscible Gas Injection." Paper presented at the Abu Dhabi International Conference and Exhibition, Abu Dhabi, United Arab Emirates, October 2004. doi: https://doi-org.proxy2.library.illinois.edu/10.2118/88775-MS

Mitchell, T. and Faulkner, D. (2009). The nature and origin of off-fault damage surrounding strike-slip fault zones with a wide range of displacements: A field study from the Atacama fault system, northern Chile. *Journal of Structural Geology*, 31(8), 802–816.

Morris, A., Ferrill, D. A., and Henderson, D. B. (1996). Slip-tendency analysis and fault reactivation. *Geology*, 24(3), 275–278.

Mousavi, S. M., Ellsworth, W. L., Zhu, W., Chuang, L. Y. and Beroza, G. C. (2020). Earthquake transformer—an attentive deep-learning model for simultaneous earthquake detection and phase picking. *Nature Communications*, 11(1), 1-12.

Münchmeyer, J., Woollam, J., Rietbrock, A., Tilmann, F., Lange, D., Bornstein, T., Diehl, T., Giunchi, C., Haslinger, F., Jozinović, D., and Michelini, A. (2022). Which picker fits my data? A quantitative evaluation of deep learning based seismic pickers. *Journal of Geophysical Research: Solid Earth*, 127(1), p.e2021JB023499.

Murray, K. E. (2015). Class II Saltwater Disposal for 2009-2014 at the Annual-, State-, and County-Scales by Geologic Zones of Completion, Oklahoma. Oklahoma Geological Survey Open-File Report OF5-2015, 18 p. http://ogs.ou.edu/docs/openfile/OF5-2015.pdf (accessed June 2017).

Nelson, W. J. (1991). "Structural styles in the Illinois Basin," in M. W. Leighton, D. R. Kolata, D. F. Oltz, and J. J. Eidel, eds., Interior Cratonic Basins. *AAPG Memoir*, 51, 209–243.

Nelson, W. J. (1995). Structural features in Illinois. *Illinois State Geological Survey Bulletin,* 100, 144 p.

Perol, T., Gharbi, M., and Denolle, M. (2018). Convolutional neural network for earthquake detection and location. *Science Advances*, 4(2), p.e1700578.

Potter, C. J., Goldhaber, M. B., Heigold, P. C., and Drahovzal, J. A. (1995). Structure of the Reelfoot-Rough Creek Rift System, Fluorspar Area Fault Complex, and Hicks Dome, southern Illinois and western Kentucky--New constraints from regional seismic reflection data. U.S. Geological Survey Professional Paper 1538-Q, 19 pp.

Potter, C. J., Drahovzal, J. A., Sargent, M. L., and McBride, J. H. (1997). Proterozoic structure, Cambrian rifting, and younger faulting as revealed by a regional seismic reflection network in the southern Illinois Basin. *Seismological Research Letters*.

Powell, R. L. (1976). Some geomorphic and hydrologic implications of jointing in carbonate strata of Mississippian age in south-central Indiana, Ph.D. thesis, Purdue University, West Lafayette, Indiana, 169 p.

Pratt, T., Culotta, R., Hauser, E., Nelson, D., Brown, L., Kaufman, S., and Hinze, W. (1989). Major Proterozoic basement features of the eastern midcontinent of North America revealed by recent COCORP profiling. *Geology*, 17, 505–509.

Pratt, T. L., Hauser, E. C., and Nelson, K. D. (1992). Widespread buried Precambrian layered sequences in the U.S. Mid-continent: Evidence for large Proterozoic depositional basins, *American Association of Petroleum Geologists Bulletin*, 76, 1,384-1,401.

Reasenberg, P. and Simpson, R. (1992). Response of regional seismicity to the static stress change produced by the Loma-Prieta earthquake. *Science*, 255(5052), 1687–1690.

Reuter, J., and Watts, D. R. (2004). An ancient river channel system incised on the Precambrian–Cambrian unconformity beneath Jackson County, Ohio. *AAPG Bulletin*, v. 88, no. 8, 1041– 1047. doi:10.1306/02240403066.

Rice, J. R. (1992). Fault stress states, pore pressure distributions, and the weakness of the San Andreas fault. *International Geophysics*, 51, 475-503.

Richards-Dinger, K., and Dieterich, J. H. (2012). RSQSim earthquake simulator. *Seismological Research Letters*, 83(6), 983-990.

Rong, K., Yoon, C. E., Bergen, K. J., Elezabi, H., Bailis, P., Levis, P. and Beroza, G. C. (2018). Locality Sensitive Hashing for Earthquake Detection: A Case Study Scaling Data-Driven Science. arXiv preprint arXiv:1803.09835.

Rutledge, J. T. (2010). Geologic demonstration at the Aneth oil field, Paradox Basin, Utah. Southwest Regional Partnership on Carbon Sequestration Phase II Topical Report. Technical report.

Sbar, M. L. and Sykes, L. R. (1973). Contemporary compressive stress and seismicity in eastern North America: an example of intra-plate tectonics. *Geologic Society of America Bulletin*, 84, 1861-1882.

Scholz, C. H. (2002). *The Mechanics of Earthquakes and Faulting*. Cambridge University Press.

Schultz, R., Skoumal, R. J., Brudzinski, M. R., Eaton, D., Baptie, B., and Ellsworth, W. (2020). Hydraulic fracturing-induced seismicity. *Reviews of Geophysics*, 58(3), e2019RG000695.

Segall, P., and Lu, S. (2015). Injection induced seismicity: Poroelastic and earthquake nucleation effects. *Journal of Geophysical Research*: Solid Earth, 120, 5082–5103.

Senel, O., Will, R., and Butsch, R. J. (2014). Integrated reservoir modeling at the Illinois Basin–Decatur project. *Greenhouse Gases: Science and Technology*, 4(5), 662-684.

Sminchak, J. (2012). Simulation framework for regional geologic CO_2 storage along arches province of Midwestern United States. Battelle Memorial Institute, Columbus, OH.

Sperrevik, S., Gillespie, P. A., Fisher, Q. J., Halvorsen, T., and Knipe, R. J. (2002). Empirical estimation of fault rock properties. *Norwegian Petroleum Society Special Publications*, 11, 109–125.

Steams, D. W. (1978). "Faulting and forced folding in the Rocky Mountains foreland" in V. Matthews, ed., *Laramide Folding Associated with Basement Block Faulting in the Western United States: Geological Society of America Memoir* 151, 1-37.

Strandli, C. W., Mehnert, E., and Benson, S. M. (2014). CO_2 plume tracking and history matching using multilevel pressure monitoring at the Illinois Basin – Decatur Project. *Energy Procedia*, 63, 4473–4484. 12th International Conference on Greenhouse Gas Control Technologies, GHGT-12.

Suppe, J. and Medwedeff, D. A. (1984). Fault-propagation folding. *Geological Society of America Abstracts with Programs*, 16, 670.

Van Schmus, W. R., Bickford, M. E., and Turek, A. (1996). Proterozoic geology of the east-central Midcontinent basement, in van der Pluijm, B. A. and Catacosinos, P. A., eds., Basement and Basins of Eastern North America. *Geological Society of America Special Paper*, 308, 7–32. doi: 10.1130/0-8137-2308-6.7.

Vilarrasa, V., and Carrera, J. (2015). Geologic carbon storage is unlikely to trigger large earthquakes and reactivate faults through which CO_2 could leak. *Proceedings of the National Academy of Sciences*, 112(19), 5938–5943.

Vilarrasa, V., Carrera, J., Olivella, S., Rutqvist, J., Laloui, L. (2019). Induced seismicity in geologic carbon storage. *Solid Earth*, 10, 871– 892. DOI: 10.5194/se-10-871-2019.

White, J. A., Chiaramonte, L., Ezzedine, S., Foxall, W., Hao, Y., Ramirez, A., and McNab, W. (2014). Geomechanical behavior of the reservoir and caprock system at the In Salah CO_2 storage project. *Proceedings of the National Academy of Sciences*, 111(24), 8747–8752.

White, J. A., and Foxall, W. (2016). Assessing induced seismicity risk at CO_2 storage projects: recent progress and remaining challenges. *International Journal of Greenhouse Gas Control*, 49, 413–424, doi: http://dx.doi.org/10.1016/j.ijggc.2016.03.021.

Whittaker, S., Rostron, B., Hawkes, C., Gardner, C., White, D., Johnson, J., Chalaturnyk, R., and Seeburger, D. (2011). A decade of CO_2 injection into depleting oil fields: Monitoring and research activities of the IEA GHG Weyburn-Midale CO_2 monitoring and storage project. *Energy Procedia*, 4, 6069–6076. 10th International Conference on Greenhouse Gas Control Technologies.

Will, R., El-Kaseeh, G., Jaques, P., Carney, M., Greenberg, S., and Finley, R. (2016). Microseismic data acquisition, processing, and event characterization at the Illinois Basin–Decatur Project, *International Journal of Greenhouse Gas Control*, 54, 404-20.

Williams-Stroud, S., Bauer, R., Leetaru, H., Oye, V., Stanek, F., Greenberg, S., and Langet, N. (2020). Analysis of microseismicity and reactivated fault size to assess the potential for felt events by CO_2 injection in the Illinois Basin. *Bulletin of the Seismological Society of America*, 110(5), 2188-220.

Willman, H. B. E., Atherton, T., Buschnach, C. T., Collinson, C., Frye, J. C., Hopkins, M. E., Lineback, J. A., and Simon, J. A. (1975). Handbook of Illinois Stratigraphy. Illinois State Geological Survey, Champaign, Illinois. *ISGS Bulletin*, 95, 261 pp.

Workman, L. E. and Bell, A. H. (1948). Deep drilling and deeper oil possibilities in Illinois. *AAPG Bulletin*, 32, 2041 –2062.

Yang, J. P. and Aggarwal, Y. P. (1981). Seismotectonics of northeastern United States and adjacent Canada. *Journal of Geophysical Research: Solid Earth*, 86(B6), 4981-4998.

Yang, Z., Yehya, A., Iwalewa, T. M., and Rice, J. R. (2021). Effect of Permeability Evolution in Fault Damage Zones on Earthquake Recurrence. *Journal of Geophysical Research: Solid Earth*, *126*(9), e2021JB021787.

Yielding, G., Freeman, B., and Needham, D. T. (1997). Quantitative fault seal prediction. *AAPG Bulletin*, 81(6), 897–917.

Yildirim A. (2014). Subsurface fracture analysis using FMI logs: Implications for regional state of stress prediction in the Black Warrior Basin, Alabama. Master thesis, Alabama University of Alabama, 98p.

Yoon, C. E., O'Reilly, O., Bergen, K. J., and Beroza, G. C. (2015). Earthquake detection through computationally efficient similarity search. *Science Advances*, 1, e1501057.

Zhai, G., Shirzaei, M., Manga, M., and Chen, X. (2019). Pore-pressure diffusion, enhanced by poroelastic stresses, controls induced seismicity in Oklahoma. *Proceedings of the National Academy of Sciences*, 116(33), 16228–16233.

Zhu, W. and Beroza, G. C. (2019). PhaseNet: a deep-neural-network-based seismic arrival-time picking method. *Geophysical Journal International*, 216(1), 261-273.

Zitnik, M. and Zupan, B. (2012). Nimfa: A python library for nonnegative matrix factorization. *Journal of Machine Learning Research*, 13, 849-853.

Zoback, M. D. and Gorelick, S. M. (2012). Earthquake triggering and large-scale geologic storage of carbon dioxide. *Proceedings of the National Academy of Sciences*, 109(26), 10164–10168.

Zoback, M. D., Moos, D., Mastin, L. G., and Anderson, R. N. (1985). Wellbore breakouts and in situ stress. *Journal of Geophysical Research*, 90, 5523-5530.

Zoback, M. D. and Zoback, M. L. (1981). State of stress and intraplate earthquakes in the United States. *Science*, 213(4503), 96-104.

Zoback, M. D. and Zoback, M. L. (1991). "Tectonic stress field of North America and relative plate motions." In *Neotectonics of North America*, eds. D. Burton Slemmons, E. R. Engdahl, Mark D. Zoback, David D. Blackwell.

Zoback, M. L. (1992). First and second order patterns of stress in the lithosphere: The World Stress Map Project. *Journal of Geophysical Research*, 97, 11703-11728.

Zoback, M. L. and Zoback, M. D. (1980). State of stress in the conterminous United States. *Journal of Geophysical Research*, 85, 6113-6156.

Zoback M. L. and Zoback, M. D. (1989). "Tectonic stress field of the continental U.S." in Pakiser, L. and Mooney, W., eds., *Geophysical framework of the continental United States: Geological Society of America Memoir*, 172, 523-539.

APPENDIX A: TASK 6 - ADVANCING THE METHODOLOGY

PRE-PROJECT STATE OF THE ART IN UNDERGROUND INJECTION FAULT IDENTIFICATION

Prior to the commencement of the SoS project, the most commonly employed methods for identifying faults were surface seismic surveys and subsurface investigations utilizing wellbore data. However, these approaches were predominantly used for the detection of larger faults, with the primary objective of locating major structures responsible for fluid trapping and, to a lesser extent, seismic activity. There was often an associated degree of uncertainty regarding the presence of additional faults. With large-scale injection projects, it is essential to have a comprehensive understanding of the existence of all faults—not only larger ones but also smaller faults that can lead to seismic events.

Another technique for fault identification involves analyzing well test data following the completion of a well. Injection tests can be utilized to measure fracture propagation pressure, which is related to rock strength and can provide valuable insights into the characteristics of existing fractures. Injection fall-off and multi-well pressure transient tests are also capable of detecting faults, contingent upon the contrast of flow properties between the fault and the host rock. For a multi-well test to identify a fault, it would have to be located between wells in the test.

An alternative indirect method to identify faults and areas prone to creating microseismicity involves the orientation of stresses. This method can be achieved through the inversion of earthquake focal mechanisms. However, this technique is limited in its capacity to identify localized stress perturbations caused by small, active faults. Wellbore breakouts, drilling-induced tensile fractures (DITFs), and core disking can provide information regarding localized stress perturbations, but the availability of well log data, particularly borehole image logs, may be restricted.

Uncertainties

The accurate identification of fault systems and precise estimation of fault locations are critical components of efforts to mitigate injection-induced seismicity in deep-injection schemes. However, conventional approaches, including surface seismic surveys, can prove ineffective in certain cases when exploring deep-seated geological formations. Complex geology and high-refraction layers can impede the propagation of weak signals that emanate from the depths, leading to distorted ray paths. Moreover, conventional methods are typically inadequate in detecting strike-slip faults, which lack vertical offsets. Consequently, these limitations can result in significant uncertainties in pinpointing the origin of microseismic events in the basement and in detecting hidden or sealed faults. In addition to surface seismic surveys, wellbore analysis represents an alternative means by which fault systems can be identified. However, this approach is limited to instances when a drilled well intersects coincidentally with a fault zone. In such cases, the fault can be distinguished via the analysis of extracted core and interpretation of petrophysical well logs. Nevertheless, it should be noted that the effectiveness of this method is restricted to the characterization of a single fault system and relies on the fortuitous intersection of a drilled well with a fault zone.

Risks

There is a correlation between induced seismic events and faults located in the older crystalline rocks that underlie the injection intervals. Given enough data on subsurface geology, permeability, fault, regional/local stress, and seismic history, injection spots prone to induced seismic activity can be

identified in advance. In some cases, seismic risk can be managed by reducing the amount of CO_2 injected and the duration of injection.

When the SoS project began, there were no standard methods for implementing risk assessments for induced seismicity. Surface seismic surveys alone were not enough to calculate and quantify induced seismic risk and design earthquake-resistant construction. Accurate interpretation of microseismic data, along with other measured field data such as pressure and geophysical data compared to data-driven models in the state-of-the-art technology, would improve field-scale operation conditions such as injection rates, intervals, and locations, and mitigate unwanted risks such as induced seismicity.

GOALS AND OBJECTIVES FOR THE ADVANCEMENT OF TECHNOLOGY IN UNDERGROUND INJECTION PROJECTS

The proposed technology aimed to advance the safety and sustainability of subsurface energy activities through the development and validation of advanced technologies for accurately predicting and managing induced seismicity during underground injection projects. This technology includes the development of a coupled model of multiphase fluid flow geomechanics in deep geologic formations that can simulate fault slip and fracture activation upon fluid injection/extraction and the use of ML techniques to determine relevant earthquake attributes from passive seismic data. The objectives of the SoS project were to validate the developed technologies in a laboratory environment and with field-level studies, advance the technology-to-technology readiness level (TRL) 5, and use it to design and optimize fluid injection/extraction processes in deep geologic formations.

PROGRESS AND IMPROVEMENT AT THE END OF THE SOS PROJECT

The SoS project aimed to develop an integrated methodology (i.e., workflow) of forward and physics-constrained, data-driven (inverse) models to identify subsurface geologic features, estimate changes to the in situ stress field, and explain pressure perturbations between the storage unit and the basement. The technology readiness level (TRL) for the key technology, the development of a coupled model of multiphase fluid flow-geomechanics in deep geologic formations, was initially at TRL 4, based on previous DOE-funded work (DE-FOA-0001826). During the SoS project, the technology advanced to TRL 5, demonstrating feasibility in a relevant environment. Significant progress was made on ML techniques to determine relevant earthquake attributes from passive seismic activity. At the SoS project's onset, this technology was at TRL 3 and advanced to TRL 4 by its validation in a laboratory environment. Implementation of both clustering and extraction of earthquake attributes using supervised learning techniques in a limited scope showed the approach's suitability for use in a variety of different injection intervals overlying crystalline basement. To meet the SoS project's overall performance requirements, a computational framework was established using a Bayesian approach that integrates multiple data sets, including microseismic data, to identify subsurface geologic features and quantify related uncertainties. The usability of this approach was successfully demonstrated at TRL 4 and validated in injection intervals overlying a crystalline basement. The generation of a 3D geological structure model of the crystalline basement and its integration with an existing 3D geologic model of the storage unit and overlying intervals is a key aspect of the SoS project's specific performance requirements. This task involved the use of appropriate geostatistical algorithms to propagate geological, physical, and geomechanical properties into grid cells to visualize and analyze the relationships between structural features and physical, geomechanical properties within geological intervals. As such, this part of the SoS project has advanced from TRL 4 to TRL 5, representing a significant milestone in the project's development. This work has

significant practical applications in predicting the impacts of fluid injection/production on subsurface geologic features and forecasting seismic and aseismic slip events.

APPENDIX B: LOG OF SIMULATION CASES WITH GEOCELLULAR MODEL VERSION 6

Below is a log of cases that were simulated from the time a new geocellular model was generated to October 2022. For most cases, an approximate difference between observed average BHP and simulated average BHP is provided. The following abbreviations are used throughout the log: Mod = modified/modification; Mult = multiplication factor or multiplier value; Kh = horizontal permeability; Kv = vertical permeability; mD = millidarcy; LPZ = low-permeability zone (comprised of layers).

Database (VDB) study	**Case**	**Description**	**Perf**	**Note**	**Mismatch (average) between predicted and observed**			
					CCS1 (~psi)	**WB1 (~psi)**	**WB2 (~psi)**	**WB3 (~psi)**
SOS_0326	Case 1-40	Mod reservoir properties	all	Did not get a match with historical field pressure data. Lost VDB files and some other files, due to Nexus computer crashing	–	–	–	–
	Case 40	No mod	all	Poor match	100	60	80	90
	Case 45	Placed hypothetical fault 200 ft north of VW1 within Mt. Simon interval. Kh of fault → 1e-05 Fault length → 4000 ft Mod Kh in layers within and above perforation interval (Mt. Simon) Layer 1-173 (mult of 0.55) Layer 174-184 (mult of 0.93) Mod Kh in layers below perforation zone (Argenta) Layer 185-219 (mult of 2.7)	all	Good match. But the incorporated faults are hypothetical and the reduction in permeability is unrealistic (based on injection test data).	<40	<5	<10	<10
	Case 46	Placed hypothetical fault 200 ft south of CCS1 within Mt. Simon interval. Kh of fault → 1e-05 Fault length → 4000 ft Kh of fault → 1e-05	all	Poor match. Shape of curve is dissimilar to that of field data	<50	40	30	30

Database (VDB) study	Case	Description	Perf	Note	Mismatch (average) between predicted and observed			
					CCS1 (~psi)	WB1 (~psi)	WB2 (~psi)	WB3 (~psi)
	Case 47	Placed hypothetical fault 200 ft south of CCS1. Height and fault length was same as case 46. Kh of fault → 1e-05	all	Poor match	–	–	–	–
	Case 48	Placed hypothetical fault 400 ft south of CCS1 Kh of fault → 1e-05 Mod Kh in layers below perforation zone (Argenta) Layer 185-219 (mult of 2.6)	all	Poor match WB2 & WB3, good match at CCS 1 and WB1	–	–	–	–
	Case 49	Placed hypothetical fault 400 ft south of CCS1 Kh of fault → 1e-05 Fault length → 4000 ft Mod Kh in layers in and above perforation zone (Mt. Simon) layer 1-173 (mult of 0.55) layer 174-184 (mult of 0.95) Mod Kh in layers below perforation zone (Argenta) Layer 185-219 (mult of 2.6)	all	Poor match. Shape of curve at WB2 & 3 has a upward trend. Pressures overpredicted at CCS1 and WB1	–	–	–	–
	Case 50	Placed hypothetical fault 400 ft south of CCS1 Kh of fault → 1e-05 Fault length → 4000 ft Mod Kh in layers in and above perforation zone (Mt. Simon) Layer 1-173 (mult of 0.95) Layer 174-184 (mult of 0.95) Mod Kh in layers below perforation zone (Argenta) Layer 185-219 (mult of 2.6)	all	Poor match WB2 & WB3, good match at CCS 1 and WB1	–	–	–	–

Database (VDB) study	Case	Description	Perf	Note	Mismatch (average) between predicted and observed			
					CCS1 (~psi)	WB1 (~psi)	WB2 (~psi)	WB3 (~psi)
	Case 51	Placed hypothetical fault 400 ft south of CCS1 Kh of fault → 1e-05 Fault length → 4000 ft Mod Kh in layers in and above perforation zone (Mt. Simon) Layer 1-173 (mult of 0.80) Layer 174-184 (mult of 0.95) Mod Kh in layers below perforation zone (Argenta) Layer 185-219 (mult of 2.6)	all		–	–	–	–
	Case 52	Placed hypothetical fault 400 ft south of CCS1 Kh of fault → 1e-05 Fault length → 4000 ft Mod Kh in layers in and above perforation zone (Mt. Simon) Layer 1-173 (mult of 0.70) Layer 174-184 (mult of 0.95) Mod Kh in layers below perforation zone (Argenta) Layer 185-219 (mult of 2.0)	all	Moderately good match at WB 1-4, but overpredicting at CCS1	–	–	–	–
	Case 53	Placed hypothetical fault 400 ft south of CCS1 Kh of fault → 1e-05 Fault length → 4000 ft Mod Kh in layers in and above perforation zone (Mt. Simon) Layer 135-173 (mult of 0.70) Layer 174-184 (mult of 0.95) Mod Kh in layers below perforation zone (Argenta) Layer 185-219 (mult of 2.0)	all	Moderately good match at all pressure points, but underpredicting pressure in the beginning at WB2 and 3.	<60	<10	<30	<30

Database (VDB) study	Case	Description	Perf	Note	Mismatch (average) between predicted and observed			
					CCS1 (~psi)	WB1 (~psi)	WB2 (~psi)	WB3 (~psi)
	Case 54	Placed hypothetical fault 400 ft south of CCS1 Kh of fault → 1e-05 Kv (unmodified) Fault length → 4000 ft Mod Kh in layers in and above perforation zone (Mt. Simon) Layer 135-173 (mult of 0.80) Layer 174-184 (mult of 0.95) Mod Kh in layers below perforation zone (Argenta) Layer 185-219 (mult of 2.0)	all	Poor match. Underpredicting pressure in the beginning at WB2 and WB3. However, pressure rises later, and approaches observed field data.	<50	30	30	30
	Case 55	Placed hypothetical fault 400 ft south of CCS1 Kh of fault → 1e-01 mD Kv (unmodified) Porosity → 5% Fault length → 4000 ft Fault height → 500 ft	all	Poor match observed at all pressure gauge points	<50	>30	>40	>40
	Case 56	Modified LPZ (selected layers with relatively low permeability) only using a mult value of 0.5	all	poor match	>100	>40	>60	>60
	Case 56a	No Fault Mod to LPZ only Mult value of 0	all	Poor match. Overpredicted at CCS1, WB1, and WB2 pressure gauge points, and underpredicted at WB3 (flat line)	>100	>40	>80	>200
	Case 57	Kh of fault → 400 mD Kv (unmodified) Porosity → 5% Fault length → 4000 ft Fault height → 500 ft	all	poor match	>100	>40	>70	>70

Database (VDB) study	Case	Description	Perf	Note	Mismatch (average) between predicted and observed			
					CCS1 (~psi)	WB1 (~psi)	WB2 (~psi)	WB3 (~psi)
	Case 58	Hypothetical E-W fault was placed 400 ft south of CCS1 Kh = Kv of fault → 400 mD Porosity → 5% Fault length → 4000 ft Fault height → Top of lower Mt. Simon to Base of Argenta (~500 ft)	all	poor match	>100	>50	>70	>70
	Case 59	Hypothetical E-W fault 400 ft south of CCS1 Kh = Kv of fault → 200 mD Porosity, fault length, and height is same as case 58 above.	all	poor match	>100	>40	>70	>70
	Case 60	Hypothetical E-W fault 400 ft south of CCS1 Kh = Kv of fault → 50 mD Porosity, fault length and height is same as case above.	all	poor match	>100	>40	>70	>70
	Case 58a	To investigate the impact of fault's Kv, hypothetical E-W fault was placed 400 ft south of CCS1 Kh of fault → 400 mD, Kv (unmodified), Porosity→ 5% Fault length and height is same as the case above.		poor match	>100	>40	>70	>70
	Case 58b	To investigate impact of changing porosity Hypothetical E-W fault 400 ft south of CCS1 (Extended to basement) Kh of fault → 400 mD, Kv (unmodified), Porosity→ 15% Fault length and height is same as case above.	all	poor match	>100	>40	>70	>70
	Case 58c	to investigate impact of fault Kv only Hypothetical E-W fault 400 ft south of CCS1 (Extended to basement) Kv of fault → 400 mD, Kh (unmodified), Porosity → 5% Fault length and height is same as above.	all	poor match	>100	>40	>70	>70

Database (VDB) study	Case	Description	Perf	Note	Mismatch (average) between predicted and observed			
					CCS1 (~psi)	WB1 (~psi)	WB2 (~psi)	WB3 (~psi)
	Case 64	to investigate lower fault perms Hypothetical E-W fault 400 ft south of CCS1 (Extended to basement) Kv=Kh of fault → 5 mD, Porosity → 5% Fault length and height is same as above.	all	poor match	<50	40	>70	>70
	Case 65	to investigate lower fault perms Hypothetical E-W fault 400 ft south of CCS1 (Extended to basement) Kv=Kh of fault → 0.5 mD, Porosity → 5% Fault length and height is same as above.	all	poor match	<100	30	>50	>50
	Case 61	2-fault case Added 2nd hypothetical fault 400 ft east of CCS1 (fault strikes N-S) Kh=Kv of faults → 400 mD Porosity of faults → 5% 2nd Fault length → 2000 ft 2nd Fault height → Top of lower Mt. Simon to Base of Argenta (~500 ft)	all	poor match	>100	>50	100	100
	Case 62	(2-fault-case, reduced perm) Added 2nd hypothetical fault 400 ft east of CCS1 (fault strikes N-S) Kh=Kv of faults → 200 mD Porosity of faults → 5% Porosity, fault length and height is same as above (Case 60).	all	poor match	>100	>50	100	100
	Case 63	(2-fault-case, reduced perm) Added 2nd hypothetical fault 400 ft east of CCS1 (fault strikes N-S) Kh=Kv of faults → 50 mD Porosity of faults → 5% Porosity, fault length and height is same as above (Case 61).	all	poor match	>100	>50	100	100
SOS_0704	Case1	(LPZ only) No Fault Mod to LPZ only Multiplier value of 0.1	all	poor match				

Database (VDB) study	Case	Description	Perf	Note	Mismatch (average) between predicted and observed			
					CCS1 (~psi)	WB1 (~psi)	WB2 (~psi)	WB3 (~psi)
	Case2	(2-fault-case, reduced perm) Added 2nd hypothetical fault 400 ft east of CCS1 (fault strikes N-S) Kh=Kv of faults → 5 mD Porosity of faults → 5% Porosity, fault length and height is same as above (VDB_0326 --> Case 61).	all	poor match	>100	>30	>60	>60
	Case3	(2-fault-case, reduced perm) Added 2nd hypothetical fault 400 ft east of CCS1 (fault strikes N-S) Kh=Kv of faults → 0.5 mD Porosity of faults → 5% Porosity, fault length and height is same as above (VDB_0326 --> Case 61).	all	Good match at WB1-3, but bad match at CCS1	>120	>20	<10	<10
	Case4	(Fault and LPZs) Added 2nd hypothetical fault 400 ft east of CCS1 (fault strikes N-S) Kh=Kv of faults → 50 mD Lpz *0.5 Porosity, fault length and height is same as above (Case 61).	all	poor match	>60	40	>70	>70
	Case5	(Fault and LPZs) Added 2nd hypothetical fault 400 ft east of CCS1 (fault strikes N-S) Kh=Kv of faults → 50 mD Lpz *0.1 Porosity, fault length and height is same as above (Case 61).	all	poor match	>50	20	30	30
	Case6	(Fault and LPZs) Added 2nd hypothetical fault 400 ft east of CCS1 (fault strikes N-S) Kh=Kv of faults → 5 mD Lpz *0.5 Porosity, fault length and height is same as above (Case 61).	all	poor match	>100	10	<20	<20

Database (VDB) study	Case	Description	Perf	Note	Mismatch (average) between predicted and observed			
					CCS1 (~psi)	WB1 (~psi)	WB2 (~psi)	WB3 (~psi)
	Case7	(Fault and LPZs) Added 2nd hypothetical fault 400 ft east of CCS1 (fault strikes N-S) Kh=Kv of faults → 5 mD Lpz *0.5 Porosity, fault length and height is same as above (Case 61).	all	poor match	>100	10	<5	<5
SOS_0716	Case 29	Addition of seismically interpreted faults (All faults included) Included faults Used transmissibility mult value = 1	all	poor match	>100	>40	100	100
	Case 29b	Included faults Except for faults 2 and 3, used transmissibility mult value = 1e-05	all	poor match	>50	>40	>70	>70
	Case 29c	Included faults All faults used transmissibility mult value = 1e-05	all	poor match				
	Case 30	(LPZ mod only) Mod LPZs perm Mult by 0.5 Mod matrix perm Mult Argenta layers by 3.2 Includes all faults Used transmissibility mult value = 1	all	poor match	>100	>40	100	100
	Case 30a	(LPZ mod only) Mod LPZs perm Mult by 1e-01 Mod matrix perm Mult Argenta layers by 3.2 Includes all faults Used transmissibility mult value = 1	all	poor match	>100	>40	100	100

Database (VDB) study	Case	Description	Perf	Note	Mismatch (average) between predicted and observed			
					CCS1 (~psi)	WB1 (~psi)	WB2 (~psi)	WB3 (~psi)
	Case 40	Mod LPZs Mult by 1e-01 Includes all faults Except for faults 2 and 3, used transmissibility mult value = 1e-05	all	Fair match	<50	<10	<30	<30
	Case 40a	Mod LPZs Mult of 1e-01 Mod matrix perm Mult Mt. Simon layers by 0.87 Mult Argenta layers by 3.2 Includes all faults Except for faults 2 and 3, used transmissibility mult value = 1e-05	1, 2-1	Good match	<30	<5	<10	<10
	Case 29d	Case 29d (all faults+matrix+LPZ) Mod LPZs Mult of 1e-01 Mod matrix perm Mult mt. Simon layers by 0.87 Mult Argenta layers by 3.2 Includes all faults Used transmissibility mult value = 1e-05	1, 2-1	Bad	>100	>50	>100	>100
	Case 29e	Case 29e (all faults) Mod LPZs Mult of 1e-01 Mod matrix perm Mult mt. Simon layers by 0.87 Mult Argenta layers by 3.2 Includes all faults Used transmissibility mult value = 1e-02	1, 2-1	Bad	>100	40	100	100
	Case 29f	Case 29f (all faults) dotted Same as 29d, changed transmissibility mult to 1e-01	1, 2-1	Bad	–	–	–	–
	Case 29g	Case 29g (all faults) Similar to 29d, changed Mt. Simon mult to 1 & fault transmissibility mult to 1e-01	1, 2-1	Bad	–	–	–	–

Database (VDB) study	Case	Description	Perf	Note	Mismatch (average) between predicted and observed			
					CCS1 (~psi)	WB1 (~psi)	WB2 (~psi)	WB3 (~psi)
	Case 29h	Case 29h (all faults) Similar to 29f, changed fault transmissibility mult to 5e-01	1, 2-1	Bad	–	–	–	–
SOS_HM_11032021	Case 1	Mod LPZs perm Mult by 1e-01 Mod matrix perm Mult Argenta layers by 3.2 Includes all faults (“not truncated”) Transmissibility mult applied based on fault orientation Fault 2= 1, Fault 3 = 0.001	1, 2-1	Bad	<10	>50	>100	>100
	Case 2	Mod LPZs perm Mult by 1e-01 Mod matrix perm Mult Argenta layers by 3.2 Includes all faults (“not truncated”) Transmissibility MULT applied based on fault orientation Fault 2= 1, Fault 3 = 0.5	1, 2-1	Bad	>20	30	>50	>50
	Case 3	Mod LPZs perm Mult by 1e-01 Mod matrix perm Mult Argenta layers by 3.2 Includes all faults (“not truncated”) Transmissibility MULT applied based on fault orientation Fault 2= 1, Fault 3 = 1	1, 2-1	Bad	>20	30	>50	>50
	Case 4	Mod LPZs perm Mult by 1e-01 Mod matrix perm Mult Argenta layers by 3.2 Includes all faults (“truncated”) Transmissibility MULT applied based on fault orientation Fault 2= 1, Fault 3 = 0.5	1, 2-1	Bad	>20	30	>50	>50

Database (VDB) study	Case	Description	Perf	Note	Mismatch (average) between predicted and observed			
					CCS1 (~psi)	WB1 (~psi)	WB2 (~psi)	WB3 (~psi)
	Case 5	Mod LPZs perm Mult by 1e-01 Mod matrix perm Mult Argenta layers by 3.2 Includes all faults (“truncated”) Transmissibility MULT applied based on fault orientation Fault 2= 1, Fault 3 = 0.5	1, 2-1	Bad	>20	30	>50	>50
SOS_HM_11032021	Case 6	Use of fault slip tolerance for fault transmissibility multiplier	1, 2-1		>50	>30	>50	>50
	Case 7	Use of fault slip tolerance (*0.5) for fault transmissibility multiplier			>50	>30	>50	>50
	Case 8	Use of fault slip tolerance (*0.1) for fault transmissibility multiplier			>50	>30	>50	>50
	Case 9	Use of fault slip tolerance (*0.01) for fault transmissibility multiplier			>50	>30	>50	>50
	Case 10	Use of fault slip tolerance (*0.0001) for fault transmissibility multiplier			>50	>30	>50	>50
SOS_0716	Case 41 (re-run)	Case 41 → Best Match case Mod LPZs Mult by 1e-01 Mod matrix perm Mult Mt. Simon layers (1-175) by 0.87 Mult Argenta layers by 3.2 Reduced the number of faults to 10 faults 2 and 3 transmissibility mult =1, the 8 other faults transmissibility mult = 1e-05	1, 2-1	Fair match	<20	<10	<30	<30
	Case 40b	Rerun 40, includes filtering/eliminating faults	1, 2-1	Fair match	–	–	–	–
	Case 44	Rerun 40, includes filtering/eliminating faults	1, 2-1	Fair match	–	–	–	–
	case 42	Rerun 40, includes filtering/eliminating faults	1, 2-1	Fair match	–	–	–	–
	Case 45	Rerun 40, includes filtering/eliminating faults	1, 2-1	Fair match	–	–	–	–
	Case 46	Rerun 40, includes filtering/eliminating faults	1, 2-1	Fair match	–	–	–	–

Database (VDB) study	Case	Description	Perf	Note	Mismatch (average) between predicted and observed			
					CCS1 (~psi)	WB1 (~psi)	WB2 (~psi)	WB3 (~psi)
	Case 48	Mod LPZs Mult by 1e-01 Mod matrix perm Mult Mt. Simon layers (1-175) by 0.87 Mult Argenta layers by 3.2 Included red box (~50ft height) and multiplied by 0.2	1, 2-1	poor match	<20	25	<40	<40
	Case 49	Mod LPZs Mult by 1e-01 Mod matrix perm Mult Mt. Simon layers (1-175) by 0.87 Mult Argenta layers by 3.2 Included blue box (~50ft height) and multiplied by 0.2	1, 2-1	poor match	<20	25	<40	<40
	Case 50	Mod LPZs Mult by 1e-01 Mod matrix perm Mult Mt. Simon layers (1-175) by 0.5 Mult Argenta layers by 3.2 Included red box (~50ft height) and multiplied by 0.2	1, 2-1	poor match, over predicting pressure at all gauge points	>100	>30	>30	>30
	Case 52	Mod LPZs Mult by 1e-01 Mod matrix perm Mult Mt. Simon layers (1-175) by 0.87 Mult Argenta layers by 3.2 Included red box (~50ft height) and multiplied by 0	1, 2-1	Poor match	>100	>30	>30	>30
	Case 55	Mod LPZs Mult by 1e-01 Mod matrix perm Mod red box (layer 165 -184) = CCS 1 well perm Mult Mt. Simon layers (1-184) by 0.87 Mult Argenta layers by 3.2	1, 2-1	Poor match	>50	30	>50	>50

Database (VDB) study	Case	Description	Perf	Note	Mismatch (average) between predicted and observed			
					CCS1 (~psi)	WB1 (~psi)	WB2 (~psi)	WB3 (~psi)
	Case 56	Mod LPZs Mult by 1e-01 Mod matrix perm Mod red box (layer 165 -184) = CCS 1 well perm Mult Mt. Simon layers (1-184) by 0. 6 Mult Argenta layers by 3.2	1, 2-1	Poor match	>50	30	>50	>50
	Case 57	Case 57 Mod LPZs Mult by 1e-01 Mod matrix perm Mod red box (layer 165 -184) = CCS 1 well perm Mult Argenta layers by 3.2	1, 2-1	Poor match	>50	30	>50	>50
	Case 1c	Old rel. perm curve	1-1, 2-1	Poor match	<20	>40	100	100
	Case 1c_1	Mod rel. perm curve (Swirr => 50%) No mod to matrix or LPZs	1-1, 2-1	Poor match	<20	>40	100	100
	Case 1f_1	Mod rel. perm curve Mod matrix perm Mult Mt. Simon layers (1-184) by 0. 8 (kh & kv) Mult Mt. Simon layers (174 only) by 0. 1 (Kv only) Mult Argenta layers by 3.2 (kh & kv)	1-1, 2-1	Poor match	>50	>40	>70	>70
	Case 1g_1	Mod rel. perm curve Mod matrix perm Mult Mt. Simon layers (1-184) by 0. 8 (kh & kv) Mult Mt. Simon layers (174 only) by 0. 01 (kv only) Mult Argenta layers by 3.2 (kh & kv)	1-1, 2-1	Poor match	>50	>40	>70	>70

Database (VDB) study	Case	Description	Perf	Note	Mismatch (average) between predicted and observed			
					CCS1 (~psi)	WB1 (~psi)	WB2 (~psi)	WB3 (~psi)
	Case 1f_2	Mod rel. perm curve Mod LPZs Mult by 0.1 (kh & kv) Mod matrix perm Mult Mt. Simon layers (1-184) by 0. 8 (kh & kv) Mult Mt. Simon layers (174 only) by 0. 1 (kv only) Mult Argenta layers by 3.2 (kh & kv)	1-1, 2-1	Poor match	>50	>40	>70	>70
	Case 1g_2	Mod rel. perm curve Mod LPZs Mult by 0.1 Mod matrix perm Mult Mt. Simon layers (1-184) by 0. 8 (kh & kv) Mult Mt. Simon layers (174 only) by 0. 01 (kv only) Mult Argenta layers by 3.2 (kh & kv)	1-1, 2-1	Poor match	>50	>40	>70	>70
	Case 1f_3	Mod rel. perm curve (reduced Krw by 50% @ 90% and 70% Sw) Mod LPZs Mult by 0.1 (kh & kv) Mod matrix perm Mult Mt. Simon layers (1-184) by 0. 8 (kh & kv) Mult Mt. Simon layers (174 only) by 0. 1 (kv only) Mult Argenta layers by 3.2 (kh & kv)	1-1, 2-1	Poor match	>50	>40	>70	>70

Database (VDB) study	Case	Description	Perf	Note	Mismatch (average) between predicted and observed			
					CCS1 (~psi)	WB1 (~psi)	WB2 (~psi)	WB3 (~psi)
	Case 1g_3	Mod rel. perm curve (#same as case 1g_1) Mod LPZs Mult by 0.1 Mod matrix perm Mod red box (layer 165 -184) = CCS 1 well perm (kh #not equal kv) Mult Mt. Simon layers (1-184) by 0. 8 (kh & kv) Mult Mt. Simon layers (174 only) by 0. 01 (kv only) Mult Argenta layers by 3.2 (kh & kv)	1-1, 2-1	Poor match	>50	>40	>70	>70
	Case 1c_1_1	Mod rel. perm curve (Swirr => 50%) No mod to matrix or LPZs **0.678 cP to 1.1918 cP**	1-1, 2-1	Poor match	>50	>50	50	50
	Case 1_2	Mod rel. perm curve (Swirr => 40%) Mod LPZs Mult by 0.1 (kh & kv) **0.678 cP to 1.1918 cP** **Changed 1st perforation (to 25 ft) and 2nd perforation (to 10 ft)**	1-1, 2-1	Poor match	>50	<20	<30	<30
SOS040222	Case 1c_1_1 (re-run)	Mod rel. perm curve (Swirr => 50%) No mod to matrix or LPZs 0.678 cP to 1.1918 cP Updated perforation depth for WBs CCS1 to 1st perforation (to 10 ft) and 2nd perforation (to 2 ft)		Poor match	>50	>50	50	50
	Case 1_2 (re-run)	Mod rel. perm curve (Swirr => 40%) 0.678 cP to 1.1918 cP Changed 1st perforation (to 25 ft) and 2nd perforation (to 5 ft) Mod LPZs Mult by 0.1 (kh & kv) Updated perforation depth for WBs		Poor match	>50	<20	<30	<30

Database (VDB) study	Case	Description	Perf	Note	Mismatch (average) between predicted and observed			
					CCS1 (~psi)	WB1 (~psi)	WB2 (~psi)	WB3 (~psi)
	Case 1_4	Rel. perm curve (Swirr => 40%) Used fluid properties from SF Mod LPZs Mult by 0.1 (kh & kv) 1st perforation (to 25 ft) and 2nd perforation (to 5 ft)		Good match. Though there is a delayed pressure response at WB1, the match observed is good	<50	<10	<20	<20
	Case 1_5	Rel. perm curve (Swirr => 40%) Used fluid properties from SF Mod LPZs Mult by 0.1 (kh & kv) Mod matrix Mult by 0.87 1st perforation (to 25 ft) and 2nd perforation (to 5 ft)		Good match, but over predicts at CCS1	>50	<10	<10	<10
	Case 1_6	Rel. perm curve (Swirr => 40%) Used fluid properties from SF Mod LPZs Mult by 0.1 (kh & kv) Mod matrix Mult by 0.87 1st perforation (to 25 ft) and 2nd perforation (to 10 ft) Rather than moving the base of the 2nd perforation up, actual base (as recorded in the field) was used		**Good Match**	<50	<10	<20	<20
	Case 1_7	Rel. perm curve (Swirr => 40%) Used fluid properties from SF Mod LPZs Mult by 0 (kv only) 1st perforation (to 25 ft) and 2nd perforation (to 10 ft)		poor match	–	–	–	–

Database (VDB) study	Case	Description	Perf	Note	Mismatch (average) between predicted and observed			
					CCS1 (~psi)	WB1 (~psi)	WB2 (~psi)	WB3 (~psi)
	Case 1_7k	Used fluid properties from SF Mod matrix Mod south of CCS1 (layer 165 -184) = CCS 1 well perm (kh #not equal kv) Mod model Mult by 0 (kv) 1st perforation (to 25 ft) and 2nd perforation (to 10 ft)		poor match	–	–	–	–
	Case 1_8	Rel. perm curve (Swirr => 40%) Used fluid properties from SF Mod LPZs Mult by 0 (kv only) 1st perforation (to 10 ft)		poor match	–	–	–	–
	Case 1_8k	Rel. perm curve (Swirr => 40%) Used fluid properties from SF Mod matrix Mod south of CCS1 (layer 165 -184) = CCS 1 well perm (kh #not equal kv) Mod model Mult by 0 (kv) 1st perforation (to 10 ft)		poor match	–	–	–	–
	Case 1_8a	Rel. perm curve (Swirr => 40%) Used fluid properties from SF Mod Matrix Mult by 0 (kv only) 1st perforation (to 10 ft)		poor match	–	–	–	–
SOS042022	Case 1	Rel. perm curve (Swirr => 40%) Used fluid properties from SF Change LPZ (between CCS1 and VW1) to 268mD 1st perforation (to 10 ft)		poor match. Simulation was focused on improving the match with gas saturation at the end of the 3rd month	–	–	–	–

Database (VDB) study	Case	Description	Perf	Note	Mismatch (average) between predicted and observed			
					CCS1 (~psi)	WB1 (~psi)	WB2 (~psi)	WB3 (~psi)
	Case 2	Rel. perm curve (Swirr => 40%) Used fluid properties from SF Hypothetical fault (between CCS1 and VW1) à kh = 0.1, kv =0.2 1st perforation (to 10 ft)		poor match. Simulation was focused on improving the match with gas saturation at the end of the 3rd month	–	–	–	–
	Case 3	Rel. perm curve (Swirr => 40%) Used fluid properties from SF Modified matrix (500 ft south of CCS 1) à assigned VW1 perm values (base) 1st perforation (to 10 ft)		poor match. Simulation was focused on improving the match with gas saturation at the end of the 3rd month	–	–	–	–
	Case 4	(Remodeled in case 5, for case 1 kv/kh =0.5) Combined case 1 and 3		poor match. Simulation was focused on improving the match with gas saturation at the end of the 3rd month	–	–	–	–
	Case 6	Rel. perm curve (Swirr => 40%) Used fluid properties from SF Hypothetical fault (between CCS1 and VW1) à kh = 0, kv =0 1st perforation (to 10 ft)		poor match. Simulation was focused on improving the match with gas saturation at the end of the 3rd month	–	–	–	–
	Case 7	Combined case 1 and 2		poor match. Simulation was focused on improving the match with gas	–	–	–	–

Database (VDB) study	Case	Description	Perf	Note	Mismatch (average) between predicted and observed			
					CCS1 (~psi)	WB1 (~psi)	WB2 (~psi)	WB3 (~psi)
				saturation at the end of the 3rd month				
	Case 8	Combined case 1, 2, and 3		poor match. Simulation was focused on improving the match with gas saturation at the end of the 3rd month	–	–	–	–
	Case 9	Combined case 1 and 3 Extend LPZ window down and modify Kh value Modified matrix (300 ft south CCS1)		poor match. Simulation was focused on improving the match with gas saturation at the end of the 3rd month	–	–	–	–
	Case 10	Extended LPZ window down and modified Kh value		poor match. Simulation was focused on improving the match with gas saturation at the end of the 3rd month	–	–	–	–
	Case 11	Modified matrix (200 ft south CCS1)		poor match. Simulation was focused on improving the match with gas saturation at the end of the 3rd month	–	–	–	–

Database (VDB) study	Case	Description	Perf	Note	Mismatch (average) between predicted and observed			
					CCS1 (~psi)	WB1 (~psi)	WB2 (~psi)	WB3 (~psi)
	Case 9a	Combined case 1 and 3 Extended LPZ window up & down direction and modified Kh Modified matrix (300 ft south CCS1)		poor match. Simulation was focused on improving the match with gas saturation at the end of the 3rd month	–	–	–	–
SOS05312022	Case 1	Base case	1-1,	poor match	>50	<20	50	50
	Case 2	Modified LPZ window between CCS1 and VW1 à Cube shaped high perm feature (~1000 x 1000 x 50 ft.) Reduced perm of entire Mt. Simon by 20%	1-1,	Fair match. Poor match at CCS1 and WB1, but good at WB2 and WB3 pressure gauge points	>50	>20	<10	<10
	Case 3	Reduced perm of entire Mt. Simon by 20%	1-1,	poor match. Overpredicted pressure at CCCS1. Pressure underpredicted at WB2 and WB3	>100	<10	25	25
	Case 4	Modified LPZ window between CCS1 and VW1 à Cube shaped high perm feature (~1000 x 1000 x 50 ft.)	1-1,	poor match observed at WB2 and WB3 pressure gauge points	<50	<10	<30	<30
	Case 5	Mimicked fracture swarm in the model by assigning high perm (10 D) within Argenta interval. High perm is a row of cells from CCS1 to WB1	1-1,	poor match	>100	>20	>40	>40
	Case 6	Mimicked fracture swarm and 1 fault in the model by assigning high perm (10 D) that cuts across parts of lower Mt. Simon and Argenta. High perm is a column of cell (next to CCS1) and a row of cells from CCS1 to WB1.	1-1,	poor match	>50	>200	>50	>50

Database (VDB) study	Case	Description	Perf	Note	Mismatch (average) between predicted and observed			
					CCS1 (~psi)	WB1 (~psi)	WB2 (~psi)	WB3 (~psi)
	Case 7	Mimicked fracture swarm and 2 faults in the model by assigning high perm (10 D) that cuts across parts of lower Mt. Simon and Argenta. High perm is 2 columns of cell (1 next to CCS1 and the other next to VW1) and a row of cells from CCS1 to WB1.	1-1,	poor match	>50	>150	>50	>50
	Case 9	Created LGR around CCS1 and VW 1, in order to represent fault Fracture Swarm --> 10D, Faults -->10D, Used 2 faults that were seismically interpreted, faults 2 & 3	1-1,	poor match	>100	>50	>50	>50
	Case 10	Created LGR around CCS1 and VW 1, in order to represent fault Fracture Swarm --> 10D, Faults -->10D	1-1,	poor match	>50	>100	<50	<50
	Case 11	Created LGR around CCS1 and VW 1 in order to represent fault Fracture Swarm --> 10D, Faults -->10D, reduced lateral extent of the fracture swarm, such that it does not go beyond the vertical faults	1-1,	poor match	–	–	–	–
	Case 12	Created LGR around CCS1 and VW 1, in order to represent fault Fracture Swarm --> 2D, Faults -->2D	1-1,	poor match	>100	>70	>40	>40
	Case 13	Created LGR around CCS1 and VW 1, in order to represent fault Fracture Swarm --> 10D, Faults -->10D	1-1,	poor match	>100	>70	>40	>40
	Case 1b	Base case, Constant BHP rate	1-1,	poor match	–	>70	>40	>40
	Case 2b	Modified LPZ window between CCS1 and VW1 à Cube shaped high perm feature (~1000 x 1000 x 50 ft.) Reduced perm of entire Mt. Simon by 20%	1-1,	poor match	–	>70	20	20
	Case 3b	Reduced perm of entire Mt. Simon by 20%	1-1,	poor match	–	>70	20	20
	Case 4b	Modified LPZ window between CCS1 and VW1 à Cube shaped high perm feature (~1000 x 1000 x 50 ft.)	1-1,	poor match	–	>70	30	30

Database (VDB) study	Case	Description	Perf	Note	Mismatch (average) between predicted and observed			
					CCS1 (~psi)	WB1 (~psi)	WB2 (~psi)	WB3 (~psi)
	Case 14_1	Similar to case 9. Created LGR around CCS1 and VW 1, in order to represent fault Fracture Swarm --> 10D, Faults -->10D. Did not use 2 faults that were interpreted from seismic data, faults 2&3	1-1,	poor match	–	>100	>50	>50
	Case 15	Constant CCS1 BHP constraint. Created LGR around CCS1 and VW 1, in order to represent fault Fracture Swarm --> 10D, Faults -->1000 mD.	1-1,	poor match	–	>100	>50	>50
	Case 16	Constant CCS1 BHP constraint. Created LGR around CCS1 and VW 1, in order to represent fault Fracture Swarm --> 1000 mD, Faults -->1000 mD.	1-1,	poor match	–	>100	>50	>50
	Case 17	Constant CCS1 BHP constraint. Created LGR around CCS1 and VW 1, in order to represent fault Fracture Swarm --> 1000 mD, Faults -->1000 mD.	1-1,	poor match	–	>100	>50	>50
	Case 18	Constant CCS1 BHP constraint. Created LGR around CCS1 and VW 1, in order to represent fault Fracture Swarm --> 100 mD, Faults -->100 mD.	1-1,	poor match	–	>100	>50	>50
	Case 19	Constant CCS1 BHP constraint. Created LGR around CCS1 and VW 1, in order to represent fault Fracture Swarm --> 100 mD, Faults -->1000 mD.	1-1,	poor match	–	>100	>50	>50
SOS_072922	Case 0 (base case)	Base Case. Fractured crystalline basement added to the base of the model	1-1,	poor match	>100	>50	>50	>50
	Case 1	Perm of Argenta mult with 3.2	1-1,	poor match	>100	>50	>50	>50
	Case 2	Mod case 1, used constant BHP	1-1,	poor match	–	>50	>100	>100

Database (VDB) study	Case	Description	Perf	Note	Mismatch (average) between predicted and observed			
					CCS1 (~psi)	WB1 (~psi)	WB2 (~psi)	WB3 (~psi)
	Case 3	Argenta => Perm *3.2 Constant CCS1 BHP Mt. Simon => Perm * 0.8	1-1,	poor match	–	>50	>100	>100
	Case 4	Argenta => Perm *3.2 Constant CCS1 BHP Mt. Simon => Perm * 0.8 Basement => Perm *0.1	1-1,	poor match	–	>50	>100	>100
	Case 5	Included faults that extend to basement Along fault (transmissibility = 1) & Across fault (transmissibility = 0.1)	1-1,	poor match	–	>100	>50	>50
	Case 6	Included faults that extend to basement Along fault (transmissibility = 1) & Across fault (transmissibility = 0.1) Mod PCB model * 0.1	1-1,	poor match	>100	>50	>50	>50
	Case 7	Included faults that extend to basement Along fault (transmissibility = 1) & Across fault (transmissibility = 0.1) Mod PCB model * 0.001	1-1,	poor match	>100	>50	>50	>50
SOS_072922U	Case 2	Added faults that extend into basement In Mt. Simon and Argenta Along fault perm = 1 md & across fault = rock matrix perm In PCB, Along fault perm = 100 md & across fault = rock matrix perm	1-1,	poor match				
	Case 3	Added faults that extend into basement In Mt. Simon, Along fault perm = 1 md & across fault = rock matrix perm In Argenta & PCB, Along fault perm = 100 md & across fault = rock matrix perm	1-1,	poor match				

Database (VDB) study	Case	Description	Perf	Note	Mismatch (average) between predicted and observed			
					CCS1 (~psi)	WB1 (~psi)	WB2 (~psi)	WB3 (~psi)
	Case 4	Reduced basement perm by 0.01 In Mt. Simon, Along fault perm = 1 md & across fault = rock matrix perm In Argenta & PCB, Along fault perm = 100 md & across fault = rock matrix perm	1-1,	poor match				
	Case 5	Reduced Argenta perm by dividing by 3 In Mt. Simon, Along fault perm = 1 md & across fault = rock matrix perm In Argenta & PCB, Along fault perm = 100 md & across fault = rock matrix perm	1-1,	poor match				
	Case 6	Reduced Argenta perm by dividing by 3 * Reduced basement perm by 0.01 In Mt. Simon, Along fault perm = 1 md & across fault = rock matrix perm In Argenta & PCB, Along fault perm = 100 md & across fault = rock matrix perm	1-1,	poor match				

APPENDIX C: LOG OF SIMULATION CASES WITH GEOCELLULAR MODEL VERSION 7

Below is a log of cases that were simulated using the geocellular model version 7.

VDB Case No.	LPZ mult	Mt. Simon mult	Argenta mult	PCB mult	All Faults transmissibility mult (except 2&3)	Fault 2 - transmissibility mult	Fault 3 - transmissibility mult	Perforation int (ft)	Fault 2 - Along fault, K (Mt. Simon)	Fault 2 - Along fault, K (Argenta+PCB)	Fault 9 = Fault 2 (F2)	Upper level of faults terminated at level of WB3	Cluster 5 fault	Cluster 15 fault	Fault 3	Fault 8	Cluster 10/13 fault	Constant CCS1 BHP	Selected faults- - Along fault, K ((Mt. Simon and Argenta)	Selected faults- - Along fault, K (PCB)	Short note
SOS_072922	x	x	x	x	x	x	x	x	x	x	x	x	x	x	x	x	x	x	x	x	
SOS_072922_1	x	x	3.2	x	x	x	x	x	x	x	x	x	x	x	x	x	x	x	x	x	
SOS_072922_2	x	x	x	x	x	x	x	x	x	x	x	x	x	x	x	x	x	✓	x	x	
SOS_072922_3	x	0.8	3.2	x	x	x	x	x	x	x	x	x	x	x	x	x	x	✓	x	x	
SOS_072922_4	x	0.8	3.2	0.1	x	x	x	x	x	x	x	x	x	x	x	x	x	✓	x	x	
SOS_072922U_3	x	x	x	x	x	x	x	x	x	x	x	x	x	x	x	x	x	✓	1	100	
SOS_072922U_4	x	x	x	0.01	x	x	x	x	x	x	x	x	x	x	x	x	x	✓	1	100	
SOS_072922U_5	x	x	0.3	x	x	x	x	x	x	x	x	x	x	x	x	x	x	✓	1	100	
SOS_072922U_6	x	x	0.3	0.01	x	x	x	x	x	x	x	x	x	x	x	x	x	✓	1	100	
SOS_072922U_7	x	x	0.3	0.01	x	x	x	x	x	x	x	x	x	x	x	x	x	x	1	100	
SOS_072922U_8	x	x	0.3	0.01	x	x	x	x	x	x	x	x	x	x	x	x	x	✓	1	100	Extended fault 2 NW by 1 cell
SOS_072922U_9	x	x	0.3	0.01	x	x	x	x	x	x	x	x	x	x	x	x	x	✓	1	100	Extended fault 2 NW by 2 cells
SOS_072922U_10	x	x	0.3	0.01	x	x	x	x	x	x	x	x	x	x	x	x	x	✓	1	100	Extended fault 2 NW by 3 cells
SOS_072922U_11	x	x	0.3	0.01	x	x	x	x	x	x	x	x	x	x	x	x	x	✓	1	100	Extended fault 2 NW by 4 cells
SOS_072922U_12	x	x	x	0.01	x	x	x	x	100	x	x	x	x	x	x	x	x	✓	1	100	Designed N-S fault as fault 2

VDB Case No.	LPZ mult	Mt. Simon mult	Argenta mult	PCB mult	All Faults transmissibility mult (except 2&3)	Fault 2 - transmissibility mult	Fault 3 - transmissibility mult	Perforation int (ft)	Fault 2 - Along fault, K (Mt. Simon)	Fault 2 - Along fault, K (Argenta+PCB)	Fault 9 = Fault 2 (F2)	Upper level of faults terminated at level of WB3	Cluster 5 fault	Cluster 15 fault	Fault 3	Fault 8	Cluster 10/13 fault	Constant CCS1 BHP	Selected faults- - Along fault, K ((Mt. Simon and Argenta)	Selected faults- - Along fault, K (PCB)	Short note
SOS_072922U_13	x	x	x	0.01	x	x	x	x	100	x	x	x	x	x	x	x	x	✓	1	1000	Designed N-S fault as fault 2
SOS_072922U_14	x	x	x	0.01	x	x	x	x	1000	x	x	x	x	x	x	x	x	✓	1	1000	Designed N-S fault as fault 3
SOS_072922U_15	x	x	x	0.01	x	x	x	x	1000	x	x	x	x	x	x	x	x	✓	1	1000	Designed N-S fault as fault 4
SOS_072922U_16	x	x	x	0.01	x	x	x	x	1000	x	x	x	x	x	x	x	x	✓	1	1000	Made Kx = Ky = Kz
SOS_072922U_17	x	x	x	0.01	x	x	x	x	10000	x	x	x	x	x	x	x	x	✓	1	1000	
SOS_072922U_18	x	x	x	0.01	x	x	x	x	1	x	x	x	x	x	x	x	x	✓	1	1000	
SOS_072922U_19	x	x	x	0.01	x	x	x	x	1	x	x	x	x	x	x	x	x	✓	1	1000	Made Kx = Ky = Kz
SOS_072922U_20	x	x	0.3	0.01	x	x	x	x	1	x	x	x	x	x	x	x	x	✓	1	1000	reran SOS_072922U_8
SOS_072922U_21	x	x	0.3	0.01	x	x	x	x	1	x	x	x	x	x	x	x	x	✓	1	1000	reran SOS_072922U_9
SOS_072922U_22	x	x	0.3	0.01	x	x	x	x	1	x	x	x	x	x	x	x	x	✓	1	1000	reran SOS_072922U_10
SOS_072922U_23	x	x	0.3	0.01	x	x	x	x	1	x	x	x	x	x	x	x	x	✓	1	1000	reran SOS_072922U_11
SOS_072922U_24	x	x	0.3	0.01	x	x	x	x	1000	x	x	x	x	x	x	x	x	✓	1	1000	
SOS_072922U_25	x	x	0.3	0.01	x	x	x	x	1000	x	x	x	x	x	x	x	x	✓	1	1000	Extended fault 2 NW by 6 cells
SOS_072922U_26	x	x	0.3	0.01	x	x	x	x	10000	x	x	x	x	x	x	x	x	✓	1	10000	
SOS_072922U_27	x	x	0.3	0.01	x	x	x	x	10000	x	x	x	x	x	x	x	x	✓	1	1000	
SOS_0922U_1	x	x	1.0	0.01	x	x	x	x	1000	10	x	x	x	x	x	x	x	✓	1	1000	Designed N-S fault as fault 2

VDB Case No.	LPZ mult	Mt. Simon mult	Argenta mult	PCB mult	All Faults transmissibility mult (except 2&3)	Fault 2 - transmissibility mult	Fault 3 - transmissibility mult	Perforation int (ft)	Fault 2 - Along fault, K (Mt. Simon)	Fault 2 - Along fault, K (Argenta+PCB)	Fault 9 = Fault 2 (F2)	Upper level of faults terminated at level of WB3	Cluster 5 fault	Cluster 15 fault	Fault 3	Fault 8	Cluster 10/13 fault	Constant CCS1 BHP	Selected faults- - Along fault, K ((Mt. Simon and Argenta)	Selected faults- - Along fault, K (PCB)	Short note
SOS_0922U_2	x	x	1.0	0.01	x	x	x	x	1000	10	x	x	x	x	x	x	x	✓	1	1000	Designed N-S fault as fault 3
SOS_0922U_3	x	x	1.0	0.01	x	x	x	x	1000	0.1	x	x	x	x	x	x	x	✓	1	1000	Designed N-S fault as fault 4
SOS_0922U_4	x	x	1.0	0.01	x	x	x	x	1000	0.01	x	x	x	x	x	x	x	✓	1	1000	Designed N-S fault as fault 5
SOS_0922U_5	x	x	1.0	0.01	x	x	x	x	5000	0.01	x	x	x	x	x	x	x	✓	1	1000	Designed N-S fault as fault 6
SOS_0922U_6	x	x	1.0	0.01	x	x	x	x	5000	0.01	x	x	x	x	x	x	x	✓	1	1000	
SOS_0922U_7	x	x	1.0	0.01	x	x	x	x	2500	0.01	x	x	x	x	x	x	x	✓	1	1000	
SOS_0922U_8	x	x	1.0	0.01	x	x	x	x	2500	0.01	x	x	x	x	x	x	x	✓	1	1000	
SOS_0922_13	1	1.6	1.0	x	1E-05	1.0	1.0	45	x	x	x	x	x	x	x	x	x	✓	x	x	
SOS_0922_14	1	1.7	1.0	x	1E-05	1.0	1.0	45	x	x	x	x	x	x	x	x	x	✓	x	x	
SOS_0922_16	1	2.0	1.0	x	1E-05	1.0	1.0	45	x	x	x	x	x	x	x	x	x	✓	x	x	
SOS_0922_17	0.1	2.0	1.0	x	1E-05	1.0	1.0	10	x	x	x	x	x	x	x	x	x	✓	x	x	
SOS_0922_18	0.1	1.4	1.0	x	1E-05	1.0	1.0	45	x	x	x	x	x	x	x	x	x	✓	x	x	
SOS_0922_19	0.1	1.6	1.0	x	1E-05	1.0	1.0	15	x	x	x	x	x	x	x	x	x	✓	x	x	
SOS_0922_20	0.1	1.7	1.0	x	1E-05	1.0	1.0	10	x	x	x	x	x	x	x	x	x	✓	x	x	
SOS_0922_21	0.1	1.7	1.0	x	1E-05	1.0	1.0	10	x	x	x	x	x	x	x	x	x	✓	x	x	
SOS_0922_22	0.1	1.7	1.0	x	1E-05	1.0	1.0	15	x	x	x	x	x	x	x	x	x	✓	x	x	

VDB Case No.	LPZ mult	Mt. Simon mult	Argenta mult	PCB mult	All Faults transmissibility mult (except 2&3)	Fault 2 - transmissibility mult	Fault 3 - transmissibility mult	Perforation int (ft)	Fault 2 - Along fault, K (Mt. Simon)	Fault 2 - Along fault, K (Argenta+PCB)	Fault 9 = Fault 2 (F2)	Upper level of faults terminated at level of WB3	Cluster 5 fault	Cluster 15 fault	Fault 3	Fault 8	Cluster 10/13 fault	Constant CCS1 BHP	Selected faults- - Along fault, K ((Mt. Simon and Argenta)	Selected faults- - Along fault, K (PCB)	Short note
SOS_0922_23	0.1	1.7	1.5	1E-03	1E-05	1.0	1.0	20	x	x	x	x	x	x	x	x	x	✓	x	x	
SOS_0922_24	0.1	1.7	1.5	1E-03	1E-05	1.0	1.0	20	2000	2000	x	x	x	x	x	x	x	✓	x	x	
SOS_0922_25	0.1	1.7	1	1E-03	1E-05	1.0	1.0	20	2500	0.01	x	x	x	x	x	x	x	✓	x	x	
SOS_0922_26	0.1	1.7	1	1E-03	1E-05	1.0	1.0	20	2500	x	x	x	x	x	x	x	x	✓	x	x	
SOS_0922_27	0.1	1.7	1	1E-03	1E-05	1.0	1.0	20	5000	0.01	x	x	x	x	x	x	x	✓	x	x	
SOS_0922_28	0.1	1.7	1	1E-03	1E-05	1.0	1.0	20	1000	0.01	x	x	x	x	x	x	x	✓	x	x	
SOS_0922_29	0.1	1.7	1	1E-01	1E-05	1	1	20	5000	0.01	x	x	x	x	x	x	x	✓	x	x	
SOS_0922_30	0.1	1.7	1	1E-01	1E-05	1	1	20	5000	10	x	x	x	x	x	x	x	✓	x	x	
SOS_0922_31	0.1	1.7	1	1	1E-05	1	1	20	5000	10	x	x	x	x	x	x	x	✓	x	x	
SOS_0922_32	0.1	1.7	1	1.5	1E-05	1	1	20	5000	10	x	x	x	x	x	x	x	✓	x	x	
SOS_0922_33	0.1	1.7	1	5	1E-05	1	1	20	5000	10	x	x	x	x	x	x	x	✓	x	x	
SOS_0922_34	0.1	1.7	1	1	1E-05	1	1	15	5000	1	x	x	x	x	x	x	x	✓	x	x	
SOS_0922_35	0.1	1.7	1	1	1E-05	1	1E-05	15	5000	1	x	x	x	x	x	x	x	✓	x	x	
SOS_0922_36	0.1	1.7	1	1	1E-05	1	1E-05	15	5000	1	x	x	x	x	x	x	x	✓	x	x	
SOS_0922_37	0.1	1.7	1	1	1E-05	1	1E-05	20	5000	1	x	x	x	x	x	x	x	✓	x	x	

VDB Case No.	LPZ mult	Mt. Simon mult	Argenta mult	PCB mult	All Faults transmissibility mult (except 2&3)	Fault 2 - transmissibility mult	Fault 3 - transmissibility mult	Perforation int (ft)	Fault 2 - Along fault, K (Mt. Simon)	Fault 2 - Along fault, K (Argenta+PCB)	Fault 9 = Fault 2 (F2)	Upper level of faults terminated at level of WB3	Cluster 5 fault	Cluster 15 fault	Fault 3	Fault 8	Cluster 10/13 fault	Constant CCS1 BHP	Selected faults- - Along fault, K ((Mt. Simon and Argenta)	Selected faults- - Along fault, K (PCB)	Short note
SOS_0922_38	0.1	1.7	1	1	1E-05	1	1E-05	10	5000	1	x	x	x	x	x	x	x	✓	x	x	
SOS_0922_39	0.1	1	1	1	1E-05	1	1E-05	10	5000	1	x	x	x	x	x	x	x	✓	x	x	
SOS_0922_40	0.1	1	1	1	1E-05	1	1E-05	10	10,000	1	x	x	x	x	x	x	x	✓	x	x	
SOS_0922_41	0.1	1	1	1	1E-05	1	1E-05	10	10,000	1	F2	x	x	x	x	x	x	✓	x	x	
SOS_0922_42	0.1	1	1	1	1E-05	1	1E-05	15	10,000	1	x	x	x	x	x	x	x	✓	x	x	
SOS_0922_43	0.1	1	1	1	1E-05	1	1E-05	15	10,000	1	F2	x	x	x	x	x	x	✓	x	x	
SOS_0922_44	0.1	1.4	1	1	1E-05	1	1E-05	15	10,000	1	x	x	x	x	x	x	x	✓	x	x	
SOS_0922_46	0.1	1	1	1	1E-05	1	1E-05	15	10,000	1	x	✓	x	x	x	x	x	✓	x	x	
SOS_0922_47	0.1	1	1	1	1E-05	1	1E-05	15	10,000	1	F2	✓	x	x	x	x	x	✓	x	x	
SOS_0922_48	0.1	1.1	1	1.4	1E-05	1	1E-05	15	10,000	1	F2	✓	x	x	x	x	x	✓	x	x	
SOS_0922_49	0.5	1.1	1	1.4	1E-05	1	1E-05	15	10,000	1	F2	✓	x	x	x	x	x	✓	x	x	
SOS_0922_50	0.3	1.1	1	1.6	1E-05	1	1E-05	15	10,000	1	x	✓	x	x	x	x	x	✓	x	x	
SOS_0922_51	0.3	1.1	0.1	1	1E-05	1	1E-05	15	10,000	5,000	x	✓	x	x	x	x	x	✓	x	x	
SOS_0922_52	0.3	1.1	0.1	2	1E-05	1	1E-05	15	10,000	10,000	x	✓	x	x	x	x	x	✓	x	x	
SOS_0922_52	0.3	1.1	0.1	100	1E-05	1	1E-05	15	10,000	10,000	x	✓	x	x	x	x	x	✓	x	x	

VDB Case No.	LPZ mult	Mt. Simon mult	Argenta mult	PCB mult	All Faults transmissibility mult (except 2&3)	Fault 2 - transmissibility mult	Fault 3 - transmissibility mult	Perforation int (ft)	Fault 2 - Along fault, K (Mt. Simon)	Fault 2 - Along fault, K (Argenta+PCB)	Fault 9 = Fault 2 (F2)	Upper level of faults terminated at level of WB3	Cluster 5 fault	Cluster 15 fault	Fault 3	Fault 8	Cluster 10/13 fault	Constant CCS1 BHP	Selected faults- - Along fault, K ((Mt. Simon and Argenta)	Selected faults- - Along fault, K (PCB)	Short note
SOS_0922_53	0.3	1.1	0.1	50	1E-05	1	1E-05	15	10,000	10,000	x	✓	x	x	x	x	x	✓	x	x	
SOS_0922_54	0.3	1.1	0.1	10	1E-05	1	1E-05	15	10,000	10,000	x	✓	x	x	x	x	x	✓	x	x	
SOS_110922_1	0.3	1.1	0.1	1	1E-05	1	1E-05	15	10,000	10,000	x	✓	x	x	x	x	x	✓	x	x	
SOS_110922_1_1	0.3	1.1	1	1	1E-05	1	1E-05	15	10,000	10,000	x	✓	x	x	x	x	x	✓	x	x	
SOS_110922_1_0	0.3	1.1	0.1	20	1E-05	1	1E-05	15	10,000	10,000	x	✓	x	x	x	x	x	✓	x	x	
SOS-110922_2	0.3	1.1	0.5	2	1E-05	1	1E-05	15	10,000	10,000	x	✓	x	x	x	x	x	✓	x	x	
SOS_110922_3	0.3	1.1	0.1	1.6	1E-05	1	1E-05	15	10,000	1	x	✓	x	x	x	x	x	✓	x	x	
SOS_110922_5	0.3	1.1	1	1	1E-05	1	1E-05	15	10,000	10,000	F2	✓	F2	F2	x	x	x	✓	x	x	
SOS_110922_6	0.3	1.1	1	1	1E-05	1	1E-05	15	5,000	5,000	F2	✓	F2	F2	x	x	x	✓	x	x	
SOS_110922_7	0.3	1.1	1	2	1E-05	1	1E-05	15	10,000	10,000	F2	✓	F2	F2	x	x	x	✓	x	x	
SOS_110922_8	0.3	1.1	2	1	1E-05	1	1E-05	15	10,000	10,000	F2	✓	F2	F2	x	x	x	✓	x	x	
SOS_110922_9	0.3	1.1	1	1	1E-05	1	1E-05	15	2,000	2,000	F2	✓	F2	F2	x	x	x	✓	x	x	
SOS_110922_10	0.3	1.1	2	1	1E-05	1	1E-05	15	2,000	2,000	F2	✓	F2	F2	x	x	x	✓	x	x	
SOS_110922_11	0.3	1.1	1	2	1E-05	1	1E-05	15	2,000	2,000	F2	✓	F2	F2	x	x	x	✓	x	x	
SOS_110922_12	0.3	1.1	0.1	1	1E-05	1	1E-05	15	2,000	2,000	F2	✓	F2	F2	x	x	x	✓	x	x	

VDB Case No.	LPZ mult	Mt. Simon mult	Argenta mult	PCB mult	All Faults transmissibility mult (except 2&3)	Fault 2 - transmissibility mult	Fault 3 - transmissibility mult	Perforation int (ft)	Fault 2 - Along fault, K (Mt. Simon)	Fault 2 - Along fault, K (Argenta+PCB)	Fault 9 = Fault 2 (F2)	Upper level of faults terminated at level of WB3	Cluster 5 fault	Cluster 15 fault	Fault 3	Fault 8	Cluster 10/13 fault	Constant CCS1 BHP	Selected faults- - Along fault, K ((Mt. Simon and Argenta)	Selected faults- - Along fault, K (PCB)	Short note
SOS_110922_12	0.3	1.1	0.1	1	1E-05	1	1E-05	15	2,000	2,000	F2	✓	F2	F2	x	x	x	✓	x	x	
SOS_110922_12_0	0.3	1.1	0.1	1	1E-05	1	1E-05	15	1,000	1,000	F2	✓	F2	F2	x	x	x	✓	x	x	
SOS_110922_12_1	0.3	1.1	0.1	1	1E-05	1	1E-05	15	2,000	2,000	F2	✓	F2	F2	x	x	x	✓	x	x	Kz only
SOS_110922_12_1_1	0.3	1.1	1	1	1E-05	1	1E-05	15	1,000	1,000	F2	✓	F2	F2	x	x	x	✓	x	x	
SOS_110922_13	0.3	1.1	0.1	2	1E-05	1	1E-05	15	2,000	2,000	F2	✓	F2	F2	x	x	x	✓	x	x	
SOS_110922_14	0.3	1.1	0.01	2	1E-05	1	1E-05	15	2,000	2,000	F2	✓	F2	F2	x	x	x	✓	x	x	
SOS_110922_15	0.3	1.1	1	1	1E-05	1	1E-05	15	x	x	x	x	x	x	x	x	x	✓	x	x	
SOS_110922_16	0.3	1.1	1	2	1E-05	1	1E-05	15	2,000	2,000	F2	✓	F2	F2	✓	✓	✓	✓	x	x	
SOS_110922_17	0.3	1.1	0.1	1	1E-05	1	1E-05	15	2,000	2,000	F2	✓	x	x	x	x	x	✓	x	x	
SOS_110922_18	0.3	1.1	1	2	1E-05	1	1E-05	15	2,000	2,000	F2	✓	x	x	x	x	x	✓	x	x	
SOS_110922_18_0	0.3	1.1	1	1	1E-05	1	1E-05	15	10,000	10,000	x	✓	x	x	x	x	x	✓	x	x	
SOS_110922_19	0.3	1.1	0.1	1	1E-05	1	1E-05	15	100	100	F2	✓	F2	F2	x	x	x	✓	x	x	
SOS_110922_19_1	0.3	1.1	1	1	1E-05	1	1E-05	15	100	100	F2	✓	F2	F2	x	x	x	✓	x	x	
SOS_110922_20	0.3	1.1	1	1	1E-05	1	1E-05	15	500	500	F2	✓	F2	F2	x	x	x	x	x	x	
SOS_110922_21	0.3	1.1	1	1	1E-05	1	1E-05	15	300	300	F2	✓	F2	F2	x	x	x	x	x	x	

VDB Case No.	LPZ mult	Mt. Simon mult	Argenta mult	PCB mult	All Faults transmissibility mult (except 2&3)	Fault 2 - transmissibility mult	Fault 3 - transmissibility mult	Perforation int (ft)	Fault 2 - Along fault, K (Mt. Simon)	Fault 2 - Along fault, K (Argenta+PCB)	Fault 9 = Fault 2 (F2)	Upper level of faults terminated at level of WB3	Cluster 5 fault	Cluster 15 fault	Fault 3	Fault 8	Cluster 10/13 fault	Constant CCS1 BHP	Selected faults- - Along fault, K ((Mt. Simon and Argenta)	Selected faults- - Along fault, K (PCB)	Short note
SOS_110922_22	0.3	1.1	1	1	1E-05	1	1E-05	15	300	10	F2	✓	F2	F2	x	x	x	x	x	x	PCB zone, K=300 mD
SOS_110922_23	0.3	1.1	1	1	1E-05	1	1E-05	15	300	x	F2	✓	F2	F2	x	x	x	x	x	x	PCB zone, K=300 mD
SOS_110922_24	0.3	1.1	1	1	1E-05	1	1E-05	15	1000	1	F2	✓	F2	F2	x	x	x	x	x	x	PCB zone, K=1000 mD
SOS_110922_25	0.3	1.1	0.1	1	1E-05	1	1E-05	15	1000	1	F2	✓	F2	F2	x	x	x				PCB zone, K=1000 mD
SOS_110922_26	0.3	1.1	0.1	1	1E-05	1	1E-05	15	1000	1	F2	ü	F2	F2	x	x	x				
SOS_110922_27	0.3	1.1	0.1	1	1E-05	1	1E-05	15	1000	0.1	F2	ü	F2	F2	x	x	x	ü	–	–	
SOS_110922_28	0.3	1.1	0.1	1	1E-05	1	1E-05	15	1000	0.1	F2	ü	F2	F2	x	x	x	ü	–	–	Made fault _9 trans =1
SOS_110922_29	0.3	1.1	0.1	1	1E-05	1	1E-05	15	2000	0.1	F2	ü	F2	F2	x	x	x	ü	–	–	Made fault _9 trans =1
SOS_110922_30	0.3	1.1	0.1	1	1E-05	1	1E-05	15	2000	0.1	F2	ü	F2	F2	x	x	ü	ü	–	–	Made fault _9 trans =2
SOS_110922_31	0.3	1.1	0.1	1	1E-05	1	1E-05	15	2000	0.1	F2	ü	F2	F2	x	x	ü	ü	–	–	Made fault _9 trans =3
SOS_110922_32	0.3	1.1	0.1	1	1E-05	1	1E-05	15	2000	0.1	F2	ü	F2	F2	x	x	ü	ü	–	–	Made fault 9 trans = 1 & connected clusters 10 and 15 faults
SOS_110922_33	0.3	1.1	0.1	1	1E-05	1	1E+00	15	2000	0.1	F2	ü	F2	F2	F2	F2	F2	ü	–	–	Made fault 9 trans = 1 & connected clusters 10 and 15 faults
SOS_110922_34	0.3	1.1	0.1	1	1E-05	1	1E-05	15	1000	0.1	F2	ü	F2	F2	F2	F2	F2	ü	–	–	Added faults 1, 10, and 17 and assigned F2 perm values

VDB Case No.	LPZ mult	Mt. Simon mult	Argenta mult	PCB mult	All Faults transmissibility mult (except 2&3)	Fault 2 - transmissibility mult	Fault 3 - transmissibility mult	Perforation int (ft)	Fault 2 - Along fault, K (Mt. Simon)	Fault 2 - Along fault, K (Argenta+PCB)	Fault 9 = Fault 2 (F2)	Upper level of faults terminated at level of WB3	Cluster 5 fault	Cluster 15 fault	Fault 3	Fault 8	Cluster 10/13 fault	Constant CCS1 BHP	Selected faults- - Along fault, K ((Mt. Simon and Argenta)	Selected faults- - Along fault, K (PCB)	Short note
SOS_110922_35	0.3	1.1	0.1	1	1E-05	1	1E-05	15	1000	0.1	F2	ü	F2	F2	F2	F2	F2	ü	–	–	Added all faults interpreted from microseismic clusters
SOS_110922_36	0.3	1.1	0.1	1	1E-05	1	1E-05	15	1000	0.1	F3	ü	F2	F2	F2	F2	F2	ü	–	–	Added all faults interpreted from microseismic clusters, and extended N-S and E-W long faults to model boundary
SOS_110922_37	0.3	1.1	0.1	1	1E-05	1	1E-05	15	1000	0.1	F2	ü	F2	F2	x	x	x	ü	–	–	Cluster fault perm (diagonal ones)= 500 mD